Architectured cellular and bulk ceramic materials based on SiC and graphene/SiC with enhanced transport properties

Memoria presentada por:

Benito Román Manso

Para optar al título de Doctor en Ciencias Físicas

Directores:

Prof. Mª Pilar Miranzo López

Dr. Manuel Belmonte Cabanillas

Instituto de Cerámica y Vidrio (ICV-CSIC)

Madrid, 2015

Esta tesis doctoral ha sido realizada en el Instituto de Cerámica y Vidrio (ICV-CSIC) y ha sido financiada por el proyecto MAT 2009-09600, y la beca FPI nº BES-2010-041382, del Gobierno de España. El autor agradece al Consejo Superior de Investigaciones Científicas (CSIC) y a la dirección del Instituto de Cerámica y Vidrio (ICV) por permitir la realización de esta memoria.

Esta memoria de tesis doctoral cumple con los requisitos necesarios para obtener la mención internacional en el Título de Doctor que se describen en la normativa de enseñanzas universitarias de doctorado de la Universidad Autónoma de Madrid y que han sido establecidos en el artículo 15 del Real Decreto 99/2011 que establece la Ordenación de las Enseñanzas Universitarias Oficiales (BOE nº 35 de 28 de enero de 2011, páginas 13909-13926). La presente memoria de tesis doctoral ha sido informada por dos doctores que pertenecen a Instituciones de Educación Superior de Estados miembros de la Unión Europea distintos de España:

Dr. Rui Ramos Ferreira e Silva

Institución: Departamento de Engenharia de Materiais e Cerâmica (CICECO), Universidade de Aveiro, Portugal.

Dr. Jesús González Julián

Institución: Institute for Energy and Climate Research (IEK-1), Forschungszentrum Jülich GmbH, Alemania

A mis padres y a mi hermana.

Agradecimientos / Acknowledgements

En primer lugar, quiero mostrar mi más sincero agradecimiento a mis directores de tesis: la Prof. Pilar Miranzo y el Dr. Manuel Belmonte. Por el afecto personal, por todo el tiempo desinteresado que me habéis dedicado, por lo que he podido aprender de vosotros; y también por la generosidad conmigo desde el primer día. Para lograr esta tesis, y muchas cosas más, nada hubiera sido igual sin vosotros. De corazón: ¡Muchísimas gracias!

Al Prof. Leonardo Soriano, por aceptar la tutela de esta tesis en la Universidad Autónoma de Madrid, y también por haberme facilitado siempre las cosas. También a toda la gente del módulo C-XII de la UAM con la que compartí buenísimos momentos.

I frankly acknowledge the excellent scientific and personal support that I received from my supervisors outside the ICV-CSIC:

Dr. Jim Smay in the Oklahoma State University, Stillwater, USA. He opened for me the way to 3D printing, and introduced me in the American lifestyle that I so much liked.

Dr. Ángel Luis Ortiz in the Universidad de Extremadura, Badajoz. Estuve en Badajoz como en casa gracias a Ángel y al magnífico grupo, lo disfruté muchísimo.

Dr. Filipe Figueiredo, in the Universidade de Aveiro, Portugal. Foi um prazer enorme aprender as técnicas de caracterização elétrica e, mais ainda, desfrutar da tua conversa e amizade.

I am really appreciative to the three of you for your help at all times.

I am also very glad to have enhanced my research activities with great scientific collaborators and extraordinary people that I had the chance to work with, and whom are gratefully recognized:

Prof. Carmen Ocal, and collaborators, from the ICMAB, Barcelona for the AFM technique.

Dr. Hanus Seiner, and also Prof. Michal Landa, Dr. Petr Sedlak and Dr. Alena Kruisova, from the Institute of Thermomechanics in Prague, for the RUS measurements.

Prof. Mauricio Terrones, Dr. Aarón Morelos and Dr. Sofía Vega, from the Shinshu University, Japan, for the carbon nanotubes growth.

Prof. Claas Mueller and Florian Zeller in the IMTEK, Freiburg University in Germany, for the EDM tests.

And also Cai, Yang and Lukasz at the Oklahoma State University; Hugo, Estíbaliz, Azadeh, Siamak, Pedro, Antonia and Fernando in Badajoz; Eddy and Paula in Aveiro; and Rafa and Bea in Madrid.

Agradecimiento que extiendo -técnica y humanamente- a todos los actuales miembros del grupo de Cerámica Técnica del ICV-CSIC, por su apoyo en todo: Maribel, Toña, Ángel, Eugenio, Javi y Andrés. Y a los fantásticos becarios que lo fueron cuando llegué: Cristina, Suso y Joana.

A todo el personal del ICV en general, por lo que he aprendido trabajando aquí. Quiero acordarme de todos/as los/as compañeros/as del departamento de Cerámica en general, de los reólogos Rodrigo y Maribel, de la gente de vidrios (Alicia, Chus, Eva, Domingo, Berta, Yoli…), de técnicos siempre dispuestos (Luque, Marisa, Luis, Soco, José Manuel, Adolfo, Sara, Sandra, David, Carmen…) y, por supuesto, de becarios como Sonia, Laura, Esther, Juli, Carlos, Juan, Ana, Zoilo, Miguel, Yhasmin, María... Y de otros que, aunque ya se fueron del instituto, conservo su recuerdo y amistad.

La familia: lo mejor que tengo. Además de los tres a quiénes dedico esta tesis, que los quiero tantísimo, a mi maravillosa abuela, a mis tíos (Petri, Irene, Mari, Angel, Conchi, y parejas), y primos. Tan atentos, simpáticos y cariñosos conmigo siempre.

Y a amigos que dan a la vida sentido y que lo harán por mucho tiempo: Raquel, Luis, Juan, Rober, Víctor, Mario, Héctor, David, Abel… Si llegáis a leer esto, es simplemente que no podíais faltar. Y a otros más, que por falta de espacio no cito.

Gracias a todos.

Index / Índice

Introduction

Silicon carbide (SiC) is a covalent compound with a rich polytypism most importantly employed for the fabrication of structural ceramics. Properties such as high elastic modulus, high hardness and high strength, all of which are maintained at intermediate and high temperatures, and the high resistance to oxidation, corrosion, abrasion and wear, among others, make SiC an extraordinary candidate for mechanical engineering components, in particular, as valves, mechanical seals, bearings, also for refractories (bricks, crucibles, …), thermal management systems like heat exchangers.

Over the last decades, growing interest has emerged for the manufacture of SiC ceramics. The strongly covalent nature of the C-Si bond, on account of which SiC displays some of the above-mentioned properties, appears also as a limitation for the sinterability of SiC powders due to a reduced atomic mobility; therefore, the addition of sintering additives has normally been attempted to overcome this deficiency. Frequently, conventional sintering techniques have been employed involving very high temperatures, above 1950 ºC, as well as mechanical or gas pressures to favor densification of SiC ceramics. Nowadays, the use of more modern sintering techniques is emerging to promote faster and more energetically efficient processes, and Spark Plasma Sintering (SPS) stands out among the group of the so-called electric current assisted sintering techniques. This method consists in the sintering of materials under the application of electric direct current pulses that induces the in-situ heating by the Joule effect of the graphite die, and the sample in the case of conductive materials, while a mechanical uniaxial pressure is simultaneously applied. SPS is more and more being considered for the sintering of SiC to obtain finer microstructures, although the influence of sintering parameters and the addition of sintering additives on the microstructure and final properties of these SPSed SiC materials is not completely known yet. In this PhD Thesis, the effects of the starting SiC particle size, SiC polytype and the electric current distribution on the sintering process and on the final microstructure and properties of SiC ceramics with Y_2O_3-Al_2O_3 additives have been addressed. For that purpose, the evolution of the current, voltage and the whole system resistance along the sintering process have been analyzed. Special attention has been paid to the possibility of in-situ growing graphene within the SiC matrix during SPS by the decomposition of SiC grains.

Nowadays, cellular ceramics are highly appreciated due to some specific structural properties: low density, large exposed surface and, especially, relatively high mechanical resistance. SiC is commonly used in a cellular form in energy storage/conversion systems, filters or supports for catalysts. The production of SiC-based cellular ceramics has habitually been focused on foams and honeycombs, by the utilization of production methods like sacrificial templates, replicas or direct foaming techniques. However, new added values such as a precise control over the porosity channels, the pore size or periodicity in more complex cellular SiC materials can potentially be attainable by additive manufacturing (AM). AM techniques include those in which the prototypes are formed by continuously adding or attaching material so that the final three-dimensional (3D) shape is obtained avoiding the use of molds, or machining processes. Modern AM procedures implement the equipment with advanced technology based on computer-controlled operation that allows the reproducibility of designs and a high level of accuracy for the smallest possible feature sizes. So far, few SiC prototypes have been created by AM techniques mainly by reaction-sintering methods, either with preceramic polymers or with reaction-bonding by infiltration of silicon. These types of structures have certain limitations regarding porosity, in the case of preceramics, and residual silicon, for reaction bonded processes. Therefore, the development of 3D structures by AM techniques from SiC powders and their subsequent sintering appears as a great challenge. In the present PhD Thesis, the knowledge on bulk SiC-based ceramics is transferred to the development of 3D SiC architectures by Robocasting from a design generated in a computer aided drafting (CAD) program. Robocasting is a filament-based manufacturing method that stands as one of the most versatile, cutting-edge AM techniques. The major difficulty is the development of the aqueous colloidal gels adequate for the printing process: with high solids loading, pseudoplastic rheology and low organic additives concentrations.

Recently, graphene fillers (GFs) have attracted great interest for improving the properties of materials, in particular, of ceramics and polymers, owing to the extraordinary electrical, thermal, tribo-mechanical and elastic properties provided by graphene, the monolayer of carbon atoms. In fact, the incorporation of graphene nanoplateles (GNPs) to some ceramics has significantly improved their mechanical and tribological properties, additionally endowing with electrical and thermal functionalities. Furthermore, the crystallographic and morphological anisotropy of the GFs and their trend to become oriented within the bulk composite when pressure-assisted fabrication methods are employed (e.g. consolidation by SPS) would

produce composites with highly anisotropic properties, which may broaden their field of application. A comprehensive examination of the sintering of SiC matrices containing GNPs, and its expected influence on a functionalization of the SiC ceramic matrix, one of the goals of this PhD Thesis, has not been reported hitherto. Thus, the emergence of a study devoted to the processing of GNPs/SiC ceramic composites and their characterization is of paramount importance. In this way, the fabrication of this sort of composites with GNPs contents of up to 20 vol.% has been addressed in both bulk and cellular materials, analyzing transport properties, mainly the electrical performance and also the thermal properties in the case of bulk materials. The electrical conduction of architectured GNPs/ceramic composites has been experimentally determined as well as simulated by using both a simple resistors model and the finite-elements method (FEM) to predict the scaffolds electrical conductivity as a function of the GNPs content.

As summary, this work intends to open a research line for the development of complex structures of functional SiC ceramics and graphene/SiC composites sintered by SPS. The combination in one material of the robustness and electrical and thermal conductivities of graphene-ceramic composites with the intrinsic characteristics of macroporous 3D structures, such as low specific weight, high specific surface area or the feasibility of hierarchical designs, has several potential advantages. These 3D composite structures are expected to present some benefits with respect to analogous graphene structures, as the ceramics would provide mechanical stability and also protection of graphene from wear damage, corrosion and thermal degradation, widening the range of application of cellular SiC materials in energy storage/conversion systems or as supports for electrocatalysis membranes and gas sensors.

The present PhD manuscript has been organized following the next scheme:

I. In Chapter 1, the state-of-the-art of the principal materials involved in this PhD Thesis has been prepared. Specifically, this chapter is focused on SiC-based materials, their properties and applications, sintering methods with especial concern for SPS, cellular SiC materials, and graphene as filler for ceramic matrices.

II. The Chapter 2 covers the AM methods, with remarkable attention for Robocasting, as one of the most emerging AM techniques, especially regarding SiC parts. Results on designing and development of SiC and GNPs/SiC inks for robocasting are

presented, as well as on the robocasting of computer designed architectures for SiC and GNPs-SiC inks.

III. In Chapter 3, results covering the SPS of all SiC-based materials developed in this PhD Thesis are presented including the following topics: i) densification of SiC ceramics from different starting powders, which show different grain sizes and polytypes; ii) analysis of the mechanism for in-situ growth of graphene at the SiC grain boundaries during SPS; iii) improvement of the efficiency of the SPS process by modifying the electric current paths during the sintering process; iv) the densification of SiC-based ceramic composites with GNPs contents of up to 20 vol.% and finally, the sintering by SPS of cellular 3D-structures based on analogous compositions to those of the bulk materials.

IV. In Chapter 4, the contact-mechanical properties for materials processed from different SiC starting powders, i.e., α-SiC, β-SiC and nano-β-SiC, are determined through Hertzian indentation tests at intermediate and elevated temperatures. In addition, considering the conductive nature of the in-situ grown graphene/SiC composites, the electrical conductivity has been deeply analyzed, including the use of nano-scale scanning probes to differentiate the graphene components and their spatial distribution.

V. The transport properties (thermal and electrical conductivities) of the GNPs/SiC bulk composites are presented in Chapter 5, and analyzed as a function of the GNPs content and temperature, elucidating the transport mechanisms with the aid of models.

VI. In Chapter 6, the electrical transport properties of robocast 3D architectures containing GNPs are shown and discussed considering the properties of the corresponding bulk composites. Models based on simple equivalent resistors circuits and finite element analysis are proposed to reproduce the electrically conductive behavior of these geometrically complex structures.

VII. Future prospects and applications for the SiC-based ceramics and composites developed within this research are explored in Chapter 7, pointing towards the relevance of possible applications for forthcoming studies in SiC materials. In particular, superhydrophobic advanced oil filtration hybrid devices are developed by the growth of multiwalled carbon nanotubes on SiC scaffolds using chemical vapor deposition techniques, or acoustic SiC metamaterials are created by Robocasting showing strong energy focusing and a phononic-like frequency band structure.

VIII. Finally, three annexes have been added at the final part of the manuscript. The first one summarizes the main methods and techniques employed for the experimental work, the second is a list of acronyms and abbreviations used in the manuscript, and the third is the list of publications for the dissemination of the scientific results obtained in this PhD Thesis.

Introducción

El carburo de silicio (SiC) es un material covalente con una rica variedad de politipos que se emplea fundamentalmente para la fabricación de materiales cerámicos estructurales. El SiC es un excelente candidato para ser utilizado en componentes de ingeniería como válvulas y sellos de cierre mecánico, rodamientos, refractarios (ladrillos, crisoles,...), sistemas térmicos como intercambiadores de calor, o en polvo como abrasivo. Entre sus propiedades destacan un elevado módulo elástico, alta dureza y resistencia mecánica, las cuales se mantienen a temperaturas intermedias y altas, así como una elevada resistencia a la oxidación, corrosión, abrasión y desgaste.

En las últimas décadas ha surgido un interés cada vez mayor por la fabricación de cerámicos de SiC. La naturaleza fuertemente covalente del enlace C-Si, que da origen a las propiedades anteriormente mencionadas, representa también una limitación para la sinterización de polvos de este material debido a su reducida movilidad atómica; por ello, para contrarrestar este problema, se añaden habitualmente aditivos de sinterización. Las técnicas convencionales de sinterización que se han empleado hasta la fecha utilizan temperaturas muy elevadas, por encima de 1950 ºC, así como presiones mecánicas o de gas para favorecer la densificación de los materiales de SiC. Hoy en día, las técnicas de sinterización que promueven procesos más rápidos y eficientes energéticamente están teniendo un gran auge, destacando la técnica de sinterización por corriente eléctrica pulsada (en inglés “Spark Plasma Sintering”, SPS) dentro del grupo de las denominadas técnicas de sinterización asistida por corriente eléctrica. El SPS consiste en la sinterización de polvos compactados mediante pulsos de corriente eléctrica directa que producen el calentamiento por efecto Joule del troquel de grafito donde se encuentran confinados los polvos, y de la muestra en el caso de materiales conductores, mientras se aplica simultáneamente una presión mecánica uniaxial. El empleo del SPS para sinterizar SiC ha aumentado progresivamente con el fin de obtener microestructuras más finas y reducir tiempos y temperaturas de sinterización. Sin embargo, la influencia de los diversos parámetros de SPS y el papel de los aditivos de sinterización en la microestructura y en las propiedades finales de estos materiales de SiC aún no se han establecido. Por tanto, en esta tesis doctoral, se ha estudiado el efecto del tamaño de partícula y del politipo de SiC, así como de la distribución de corriente eléctrica en el SPS, sobre el proceso de sinterización, la microestructura y las

propiedades finales de las cerámicas de SiC, empleando Y_2O_3-Al_2O_3 como sistema de aditivos. Para ello, se ha analizado la evolución de la corriente, el voltaje y la resistencia eléctrica del sistema durante el proceso de SPS. Además, se ha prestado especial atención a la posibilidad de crecer grafeno in situ en la matriz de SiC durante el proceso de SPS mediante la descomposición de los granos de SiC.

Hoy en día las cerámicas celulares son muy apreciadas debido a sus propiedades estructurales específicas: baja densidad, grandes áreas superficiales expuestas y, sobre todo, resistencia mecánica relativamente alta. El SiC se ha utilizado comúnmente en forma celular en sistemas de almacenamiento/conversión de energía, filtros o como soporte para catalizadores. La producción de cerámicas celulares basadas en SiC se ha centrado habitualmente en el desarrollo de esponjas y estructural tipo panal de abeja mediante métodos de producción tales como el basado en el uso de patrones fugitivos, la impregnación de esponjas poliméricas con suspensiones cerámicas, o las técnicas de espumado. Sin embargo, las técnicas de fabricación aditiva (en inglés “additive manufacturing”, AM) permiten lograr nuevos valores añadidos en los materiales celulares, como son el control preciso sobre los canales de porosidad (tamaño de poro, periodicidad,…). Las técnicas de AM son aquéllas en las que los prototipos se conforman mediante la adición o fijación continua de material en verde de modo que se obtiene la forma tridimensional (3D) final, evitando el uso de moldes o procesos de mecanizado. Las técnicas modernas de AM se implementan con equipos con tecnología avanzada basados en un funcionamiento robotizado que permite la reproducibilidad de los diseños y un alto nivel de precisión en estructuras pequeñas. Hasta ahora, el desarrollo de componentes de SiC empleando técnicas de AM es muy limitado y se centra principalmente en métodos de sinterización por reacción, bien a partir de polímeros precerámicos bien infiltrando silicio en una preforma. Estas estructuras tienen ciertas limitaciones en cuanto a porosidad, en los casos derivados del uso de polímeros precerámicos, y en cuanto a silicio residual, cuando el proceso es por infiltración. Por tanto, el gran desafío que se plantea es el desarrollo de estructuras 3D mediante técnicas de AM a partir de polvos de SiC y su posterior sinterización. El conocimiento adquirido en cerámicas masivas de SiC se ha transferido al desarrollo de arquitecturas cerámicas 3D de SiC mediante colaje controlado por ordenador, o “Robocasting” en su terminología inglesa. La técnica de Robocasting es una de las más versátiles y vanguardista dentro del grupo de AM, y consiste esencialmente en el conformado de materiales a partir de la extrusión continua de una tinta en forma de filamento. La mayor dificultad ha sido, por tanto, el desarrollo de tintas coloidales

acuosas, de alto contenido en sólidos y baja concentración de aditivos orgánicos, con las características reológicas adecuadas.

La incorporación de nanoestructuras basadas en grafeno, la monocapa de átomos de carbono, como fase dispersa en matrices cerámicas y poliméricas ha adquirido recientemente un gran interés para mejorar las propiedades de estos materiales debido a las extraordinarias propiedades eléctricas, térmicas, tribo-mecánicas y elásticas del grafeno. De hecho, la incorporación de nanoplaquetas de grafeno (en inglés “graphene nanoplatelets”, GNPs) en el seno de algunas matrices cerámicas ha dado lugar a mejoras significativas en sus propiedades mecánicas y tribológicas, dotando además a estos cerámicos de funcionalidades eléctrica y térmica adicionales. Asimismo, la anisotropía morfológica y cristalográfica de las GNPs y su tendencia a orientarse dentro de las matrices cerámicas cuando se emplean métodos de fabricación asistida por presión mecánica, como en el caso del SPS, dan lugar a materiales compuestos con propiedades altamente anisótropas, lo cual permitiría ampliar su campo de aplicación. Así, esta tesis doctoral también tiene como objetivo el examen exhaustivo de los procesos de sinterización de los materiales cerámicos de SiC conteniendo GNPs, y el efecto de éstas en la funcionalización de la matriz cerámica, lo que hasta la fecha no se ha descrito en la literatura. Por lo tanto, la fabricación de este tipo de materiales con contenidos de GNPs de hasta el 20 vol.% ha sido abordada tanto para materiales masivos como para materiales celulares, así como el análisis de sus propiedades de transporte, principalmente el comportamiento eléctrico, y también térmico en el caso de materiales masivos. La conducción eléctrica de los estructuras 3D de compuestos GNPs/SiC se ha determinado experimentalmente y, además, se ha simulado con modelos simples de resistencias y por métodos de elementos finitos para predecir la conductividad eléctrica de este tipo de estructuras en función del contenido de GNPs.

En resumen, se puede decir que esta tesis pretende abrir una nueva línea de investigación para el desarrollo de estructuras complejas de cerámicos funcionales de compuestos cerámicos con grafeno. La combinación en un único material de la resistencia y la conductividad eléctrica y térmica de los materiales compuestos de grafeno/cerámico con las características intrínsecas de las estructuras macroporosas en 3D, tales como baja densidad, alta superficie específica o viabilidad de diseños jerárquicos, presentan numerosas ventajas potenciales. Se espera que estas estructuras 3D compuestas muestren ciertos beneficios respecto a estructuras análogas formadas exclusivamente por grafeno, como son la estabilidad mecánica que proporcionaría la matriz cerámica, así como la protección del grafeno frente al

desgaste, la corrosión o la degradación térmica. Esto permitiría ampliar el rango de aplicación de los materiales de SiC celulares a sistemas de almacenamiento o conversión de energía, o como soportes para membranas de electrocatálisis y sensores de gas.

El manuscrito de la tesis doctoral se ha organizado de acuerdo con el siguiente esquema:

I. En el Capítulo 1 se ha elaborado una revisión del estado del arte de los materiales de esta tesis doctoral. Este capítulo se centra específicamente en: i) los materiales basados en SiC, sus propiedades y aplicaciones, asi como en los métodos de sinterización, dedicando especial atención al SPS, ii) los materiales de SiC celulares y, por último, iii) el grafeno como fase dispersa en matrices cerámicas.

II. En el Capítulo 2 se ha realizado un compendio de los métodos de AM, prestando especial atención al Robocasting como una de las técnicas de AM emergentes y al conformado de componentes de SiC mediante este tipo de técnicas. Se presentan resultados relativos al diseño y desarrollo de tintas de SiC y GNPs/SiC para Robocasting, así como al colaje por esta técnica de arquitecturas diseñadas por ordenador a partir de dichas tintas.

III. En el Capítulo 3 se muestran los resultados que engloban la sinterización por SPS de todos los materiales basados en SiC desarrollados en esta tesis doctoral, incluyendo las siguientes materias: i) densificación de los cerámicos de SiC empleando diferentes polvos de partida de SiC, los cuales presentan diferentes politipos y tamaños de grano; ii) análisis del mecanismo de crecimiento in situ de grafeno en las fronteras de grano de SiC durante el proceso de SPS; iii) mejora de la eficiencia energética del proceso de SPS mediante la modificación de los caminos de corriente eléctrica durante el proceso de sinterización; iv) densificación de compuestos cerámicos basados en SiC con contenidos de GNPs de hasta el 20% en volumen y; v) sinterización por SPS de estructuras 3D celulares basadas en composiciones análogas a las de los materiales masivos.

IV. En el Capítulo 4 se detalla el comportamiento frente al daño por contacto de los materiales de SiC procesados con los diferentes polvos de partida a través de ensayos de indentación hertziana a temperaturas intermedias y elevadas. Además, teniendo en cuenta la naturaleza conductora del grafeno crecido in situ en los materiales de SiC, la conductividad eléctrica han sido analizada, incluyendo el uso de

sondas de barrido a escala nanométrica para diferenciar los componentes de grafeno y su distribución espacial.

V. Las propiedades de transporte (conductividad térmica y eléctrica) de los materiales compuestos masivos de GNPs/SiC se presentan en el Capítulo 5. Estas propiedades se han analizado en función del contenido de GNPs y de la temperatura, desarrollando modelos para explicar los mecanismos de transporte.

VI. En el Capítulo 6 se muestran y discuten las propiedades eléctricas de las arquitecturas 3D fabricadas por Robocasting conteniendo GNPs, teniendo en cuenta para ello las propiedades de los materiales compuestos masivos correspondientes. Se han empleado modelos basados en circuitos de resistencias equivalentes y en el análisis de elementos finitos para reproducir el comportamiento conductor de estas estructuras geométricamente complejas.

VII. Las perspectivas de futuro de los cerámicos basados en SiC desarrollados en esta tesis doctoral se exploran en el Capítulo 7, incidiendo en algunas aplicaciones relevantes. En concreto, se muestran dispositivos híbridos desarrollados mediante el crecimiento por deposición química en fase vapor de nanotubos de carbono de pared múltiple sobre andamios 3D de SiC, los cuales presentan propiedades superhidrofóbicas que les permitiría ser empleados para el filtrado de aceite en agua; o la creación de metamateriales acústicos de SiC por Robocasting que muestran una fuerte focalización de la energía y unas estructuras de bandas de frecuencia similares a las de los fonones.

VIII. Finalmente, se han incluido tres anexos en la parte final del manuscrito. En el primero se resumen las principales técnicas experimentales y métodos empleados en esta tesis, en el segundo se proporciona una lista de acrónimos y abreviaturas utilizadas en el manuscrito, y el tercero es la lista de publicaciones mediante las que se han difundido los resultados científicos de la tesis.

Chapter 1

Silicon carbide-based ceramic materials and graphene fillers for ceramics

1.1.- Silicon carbide (SiC)

1.1.1.- Structure, polytypism and properties

Silicon carbide is the only possible compound at equilibrium resulting from the combination of silicon (Si) and carbon (C), as demonstrated by Olesinski and Abbaschian (phase diagram of the Si-C system shown in Fig. 1.1),[1] whose chemical formula is SiC. It has been very rarely found in nature as a mineral, and named moissanite after Henri Moissan was the first to synthesize SiC in an attempt to obtain synthetic diamonds.

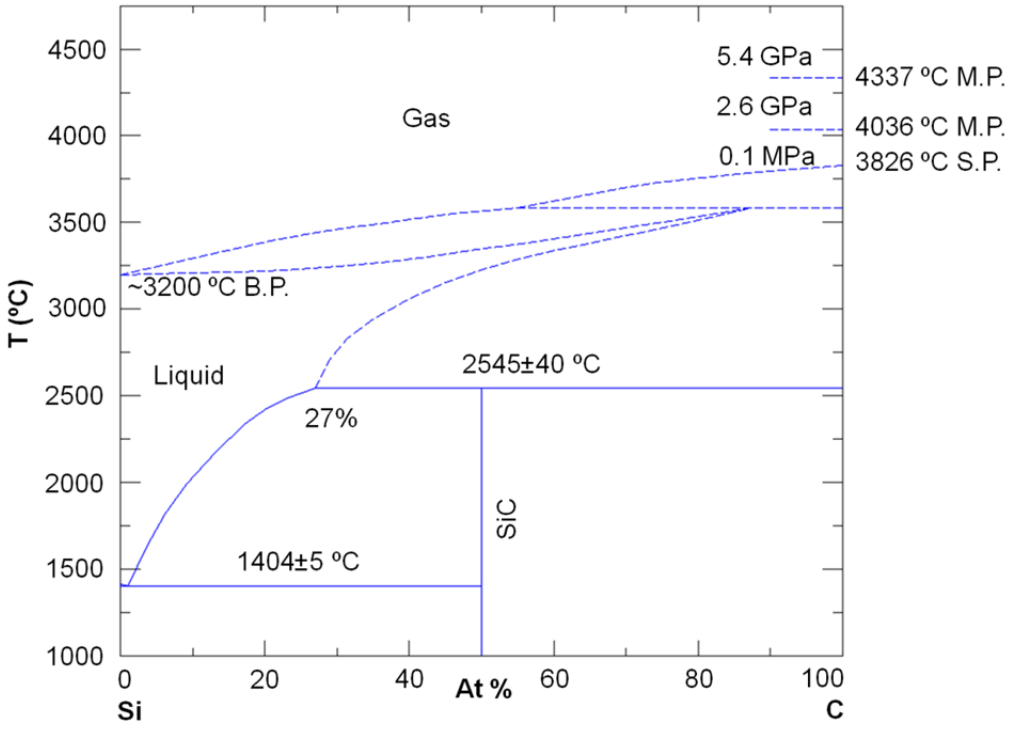

Figure 1.1.- The equilibrium phase diagram of the Si-C system.[1]

In SiC crystals, Si and C atoms present covalent bonds in a tetrahedral coordination, similarly as for most compounds belonging to the group IV of elements of the periodic table (Fig. 1.2). Tetrahedra are then set up with all atoms lying in parallel planes on hexagonal networks. This tetrahedral distribution of C and Si atoms still leaves certain degrees of freedom for the formation of different crystalline structures, which are essentially reflected in the different stackings of tetrahedra in one crystallographic direction. What distinguishes one polytypic structure from another is the repetition distance or, in other words, the stacking pattern of these identical layers.

Consequently, SiC is one of the compounds with a richer variety of polytypes and a set of up to 250 different polymorphs have been found.[2] Particularly, the most frequent and well-known polytypes are 3C, 2H, 4H, 6H, and 15R. The letters are related to the crystalline structure; thus, C, H and R stand for cubic, hexagonal and rhombohedral, respectively, and the digits (2, 3, 4, 6…) are associated to the number of atomic layers that define the lattice periodicity. A deep-rooted nomenclature for SiC polytypes is to classify them as β-SiC or α-SiC, being β-SiC the 3C polytype, and α-SiC the group formed by any of all the rest. At very high temperatures (comparable to the SiC sintering temperatures), α-SiC polytypes are more stable than β-SiC[3] and, therefore, polytypic transformations can be observed. With regard to the physical parameters of SiC polytypes, the most distinctive are the thermal conductivity and the band gap, as shown in Table 1.1. Actually, SiC behaves as a semiconductor with fairly large band gap energies ranging from ~2.4 to 3.4 eV.

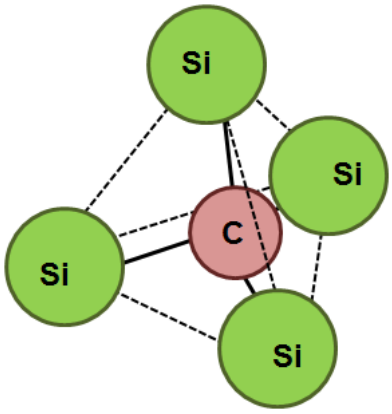

Figure 1.2.- Illustration of the tetrahedral coordination of C and Si atoms in a Si_4C tetrahedron, with the Si atoms at the vertices.

Table 1.1.- Physical properties of monocrystalline 3C-, 6H- and 4H-SiC polytypes.[4-6]

PROPERTY	**3C-SiC**	**6H-SiC**	**4H-SiC**
Lattice constant a (nm)	0.4359	0.3081	0.3081
Lattice constant c (nm)	-	1.5092	1.0061
Density ($g \cdot cm^{-3}$)	3.215	3.215	3.215
Band gap (eV)	2.39	3.0 - 3.1	3.26
Thermal conductivity ($W \cdot m^{-1} \cdot K^{-1}$)	360	490	490

SiC exhibits a distinctive combination of properties, such as high resistance to oxidation, corrosion, thermal shock or wear, high hardness and thermal conductivity and good mechanical stability up to high temperatures.[7-9] The highly covalent C-Si

bonds are accountable for all these properties, making it an ideal candidate for the manufacture of structural ceramics. This strong covalent bond presents, however, a problem for the manufacture of dense SiC bodies from SiC powders. Due to the extremely low diffusion coefficient, densification of powders is possible only at very high pressure and temperature (above 2100 °C). Thus, for an efficient densification of SiC, the use of sintering additives is required. These additives can commonly be classified either as additives to develop a solid-state sintering process (generally boron and carbon compounds) or liquid-phase-forming additives, which might be oxide (Al_2O_3, BeO, Y_2O_3 ...) or non-oxide (like AlN) compounds or a combination of both types. The main microstructural factors that affect the physical properties of SiC ceramic materials are the size of SiC grains, and the composition and amounts of grain boundary secondary phases, all of them closely related to the additives used to facilitate the sintering at high temperatures.

From the thermal conduction viewpoint, pure monocrystalline SiC crystals are highly conductive exhibiting a room temperature thermal conductivity of up to 490 $W \cdot m^{-1} \cdot K^{-1}$ in the case of α-SiC (Table 1.1).[10] However, the majority of experimentally obtained values evidence the presence of phonon-scattering processes that largely reduce thermal conductivity, most likely due to the presence of lattice defects and impurities (sometimes forming solid-solutions) and, also, as a consequence of the lower thermal conductivity of the grain boundary phase of polycrystalline SiC-based ceramics especially derived from liquid-phase-forming additives.

As stated before (Table 1.1), SiC is a semiconductor with a broad band gap. Generally, this sort of ceramics exhibits electrical conductivity dependent on the level of doping, with values within a range from 10^{-9} to 10^{5} $S \cdot m^{-1}$ depending on the type and amount of sintering additives used. In this regard, the case of sintering additives containing N is especially significant, since N atoms can easily be incorporated into the SiC lattice substituting for C in a diffusion process during sintering,[11] leading to higher electrical conductivities.

SiC mainly stands out as a structural material. Mechanical properties can be very different depending on the fabrication method, which may result in materials with different porosities, grain sizes, elongation of grains, type and amounts of secondary phases, doping, structural defects, etc. In Table 1.2, the main mechanical properties of SiC have been listed with the most frequently attained ranges.

Table 1.2.- Mechanical parameters of different SiC materials, and reported ranges.[5]

Elastic modulus (GPa)	400 - 500
Poisson's ratio	0.14 - 0.20
Shear modulus (GPa)	~ 195
Hardness (GPa)	18 - 30
Fracture toughness (MPa·$m^{1/2}$)	~ 2 - 5.4
Weibull modulus	2 - 12
Strength (MPa)	200 - 2200

1.1.2.- Manufacture

Several industrial processes have been designed to synthesize large amounts of SiC. Actually, more than a few patents have been registered where descriptions of different synthesis processes are put forward.[12-15] Cowles[12] and Acheson[13] were the first to obtain, in the XIX century, synthetic SiC and the production has been increased and improved ever since. The Acheson process consists in the transformation of carbon (usually derived either from coke, a solid fuel originated from bituminous coal, or petroleum coke) and SiO_2 at very elevated temperatures to fabricate SiC as a reaction product. Since 1896, after the patent by Acheson,[13] the process has been improved producing larger amounts of SiC more efficiently. Typically, a graphite rod (Fig. 1.3) is introduced within a refractory chamber acting as a resistive heater when an electric current is applied to this graphite core.[16] When the temperature at the core is sufficiently high (1700 ºC < T < 2500 ºC) to initiate the reactions, a layer of SiC surrounding the graphite resistance is formed, eventually resulting in a hollow cylinder around the void left by the graphite rod, rich in C, which is partially ejected as CO gas. In the inner parts of the SiC cylinder and the bordering areas on the outside, some unreacted materials can be found, including impurities insoluble in SiC.

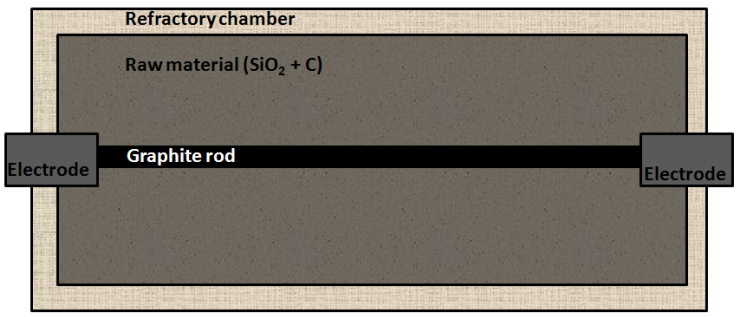

Figure 1.3.- Schematic illustration of a refractory chamber for the Acheson process.

The basic reactions that take place for the fabrication process are:[16]

$$C\ (s) + SiO_2\ (s) \rightarrow SiO\ (g) + CO\ (g) \quad (1)$$

$$SiO_2\ (s) + CO\ (g) \rightarrow SiO\ (g) + CO_2\ (g) \quad (2)$$

$$C\ (s) + CO_2\ (g) \rightarrow 2CO\ (g) \quad (3)$$

$$2C\ (s) + SiO\ (g) \rightarrow SiC\ (s) + CO\ (g) \quad (4)$$

The understanding of the interactions of gases is fundamental, since solid diffusion is not so high as to assume only the direct reactions between SiO_2 and C, being the large-scale use of waste gases still a challenge. Initially, small crystals of β-SiC are produced, which might transform into α-SiC if temperature rises above 1900 ºC. Salt is sometimes included within the mixtures to eliminate iron, forming volatile iron chlorides. Iron is a common impurity in SiO_2 materials and is useful here as a catalytic agent for reaction between C and CO_2; Fe is, moreover, insoluble in SiC and driven to the peripheral reaction areas. Other elements, soluble in SiC, can be found like B, N or Al. The presence of aluminum, for instance, favors the formation of the 4H polytype at the expense of 6H at T > 2000 ºC. Impurities can determine the color of the as-produced SiC crystals. Eventually, SiC is separated from the graphite and other reaction products. For the final achievement of specific properties, SiC can be crushed, sieved, often milled and chemically treated.

Beyond the Acheson process, a group of diverse manufacturing methods are at present exploited for the synthesis of SiC in view of precise applications like highly-crystalline electronic devices. In fact, as mentioned before, the high level of impurities in SiC associated to the Acheson process is the main drawback, and different approaches are required for the production of high purity SiC crystals, using techniques such as bulk large crystal growth, epitaxial layer growth for thin layers (both related to the Chemical Vapor Deposition (CVD) technique)[17,18] and ion beam synthesis, where carbon is implanted into silicon substrates.[19]

Finally, for the fabrication of SiC-based ceramics, the central route is the sintering of SiC powders (those generally obtained by the Acheson method), further explained in detail in Section 1.2. However, there are also other methods such as the use of preceramic polymers (silicon-containing polymers, namely polysilanes, polycarbosilanes, polysilazanes and polysiloxanes) which, after curing and pyrolytic steps, give way to SiC-based ceramic parts,[20-22] showing the advantage that the polymer preform can previously be shaped avoiding a costly machining.

Another important in-situ procedure to synthesize SiC-based parts is that known as reaction-bonding method. Normally, the product of these reactions is referred to as reaction bonded silicon infiltrated silicon carbide (SiSiC). The process for the fabrication of SiSiC ceramic composites starts by the forming of a compact that consists of graphite and polymeric surfactants and, sometimes, also SiC powders. Habitually, these complex porous green materials undergo a pyrolysis stage in an inert atmosphere to decompose organic additives and rearrange amorphous carbon. Next, the sample is infiltrated with liquid silicon; the process of infiltration consists in placing the C/SiC preforms in a crucible with a powders-bed of granulized silicon that melts upon heating above 1410 ºC, and then the liquid silicon penetrates through the material by capillary action; the formed C-Si liquid mixture becomes supersaturated in carbon and SiC precipitates.[23] The original SiC particles are introduced to act as nucleation sites for the precipitation of the formed SiC. The penetration of Si through the material depends on the pore size, the temperature and the morphology of the sample. The main advantages of this procedure are its quick development and cost-effectiveness.

1.1.3.- Applications

Initially, SiC powders manufactured by the Acheson process[13] were widely employed as an abrasive owing to its relatively low cost and prolonged durability; machining processes that involve abrasion like grinding or sandblasting make use of SiC as a primary material. Indeed, many works have been published where SiC is used as an abrasive.[24,25] Also, sandpapers based on SiC showing different particle sizes are habitually employed. Few years after the fabrication of synthetic SiC, elementary electronic applications were also envisaged: in 1907, the first observation of electroluminiscence by applying a voltage to a SiC crystal with yellow, green and orange emissions at the cathode was developed by H.J. Round, as a preliminary concept to the light-emitting diodes (LEDs). Definitely, SiC has been employed as a semiconductor for the accomplishment of electronic devices such as Schottky diodes[26] or metal-oxide-semiconductor field effect transistors (MOSFETs),[27,28] with distinctive features as compared to other semiconductors, like wider band gaps, and the endurance to high temperature and high power working conditions. However, the main drawback of SiC electronic devices is the presence of defects, especially plane dislocations, which induce undesired effects on the performance of these devices. Another disadvantage of SiC is to have an indirect band gap, which makes luminescence phenomena less efficient as compared to semiconductors with direct

band gap (like GaN). In spite of this, LEDs and blue diodes are regularly fabricated with 6H-SiC.[29,30]

On the basis of the wide range of different properties mentioned in the previous section, together with the high resistance to oxidation or wear, SiC-based ceramics have widely been used for industrial purposes, most importantly where mechanical engineering devices and components where required, especially at elevated temperatures. Therefore, SiC-based items such as valves,[31] mechanical sealings,[32] or bearings of high durability[33,34] have been manufactured. As an example, in Fig. 1.4 several SiC based components are shown. Also, the relatively high corrosion resistance and thermal conductivity have contributed to the use of SiC ceramics as refractories (bricks, tubes, crucibles, kiln shelves…) and for devices related to thermal management and storage, such as heat sinks or thermal storage systems.[35-37]

Figure 1.4.- Some commercial products (bearings, sealings, rolling elements) made of SiC. Images from www.hexoloy.com (left) and www.ceramtec.com (right).

Other structural applications for SiC are developed as ceramic plates in bulletproof vests and, most generally, as an armor material for various purposes.[38-40] Ceramic break discs have been the most important contribution of SiC-based ceramics (particularly, SiSiC materials or carbon fibers reinforced SiC composites) to the automotive industry.[41]

Cellular SiC components have been employed as particulate filters for the gaseous emissions of cars, filters for molten metals[42] and also as supports for catalytic chemical species[43,44] thanks to the strength and the oxidation resistance of these ceramics.[45,46] Also SiC-based cellular ceramics with improved thermal conductivity (have been employed in the manufacture of radiant burners and thermal flow management systems like heat sinks or heat exchangers (Fig. 1.5).[47]

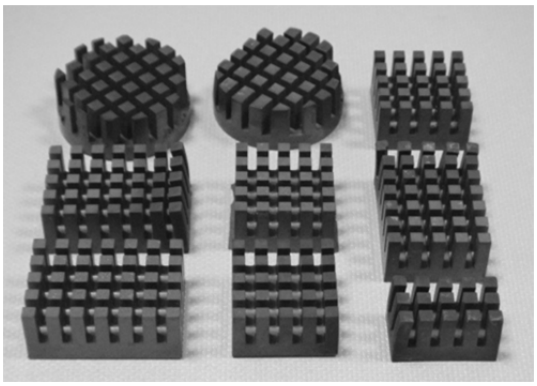

Figure 1.5.- Heat exchangers made of SiC intended with high thermal conductivity and emissivity (www.kallex.com.tw).

Less common applications include SiC optics (as a high-quality mirror for telescopes) based on the high elastic modulus and low thermal expansion of SiC grown by CVD.[48,49]

1.2.- Sintering of SiC-based ceramic materials

In order to obtain a good densification of SiC as a structural ceramic material, conventional sintering techniques such as Pressureless Sintering (PS), Hot Pressing (HP), Hot Isostatic Pressing (HIP) and Gas Pressure Sintering (GPS) have ordinarily been employed. All of them involve very high temperatures, above 1950 ºC, and mechanical or gas pressures in order to favor densification. In addition, liquid phase forming additives are usually employed to reduce the sintering temperature and increase densification. However, in certain applications, it is crucial to avoid the formation of intergranular phases because of their typically lower corrosion resistance compared to the SiC matrix, and/or the decrease in mechanical properties such as hardness or bending strength[5,8] at high temperature due to the intergranular phase softening. In these cases, solid state sintering and additive-free sintering by a SiC recrystallization process have classically been achieved.

The recrystallization of SiC is based on the consolidation of the SiC ceramic bodies through a partial evaporation and condensation of SiC at temperatures within the range 2100 ºC < T < 2500 ºC in inert atmospheres.[50] The as-sintered ceramics present a high degree of porosity, above 20%.

Solid-state sintering for SiC is performed by generally adding small contents of either B and C (normally < 3 wt.%) or compounds containing B and C (like B_4C).[51] The roles played by these additives are fairly different as B tends to reduce the surface energy of SiC grains by entering within the SiC lattice as a solid solution, thus forming point defects that improve[52,53] diffusion processes allowing densification by volume mass transport mechanisms. Meanwhile, C, in addition to reducing the native SiO_2 layer of the SiC, limits those mass transport mechanisms which are ineffective in the sintering process. When these are arrested at temperatures lower than the onset of sintering, the grain growth of SiC is limited up to the temperatures where boron activates the mass transport mechanisms.[54,55] The first attempts towards the development of solid-state sintered SiC ceramics were carried out in the 1970's decade using 2100 ºC for β-SiC[51] and α-SiC[56] powders.

Other methods for achievement of SiC materials are based on reaction-sintering processes, including reaction-bonding[23,57] that has been previously described in Subsection 1.1.2 and the pyrolysis of preceramic polymers.[20]

Finally, it should be mentioned that the most modern Electric Current Activated Sintering (ECAS) techniques have also been employed for either the reaction of homogeneous silicon and carbon mixtures to yield SiC or simply densify raw SiC powders, obtaining moderately good results in terms of densification. Details of the ECAS of SiC are given in Section 1.3.

1.2.1.- Liquid-phase sintering (LPS)

The formation of a liquid phase to promote transport phenomena and increase the diffusivity of atoms through the liquid is the main goal of the LPS of ceramics, in particular of SiC, which imperatively depends on the adequate choice of the type and amounts of sintering aids. The first theoretical approach to the additives selection for SiC was based on the evaluation of the reactivity of SiC with certain compounds,[58] most of which are metal oxides. The use of these metal oxides may involve the interaction of gaseous O_2 with SiC yielding either volatile species such as CO, CO_2 or SiO, or liquid SiO_2. The reactions where gases are formed may imply significant weight losses and, therefore, must be avoided.

Additionally, from the interaction of SiC with metal oxides at the sintering temperatures, the formation of free Si and metallic carbides should be avoided, in reactions like:

$$2SiC\ (s) + xM_aO_b\ (s) \rightarrow 2Si\ (l) + yM_cC_d\ (s) + zCO\ (g) \quad (5)$$

According to thermodynamic analyses, only some metallic oxides do not react with SiC at the sintering temperatures in inert atmospheres, such as Al_2O_3, BeO, Y_2O_3, HfO_2 and some rare earth oxides. Furthermore, the presence of the native SiO_2 in the surface of SiC particles is also accountable for the formation of the glassy phase in the considered oxide additives system, and the temperature reduction of the expected liquid phase formation. Indeed, the use of Al_2O_3, Y_2O_3, $Y_3Al_5O_{12}$ (YAG), La_2O_3, Sm_2O_3, or Sc_2O_3 has often been reported to successfully sinter SiC.[59-67]

It should be mentioned that LPS processes generally consist in a sequence of three dominant stages, also valid for the case of SiC-based ceramics:

i) Particle rearrangement. As liquids melts, redistribution of the liquid and particle rearrangement takes place under the action of the capillary forces and thermal gradients in the material; this step is sometimes favored by the application of mechanical pressure.
ii) Solution-precipitation. Densification and grain shape accommodation occur by mass transport through the liquid phase.
iii) Final stage. A decrease in the densification rate occurs and grain growth takes place usually by an Ostwald ripening mechanism. This process occurs because larger particles (lower curvature) are more energetically favored than smaller particles (higher curvature). Accordingly, dissolution of small particles and reprecipitation of dissolved species on the surface of large particles takes place, leading to an increase of the overall average size.

Microstructures of LPS-SiC can easily be designed to display different grain sizes and aspect ratios for SiC, by way of techniques which normally entail the β→α-SiC transformation. A well-known example of this is the use of post-sintering annealing treatments in inert atmospheres. Nonetheless, extended heat treatments may cause elevated weight losses and degradation,[68] as well as the segregation of secondary phases.

For the LPS of SiC, the most widely studied additive system is that of SiO_2-Y_2O_3-Al_2O_3. This system is particularly interesting since the garnet of Y and Al, YAG, may precipitate at the SiC grain boundaries (Fig. 1.6) producing materials of very low creep rate and with adequate interfacial bonding for activating toughening mechanisms.[69,70] In this system, SiC can interact with Y_2O_3, Al_2O_3 and SiO_2 producing volatile species (generally gaseous SiO and CO). To avoid or reduce these reactions, the technique of seeding the initial powders of β-SiC with larger grains of α-SiC or β-SiC enables a more rapid β→α-SiC transformation, and also reinforcement with elongated grains.[71]

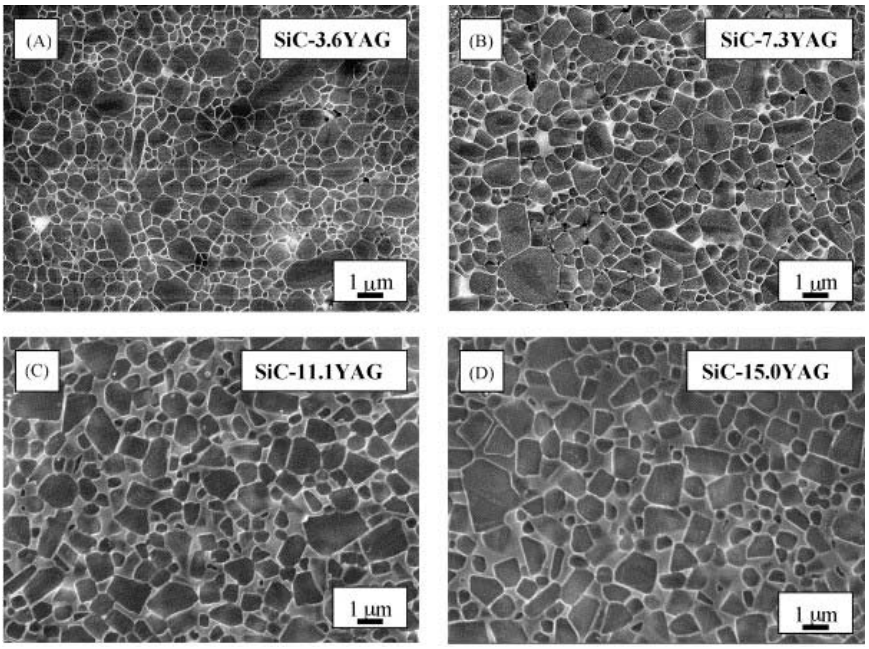

Figure 1.6.- Scanning electron microscopy (SEM) micrographs of polished and plasma-etched cross-sections of four LPSed-SiC ceramics prepared with Y_2O_3 and Al_2O_3 in stochiometric proportions to yield the amounts of YAG in the legends (light regions represent YAG). Adapted from Borrero et al.[72]

Comparable microstructures have been found for the Y_2O_3-AlN additive system.[67-73] Solid solutions formed by SiC and AlN[74-76] allow the control of grain boundary phase compositions to yield different properties and microstructures. Actually, a preliminary study in the AlN–Y_2O_3–Al_2O_3 ternary system[77] showed the abundant liquid phase formation at the sintering temperatures for certain compositions. The use of rare-earth oxides has also been attempted in the particular case of SPS, and examples of that are given in Section 1.3.

1.3.- Spark Plasma Sintering (SPS) of SiC

Among the most modern and fast sintering methods, SPS stands out among the group of the so-called ECAS techniques, which also includes others, such as flash sintering. These techniques were mostly developed in Japan in the 70's, and were extended worldwide in the late 90's. Orru et al.[78] proposed a classification of ECAS as (i) electrical discharge sintering and (ii) resistive sintering (RS) techniques. In the first case, a high voltage electric discharge pulse is applied to a conductive material within an electrically insulating die (such as glass), which may undergo softening at high temperatures (above 800 ºC), hindering a possible sintering process at temperatures above that value. It makes use of the energy stored in a capacitor, suddenly released to the powder compacts. In the second group of techniques (RS), the application of low voltages (1-10 V) and high electric currents is done through an electrically conducting die, exerting mechanical pressure on the punches. This group includes the most well-known techniques such as SPS, Pulsed Electric Current Sintering (PECS), Plasma Activated Sintering (PAS) and Field Activated Sintering (FAST), among others. A recent study showed the ultrafast densification (as a sudden sintering event) by the direct application of a direct current (DC) or alternating current (AC) voltage across the ceramic powders during heating in a furnace (the so-called flash sintering).[79] At high electric fields (above a certain threshold depending on the different materials), a transition from electrically insulating to electrically conductive ceramics has been observed which allows the sintering in a few seconds. The temperature for this transition becomes lower and lower with increasing field values.

The SPS method, in particular, consists in the sintering of materials under the application of electric direct current pulses that induce the Joule heating of the sample or the graphite die, since the current passes through the powdered compacts in the case of conductive materials, or surrounding the specimen through the graphite tooling of the furnace in the case of insulators. A mechanical uniaxial pressure is simultaneously applied to enhance sintering. On the whole, the preparation of the SPS ceramic compacts requires the introduction of the ceramic powders in a graphite die and punches system (Fig.1.7) that allows the subsequent application of pressure, and the use of the punches as electrodes for the current flow through the graphite-ceramic set-up. In a standard configuration, these elements are symmetrically placed within the SPS vacuum chamber, and the short current pulses (typically ~ 3 ms) are made to flow through the system generating the in-situ heating by the Joule effect. The use of graphite elements inevitably requires vacuum or inert atmospheres to

prevent degradation. Parameters such as powder compaction, die arrangement, temperature sensor location, current pulse pattern, as well as the electric and thermal resistances of the whole system (specimen plus graphite tools) strongly determine the current/heat flow and sintering kinetics.[78,80,81]

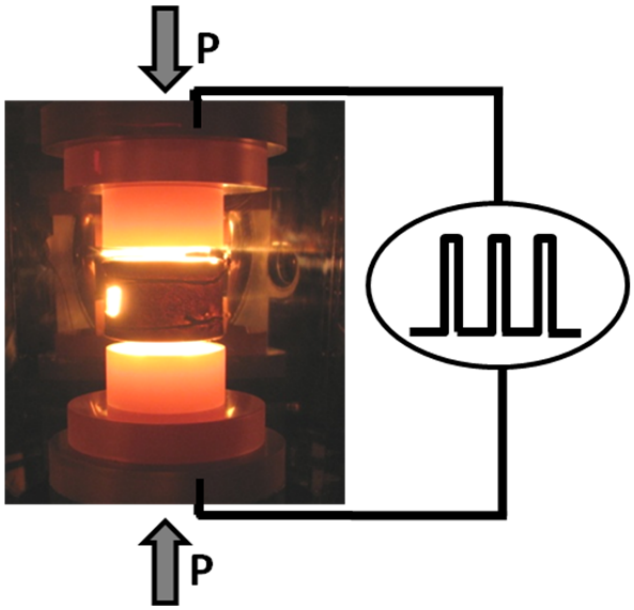

Figure 1.7.- Optical image of the employed SPS furnace chamber while sintering a SiC specimen.

Furthermore, variations of the current density in the SPS furnace by modifying the punches/die set-up could also be explored to achieve controlled temperature gradients within the powder compact, which has allowed in-situ developing functionally graded Si_3N_4 materials.[82,83] In addition, electric current flow isolation can be induced by using highly resistive films, like powdered boron nitride (BN) or Al_2O_3 fibers, affecting the sintering kinetics by SPS, as proved for various ceramics, such as Al_2O_3, HfB_2-SiC, ZrB_2 and $MoSi_2$.[84,85]

One of the main advantages of the ECAS techniques and, in particular, of SPS, is the shorter sintering times and lower sintering temperatures required to fully densify ceramic materials as compared to conventional sintering methods such as HP. The key factor that affects these beneficial sintering conditions is the rapid heating rate achievable on account of the in-situ Joule heating: heating ramps in the range of 100-400 ºC·min^{-1} can be developed.[78,80] There has been prolonged scientific controversy on the mechanisms that act as the driving forces for the SPS process; this is because there is an intrinsic problem to elucidate the role played by electric current, as both temperature and electric current are not independent parameters, which hampers any

simple analysis. Actually, the formation of plasma had often been discussed as a possible mechanism, but it could not be clearly confirmed by tests that normally compared different microstructures under distinct SPS sintering conditions.[86-88] Later on, Hulbert et al.[89] ruled out the possibility of the formation of plasma in SPS. Olevski et al.[90] classified the parameters affecting the densification and grain growth kinetics of ceramics into two groups: thermal and non-thermal. Among the first group, the heating rate, creep phenomena under the effects of pressure, or temperature gradients are the most remarkable. Among the second group are phenomena like surface oxide cleaning leading to contact fritting and channeling effects, electromigration or electroplasticity. Finally, electrowetting mechanism, which predicts an improved wetting of the grain boundary liquid phase proportional to the square of voltage, has been proposed to explain to explain the enhanced densification of Si_3N_4 ceramics occurring in the particle rearrangement stage during SPS in the presence of a liquid phase (LPSPS).[91]

Anyhow, the short sintering times and low sintering temperatures of SPS allowed to envisage this system as an efficient sintering method for nanoceramics, inhibiting grain growth, and for the sintering of ceramic composites containing carbon nanostructures (CNs) as fillers due to their reduced degradation or damage. As examples, the accomplishment of these objectives was achieved by Nishimura et al.[92] in 1995, who fabricated a β-Si_3N_4–based nanoceramics, or by Osendi et al.[93] in 2009 with the successful densification of a ceramic matrix (Si_3N_4) containing highly-dispersed carbon nanotubes without degradation. Nowadays, SPS has actually been used for the consolidation of the majority of the most commonly used ceramic materials and composites.

Recently, the SPS technique is increasingly being considered as a rapid method for the sintering of SiC. Consequently, finer microstructures for SiC ceramics are normally developed. At present, the influence of sintering parameters on the microstructure and final properties of these SPSed SiC materials is not completely known. As described for other sintering techniques, the addition of sintering additives has also been considered in SPS to overcome the lack of sinterability of SiC. Nonetheless, as sintering additives increase radiation absorption, the challenge of reaching full densification by SPS has been faced in view of nuclear applications for additive-free micro- and nano-sized SiC powders; indeed, SPS appears as one of the few techniques that allows to obtain nearly-dense SiC ceramics without the use of sintering additives.[94-101] In general, these studies confirmed that no sintering occurred

for temperatures below 1700°C and porosities in the range of 8-20% for temperatures of 1850 ºC were reported,[94,95] even in spite of applying high sintering loads (75 MPa).[94] In fact, temperatures above 2050 ºC, holding times longer than 5 min and uniaxial loads of 69 MPa were required to fully densify micro-sized α-SiC powders.[96] In order to lessen those arduous sintering conditions for additive-free SiC ceramics, different strategies have been attempted. For example, by way of a previous agglomeration step to form granules of 80 μm, relative densities ≥ 98% were attained at 1860 ºC.[95] Alternatively, dense samples were obtained at 1700 ºC applying only 40 MPa by using raw materials obtained by a mechano-chemical synthesis.[97] In the case of nanostructured powders of β-SiC synthesized by laser pyrolysis, relatively dense materials (~ 96%) were also processed by SPS at 1850 ºC.[100,101]

Diverse results are also reported for the SiC densification in the presence of non-oxide additives.[53,102-104] Zhou et al.[102] achieved densities of 99% of the theoretical value at temperatures of as low as 1600 ºC for nanometer sized β-SiC powders containing 2.0 wt.% of Al_4C_3 and 0.4 wt.% of B_4C. On the other hand, Maître et al.[53] showed slightly enhanced densification by SPS at 1950 ºC when boron plus carbon were used as sintering aids reporting 98.8% of relative density versus 97.5% for pure SiC powders.

Lastly, advanced LPSed-SiC ceramics are nowadays densified by SPS at noticeably lower temperatures and shorter times than those for conventional methods.[105] Surprisingly, scarce research has been devoted to studying the LPSPS of SiC with liquid phase forming additives in the Y_2O_3-Al_2O_3 system.[106,107] Zhou et al.[106] were in 1999 the first to make a comparison between non-oxide (Al_4C_3-B_4C-C) and Y_2O_3-Al_2O_3 sintering aids, and reported relative densities of 99.7% and 95.2%, respectively, for materials SPSed at 1700 ºC. These authors concluded that the addition of Al_4C_3-B_4C-C profoundly promoted phase transformation, densification rate, and grain growth, leading to materials with lower fracture toughness and greater hardness, as compared to the Y_2O_3-Al_2O_3 system. Recently, hardness of 31 GPa and fracture toughness of 6.6 $MPa \cdot m^{1/2}$ have been reported for SiC ceramics processed by SPS containing YAM (yttrium aluminum monoclinic, $Y_4Al_2O_9$) as a grain boundary phase.[108] There are other works on the topic where non-oxide and oxide sintering additives were combined; for example, studies on SPSed SiC at 1900 ºC with Y_2O_3-AlN additives (up to 10 vol.%), which produced fully dense materials.[109,110] Finally, the feasibility of flash sintering of SiC (with Al_2O_3-Y_2O_3 as sintering aids) at temperatures of as low as 1170°C was demonstrated under an applied electric field of $100V \cdot cm^{-1}$.[111]

Despite the variety of studies listed above on the SPS of SiC powders, there is still a significant lack of fundamental research dealing with the effect of the starting particle size, the SiC polytype or the electric current distribution on the sintering process of SiC ceramics with Y_2O_3-Al_2O_3 additives. Those points will be tackled within the study of this PhD Thesis.

1.4.- SiC-based cellular ceramics: processing routes

The fabrication of SiC-based cellular ceramics has traditionally consisted in the manufacture of foams and honeycombs with appreciated structural properties (low density, large exposed surface and, especially, relatively high mechanical resistance).[112-117] The most common processing routes for cellular ceramics have as well been employed for SiC:[118] i) the use of sacrificial templates, ii) the replica technique, and iii) the direct foaming. Below, some examples of these methods are given when applied to SiC based ceramics, regardless of the method for the synthesis of SiC (from SiC powders, preceramic polymers, reaction-bonding, etc). More recently, some attempts have been done to develop SiC cellular materials by additive AM mainly by reaction-sintering methods. This topic will be addressed in Chapter 2.

The use of sacrificial templates (being natural or synthetic materials) consists in homogeneously dispersing a sacrificial phase by employing colloidal processing methods within a continuous matrix of either ceramic particles or ceramic precursors; subsequently, this sacrificial phase is eliminated, which entails the origination of pores within the material to be eventually sintered. A usual approach is to obtain a homogeneous mixture of both phases, and then, the application of pressure to form the biphasic compacts. Alternatively, a casting technique can be applied from the formation of a biphasic suspension. When sacrificial templates are organic materials, the most habitual method for their removal is via slow pyrolysis (less common methods employ other alternatives such as acids etching depending on the type of sacrificial template used). Several works can be found in the literature where the sacrificial templating of cellular SiC ceramics is reported.[119-122] In most of these studies, open-cell, microcellular SiC ceramics with different morphologies were fabricated using preceramic polymers (polymethylsilane or polisiloxane) as SiC precursors and different sacrificial templates such as polymer microbeads, glass fibers silica or different carbon materials.[119,120] Synthesis of SiC is carried out first by

the pyrolysis of the precursors at ~ 1200 – 1250 ºC in Ar or N_2 atmospheres, forming SiOC and C. The range of porosity for the as-obtained materials oscillates from 60% to 95%. Another example is the development of bimodal cell structures by simultaneously using two kinds of pore formers (expandable microspheres and smaller polymethylmethacrylate, also known as PMMA, spheres) and using SiC, Y_2O_3 and Al_2O_3 particles as starting powders.[122] In Fig. 1.8, fracture surfaces of these cellular SiC ceramics are shown, where the large pores derive from the expandable microspheres and the small pores in the strut in Fig. 1.8b are caused by the PMMA spheres. Finally, starch additions have also been used as pore-forming agents to either produce alternate laminates of dense and porous SiC layers[123] or porous honeycomb structures.[124]

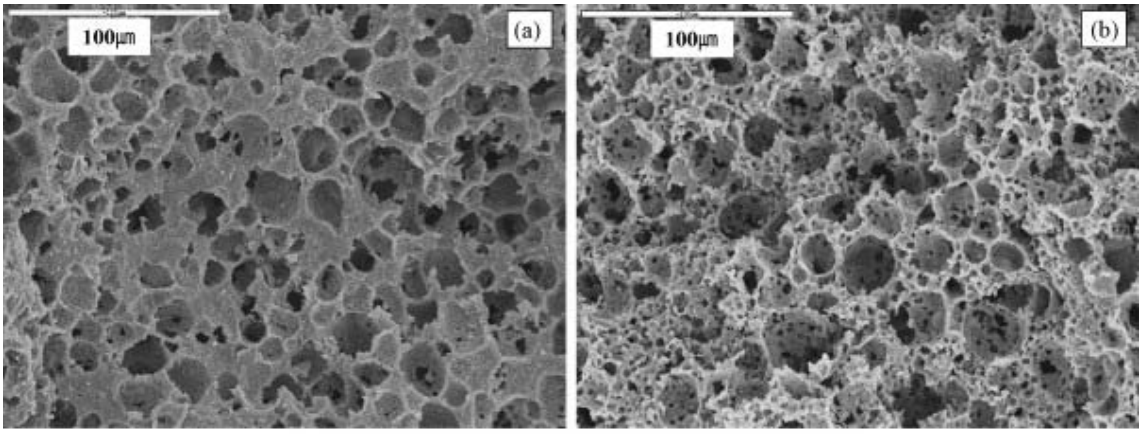

Figure 1.8.- SEM images corresponding to the fracture surfaces of microcellular SiC ceramics sintered at 1850 °C for 3 h, with no PMMA additions (a), and using 20 wt.% PMMA (b).[122]

The replica technique consists in the use of either a ceramic powder suspension or a ceramic precursors solution to impregnate a cellular structure and finally produce a cellular ceramic material with the same shape as the template. The impregnating structure is typically made of organic materials (as polymers) to facilitate their subsequent elimination, and might be either natural or synthetically created. Actually, polymeric sponges were the first used templates, patented in 1963.[125] Sponge replicas yield highly interconnected open porosity (40%-95%), with pore sizes being within the range 200 μm—3 mm. The rheology of these suspensions must satisfy certain requirements to allow the elimination of excess suspension in the sponges avoiding dripping at the same time; in this regard, the suspensions must be sufficiently viscous and show shear-thinning rheology. In the case of SiC, the use of preceramic polymers is still preferred, as compared to SiC suspensions, to impregnate the cellular templates and subsequently convert them into SiC after

pyrolysis and sintering stages.[126-128] As an example, Bao et al.[126] prepared SiC foams by immersing polyurethane templates in polysilane solutions. Most impressively, using polymeric templates constructed by additive manufacturing methods, complex 3D periodic structures of SiC showing dense struts, as shown in Fig. 1.9, were obtained by impregnating the 3D-templates into an α-SiC powders-based slurry, followed by the pyrolysis of the polymeric templates and a Si reactive infiltration.[127]

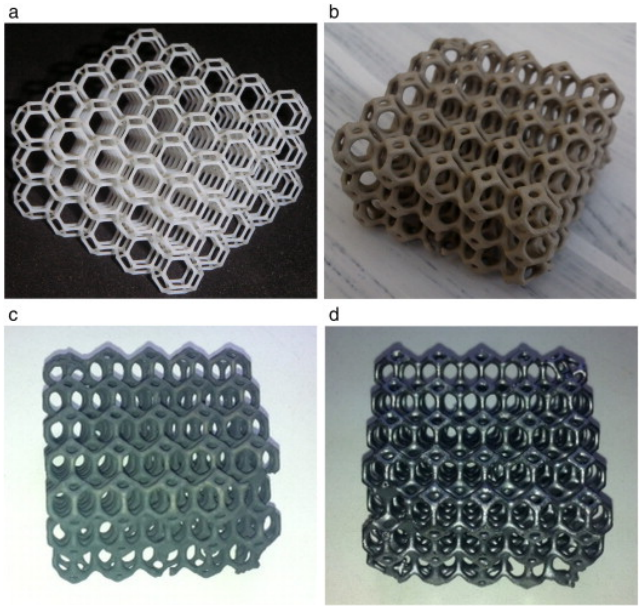

Figure 1.9.- Optical images of the manufacturing stages: (a) 3D polymeric template, (b) slurry replication, (c) pyrolysis, and (d) silicon infiltration.[127]

Cellular structures found in nature have also been used as templates in the manufacture of ceramic foams, showing advantages like the achievement of different pore shapes and microstructures as compared to polymeric sponges. In particular, corals and wood have been the most popular natural templates. In the case of SiC, wood has been the most widespread,[129-135] using impregnation either with precursors, with SiC suspensions or by using Si-vapor infiltration. As an example of the latter, Vogli et al.[129] developed these method with pine-wood templates that undergo a pyrolysis step and react with Si, obtaining β-SiC cellular materials with porosity in the region of 70%. Another example is the impregnation of pine-wood with a SiO_2 sol in a sol-gel process,[130] to be next dried and subjected to a pyrolysis at 500 ºC, and a stage for SiC synthesis at 1600 ºC in argon. Fig. 1.10 shows characteristic micrographs of these materials.

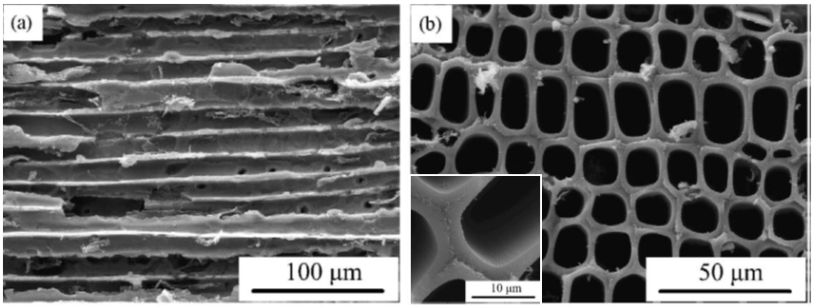

Figure 1.10.- SEM micrographs of: (a) longitudinal and (b) transverse views of SiC cellular samples developed by impregnating pine-wood templates with a SiO_2 sol and its subsequent pyrolysis and sintering at 1600 ºC for 4 h.[130]

The third key route for the production of SiC ceramic foams is the direct foaming method.[136,137] In this method, bubbles of air are introduced into ceramic suspensions or solutions of preceramics in such a way that the structure is commonly fixed by freezing. Afterwards, these macroporous green bodies undergo a sintering process. The kinetics related to the coalescence of bubbles is the main parameter to control the pore sizes achievable by this technique. Consequently, controlling the stabilization of air bubbles is fundamental for tailoring the final properties of these materials. Sometimes, amphiphilic molecules or lipids or proteins, or alternatively solid particles, may be added to the suspensions for stabilizing these gels. An example of a SiC foam is given in Fig. 1.11.

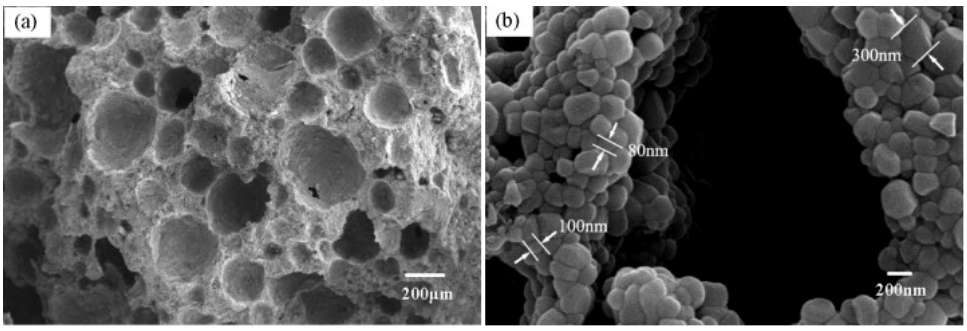

Figure 1.11.- SEM micrographs of a SiC foam in the combustion synthesized SiC foam.[137]

1.5.- Graphene

1.5.1.- Properties and production processes

Graphene can be defined as a monolayer of carbon atoms (Fig. 1.12) arranged in a hexagonal lattice, and united by sp^2-hybridized chemical bonds. Graphene constitutes the basic unit for the formation of the family of carbon allotropes, such as carbon nanotubes when rolled up in a cylinder, fullerenes when graphene structures are closed in spherical shapes, and graphite when a very large number of layers are considered to be repetitively piled up.

Graphene exhibits exceptional functional properties. As for the reported electric transport phenomena,[139,140], an electron mobility of as high as 2 x 10^5 $cm^2 \cdot V^{-1} \cdot s^{-1}$ was recorded,[141] which arises from the peculiarity of the band structure that resembles a semiconductor with a zero band gap energy. Also, the graphene elastic modulus has been reported to be of as high as 1 TPa.[142]

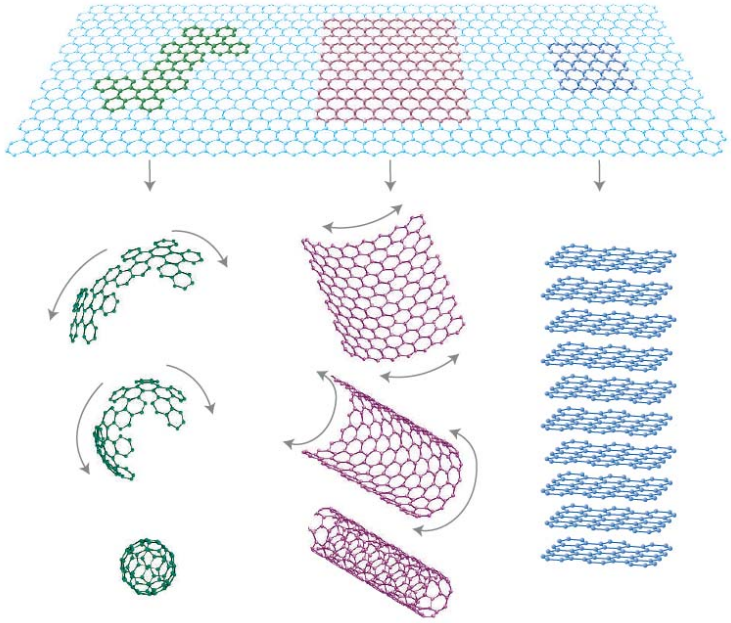

Figure 1.12.- Monolayered graphene: the 2D building element of carbon nanomaterials (fullerene (left), carbon nanotubes (center), graphite (right)).[138]

Moreover, thermal conductivity is also extraordinary: most measurements are developed on suspended monolayers resulting in very elevated in-plane conductivity values (from 5000 to 2000 $W \cdot m^{-1} \cdot K^{-1}$),[143-146] which coincide with computed estimations (~2000 $W \cdot m^{-1} \cdot K^{-1}$),[147] tending to decrease in the case of supported graphene (graphene supported on SiO_2 exhibited ~600 $W \cdot m^{-1} \cdot K^{-1}$).[148] These figures also tend to

decrease, as shown by Ghosh et al.,[149] with an increasing number of atomic planes (n) in the graphene sheets due to boundary scattering of phonons, finally reaching values similar to those of graphite for the case of graphene nanoplatelets (GNPs), where n>8. Also, optical properties are noteworthy on account of its low absorption.[150] Actually, graphene-based prototypes have been an efficient alternative for the replacement of transparent conductive oxides in solar cells.[151,152]

Novoselov et al.[153] were the first in 2004 to report the stable isolation of a single monoatomic layer of graphite, eventually called graphene (name assigned by H.P. Boehm),[154] by mechanical cleavage. This method is essentially based on the separation of graphene layers from graphite, which are mutually bonded by π orbitals in the direction perpendicular to the planes. Normally, the cleavage can be accomplished by the use of a scotch tape where the graphene layers remain sticked, and transferring them later onto a substrate by the application of pressure.[155] Another means to produce graphene layers is carried out by epitaxial growth on 6H-SiC wafers by thermal decomposition of the substrate in ultra-high vacuum or in argon,[156,157] typically by sublimating the Si, thus avoiding the transfer process for microelectronic applications. Attempts to develop this process by using lasers have also been accomplished: epitaxial, few-layered and low strain graphene films were obtained on SiC (0001).[158] In any case, these methods give way to tiny amounts of graphene, and others with more profuse productions are searched especially for the fabrication of composites.

At present, producing graphene in large amounts and at a relatively low cost is the aim of certain production methods like liquid-phase exfoliation, or also CVD techniques, as shown in Fig. 1.13.[159] CVD is in fact one of the most common methods to produce large-surface graphene layers on metallic substrates.[160,161] In a vacuum atmosphere at high temperatures, different hydrocarbons can be made to flow in contact with the metallic surfaces allowing the carbon atoms to slightly penetrate within the metals, and eventually segregating the carbon during cooling forming a surface layer of graphene. The CVD conditions (mainly temperature and growing time) determine the final properties of the as-created graphene layers (thickness, size, doping, crystallinity…). Plasma-assisted CVDs allow reducing reaction temperatures. Also, even 3D-structured graphene has been created with the use of metallic Ni foams as sacrificial templates.[162,163]

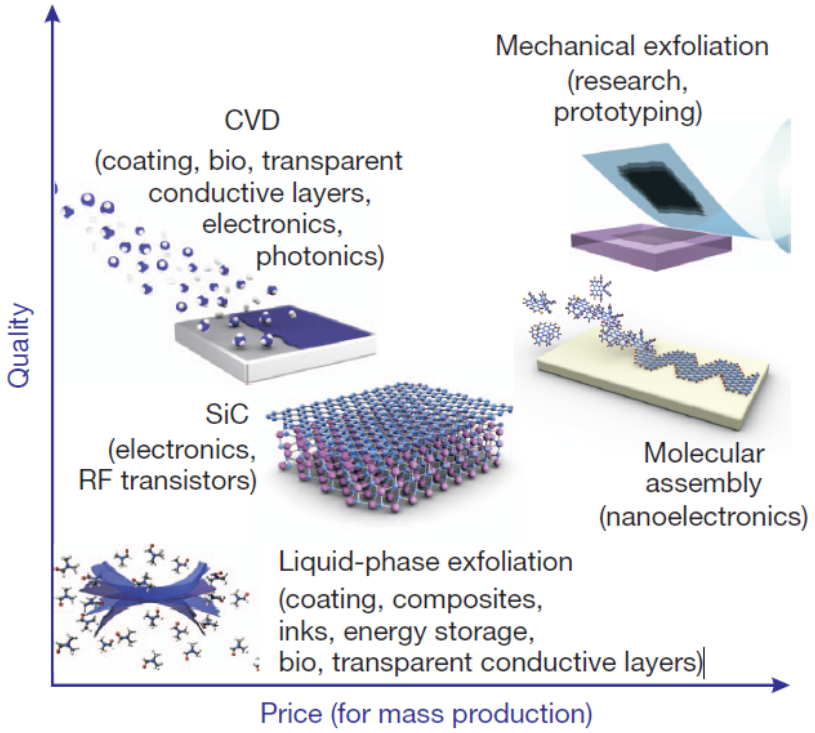

Figure 1.13.- Some methods for the production of graphene depending on the quality and price.[159]

For the fabrication of ceramic composites using graphene as a dispersed phase, profuse productions of graphene are intended, and methods that result in GNPs or graphene oxide (GO) nanoplatelets such as the mechanical and chemical exfoliation, respectively, are commonly employed.[164] As for the mechanical exfoliation, a characteristic route is the use of ultrasonication of graphite in a liquid, such as organic solvents, aqueous solutions of surfactants or ionic liquids. On the other hand, the method proposed by Hummer, as described later by Dreyer et al.,[165] using $NaNO_3$ and H_2SO_4 mixed with $KMnO_4$ is commonly used for GO production. The fundamental point is that oxidized graphite becomes highly hydrophilic, in contrast to graphite, with hydroxyl and epoxide groups attached to the surfaces and carbonyl and carboxylic groups to the edges, which permits water molecules to penetrate and intercalate the different layers. Ultimately, an agitation or sonication process brings in the exfoliation of the different layers. The Hummer's method for the production of GO has often been modified employing $K_2S_2O_8$ and P_2O_5 in H_2SO_4.[166] GOs can still undergo a reduction process (rGO) that releases the attached chemical groups, recovering most of the structure and properties of pure graphene; these processes might include thermal treatments or the use of chemical reagents like hydrazine hydrate.

1.5.2.- Graphene ceramic composites

Using GNPs and GOs, instead of graphene, for the manufacture of ceramic-based composites has certain advantages such as the cost-effectiveness of the process, and the ability to obtain abundant batches of materials, enabling a larger scale production. Nevertheless, the reported paramount properties of pure, monolayered graphene tend to decrease when multilayered sheets are employed (as in the case of GNPs), or when a plentiful presence of defects (normally the case of rGOs) impairs the conduction phenomena along the graphene plane. For any of these fillers, homogeneous dispersions have been accomplished after adequate processing resulting in well-dispersed composites.

The above-mentioned methods to abundantly produce GNPs and GO are of singular interest for the fabrication of composite materials where polymers or ceramics act as matrices, whose properties are significantly modified by the incorporation of those graphene-based structures. In particular, thermal and electrical conductivities are expected to be enhanced, a priori, by these graphene additions. Several works have been published where ceramic matrices containing GNPs or rGOs exhibit increased and anisotropic electrical conductivity.[167-173] As for the electrical conductivity, increments of up to 14 orders of magnitude for insulating Al_2O_3 and Si_3N_4 matrices have been reached, showing values of $5.7x10^3$ $S{\cdot}m^{-1}$ in Al_2O_3 containing 15 vol.% GNPs[167] and $4x10^3$ $S{\cdot}m^{-1}$ for Si_3N_4 with 24 vol.% GNPs,[168] defining in both cases a threshold for percolation for GNPs amounts below 8 vol.%. High electrical conductivity and lower percolation threshold (< 4.3 vol.%) as compared to that of GNPs composites have been reported for ceramic composites containing rGOs,[169-171] thermally reduced in-situ during sintering. Values of up to 700 $S{\cdot}m^{-1}$ have been reported for Si_3N_4 composites with 7.2 vol.% of finely exfoliated rGOs;[169] furthermore, $1.2x10^4$ $S{\cdot}m^{-1}$ for yttria-stabilized zirconia (YSZ) ceramics have been reached with a filler content of 4.1 vol.% rGOs,[170] and 10^3 $S{\cdot}m^{-1}$ for Al_2O_3 with rGOs contents of only 2.35 vol.%.[171]

GNPs also appear as an interesting dispersed phase for the thermal functionalization of ceramic matrices.[170,174-180] Some common features can be pointed out regarding the thermal conduction phenomena in the composites. Firstly, due to the preferential orientation of the ab basal plane of graphene sheets perpendicular to pressing axis during pressure-assisted sintering, as in SPS or HP, the enhancement of thermal conductivity (K_T) in the direction defined by the ab plane[174-176] emerges as the most significant feature, whereas a decrease with increasing amounts of GNPs is typically

reported when measuring in the direction parallel to the pressing axis.[170,174-179] Thus, a high level of thermal anisotropy is created, as observed in the cases of Si_3N_4[174,175] and Al_2O_3[176] matrices. Accordingly, using the $K_T^{\perp}/K_T^{||}$ ratio as a measurement of thermal anisotropy between in-plane ($\perp$) and through thickness (||) directions, values of ~2-3 have been reported for composites containing 10-12 wt.% of GNPs in Si_3N_4[174,175] and Al_2O_3[176] matrices. Secondly, the more defective nature of rGOs results in more abrupt decreases in $K_T^{||}$ than in the case of GNPs-containing ceramics. As an example, $K_T^{||}$ was reduced to more than half its value with rGO additions of only 2 wt.% (92.5 → 37.4 $W \cdot m^{-1} \cdot K^{-1}$) in an AlN matrix[177] whereas a similar decrease was only attained for ~10 vol.% GNPs[178] also in a similar AlN-based matrix. An analogous $K_T^{||}$ reduction was observed for Si_3N_4 ceramics.[179] Lastly, the thermal conductivity of GNPs/SiC composites has preliminarily been investigated for specimens fabricated by a solid-state pressureless-sintering method as a function of the graphene content.[180] Unluckily, the pressureless process led to evident porosity for GNPs contents higher than 3 wt.% and, besides, no considerations on the temperature dependence or the anisotropy were made in that study. It was found that the thermal conductivity increased with GNPs content up to ~ 20% for 2.0 wt.% of GNPs, and it significantly decreased for higher GNPs amounts due to the remaining porosity.

Recently, graphene-based nanostructures have attracted a great interest as efficient reinforcement fillers for toughening some oxide and non-oxide ceramics due to their capability for promoting toughening mechanisms such as crack deflections, or the bridging of the cracks by the fillers.[170,178,181-188] By way of example, an illustration of the bridging mechanism by Ramirez et al.[181] is given in Fig. 1.14. Al_2O_3 and Si_3N_4 composites are the most investigated systems, and for which the most remarkable fracture toughness (K_{IC}) results have been obtained until now. Focusing on the Al_2O_3-based composites, Lee et al.[182] reported K_{IC} values of up to 10.5 $MPa \cdot m^{1/2}$ when an amount of 2 vol.% of rGO was added, which corresponded to an increment of ~150% as compared to the monolithic ceramics; the flexural strength (σ_f) of the composite was also increased in 21%. Centeno et al.[183] found improvements in σ up to 80% for 0.22 wt.% rGOs composites, suggesting that the restriction of the Al_2O_3 grain growth during the sintering process due to the presence of rGOs is the cause for that increment. Furthermore, Fan et al. reported a drastic increase of strain tolerance by ~40% for a 2.2 vol.% rGOs/Al_2O_3 composite.[184] In the case of graphene/Si_3N_4 composites, a toughness increase as high as 135 % was reported by Walker at al.[185] and Ramirez et al.[186] The latter authors reported, when 4.3 vol.% rGOs were added to a Si_3N_4 matrix, a maximum K_{IC} value of 10.4 $MPa \cdot m^{1/2}$, jointly with an increase in σ_f of

10% (being the maximum value of 1050 MPa).[186] Other ceramics have been explored for graphene reinforcement with dissimilar results. For example, Shin et al.[170] increased the fracture toughness of YSZ ceramics in ~34% by adding 4 vol.% of rGOs, while Nieto et al.[187] reached K_{IC} improvements of ~100% for tantalum carbide (TaC) ceramics with 5 vol.% of GNPs, attaining top K_{IC} values of 11.7 MPa·$m^{1/2}$. Yun et al.[178] recently reported the mechanical performance of 1.5 vol.% GNPs/AlN composites, showing increases in K_{IC} and σ_f of about 30% and 17%, respectively.

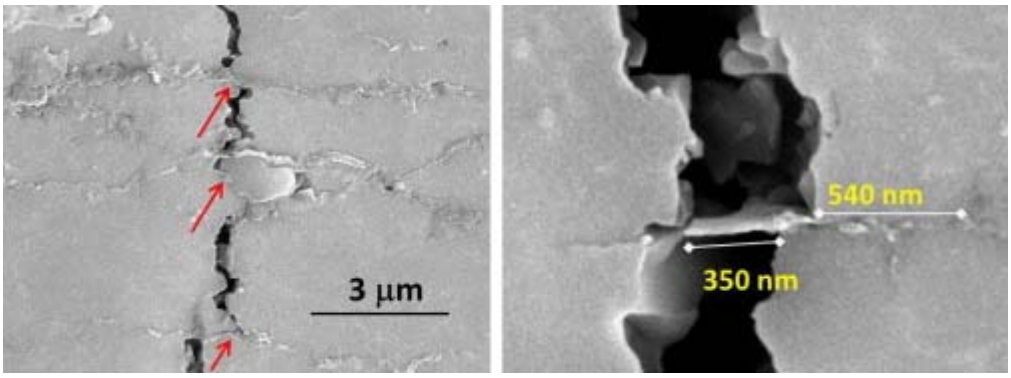

Figure 1.14.- SEM image of an indentation crack path in 4 vol.% rGOs/Si_3N_4 composite with rGOs fillers intercepting the crack, and a broken/extracted sheet with indication of debond lengths.[181]

Finally, it should be mentioned that due to the effects of the solid-lubricating properties of graphitic materials, graphene has been incorporated into ceramics as a self-lubricating filler, using matrices such as Si_3N_4,[189-191] Al_2O_3[192,193] and SiO_2.[194] In particular, in these composites, GNPs exfoliation is produced during the wear processes, giving way to the in-situ formation of a self-lubricated tribofilm that protects materials from abrasion and wear processes. In this way, the addition of 3 wt.% of GNPs to a Si_3N_4 matrix reduced the friction and improved the wear resistance up to 56% under isooctane lubricated conditions[189] and decreased wear in a 60% under dry sliding conditions[190], although GNPs additives did not decrease the friction coefficient in that case. Graphene/Al_2O_3 composites[192,193] also showed remarkable improvements (up to one order of magnitude) on the wear resistance when compared to the monolithic alumina jointly with slight decreases in friction. Finally, it was found by Porwal et al.[194] that the addition of 5 vol.% of GNPs to a SiO_2 matrix improved the wear resistance up to 8.5 times.

In spite of the variety of works devoted to the fabrication and properties of ceramic-based composites containing graphene fillers, no works have been accomplished for

a thorough investigation of SiC matrices containing graphene, with the only exception of a spare work by Li et al.[180] on the thermal properties of GNPs/SiC materials obtained by presureless sintering. Thus, the emergence of a study devoted to the processing of GNPs/SiC ceramic composites and structures and the analysis of their properties is of paramount importance. In this PhD Thesis, the fabrication of this sort of ceramics and composites will be addressed in both bulk and 3D-structured materials.

1.6.- References

1. Olesinski RW, Abbaschian GJ. The C− Si (Carbon-Silicon) system. J Phase Equilib 1984; 5(5): 486-9
2. Fisher GR, Barnes P. Towards a unified view of polytypism in silicon carbide. Philos Mag B 1990: 61(2), 217-36
3. Limpijumnong S, Lambrecht WR. Total energy differences between SiC polytypes revisited. Phys Rev B 1998; 57(19): 12017.
4. Lebedev AA. Heterojunctions and superlattices based on silicon carbide. Semicond Sci Tech 2006; 21(6): R17.
5. Snead LL, Nozawa T, Katoh Y, Byun TS, Kondo S, Petti DA. Handbook of SiC properties for fuel performance modeling. J Nucl Mater 2007; 371(1): 329-77.
6. Kukushkin SA, Osipov AV, Bessolov VN, Medvedev BK, Nevolin VK, Tcarik KA. Substrates for epitaxy of gallium nitride: New materials and techniques. Rev Adv Mater Sci 2008; 17(1/2), 1-32.
7. Roewer G, Herzog U, Trommer K, Müller E, Frühauf S. Silicon carbide—a survey of synthetic approaches, properties and applications. In High Performance Non-Oxide Ceramics I (pp. 59-135). Vol.101. Springer, 2002.
8. Munro RG. Material properties of a sintered α-SiC. J Phys Chem Ref Data 1997; 26(5): 1195-203.
9. Schwetz KA. Silicon carbide based hard materials. In Handbook of Ceramic Hard Materials (pp. 683-748). Edited by R. Riedel. Wiley-VCH Verlag GmbH, 2000.
10. Slack GA. Thermal conductivity of pure and impure silicon, silicon carbide, and diamond. J Appl Phys 1964, 35(12), 3460-6.
11. Persson C, Lindefelt U, Sernelius BE. Doping-induced effects on the band structure in n-type 3C-, 2H-, 4H-, 6H-SiC, and Si. Phys Rev B 1999; 60(24): 16479.

12. Cowles EH. U.S. Patent No. 319,945. 1885. Washington, DC: U.S. Patent and Trademark Office.
13. Acheson EG. English Patent 17911. 1892. Production of artificial crystalline carbonaceous materials, carborundum.
14. Baney RH, Gaul Jr. JH. U.S. Patent No. 4,310,651. 1982. Washington, DC: U.S. Patent and Trademark Office.
15. Manfred M, Wolfgang V, Gerhard W. U.S. Patent No. 3,892,583. 1975. Washington, DC: U.S. Patent and Trademark Office.
16. Weimer, AW (Ed.). Carbide, nitride and boride materials synthesis and processing (Acheson process by Guichelaar, PJ). Chapman & Hall, 1997.
17. Neudeck PG. Progress in silicon carbide semiconductor electronics technology. J Electron Mater 1995; 24(4): 283-8.
18. Suzuki A, Furukawa K, Higashigaki Y, Harada S, Nakajima S, Inoguchi T. Epitaxial growth of β-SiC single crystals by successive two-step CVD. J Cryst Growth 1984; 70(1): 287-90.
19. Wesch W. Silicon carbide: synthesis and processing. Nucl Instrum Meth B 1996; 116(1): 305-21.
20. Greil P. Active-Filler-Controlled Pyrolysis of Preceramic Polymers. J Am Ceram Soc 1995; 78: 835–48.
21. Laine RM, Babonneau F. Preceramic polymer routes to silicon carbide. Chem Mater 1993; 5(3): 260-79.
22. White DA, Oleff SM, Fox JR. Preparation of silicon carbide from organosilicon gels: II. Gel pyrolysis and SiC characterization. Adv Ceram Mater 1987; 2(1).
23. Ness JN, Page TF. Microstructural evolution in reaction-bonded silicon carbide. J Mater Sci 1986; 21(4): 1377-97.
24. Deng JX, Zheng ZC, Ding ZL, Wang JH. Erosion wear of ceramic and cemented carbide nozzles in dry sand blasting process. Brit Ceram T 2003; 102(2): 61-5.
25. Phillips K, Crimes GM, Wilshaw TR. On the mechanism of material removal by free abrasive grinding of glass and fused silica. Wear 1977; 41(2): 327-50.
26. Bhatnagar M, McLarty PK, Baliga BJ. Silicon-carbide high-voltage (400 V) Schottky barrier diodes. Electron Devic Lett, IEEE 1992; 13(10): 501-3.
27. Brown DM, Downey E, Ghezzo M, Kretchmer J, Krishnamurthy V, Hennessy W, Michon G. Silicon carbide MOSFET technology. Solid State Electron 1996; 39(11): 1531-42.
28. Weitzel CE, Bhatnagar M. U.S. Patent No. 5,661,312. 1997. Washington, DC: U.S. Patent and Trademark Office.

29. Palmour JW, Edmond JA, Kong HS, Carter CJ. 6H-silicon carbide devices and applications. Physica B 2012; 461-5.
30. Matsumoto T, Takahashi J, Tamaki T, Futagi T, Mimura H, Kanemitsu Y. Blue-green luminescence from porous silicon carbide. Appl Phys Lett 1994; 64(2): 226-8.
31. Weill P. The relationship between investment in information technology and firm performance: A study of the valve manufacturing sector. Inform Syst Res 1992; 3(4): 307-33.
32. Wang X, Kato K. Improving the anti-seizure ability of SiC seal in water with RIE texturing. Tribol Lett 2003; 14(4): 275-80.
33. Wang X, Kato K, Adachi K, Aizawa K. Loads carrying capacity map for the surface texture design of SiC thrust bearing sliding in water. Tribol Int 2003; 36(3): 189-97.
34. Andersson P, Nikkila AP, Lintula P. Wear characteristics of water-lubricated SiC journal bearings in intermittent motion. Wear 1994; 179(1): 57-62.
35. Sommers A, Wang Q, Han X, T'Joen C, Park Y, Jacobi A. Ceramics and ceramic matrix composites for heat exchangers in advanced thermal systems—a review. Appl Therm Eng 2010; 30(11): 1277-91.
36. Merkel GA, Cutler WA, Warren CJ. Thermal durability of wall-flow ceramic diesel particulate filters SAE technical paper. doi:10.4271/2001-01-0190
37. Brendel A, Popescu C, Leyens C, Woltersdorf J, Pippel E, Bolt H. SiC-fibre reinforced copper as heat sink material for fusion applications. J Nucl Mater 2004; 329: 804-8.
38. Medvedovski E. Ballistic performance of armour ceramics: Influence of design and structure. Part 1. Ceram Int 2010; 36(7): 2103-15.
39. Heidenreich B, Gahr M, Straβburger E, Klingelberg A, Lutz IE. Biomorphic SiSiC-materials for lightweight armour. Advances in Ceramic Armor II, Ceramic Engineering and Science Proceedings, Cocoa Beach 2009; 314: 21.
40. Jiang BQ, Li YL, Liu YY, Yu QJ. Effects of SiC particle reinforcement distribution on the penetration of functionally graded armour. Explosion and Shock Waves 2005; 25(6): 493.
41. Krenkel W, Berndt F. C/C–SiC composites for space applications and advanced friction systems. Mater Sci Eng A 2005; 412(1): 177-81.
42. Gauckler LJ, Waeber MM, Conti C, Jacobduliere M. Ceramic Foam for Molten-Metal Filtration. JOM-J Met 1985; 37(9): 47–50.
43. Ivanova S, Louis B, Madani B, Tessonnier JP, Ledoux MJ, Pham-Huu C. ZSM-5 coatings on β-SiC monoliths: Possible new structured catalyst for the methanol-to-olefins process. J Phys Chem C 2007; 111(11): 4368-74.

44. Bauer C, Scheffler F, Schwidder M. Direct crystallization of silicoaluminophosphates onto the surface of open-celled SiC foam. Adv Eng Mater 2014, doi: 10.1002/adem.201400278.
45. Ledoux MJ, Hantzer S, Huu CP, Guille J, Desaneaux MP. New synthesis and uses of high-specific-surface SiC as a catalytic support that is chemically inert and has high thermal resistance. J Catal 1988; 114(1): 176-85.
46. Okazoe H, Shimizu K, Watanabe Y, Santiago E, Kugland P, Ruth W. Development of a full-flow burner regeneration type diesel particulate filter using SiC honeycomb. SAE Technical Paper 1996, No. 960130.
47. Füssel A, Böttge D, Adler J, Marschallek F, Michaelis A. Cellular ceramics in combustion environments. Adv Eng Mater 2011; 13: 1008-14.
48. Kaneda H, Onaka T, Kawada M, Murakami H. Cryogenic optical testing of sandwich-type silicon carbide mirrors. Appl Optics 2003; 42(4): 708-14.
49. Petrovsky GT, Tolstoy MN, Ljubarsky SV, Khimitch YP, Robb PN. 2.7-meter-diameter silicon carbide primary mirror for the SOFIA telescope. In 1994 Symposium on Astronomical Telescopes & Instrumentation for the 21st Century (pp. 263-70). International Society for Optics and Photonics.
50. Kriegesmann J. Processing Phenomena for Recrystallized Silicon Carbide. In Grain Boundary Controlled Properties of Fine Ceramics (pp. 176-188). Springer Netherlands. 1992.
51. Prochazka S. High-Performance Applications: Proceedings of the Second Army Materials Technology Conference , ed. JJ Burke, AE Gorum and RN Katz, pp. 239 –52, Brook Hill Publishing Co., Chestnut Hill, OH (1975).
52. Clegg WJ. Role of Carbon in the Sintering of Boron-Doped Silicon Carbide. J Am Ceram Soc 2000; 83: 1039–43.
53. Maitre A, Put AV, Laval JP, Valette S, Trolliard G. Role of boron on the Spark Plasma Sintering of an α-SiC powder. J Eur Ceram Soc 2008; 28(9): 1881-90.
54. Rijswijk WV, Shanefield DJ. Effects of carbon as a sintering aid in silicon carbide. J Am Ceram Soc 1990; 73(1): 148-9.
55. Stobierski L, Gubernat A. Sintering of silicon carbide. Effect of carbon. Ceram Int 2003; 29(3): 287-92.
56. Coppola JA, Hawler HA, McMurtry CH, US Patent 4,123,286 (1978)
57. Suyama S, Kameda T, Itoh Y. Development of high-strength reaction-sintered silicon carbide. Diam Relat Mater 2003; 12(3): 1201-4.
58. Negita K. Effective sintering aids for silicon carbide ceramics: reactivities of silicon carbide with various additives. J Am Ceram Soc 1986; 69(12):C-308-10.

59. Omori M, Takei H. Preparation of pressureless-sintered SiC-Y_2O_3-Al_2O_3. J Mater Sci 1988; 23(10): 3744-9.
60. Lee SK, Kim YC, Kim CH. Microstructural development and mechanical properties of pressureless-sintered SiC with plate-like grains using Al_2O_3-Y_2O_3 additives. J Mater Sci 1994; 29(20): 5321-6.
61. Zhang J, Iwasa M, Jiang D. Dispersion of SiC in aqueous media with Al_2O_3 and Y_2O_3 as sintering additives. J Am Ceram Soc 2005; 88(4):1013-6.
62. Kim JY, Kim YW, Mitomo M, Zhan GD, Lee JG. Microstructure and Mechanical Properties of alpha-Silicon Carbide Sintered with Yttrium-Aluminum Garnet and Silica. J Am Ceram Soc 1999; *82*(2): 441-4.
63. Kim YW, Mitomo M, Zhan GD. Mechanism of grain growth in liquid-phase-sintered β–SiC. J Mater Res 1999; 14(11): 4291-3.
64. Zhou Y, Hirao K, Yamauchi Y, Kanzaki S. Effects of rare-earth oxide and alumina additives on thermal conductivity of liquid-phase-sintered silicon carbide. J Mater Res 2003; 18(08):1854-62.
65. Balog M, Sedlackova K, Zifcak P, Janega J. Liquid phase sintering of SiC with rare-earth oxides. Ceram Silikaty 2005; 49(4): 259-62.
66. Ko SI, Lee SJ, Roh MH, Kim W, Kim YW. Effect of annealing on mechanical properties of silicon carbide sintered with aluminum nitride and scandium oxide. Met Mater Int 2009; 15(1): 149-53.
67. Kim YW, Mitomo M, Nishimura T. High-Temperature Strength of Liquid-Phase-Sintered SiC with AlN and Re_2O_3 (RE= Y, Yb). J Am Ceram Soc 2002; 85(4): 1007-9.
68. Grande T, Sommerset H, Hagen E, Wiik K, Einarsrud MA. J Am Ceram Soc 1997; 80: 1047-52
69. Padture NP. In situ-toughened silicon carbide. J Am Ceram Soc 1994; 77(2): 519-23.
70. Lee SK, Kim CH. Effects of α-SiC versus β-SiC starting powders on microstructure and fracture toughness of SiC sintered with Al_2O_3-Y_2O_3 additives. J Am Ceram Soc 1994; 77(6): 1655-8.
71. Kim YW, Mitomo M, Emoto H Lee JG. Effect of Initial α-Phase Content on Microstructure and Mechanical Properties of Sintered Silicon Carbide. J Am Ceram Soc 1998; 81: 3136–40.
72. Borrero-López O, Ortiz AL, Guiberteau F, Padture NP. Effect of Liquid-Phase Content on the Contact Mechanical Properties of Liquid-Phase-Sintered α-SiC. J Eur Ceram Soc 2007; 27(6): 2521-7.

73. Kumar BM, Roh MH, Kim YW, Kim W, Park SW. Mechanical properties of SiC ceramics sintered with RE_2O_3 (RE: Sc, Lu, Y) and AlN additives. Met Mater Int 2010; 16(2): 229-33.
74. Landon M, Thevenot F. The SiC-AlN system: Influence of elaboration routes on the solid solution formation and its mechanical properties. Ceram Int 1991; 17(2): 97-110.
75. Ruh R, Zangvil A. Composition and Properties of Hot-Pressed SiC-AIN Solid Solutions. J Am Ceram Soc 1982; 65(5): 260-5.
76. Huang R, Gu H, Rixecker G, Aldinger F, Scheu C, Rühle M. Analytical TEM study of microstructure—property relations in liquid-phase-sintered SiC with AlN—Y_2O_3 additives. Z Metallkd 2005; 96(5): 496-502.
77. Kim NH, Fun QD, Komeya K, Meguro T. Phase Reaction and Sintering Behavior in the Pseudoternary System AlN-Y_2O_3-Al_2O_3. J Am Ceram Soc 1996; 79(10): 2645-51.
78. Orru R, Licheri R, Locci AM, Cincotti A, Cao G. Consolidation/synthesis of materials by electric current activated/assisted sintering. Mat Sci Eng R 2009; 63(4-6): 127-287.
79. Cologna M, Rashkova B, Raj R. Flash sintering of nanograin zirconia in <5 s at 850 °C. J Am Ceram Soc 2010; 93(11): 3556-9.
80. Munir ZA, Anselmi-Tamburini U, Ohyanagi M. The effect of electric field and pressure on the synthesis and consolidation of materials: A review of the spark plasma sintering method. J Mater Sci 2006; 41: 763-77.
81. Belmonte M, Osendi MI, Miranzo P, Modeling the effect of pulsing on the spark plasma sintering of silicon nitride materials, Scripta Mater 2011; 65(3): 273-6.
82. Belmonte M, González-Julián J, Miranzo P, Osendi MI, Continuous in situ functionally graded silicon nitride materials. Acta Mater 2009; 57(9): 2607-12.
83. Belmonte M, Miranzo P, Osendi MI. Enhanced microstructural and mechanical gradients on silicon nitride ceramics. Ceram Int 2015; 41(2): 2594-8.
84. Carney CM, Mah TI. Current isolation in spark plasma sintering of conductive and nonconductive ceramics. J Am Ceram Soc 2008; 91(10): 3448-50.
85. Zapata-Solvas E, Gómez-García D, Domínguez-Rodríguez A, Todd RI. Ultra-fast and energy-efficient sintering of ceramics by electric current concentration. Scientific reports 2015, 5. doi:10.1038/srep08513
86. Wang SW, Chen LD, Hirai T, Kang YS. Microstructure inhomogeneity in Al_2O_3 sintered bodies formed during the plasma-activated sintering process. J Mater Sci Lett 1999; 18: 1119-21.

87. Yanagisawa O, Kuramoto H, Matsugi K, Komatsu K. Observation of particle behavior in copper powder compact during pulsed electric discharge. Mater Sci Eng A 2003; 350: 184-9.
88. Chaim R. Densification mechanism in spark plasma sintering of nanocrystalline ceramics. Mater Sci Eng A 2007; 443, 25–32.
89. Hulbert DM, Anders A, Dudina DV, Andersson J, Jiang D, Unuvar C, Anselmi-Tamburini U, Lavernia EJ, Mukherjee AK. The absence of plasma in "spark plasma sintering". J Appl Phys 2008; 104(3): 033305.
90. Olevsky E, Bogachev I, Maximenko A. Spark-plasma sintering efficiency control by inter-particle contact area growth: A viewpoint. Scripta Mater 2013; 69(2): 112-6.
91. Miranzo P, González-Julián J, Osendi MI, Belmonte M. Enhanced particle rearrangement during liquid phase spark plasma sintering of silicon nitride-based ceramics. Ceram Int 2011; 37(1):159-66.
92. Nishimura T, Mitomo M, Hirotsuru H, Kawahara M. Fabrication of silicon nitride nano-ceramics by spark plasma sintering. J Mater Sci Lett 1995; 14: 1046-7.
93. Osendi MI, Gautheron F, Miranzo P, Belmonte M. Dense and homogeneous silicon nitride composites containing carbon nanotubes. J Nanosci Nanotechnol 2009; 9: 6188-94
94. Guillard F, Allemand A, Lulewiczand J, Galy J. Densification of SiC by SPS-effects of time, temperature and pressure. J Eur Ceram Soc 2007;27(7):2725-8.
95. Zhang ZH, Wang FC, Luo J, Lee SK, Wang L. Processing and characterization of fine-grained monolithic SiC ceramic synthesized by spark plasma sintering. Mater Sci Eng A 2010; 527(7-8): 2099-103.
96. Hayun S, Paris V, Mitrani R, Kalabukhov S, Dariel MP, Zaretsky E, Frage N. Microstructure and mechanical properties of silicon carbide processed by spark plasma sintering (SPS). Ceram Int 2012; 38(8): 6335-40.
97. Ohyanagi M, Yamamoto T, Kitaura H, Kodera Y, Ishii T, Munir ZA. Consolidation of nanostructured SiC with disorder-order transformation. Scripta Mater 2004; 50(1):111-4.
98. Lara A, Ortiz AL, Muñoz A, Dominguez-Rodríguez A. Densification of additive-free polycrystalline β-SiC by spark-plasma sintering. Ceram Int 2012; 38(1): 45-53.
99. Yamamoto T, Kondou T, Kodera Y, Ishii T, Ohyanagi M, Munir ZA. Mechanical properties of β-SiC fabricated by spark plasma sintering. J Mater Eng Perform 2005; 14(4): 460-6.

100. Lorrette C, Reau A, Briottet L. Mechanical properties of nanostructured silicon carbide consolidated by spark plasma sintering. J Eur Ceram Soc 2013; 33(1): 147-56.
101. Lomello F, Bonnefont G, Leconte Y, Herlin-Boime N, Fantozzi G. Processing of nano-SiC ceramics: densification by SPS and mechanical characterization. J Eur Ceram Soc 2012; 32(3): 633-41.
102. Zhou Y, Hirao K, Toriyama M, Tanaka H. Very rapid densification of nanometer silicon carbide powder by pulse electric current sintering. J Am Ceram Soc 2000; 83(3): 654-6.
103. Gephart S, Singh J, Kulkarni A. Structure-property relationship for sintered SiC by field assisted sintering technique. Int J Refract Met H 2013; 37: 33-9.
104. Gephart S, Singh J, Kulkarni A. Field assisted sintering of SiC using extreme heating rates, J Mater Sci 2011; 46: 3659-63.
105. Kriegesmann J. Processing of Silicon Carbide-Based Ceramics. In Comprehensive Hard Materials (pp. 89–175), Ed. V.K. Sarin & L. Llanes, D. Mari, Elsevier, 2014. ISBN: 9780080965277
106. Zhou Y, Hirao K, Toriyama M, Tanaka H. Silicon carbide ceramics prepared by pulse electric current sintering of β-SiC and α-SiC powders with oxide and nonoxide additives. J Mater Res 1999; 14(8): 3363-9.
107. Herrmann M, Neher R, Brandt K, Hoehn S. Micro-segregations in liquid phase sintered silicon carbide ceramics. J Eur Ceram Soc 2010; 30(6): 1495-501.
108. Yi J, Xue WJ, Xie ZP, Liu W, Cheng LX, Chen J, Wang L, Cheng H, Gao YX, Wang HB. The dependence of interlocking and laminated microstructure on toughness and hardness of β-SiC ceramics sintered at low temperature. Mat Sci Eng A Struct 2013; 586: 338-41.
109. Hotta M, Hojo J. Inhibition of grain growth in liquid-phase sintered SiC ceramics by AlN additive and spark plasma sintering. J Eur Ceram Soc 2010; 30(10): 2117-22.
110. Hotta M, Kita H, Hojo J. Nanostructured silicon carbide ceramics fabricated through liquid-phase sintering by spark plasma sintering, J Ceram Soc Jpn 2011; 119(1386): 129-32.
111. Zapata-Solvas E, Bonilla S, Wilshaw PR, Todd RI. Preliminary investigation of flash sintering of SiC. J Eur Ceram Soc 2013; 33(13-14): 2811-6.
112. Gibson LJ, Ashby MF. Cellular Solids, Structure and Properties, 2nd ed., Cambridge University Press, Cambridge, UK, 1997.
113. Scheffler M, Colombo P. Cellular ceramics. John Wiley & Sons,Germany, 2006.
114. Brezny R, Green DJ. Mechanical behavior of cellular ceramics. Mat Sci Tech 1991; 11: 463-516.

115. Schwartz DS, Shih DS, Evans AG, Wadley HNG. Porous and Cellular Materials for Structural Applications. Materials Research Society Proceedings Vol. 521, MRS, Warrendale, PA, USA, 1998.
116. Green DJ, Colombo P. Cellular Ceramics: Intriguing Structures, Novel Properties, and Innovative Applications. MRS Bull 2003; 28: 296-300.
117. Woesz A, Rumpler M, Stampfl J, Varga F, Fratzl-Zelman N, Roschger P, Klaushofer K, Fratzl P. Towards bone replacement materials from calcium phosphates via rapid prototyping and ceramic gelcasting. Mater Sci Eng C 2005; 25(2): 181-6.
118. Studart AR, Gonzenbach UT, Tervoort E, Gauckler LJ. Processing routes to macroporous ceramics: a review. J Am Ceram Soc 2006; 89(6): 1771-89.
119. Kim YW, Kim SH, Song IH, Kim HD, ParkCB. Fabrication of Open-Cell, Microcellular Silicon Carbide Ceramics by Carbothermal Reduction. J Am Ceram Soc 2005; 88(10): 2949–51.
120. Wang H, Sung IY, Li XD, Kim D. Fabrication of Porous SiC Ceramics with Special Morphologies by Sacrificing Template Method. J Porous Mater 2004; 11(4): 265–71.
121. Sun Y, Tan SH, Jiang DL. Synthesis of Porous Silicon Carbide and its Catalysis. J Inorganic Mater 2003; 18(4): 830–6.
122. Song IH, Kwon IM, Kim HD, Kim YW. Processing of microcellular silicon carbide ceramics with a duplex pore structure. J Eur Ceram Soc 2010; 30(12): 2671-6.
123. Reynaud C, Thévenot F, Chartier T, Besson JL. Mechanical properties and mechanical behaviour of SiC dense-porous laminates. J Eur Ceram Soc 2005; 25(5): 589-97.
124. Guo X, Cai X, Zhu L, Zhang L, Yang H. Preparation and properties of SiC honeycomb ceramics by pressureless sintering technology. J Adv Ceram 2014; 3(1): 83-8.
125. Schwartzwalder K Somers AV. Method of Making Porous Ceramic Articles, US Pat. No. 3090094, May 21, 1963.
126. Bao X, Nangrejo MR, Edirisinghe MJ. Preparation of Silicon Carbide Foams Using Polymeric Precursor Solutions. J Mater Sci 2000; 35(17): 4365–72.
127. Ortona A, D'Angelo C, Gianella S, Gaia D. Cellular ceramics produced by rapid prototyping and replication. Mater Lett 2012; 80: 95-8.
128. Nangrejo MR, Edirisinghe MJ. Porosity and Strength of Silicon Carbide Foams Prepared Using Preceramic Polymers. J Porous Mater 2002; 9(2): 131–40.
129. Vogli E, Sieber H, Greil P. Biomorphic SiC–Ceramic Prepared by Si–Vapor Phase Infiltration of Wood. J Eur Ceram Soc 2002; 22(14–15): 2663–8.

130. Locs J, Berzina-Cimdina L, Zhurinsh A, Loca D. Effect of processing on the microstructure and crystalline phase composition of wood derived porous SiC ceramics. J Eur Ceram Soc 2011; 31(1): 183-8.
131. Ota T, Takahashi M, Hibi T, Ozawa M, Suzuki S, Hikichi Y, Suzuki H. Biomimetic Process for Producing SiC “Wood”. J Am Ceram Soc 1995; 78(12): 3409–11.
132. Qian JM, Wang JP, Jin ZH. Preparation of Biomorphic SiC Ceramics by the Reactive Infiltration on of Si into Carbon Template Derived from Basswood. Rare Metal Mater Eng 2004; 33(10): 1065–8.
133. Varela-Feria FM, Martinez-Fernandez J, de Arellano-Lopez AR, Singh M. Low Density Biomorphic Silicon Carbide: Microstructure and Mechanical Properties. J Eur Ceram Soc 2002; 22(14–15): 2719–25.
134. Greil P, Lifka T, Kaindl A. Biomorphic Cellular Silicon Carbide Ceramics from Wood: I. Processing and Microstructure. J Eur Ceram Soc 1998; 18(14): 1961–73.
135. Herzog A, Klingner R, Vogt U, Graule T. Wood-Derived Porous SiC Ceramics by Sol Infiltration and Carbothermal Reduction. J Am Ceram Soc 2004; 87(5): 784–93.
136. Mouazer R, Thijs I, Mullens S, Luyten J. SiC Foams Produced by Gel Casting: Synthesis and Characterization. Adv Eng Mater 2004; 6(5): 340–3.
137. Qiu JF, Li JT, Smirnov KL. Combustion synthesis of high porosity SiC foam with nanosized grains. Ceram Int 2010; 36(6): 1901-4.
138. Geim AK, Novoselov KS. The rise of graphene. Nature materials 2007; 6(3): 183-91.
139. Mattevi C, Eda G, Agnoli S, Miller S, Mkhoyan KA, Celik O, Mastrogiovanni D, Granozzi G, Garfunkel E, Chhowalla M. Evolution of electrical, chemical, and structural properties of transparent and conducting chemically derived graphene thin films. Adv Funct Mater 2009; 19(16): 2577-83.
140. Wu ZS, Ren W, Gao L, Zhao J, Chen Z, Liu B, Tang D, Yu B, Jiang C, Cheng HM. Synthesis of graphene sheets with high electrical conductivity and good thermal stability by hydrogen arc discharge exfoliation. ACS Nano 2009; 3(2): 411-7.
141. Bolotin KI, Sikes KJ, Jiang Z, Klima M, Fudenberg G, Hone J, Kim P, Stormer HL. Ultrahigh electron mobility in suspended graphene. Solid State Commun 2008; 146 (9–10): 351–5.
142. Lee C, X. Wei X, J.W. Kysar JW, J. Hone J. Measurement of elastic properties and intrinsic strength of monolayer graphene. Science 2008; 321: 385-8.
143. Pop E, Varshney V, Roy AK. Thermal properties of graphene: Fundamentals and applications. MRS Bull 2012; 37(12): 1273-81.

144. Nika DL, Pokatilov EP, Askerov AS, Balandin AA. Phonon thermal conduction in graphene: Role of Umklapp and edge roughness scattering. Phys Rev B 2009; 79(15): 155413.
145. Balandin AA, Ghosh S, Bao W, Calizo I, Teweldebrhan D, Miao F, Lau CN. Superior thermal conductivity of single-layer graphene. Nano Lett 2008; 8(3): 902-7.
146. Chen S, Moore AL, Cai W, Suk JW, An J, Mishra C, Amos C, Magnuson CW, Kang J, Shi L, Ruoff RS. Raman measurements of thermal transport in suspended monolayer graphene of variable sizes in vacuum and gaseous environments. ACS Nano 2010; 5(1): 321-8.
147. Alofi A, Srivastava GP. Thermal conductivity of graphene and graphite. Phys Rev B 2013; 87(11):115421.
148. Seol JH, Jo I, Moore AL, Lindsay L, Aitken ZH, Pettes MT, Li X, Yao Z, Huang R, Broido D, Mingo N, Ruoff RS, Shi L. Two-dimensional phonon transport in supported graphene. Science 2010; 328(5975): 213-6.
149. Ghosh S, Bao W, Nika DL, Subrina S, Pokatilov EP, Lau CN, Balandin AA. Dimensional crossover of thermal transport in few-layer graphene. Nat Mater 2010; 9(7): 555-8.
150. Nair RR, Blake P, Grigorenko AN, Novoselov KS, Booth TJ, Stauber T, Peres NMR, Geim AK. Fine structure constant defines visual transparency of graphene. Science 2008; 320: 1308.
151. Wang X, Zhi L, Müllen K. Transparent, conductive graphene electrodes for dye-sensitized solar cells. Nano Lett 2008; 8(1): 323-7.
152. Yin Z, Zhu J, He Q, Cao X, Tan C, Chen H, Yan Q, Zhang H. Graphene-Based Materials for Solar Cell Applications. Adv Energy Mater 2014; 4: 1300574.
153. Novoselov KS, Geim AK, Morozov SV, Jiang D, Zhang Y, Dubonos SV, Grigorieva IV, Firsov AA. Electric field effect in atomically thin carbon films. Science 2004; 306: 666-9.
154. Boehm HP, Setton R, Stumpp E. Nomenclature and terminology of graphite intercalation compounds. Carbon 1986; 24: 241-5.
155. Singh V, Joung D, Zhai L, Das S, Khondaker SI, Seal S. Graphene based materials: past, present and future. Prog Mater Sci 2011; 56: 1178-271.
156. de Heer WA, Berger C, Wu X, First PN, Conrad EH, Li X, Li T, Sprinkle M, Hass J, Sadowski ML, Potemski M, Martinez G. Epitaxial graphene. Solid State Commun 2007; 143: 92-100.

157. Emtsev KV, Speck F, Seyller T, Ley L, Riley JD. Interaction, growth, and ordering of epitaxial graphene on SiC {0001} surfaces: A comparative photoelectron spectroscopy study. Phys Rev B 2008; 77(15): 155303.
158. Yannopoulos SN, Siokou A, Nasikas NK, Dracopoulos V, Ravani F, Papatheodorou GN. CO_2-Laser-Induced Growth of Epitaxial Graphene on 6H-SiC (0001). Adv Funct Mater 2012; 22(1): 113-20.
159. Novoselov KS, Fal VI., Colombo L, Gellert PR, Schwab MG, Kim K. A roadmap for graphene. Nature 2012; 490 (7419): 192-200.
160. Bonaccorso F, Lombardo A, Hasan T, Sun Z, Colombo L, Ferrari AC. Production and processing of graphene and 2d crystals. Mater Today 2012; 15: 564-99.
161. Obraztsov AN. Chemical vapour deposition: making graphene on a large scale. Nat Nanotechnol 2009; 4(4): 212-3.
162. Chen Z, Ren W, Gao L, Liu B, Pei S, Cheng HM. Three-dimensional flexible and conductive interconnected graphene networks grown by chemical vapour deposition. Nat Mater 2011; 10(6):424-8.
163. Cao X, Shi Y, Shi W, Lu G, Huang X, Yan Q, Zhang Q, Zhang H. Preparation of novel 3D graphene networks for supercapacitor applications. Small 2011; 7(22): 3163-8.
164. Hernández Y, Nicolosi V, Lotya M, Blighe FM, Sun Z, De S, McGovern IT, Holland B, Byrne M, Gun'Ko YK, Boland JJ, Niraj P, Duesberg G, Krishnamurthy S, Goodhue R, Hutchison J, Scardaci V, Ferrari AC, Coleman JN. High-yield production of graphene by liquid-phase exfoliation of graphite. Nat Nanotechnol 2008; 3(9): 563-8.
165. Dreyer D, Park S, Bielawski CW, Ruoff R. The chemistry of graphene oxide. Chem Soc Rev (2010); 39: 228-40.
166. Gilje S, Han S, Wang M, Wang KL, Kaner RB. A chemical route to graphene for device applications. Nano Lett 2007; 7(11): 3394-8.
167. Fan Y, Wang L, Li J, Li J, Sun S, Chen F, Chen L, Jiang W. Preparation and electrical properties of graphene nanosheet/Al_2O_3 composites. Carbon 2010; 48: 1743-9.
168. Ramírez C, Figueiredo FM, Miranzo P, Poza P, Osendi MI. Graphene nanoplatelet / silicon nitride composites with high electrical conductivity. Carbon 2012; 50: 3607-15.
169. Ramírez C, Vega-Díaz SM, Morelos-Gómez A, Figueiredo FM, Terrones M, Osendi MI, Belmonte M, Miranzo P. Synthesis of conducting graphene/Si_3N_4 composites by spark plasma sintering. Carbon 2013; 57: 425-32.

170. Shin JH, Hong SH. Fabrication and properties of reduced graphene oxide reinforced yttria-stabilized zirconia composite ceramics. J Eur Ceram Soc 2014; 34(5): 1297-302.
171. Fan Y, Jiang W, Kawasaki A. Highly Conductive Few-Layer Graphene/Al_2O_3 Nanocomposites with Tunable Charge Carrier Type. Adv Funct Mater 2012; 22: 3882–9.
172. Ramirez C, Garzon L, Miranzo P, Osendi MI, Ocal C. Electrical conductivity maps in graphene nanoplatelet/silicon nitride composites using conducting scanning force microscopy. Carbon 2011; 49(12): 3873-80.
173. Čapková P, Matějka V, Tokarský J, Peikertová P, Neuwirthová L, Kulhánková L, Beňo J, Stýskala V. Electrically conductive aluminosilicate/graphene nanocomposite. J Eur Ceram Soc 2014;34:3111-7.
174. Miranzo P, García E, Ramírez C, González-Julián J, Belmonte M, Osendi MI. Anisotropic thermal conductivity of silicon nitride ceramics containing carbon nanostructures. J Eur Ceram Soc 2012; 32(8): 1847-54.
175. Rutkowski P, Stobierski L, Górny G. Thermal stability and conductivity of hot-pressed Si_3N_4–graphene composites. J Therm Anal Calorim 2014;116(1):321-8.
176. Rutkowski P, Klimczyk P, Jaworska L, Stobierski L, Dubiel A. Thermal properties of pressure sintered alumina–graphene composites. J Therm Anal Calorim 2015. Doi: 10.1007/s10973-015-4694-x.
177. Xia H, Zhang X, Shi Z, Zhao C, Li Y, Wang J, Qiao G. Mechanical and thermal properties of reduced graphene oxide reinforced aluminum nitride ceramic composites. Mat Sci Eng A 2015; 639: 29-36.
178. Yun C, Feng Y, Qiu T, Yang J, Li X, Yu L. Mechanical, electrical, and thermal properties of graphene nanosheet/aluminum nitride composites. Ceram Int 2015; 41(7): 8643-9.
179. Ramírez Maglione MC. PhD Thesis: Materiales multifuncionales de nitruro de silicio con nanoestructuras reforzanters basadas en grafeno. 2014. http://hdl.handle.net/10486/662461
180. Li Q, Zhang Y, Gong H, Sun H, Li T, Guo X, Ai S. Effects of graphene on the thermal conductivity of pressureless-sintered SiC ceramics. Ceram Int 2015. Doi: 10.1016/j.ceramint.2015.07.149
181. Ramirez C, Osendi MI. Toughening in ceramics containing graphene fillers. Ceram Int 2014; 40(7): 11187-92.
182. Lee B, Koo MY, Jin SH, Kim KT, Hong SH. Simultaneous strengthening and toughening of reduced graphene oxide/alumina composites fabricated by molecular-level mixing process. Carbon 2014; 78: 212-19.

183. Centeno A, Rocha VG, Alonso B, Fernández A, Gutierrez-Gonzalez CF, Torrecillas R, Zurutuza A. Graphene for tough and electroconductive alumina ceramics. J Eur Ceram Soc 2013; 33(15): 3201-10.
184. Fan Y, Igarashi G, Jiang W, Wang L, Kawasaki A. Highly strain tolerant and tough ceramic composite by incorporation of graphene. Carbon 2015; 90: 274-83.
185. Walker LS, Marotto VR, Rafiee MA, Koratkar N, Corral EL. Toughening in graphene ceramic composites. ACS Nano 2011; 5(4): 3182-90.
186. Ramirez C, Miranzo P, Belmonte M, Osendi MI, Poza P, Vega-Diaz SM, Terrones M. Extraordinary toughening enhancement and flexural strength in Si_3N_4 composites using graphene sheets. J Eur Ceram Soc 2014; 34(2): 161-9.
187. Nieto A, Lahiri D, Agarwal A. Graphene NanoPlatelets reinforced tantalum carbide consolidated by spark plasma sintering. Mater Sci Eng A 2013; 582: 338-46.
188. Kvetková L, Duszová A, Hvizdoš P, Dusza J, Kun P, Balázsi C. Fracture toughness and toughening mechanisms in graphene platelet reinforced Si_3N_4 composites. Scripta Materialia 2012; 66(10): 793-6.
189. Belmonte M, Ramírez C, González-Julián J, Schneider J, Miranzo P, Osendi MI. The beneficial effect of graphene nanofillers on the tribological performance of ceramics. Carbon 2013; 61: 431-5.
190. Hvizdos P, Dusza J, Balázsi C. Tribological properties of Si_3N_4-graphene nanocomposites. J Eur Ceram Soc 2013; 33 (12); 2359-64.
191. Rutkowski P, Stobierski L, Zientara D, Jaworska L, Klimczyk P, Urbanik M. The influence of the graphene additive on mechanical properties and wear of hot-pressed Si_3N_4 matrix composites. J Eur Ceram Soc 2015; 35 (1); 87-94.
192. Kim HJ, Lee SM, Oh YS, Yang YH, Lim YS, Yoon DH, Lee C, Kim JY, Ruoff RS. Unoxidized graphene/alumina nanocomposite: fracture- and wear-resistance effects of graphene on alumina matrix. Sci Rep-UK 2014; 4: 5176.
193. Gutierrez-Gonzalez CF, Smirnov A, Centeno A, Fernández A, Alonso B, Rocha VG, Torrecillas R, Zurutuza A, Bartolomé JF. Wear behavior of graphene/alumina composite. Ceram Int 2015; 41 (6): 7434-8.
194. Porwal H, Tatarko P, Saggar R, Grasso S, Mani MK, Dlouhý I, Dusza J, Reece MJ. Tribological properties of silica-graphene nanoplatelet composites. Ceram Int 2014; 40(8): 12067-74.

Chapter 2

Development of 3D architectures of SiC by Robocasting

2.1.- Introduction: the additive manufacturing techniques & Robocasting

The new advances achieved in materials science over the last years, particularly in the field of ceramics, have oriented research activities towards new applications that require the development of dense or porous ceramic components and structures with more and more complex designs, and smaller feature sizes at the microscale. Significant examples of present and near-future applications envisaged for ceramic materials are listed in Table 2.1.

Table 2.1.- Some of the most relevant present and near-future applications of complex ceramic components in different fields.

Field of interest	Specific applications
Acoustics	Acoustic metamaterials, lenses, cloaks
Biomaterials	Bone implants, dental prostheses
Chemistry	Advanced filters, catalytic supports, sensors
Electromagnetism	Electrodes, electromagnetic interference shields, memories
Electronics	Ceramic substrates, capacitors, piezo-actuators, thermistors
Energy	Fuel cells, gas turbines, burners, batteries, solar cells
Nuclear	Fuel cladding
Optics	Optical fibres, electro-optic devices
Structural ceramics	Tools (seals, bearings, valves), engine parts, lightweight components
Thermal management	Heat sinks, heat exchangers, thermal insulators

For the accomplishment of these uses and functionalities, the manufacture of components has traditionally been limited by the unavailability of techniques capable to produce 3D-shaped ceramic bodies, where a higher approach from the initial (green) to the final (sintered) state of the finished materials is attained. As far as possible, the objective should be to avoid machining processes that raise the price of the final product, and prolong the production time at large-scale.[1]

The concept of AM is the opposite of machining.[2] Machining processes of ceramics involve the removal of material, once the ceramic body is sintered, to obtain a shaped structure; conversely, AM techniques include those which consist in forming the prototypes by continuously adding or attaching material so that the final 3D shape is in that way obtained. Consequently, the use of molds is completely unnecessary.

Modern AM procedures implement the equipment with advanced technology based on computer-controlled operation that allows the reproducibility of designs and a high level of accuracy for the smallest possible feature sizes.[3,4]

Initially, the development of AM techniques was not envisaged for mass production methods of ordinary products. The attention is normally put on the fact that the as-fabricated parts have a high added value for certain applications that require especial geometries, which are impossible to fabricate either by using molds or by machining, owing to their small size and geometrical intricacy. Therefore, those specific needs for accurate complex shapes justified the high costs in AM; today, the advanced development in the field of AM has already lowered the production costs. At the time being, when there are already different AM techniques available for ceramics, materials with new functionalities, scalability issues (size, resolution), and a more effective production are being investigated.

Depending on the different authors, there are several classifications of the AM techniques. Travitzky et al.[5] presented a categorization (Fig. 2.1) where the main AM processes are arranged, in essence, in relation to the dimensional order of the material being added or delivered to form the final component, to the state of aggregation of the starting material, and to the type of layer formation.

The main differences and characteristics of the potential achievable shapes of the structures to be created by using an AM technique, or in other words, the limits for the fabrication of very complex morphologies and cellular architectures, are attributable to the ink delivery system, taking into account the general classification of zero-, one- and two-dimensional-order “printing units” that can be considered for material deposition (drops, filaments or plates, respectively). In this way, AM techniques are often referred to as droplet-, filament- or plate-based manufacturing, respectively.

A more detailed description of these techniques as a function of the dimensional order of the printable ceramic units is given below.

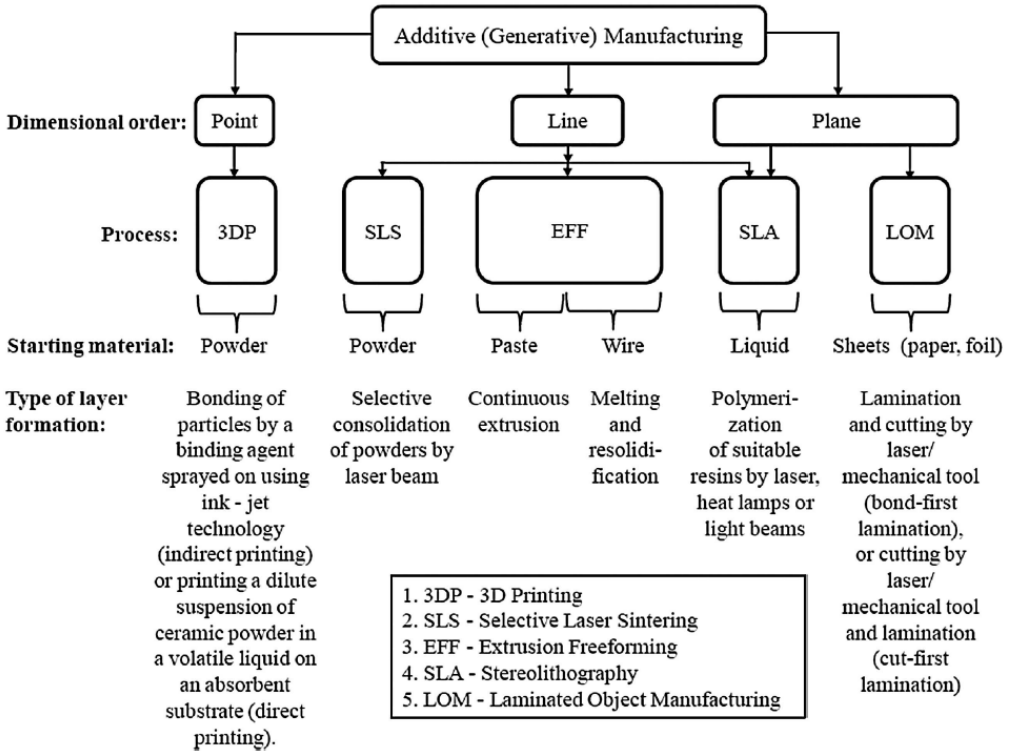

Figure 2.1.- General classification of the AM techniques according to Travitzky et al.[5]

2.1.1.- The zero-dimensional-order techniques

The zero-dimensional-order techniques based on a droplet delivery approach comprise direct[6-8] and indirect ink-jet printing (the latter is also known as 3D printing, 3DP).[9-11] As in all of AM methods, structures are constructed in a layer-by-layer fashion, each layer being considered in these cases as an arrangement of pixels filled (or not) by a single droplet each. The droplet size determines the layer thickness and lateral resolution of each pixel, which are also affected by the spreading and deformation of droplets once deposited. Both direct and indirect ink-jet printing methods fail, as compared to other AM techniques, in relation to the attainable accuracy and finishing of the final structures.

Direct ink-jet printing (Fig. 2.2a) is typically developed in air with colloidal inks or waxes containing ceramic powders that rapidly solidify after drying or freezing, respectively. The use of waxes, held in a melted state, makes the process of solidification easier since they cool and solidify instantly, although they are more difficult to remove than binders after being printed.[12-15] Also, by implementing the direct ink-jet printing methods with two nozzles, there is an approach for the fabrication of floating parts within the structures by consisting in the deposition of a

fugitive ink (eventually removable by calcination) that acts as a supporting element for the floating parts of the as-printed structures, which gives a higher versatility towards the fabrication of complex structures.

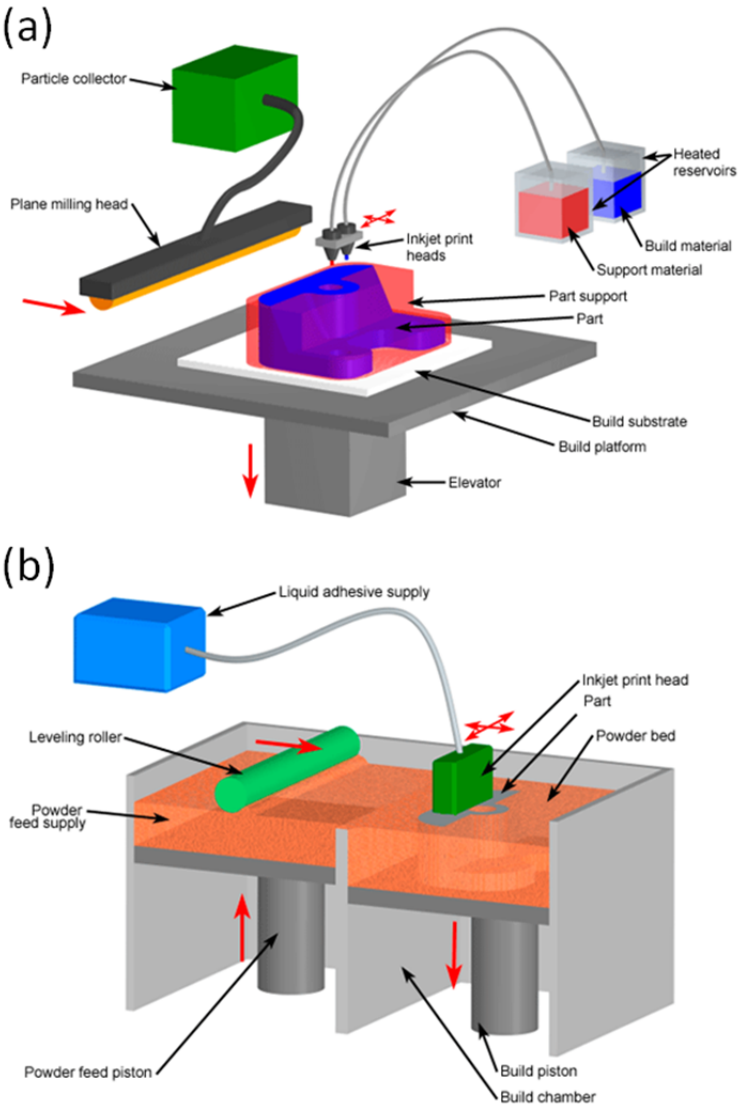

Figure 2.2.- Representative illustrations of (a) direct ink-jet printing and (b) indirect ink-jet printing methods (images from costumpartnet.com)

In contrast, solutions consisting of only binders are capable to create local aggregates of ceramic particles once deposited onto a ceramic powdered substrate. This principle is used to build up the structures in indirect ink-jet printing (Fig. 2.2b). The procedure is essentially based on a powders-bed constructed in a layer-by-layer sequence with a powder spreader, with droplets of binders being deposited onto the bed where required in each layer. The powders-bed sustains the printed droplets in each layer, providing support for the subsequent levels, which allows the fabrication of floating elements within the structures, once the free remaining powders are finally

removed. This versatility is not always an advantage since undesired trapped powders may be present within the most intricate morphologies (requiring at least one open hole to remove the surplus powders).

Both the direct and the indirect ink-jet printing methods have been put into operation with two possible types of ink delivery methods: constant-frequency[7,16] and drop-on-demand[6,12,13,17] systems. In the constant-frequency delivery systems, droplets of ink are dispensed through the nozzle at a certain fixed frequency. These droplets are electrically charged when coming out of the nozzle, and it allows selecting which droplets are deposited to form the structure, and which ones are rejected, by using deflecting electrodes, before they reach the substrate. These unselected droplets are recovered for the ink reservoir. This method is especially apt for rapidly patterning large areas. In the drop-on-demand delivery systems, droplets of ink are normally generated by a piezo-actuator when deposition is required, which makes deposition more appropriate for smaller areas and highly precise patterns.

Up to now, ink-jet printing techniques have been employed for the preliminary design of prototypes of structural ceramics of Al_2O_3,[18] ZrO_2,[19,20] Si_3N_4,[21] and SiSiC[22-24] composites, as well as approaches for functional ceramics like TiO_2.[25] However, the biggest efforts for ink-jet printing devices have been focused on the development of bioceramic structures of hydroxyapatite[26-28] and tricalcium phosphate.[29,30]

2.1.2.- The one-dimensional-order techniques

Among the one-dimensional-order additive-manufacturing techniques, there are two main types of approaches facing the construction of 3D structures: laser-based techniques and filament-based manufacturing.

2.1.2.1.- Selective Laser Sintering (SLS)

SLS,[31,32] developed at the University of Texas in Austin by Carl Deckard, uses a high power laser beam as the source to the in-situ sintering, in a layer-by-layer fashion, of 3D complex ceramic bodies. In this technique, thin layers of powders are extended over a platform (Fig. 2.3) and, after spreading each of them, the horizontal cross-sections of the 3D structure generated in the CAD file are reproduced by selective sintering of powders. Once each layer is sintered, the platform goes down the distance corresponding to the layer thickness, and a new layer of powders is added on the upper part to continue the process. Each successive cross-section of the

structure is, thus, sintered and bonded to the previous. The powders bed surrounding the sintered body enables the construction of floating parts as it totally supports the structures. SLS is very similar to the indirect ink-jet printing as for the role played by the powders-bed, although SLS allows higher levels of accuracy.

To achieve highly dense bodies owing to an effective sintering, pulsed lasers (normally obtained by mode-locking) are commonly employed due to the highly energetic output. The powders platform is normally maintained at elevated temperatures so that the laser energy is efficiently employed to induce the sintering rather than heating the material. In this way, the gap between operation temperature and sintering temperature is conveniently reduced by amounts that depend on the nature of the ceramic material to be sintered.

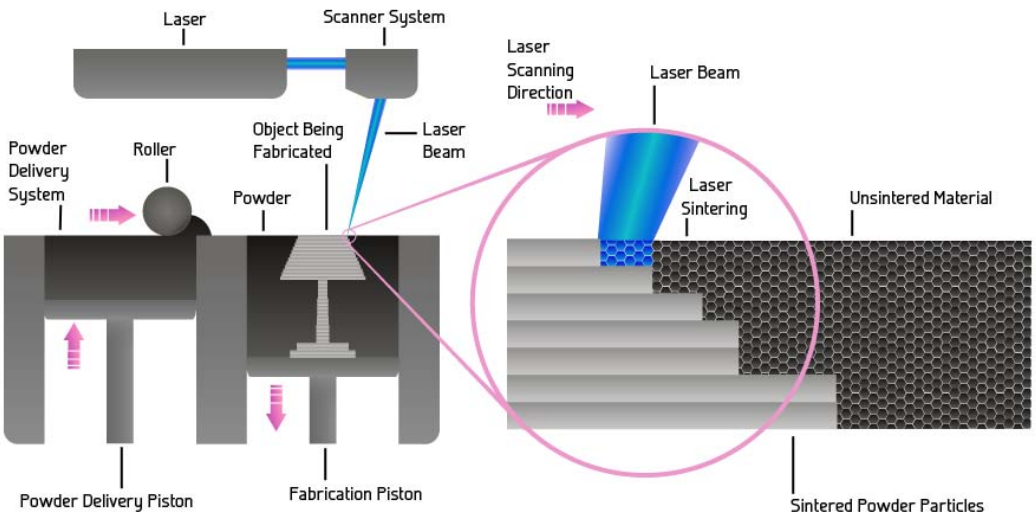

Figure 2.3.- Schematic illustration of SLS (www.rapidprototypingservicescanada.com).

The SLS technique has successfully been applied for a certain number of ceramic materials, particularly in the case of technical ceramics where Al_2O_3,[33,34] ceramics in the Al_2O_3-SiO_2 system[35] or ZrO_2[33,36] are the most noteworthy. This technique is also used for different materials other than ceramics like polymers[37] or metals[38,39].

2.1.2.2.- Filament-based manufacturing

Based on the continuous extrusion of a filament through a nozzle, a group of techniques can be classified under the general term of filament-based manufacturing, among others, *fused deposition of ceramics (FDC)*, *robocasting (RC)*, and *thermoplastic 3D printing*. The main difference between robocasting and other filament-based manufacturing methods is related to the type of ink design: whereas aqueous colloidal gels are employed in RC systems at room temperature, other techniques require thermoplastic polymers to operate the extrusion process at elevated temperatures.

- Fused deposition of ceramics (FDC)

FDC is a modification of the fused deposition modeling (FDM) for polymers[40,42], created by Scott Crump[43] at Statrasys™. A thermoplastic feedstock, highly loaded with ceramic powders, is set at the top of a hot liquefier to extrude the molten material, at a constant rate upon heating. At the same time, a CAD design guides the movements of the computer-controlled ink delivery system. The nozzle is equipped with heaters to maintain the feedstock at a temperature above the melting point of the thermoplastic material to keep the mixture flowing effortlessly (Fig 2.4). Then, the extruded material hardens right after being deposited. The solidification of the as-printed structures should take place as a rapid process, which requires a precise control over the viscosity of the molten thermoplastic ink, the melting temperature, and any other geometrical parameter (e.g. the printing speed) involved in the swiftness of cooling.

Although FDC has been proved capable to produce morphologically complex green ceramic bodies, there is an important drawback to tackle when employing this system. The printed structures contain large amounts of binders and polymeric elements that must be eliminated before sintering, which is complicated due to their thermoplastic nature. Burning out these organics might, therefore, originate deformation or blistering phenomena as polymers melt, several days being usually indispensable for a complete binders removal. By using the FDC technique, components made of Al_2O_3,[41] Si_3N_4,[42,44] lead zirconate titanate ($Pb[Zr_xTi_{1-x}]O_3$ with $0 \leq x \leq 1$, PZT)[41,45] or mullite[46] have been attained.

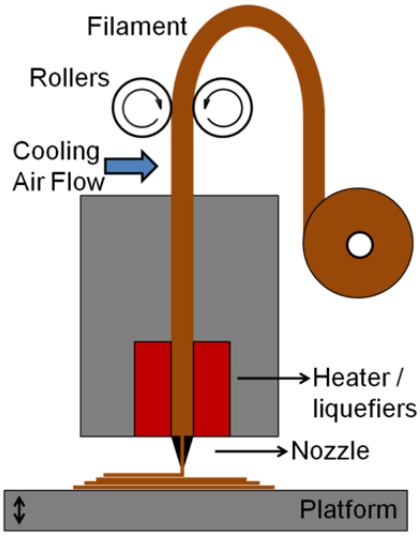

Figure 2.4.- Schematic illustration of the FDC system.

- Robocasting (RC)

The most widely known filament-based manufacturing system for ceramics is the Robocasting technique (developed at the Sandia National Laboratories), which has been utilized for the research activities within the development of this PhD Thesis. In RC,[47-49] 3D ceramic architectures are fabricated from a design generated in a CAD program (RoboCAD 4.0, 3-D Inks LLC), where the 3D object is decomposed into horizontal planes or layers, parallel to each other, to eventually accomplish the construction of the structure in a layer-by-layer fashion by printing a ceramic-based, aqueous colloidal gel onto a substrate, with each subsequent layer built onto the preceding ones. In Fig. 2.5, the RC system used for this PhD Thesis is shown, together with a simple illustration.

The ink delivery process in the case of RC is achieved by extruding a colloidal, pseudoplastic ink through a nozzle or tip of variable inner diameter (typically ranging 100 – 500 μm) that moves according to the patterned trail of the 3D design in the CAD program. After being formed, the ink retains the shape of the extruded filaments due to its high yield stress, which endows the 3D structures with sufficient strength for self-support in the green state. Normally, the printing process of the structures is executed within a non-wetting oil-bath to avoid clogging events of the ink while being extruded through the tip; the high solids loadings and the small diameter of the tips facilitate the quick drying of the extruded filaments. Then, once the structures are printed, the substrate is removed from the oil bath to let the green samples dry in air,

to completely eliminate water and oil, which might take from days to a few weeks. Finally, an organics burnout process prior to the sintering is required to assure the cleanness of the ceramic powders compact with the removal of the polymers used as organic additives during the ink processing. It is possible to operate in RC with more than one ink at the same time by using two coordinated nozzles to create composite structures where, for example, different layers are comprised of different materials in the same structure.

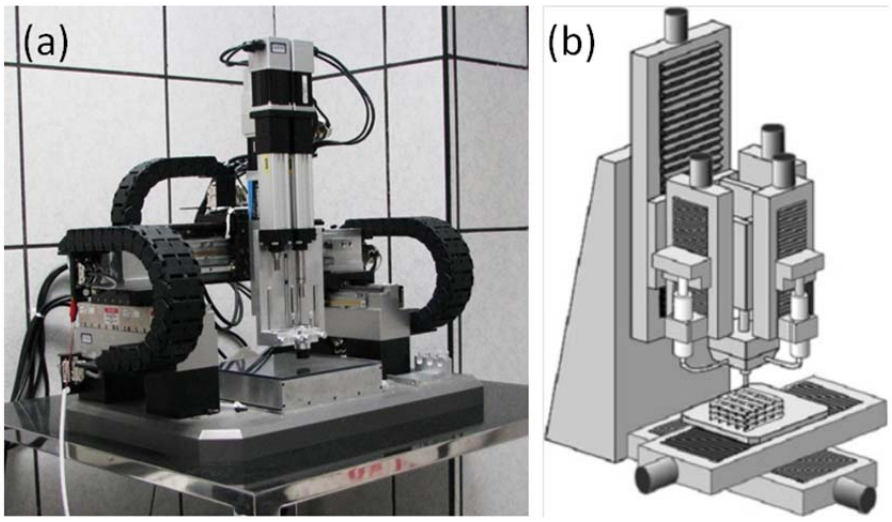

Figure 2.5.- (a) Robocasting system used in this thesis and located at ICV-CSIC, (b) and a simple schematic illustration from Smay et al.[50]

Regarding the preparation of the aqueous colloidal gels for RC, the most important requirements are to produce pastes with a high solids loading (for a minimal shrinkage during drying and sintering) and the lowest possible organic additives concentrations (for the reduction of green porosity).[50,51] The most habitual approach for the formulation of pastes is a two-step process in which the creation of a well-dispersed colloidal gel is followed by a controlled flocculation stage (Fig. 2.6). A polyelectrolyte of opposite charge to the one used as dispersant is employed to produce bridging and cross-linking phenomena between ceramic particles, owing to a modification in the pH of the suspension. This method involves a sudden decrease in the repulsive energy between particles. The resulting ink should possess a shear-thinning behavior to enable extrusion through fine deposition nozzles with rapid recovery of yield stress after deposition. Typically, a viscosifying agent (like methylcellulose, MC) can be added into the suspension providing stability to the colloidal structure of the gel, and preventing phase segregation phenomena within the gel during ink extrusion. Also, for the accomplishment of highly complex designs or floating parts, the design of fugitive inks has already been proved.[52]

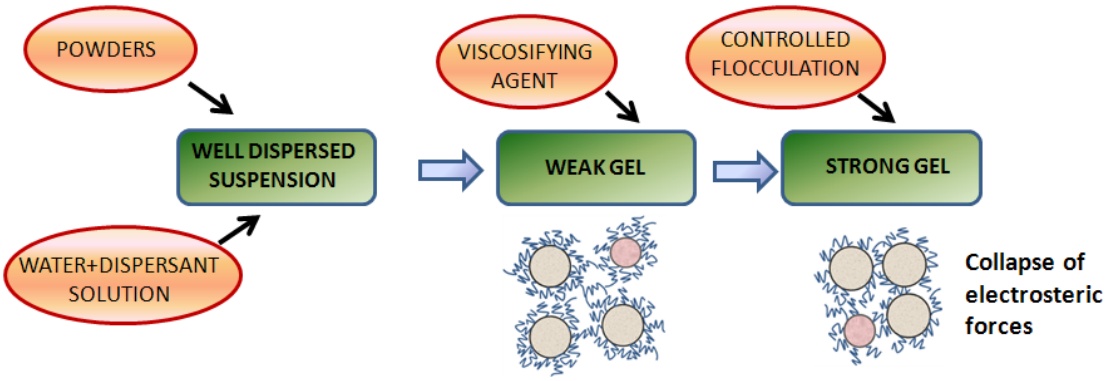

Figure 2.6.- Typical route for the optimization of inks for RC.

RC has already been employed for the fabrication of structural ceramic parts. Specifically, ceramic materials like Al_2O_3,[53] ZrO_2,[54] Si_3N_4,[55] or mullite,[56] functional ceramics such as $BaTiO_3$,[57] PZT,[58] and bioceramics like hydroxyapatite (HA)[59] and tricalcium phosphate (TCP)[60], or bioglasses[61].

- Thermoplastic 3D Printing

This a new system recently created as a combination of FDC and RC processes, looking for an enhanced manufacturing process of ceramic 3D-structures.[62] Thermoplastic binders are used to arrange highly loaded feedstock material ready for extrusion upon heating the dispensing nozzle. The delivery of this thermoplastic inks is, therefore, carried out in the same way as for RC: the dispensing nozzle is moved in the xy plane according to the CAD design in each layer, moving the unit upwards the distance of a layer thickness once each plane is finished. Operation temperature for extrusion is around 100 ºC, and the suspension solidifies immediately after being printed. The viscosity of the hot extruded inks is relatively low, which allows not only the formation of the continuous filament, as in RC, but also the production of droplets by micro-dispensing technology. By this technique, materials of Al_2O_3 and ZrO_2[62] and steel-zirconia composites[63] have been developed.

2.1.3.- The two-dimensional-order techniques

For the present case, the printing units considered for the material deposition are the whole successive plates built one on top of the previous, where an analysis of the geometry of the prototypes decomposes them into a sequence of bonded cross-

sections, broadly used as the basis of two-dimensional-order techniques. Stereolithography and Laminated Object Manufacturing are the most noteworthy.

2.1.3.1.- Stereolithography (SLA)

SLA, as a rapid prototyping process, was created in 1988 by 3D systems for the implementation of highly detailed and accurate 3D structures of polymers, basing this technology on the selective curing of a resin.[64] The design approach consists in a layer-by layer fabrication in which the contours (or cross-sectioned profiles) of each successive layer are shaped by a low-power ultraviolet (UV) laser beam that solidifies a liquid photosensitive polymer, bonding it to the underlying layer. After finishing each layer, a leveling sweeper is used to smooth the surface of the printed layer prior to the construction of the following. Similarly as in the case of 3D printing, the platform -where the structure is being built (Fig. 2.7)- descends by a distance equal to a single layer thickness before printing each subsequent layer on the upper part of the previous, until the structure is finished. Next, the structure is removed from the polymer bath and the prototype is finally dried. A post-cure is often given to the structure in a UV oven. Surfaces can be polished afterwards for a better finish. The nature of the resin and the laser spot size determine the width of the cured area, as well as the thickness of each layer (usually in the region of 50-100 μm). Ikuta et al.[65] were the first to develop a variation for SLA called microstereolithography (μSLA), where the spot of the laser has just a few micrometers diameter and photopolymer solidifies in a smaller area as compared to SLA. Resolution for thickness is within the range 1-10 μm. This variation is very useful for micromachining[66] or photonic band gap structures.[67]

The most significant parameters of SLA applied to ceramics are the viscosity of the suspension, the ceramic particle size and distribution, and the refractive index of particles.[68,69] A high volume fraction (> 50 vol.%) of ceramic particles in the curable resin is required to confer sufficient cohesion to the green part, during and after debinding. The main problem associated to SLA considered as an AM technique for ceramics is the fact that the addition of ceramic powders into the resin bath causes increased scattering of the laser beam (mostly when the size of the ceramic particles is comparable to the laser wavelength), which requires optimization in terms of the optical properties of the resin and the ceramic particles, and the solids loadings within the resin bath. Alternatively, there have been attempts to fabricate ceramic structures from pyrolyzed polymers.

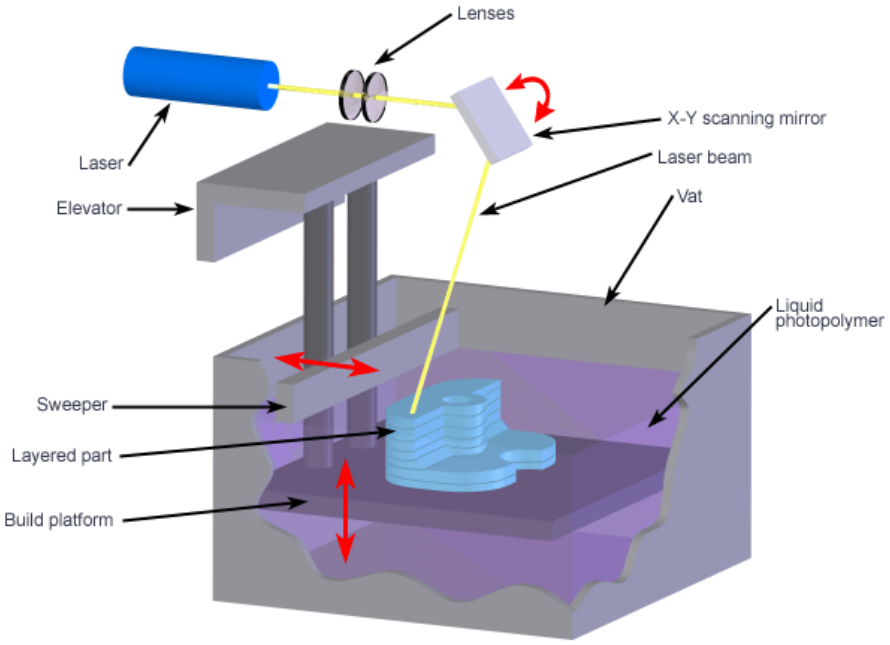

Figure 2.7.- Illustration of a SLA system (custompartnet.com)

Up to now, the research on the ceramic field is still limited, Al_2O_3 being the most studied material, both by SLA[68,70] and μSLA,[69,71,72] although some other ceramics have been studied (SiO_2,[68] ZrO_2[69] or SiCN[73]).

2.1.3.2.- Laminated Object Manufacturing (LOM)

Created by Helisys Inc., LOM is based on adhesive-coated sheets containing ceramic powders successively put over a built platform, which are cut to shape, one by one, with a laser. A schematic diagram is shown in Fig. 2.8. Once the first sheet, which is adhered to the platform, is cut, a feed mechanism rolls the following sheet on top, and heat and pressure are applied to bond the laminate to the layer below. Then, the laser cuts the corresponding contour of the part in that layer. This process is repeated as many times as layers are required to build the final structure. Variations of this method can be found replacing the laser by a mechanical cutting tool. As in the cases for SLA or indirect ink-jet printing methods, the platform is lowered a distance equal to the sheet thickness after each layer is cut and before rolling the following over the previous. After cutting the material, the undesired parts remain in place to help sustain the structure during construction.[74]

By employing the LOM technique, achievements in the field of structural ceramics have been obtained for ZrO_2,[74] Al_2O_3,[75] or Si_3N_4[76] ceramics.

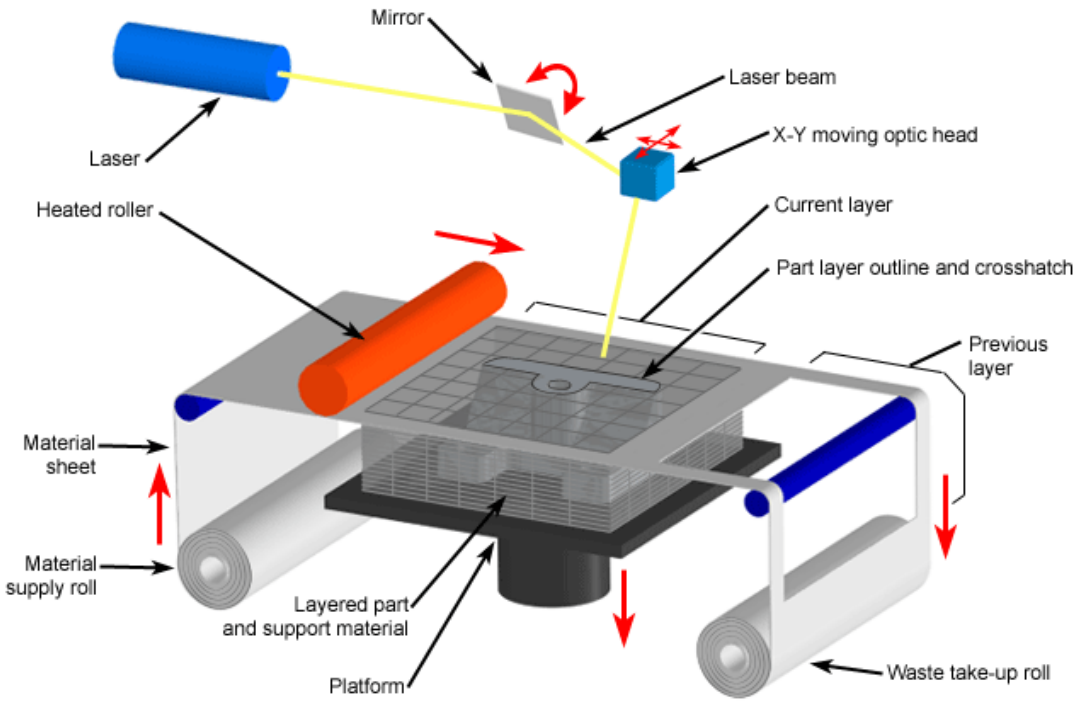

Figure 2.8.- Illustration of a LOM system (costumpartnet.com)

2.1.4.- State-of-the-art of AM of SiC ceramics

To date, very few works have been done on SiC-based ceramics produced by AM techniques, in spite of the high interest that might be generated for structural applications that demand these highly resistant, morphologically complex ceramics. Actually, the focus has been pointed on SiSiC processes (Section 1.1.2) due to its ability to be processed in near net complex shapes and the lower temperatures required for sintering compared to conventional methods. In fact, 3D SiC-based structures has been only developed by SLS[77] as the appropriate focalization of the laser beam leads to extreme local heating that induces some surface oxidation of the SiC powders and improves sintering by liquid phase mechanisms. Generally, the process for the fabrication of 3D SiSiC structures by AM methods consists in forming the 3D green structures from a mixture of SiC or SiC precursors, the carbon source and the polymeric surfactants. Then, these green structures are pyrolyzed when needed and infiltrated with the liquid silicon to form the final reaction bonded SiC structures.

Only two studies, developed by Travitzky's group,[23,24] have been found in the literature devoted to the fabrication of complex 3D-SiSiC materials by using the droplet-based AM techniques, particularly by indirect ink-jet printing. In the first work, SiC powders and dextrin, $(C_6H_{10}O_5)_n$, were employed for the creation of the 3D powders-beds, while an aqueous glycerin solution was used as binder[23] for the 3D printing process. A pyrolysis process in N_2 at 1000 ºC was needed to decompose dextrin and rearrange amorphous carbon. Fig. 2.9 shows one of the SiSiC specimens fabricated by this procedure. The potential application for these materials in high-pressure diesel injection reactors was proved with an enhanced redistribution of diesel. In the second work,[24] SiSiC lattice strut structures were also assembled by indirect ink-jet printing, using a preceramic polymer infiltration and associated pyrolysis steps prior to the pressureless liquid Si infiltration.

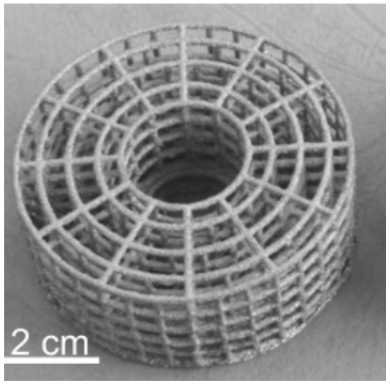

Figure 2.9.- SiSiC component fabricated by 3D printing.[23]

Besides this, two studies report the fabrication of SiSiC structures by using SLS manufacturing techniques.[77,78] Friedel et al.[78] employed a selective laser curing of preceramic polymeric powders (polymethylsilsesquioxan, also known as PMS) which, owing to its reactive groups, yield a ceramic part by local pyrolysis; in this case, the powders-bed must be kept necessarily at room-temperature to avoid uncontrolled melting during curing. Samples underwent a pyrolysis stage at 1100 ºC before being infiltrated by the liquid silicon (Fig. 2.10). Löschau *et al.*[77] also attained SiC-based structures with elevated densities by direct SLS of SiC powders.

SLA has also been utilized for the production of SiC specimens combined with a reaction-infiltration step,[79] by using a photo-curable resin with high carbon yield. The resin prototypes were pyrolyzed to eventually form a carbon preform, which was finally infiltrated with molten silicon.

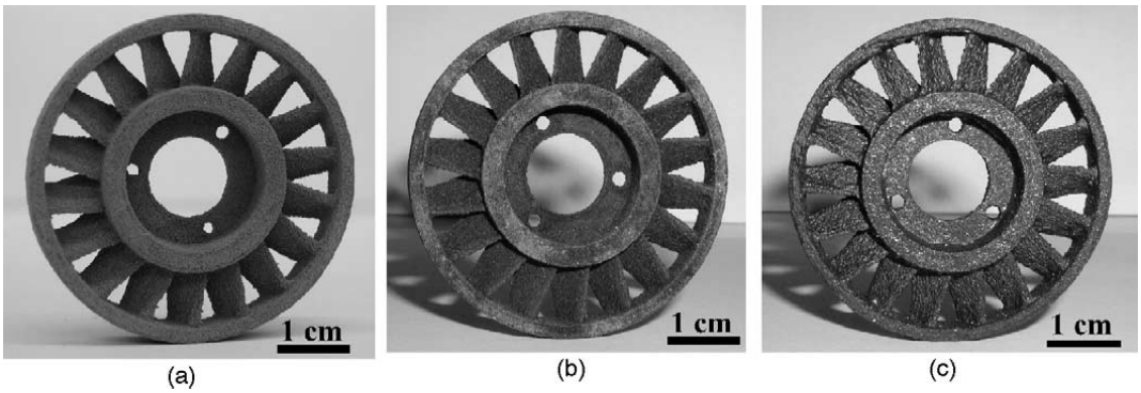

Figure 2.10.- 3D- SiSiC turbine wheel developed by SLS at the different stages: (a) laser-cured, (b) pyrolysed, and (c) infiltrated with silicon.[78]

LOM has also been employed for the production of 3D SiSiC composites[80] in a similar way as for the previous examples by creating laminate from a cellulosic paper loaded with ~77 wt.% of SiC particles, which was cut with a CO_2 laser before pyrolyzation and liquid silicon infiltration (Fig. 2.11). These materials showed strongly anisotropic mechanical properties with higher fracture toughness for cracks propagating in the direction perpendicular to the laminate plane (3.8 $MPa \cdot m^{1/2}$) than in the in the horizontal plane (1.3 $MPa \cdot m^{1/2}$). SiC-based tapes composed of SiC powders, carbon black graphite powders and 15-20 wt.% binders, with ~250 μm thickness have been developed as sheets for the LOM process.[81] In that work, flaws associated to Si in excess at the laminate interfaces were observed and removed by improving wetting at the interface and applying a post-pressing cycle (Fig. 2.12).

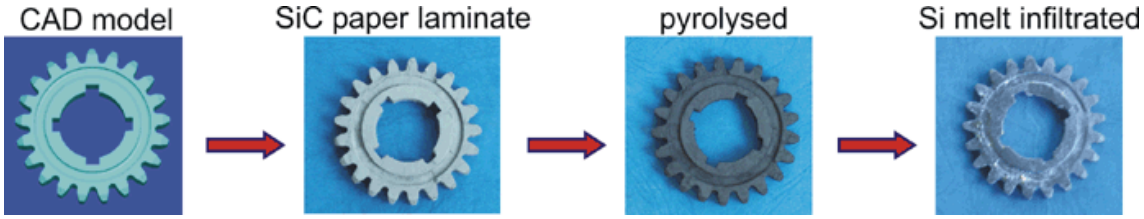

Figure 2.11.- Geometrically complex, 18-layered SiSiC gearwheel at different stages of a LOM process.[80]

All of the above methods have been plausible approaches toward the formation of new 3D complex morphologies based on SiC with structural applications. However, there is a lack in the filament-based approaches for SiC (RC, FDC, Thermoplastic 3D Printing), where more complex cellular architectures are attainable. Also, the reaction-bonding involves relatively high contents of remaining Si that reduces the mechanical properties above 1400 ºC when compared to conventional sintered SiC Furthermore, as SiC ceramics require demanding conditions for high densifications (T ~ 1900 ºC, vacuum, high applied mechanical pressure), this fact has hindered the use of SiC as

a starting material in AM routes. All of these shortcomings that affect the production of pure 3D complex SiC structures have been addressed within the scope of this PhD Thesis. The design of aqueous SiC-based pastes for the production of green architectures of SiC by RC, to subsequently undergo a pressureless sintering process, is in summary the chosen route to accomplish the formation of these new ceramic materials.

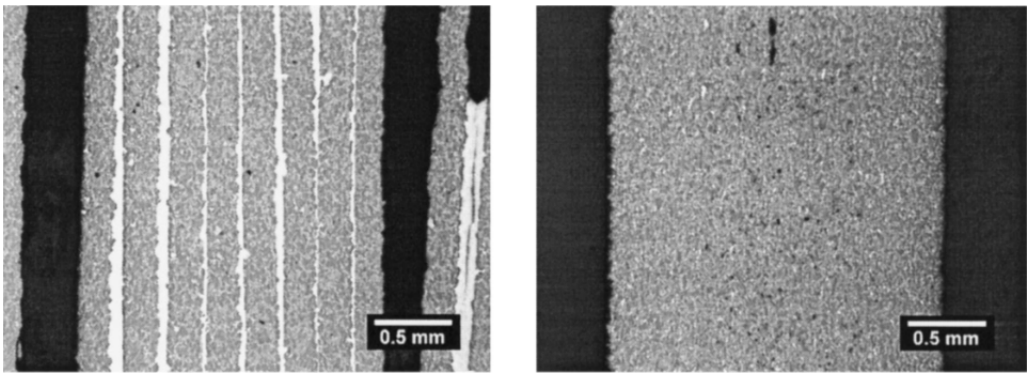

Figure 2.12.-SiSiC part fabricated with LOM using (a) thermal lamination and (b) solvent lamination and a post-press cycle.[81]

2.2.- Materials processing. Development of SiC-based ceramic inks for Robocasting

2.2.1.- SiC inks

Three different powder compositions have been developed for the fabrication of SiC-based-ceramic inks, designated as β7, β20 and N20 (Table 2.2). In each composition, the "β" and "N" symbols stand for β-SiC (median particle size, d_{50} = 0.50 μm) and nano-β-SiC (d_{50} = 0.05 μm) starting powders, respectively, whereas "7" and "20" correspond to the sintering additives (Al_2O_3 and Y_2O_3) content (in wt.%). The objective for designing different additive contents with different starting SiC powders is to study their effects on the final microstructure of the robocast SiC materials once sintered, and on mechanical properties such as hardness or elastic modulus. From the powders processing point of view, there is an extra difficulty as compared to more simple systems when formulating these inks, since three distinct ceramic powder species are present in the suspension: SiC, Al_2O_3 and Y_2O_3. Unless otherwise stated, SiC powders and sintering additives are utilized in the weight proportions specified in Table 2.2.

As it was previously mentioned in the Subsection 2.1.2.2, the preparation of 3D-structures by the RC technique requires the initial dispersion of the ceramic powder composition in an aqueous polymer solution. When ceramic powder particles are immersed in a polar liquid, particularly in water, there is a net charge density on the surface in contact with the liquid. This charge density creates an electric field in the suspension that pulls oppositely charged ions (counterions) together and repels like-charged ions. This shielding layer is commonly referred to as the double layer and, therefore, a slipping plane can be defined as the surface that separates the bulk free fluid from that attached to the particle surface, being ζ the zeta potential defined as the potential difference between the bulk dispersion medium and the slipping plane of the dispersed particles. Zeta potential is considered as a natural parameter of ceramic suspensions that basically depends on the nature of the surface of powdered material and the pH of the suspension.[82]

Table 2.2.- Powder mixture compositions and printable ink formulations for the different SiC-based robocast scaffolds.

Material		**β20**	**N20**	**β7**
Powder composition	β-SiC (wt.%)	80.0	80.0	93.0
	Al_2O_3 (wt.%)	8.6	8.6	2.0
	Y_2O_3 (wt.%)	11.4	11.4	5.0
	Specific Surface ($m^2 \cdot g^{-1}$)	14.8 ± 0.1	26.2 ± 0.2	16.1 ± 0.1
Ink composition	Solids Loading (wt.%)	72.5	61.2	71.4
	Solids Loading (vol.%)	43.8	31.8	42.5
	H-PEI, 100% organics (wt.%)	2	3.7	2.6
	L-PEI, 55% organics (wt.%)	2.1	3.6	2.8
	APA, 40% organics (wt.%)	0.5	0.4	0.3
	MC, 5% organics (wt.%)	3.6	6.1	4.8
	Total additives (wt.%) with/without water	8.2/3.6	13.8/6.1	10.5/4.5

In Fig 2.13, ζ measurements carried out in deionized water (DIW) as a function of the pH were represented for the three powders. It can be seen that the isoelectric point (pH_{iep}), i.e. the pH value for which ζ =0 (where the suspended ceramic particles carry

no net electric charge), is ~4.5, being negatively charged at the starting pH (~7). The Al_2O_3 and Y_2O_3 suspensions present very high pH_{iep} values 8.1 and 9.5, respectively, being positively charged at pH (~7) (Fig. 2.13). According to these results, an adequate working pH range for the three oxide components is not deduced from the Fig. 2.13 and the use of dispersants is then mandatory.

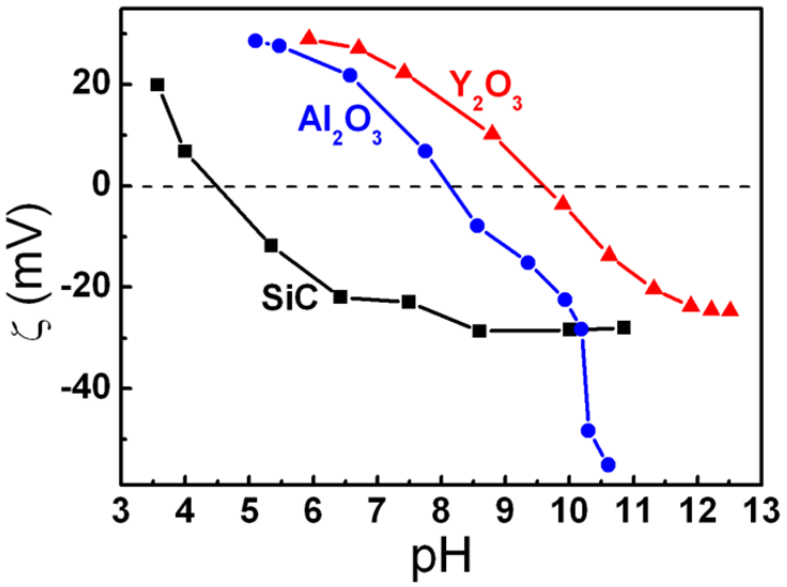

Figure 2.13.- Zeta potential (ζ) plotted as a function of pH values for (SiC, Al_2O_3 and Y_2O_3 powders dispersed in water. All the tested slurries have the same volume fraction of particles (1%).

PEI is a polymer with repeating units composed of the amine group and a two-carbon aliphatic CH_2CH_2 spacer. Linear polyethyleneimines contain all secondary amines, in contrast to branched PEIs which contain primary, secondary and tertiary amino groups. They behave like moderately charged cationic polyelectrolytes, which then may act as dispersant adsorbing layers. In this PhD Thesis a mixture of two branched PEIs was employed as dispersant: one of low molecular weight (M_w = 2000 g·mol^{-1}, L-PEI, Aldrich Chemical Co. Milwaukee) and the other one of high molecular weight (M_w= 25000 g·mol^{-1}, H-PEI, Aldrich Chemical Co. Milwaukee), in a 1:2 proportion (in vol.), as shown in Table 2.2 considering that the as-used L-PEI solution was diluted in water (55 wt.% L-PEI, 45 wt.% water). The structure of these PEI molecules is shown in Fig. 2.14. The reason to employ both H-PEI and L-PEI is that the longer branches of H-PEI help to maintain larger electrosteric forces between particles, allowing higher solids volume contents, whereas the use of L-PEI is required for achieving satisfactory shear-thinning behavior; the use of only H-PEI precludes the

development of 3D-structures due to a lack in the required pseudoplasticity of the ink, therefore, attainable by the combined action of H-PEI and L-PEI.

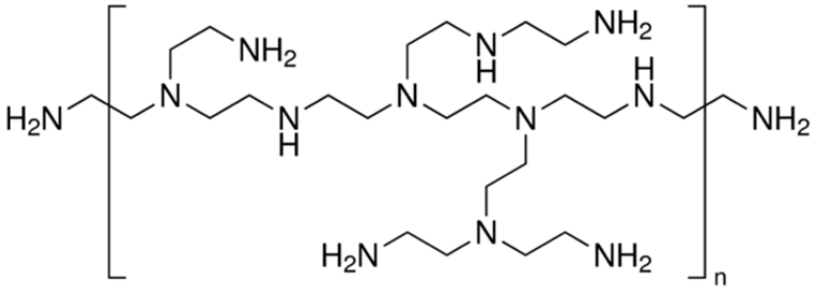

Figure 2.14.- Schematic illustration of the branched polyethileneimine monomer, similar for the used L-PEI and H-PEI.

Aqueous suspensions consisting of ceramic powders and PEI in the above-mentioned proportion of 1:2 for the L- and H-PEI, respectively, were characterized for ζ as a function of pH (Fig. 2.15). Interestingly, the addition of PEI to DIW raises the starting pH of the aqueous suspension from 7 to 12.5. In this way, when SiC is added to the aqueous PEI solution, the particle surface is coated with PEI resulting in the ζ behavior illustrated in Fig. 2.15; namely, a shift of the pH_{iep} to 11.7 is observed. Similar behaviors were observed for Al_2O_3 and Y_2O_3 powders where the pH_{iep} are 11.4 and 11.2, respectively. The similarity in zeta potential behavior of the PEI coated particles demonstrates that the surface is dominated by the adsorbed polyelectrolyte after the PEI is added, allowing a stable dispersion of the combined three powders which is the first step for developing printable inks (Fig. 2.6).

For the preparation of the printable inks, the ceramic powders (SiC, Al_2O_3 and Y_2O_3) were previously mixed using an attrition miller (as described in A.2.2) and gradually added to the PEI aqueous suspension to avoid the formation of agglomerates that might produce clogging during ink extrusion through the tips. The ink was then also gradually homogenized in a planetary centrifugal mixer at a speed of ~ 1800 rpm for 60 s. The required amount of PEI is expected to be related to the total surface area of the ceramic powders in the suspension, which can be calculated from the solids content and the specific surface area of the ceramic powders (collected in Table 2.2). In this way, as shown in Fig. 2.16, the amount of additives required for the colloidal processing increases with the specific surface area, establishing the proportions of ~2 $mg \cdot m^{-2}$ of H-PEI plus ~1 $mg \cdot m^{-2}$ of L-PEI (2 $mg \cdot m^{-2}$ of the commercial diluted aqueous solution used) for all the SiC-based inks.

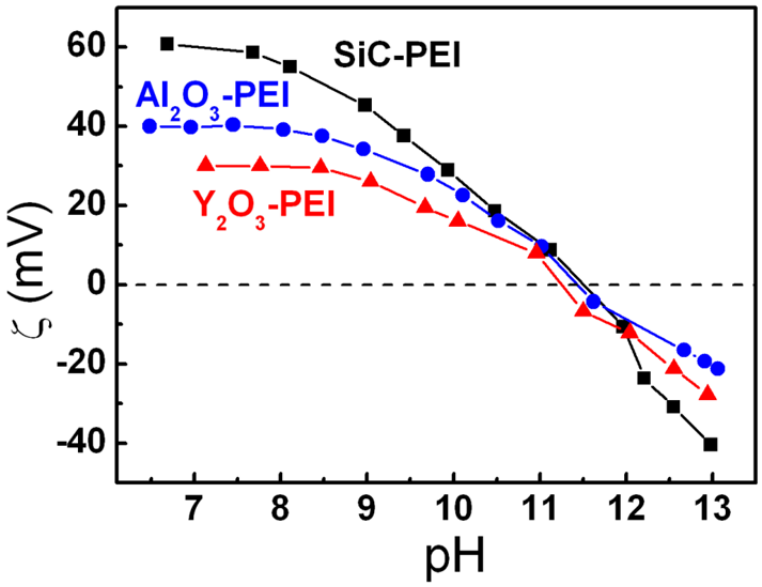

Figure 2.15.- Zeta potential (ζ) plotted as a function of pH values for SiC, Al_2O_3 and Y_2O_3 powders dispersed in a PEI-water solution. All the tested slurries have the same volume fraction of particles (1%). The amount of PEI used to disperse the particles was set in the proportion of 1:2 for the L- and H-PEI.

The next step of the ink preparation is the formation of a weak gel (Fig. 2.6), which was obtained adding a viscosifier, methylcellulose in this case (MC, Methocel F4M, Mw=3500 $g \cdot mol^{-1}$, 10 wt.%; Dow Chemical Company, Midland, MI). MC has been proved to minimize the formation of inhomogeneous agglomerates during ink extrusion, which are caused by the rupture of the colloidal ink structure due to the development of high pressures within the syringe reservoir. As seen in Fig. 2.16, the amount of MC was also proportional to the surface area of the ceramic composition in the suspension (~3.6, 4.8 and 6.1 wt.% for β20, β7 and N20), respectively, which represents 0.2 $mg \cdot m^{-2}$ of pure MC for all of the inks).

Finally, controlled flocculation was triggered by adding a counter polyelectrolyte (ammonium polyacrylate, APA, Darvan-821; R. T. Vanderbilt Company) to create a strong colloidal gel with high solids loadings showing pseudoplastic behavior with yield stress. The amount of the APA for achieving controlled flocculation of the ink did not depend strongly on the surface area, being in the 0.3-0.5 wt.% range. Larger amounts of APA destroyed the colloidal structure of the inks due to a total collapse of electrosteric forces. As seen in Fig. 2.17 for the case of the β20 ink, the addition of APA resulted in higher shear modulus and viscosity; the rheological behavior of the weak and strong gels, before and after flocculation, is highly shear thinning both exhibiting similar viscosity drops on the log-log plot of apparent viscosity (η_{app}) measured as a function of increasing shear rate ($\dot{\gamma}$) from $\dot{\gamma}$ = 0.01-150 s^{-1}. This

viscosity values enables low pressure extrusion in the working shear rate region of $\dot{\gamma}$= 30-70 s^{-1}.

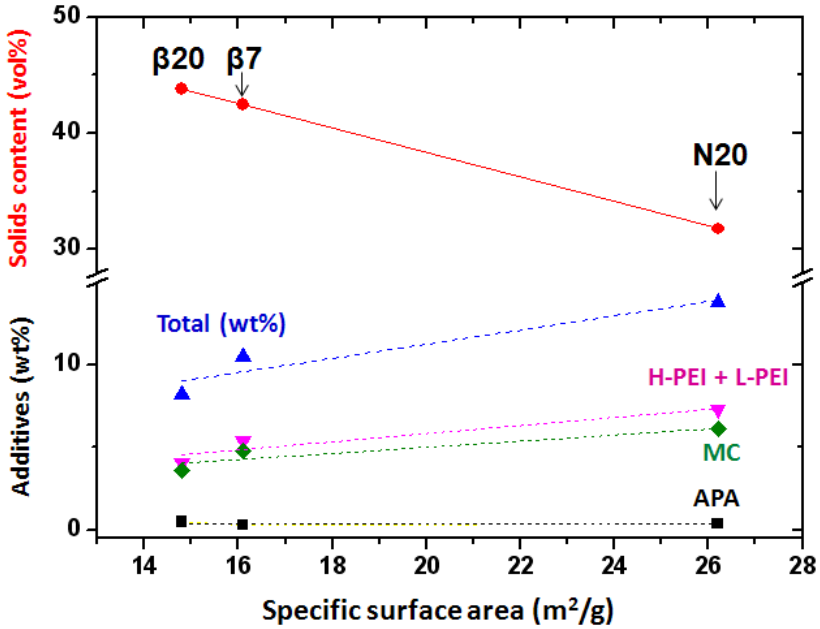

Figure 2.16.- Schematic plot of organic additives and solids contents used for the processing of SiC-based inks as a function of the specific surface area.

Fig. 2.17(b) shows that the shear elastic modulus of the ink (G′) exhibits a linear viscoelastic plateau quantified by the equilibrium modulus (G'_{eq}) followed by a rapid decline in G′ above a critical shear stress magnitude recognized to be the yield stress (τ_y). For the weak ink, G'_{eq} ~9 x 10^4 Pa and τ_y ~300 Pa, increasing to ~ 1.5 x 10^5 Pa and ~350 Pa, respectively, for the strong ink. The strong gel was found to be strong enough to easily retain the shape of extruded filaments and the overall geometry of the deposited lattice structures.

As seen in Fig. 2.18, the η_{app} versus $\dot{\gamma}$ curves of the three formulated SiC inks (β7, β20, N20) obtained using cone-plate configuration are quite similar to that for the β20 composition using the serrated cup and bob measuring system. The rheology is highly shear thinning and similar slopes are observed for the three cases.

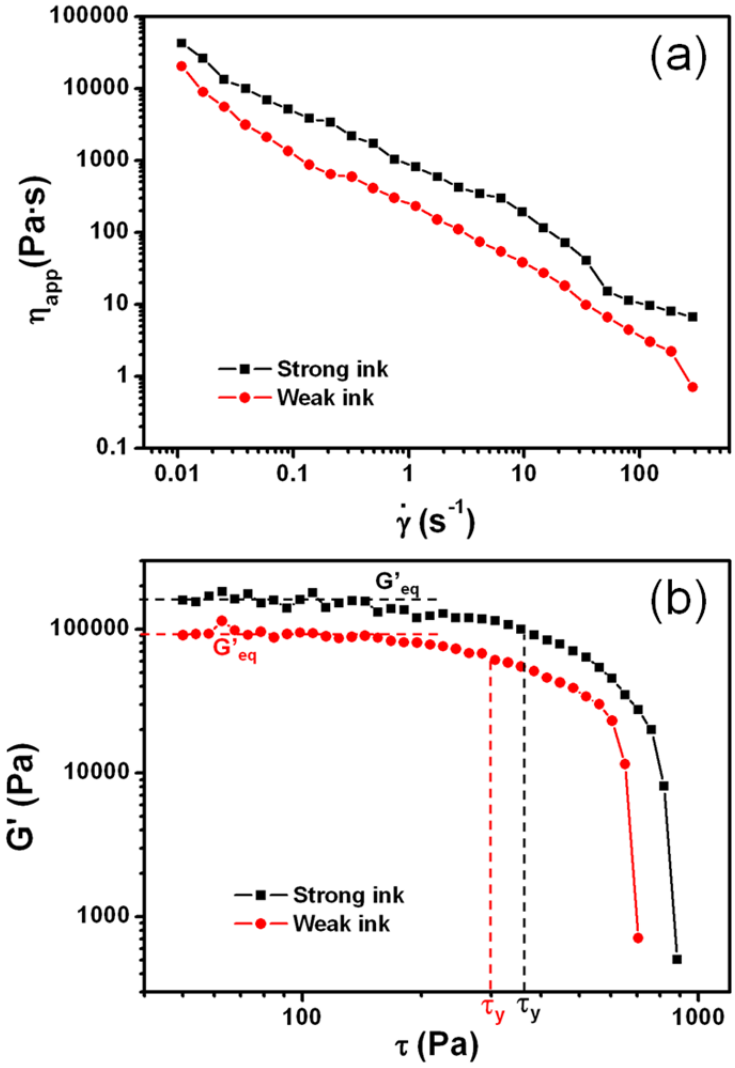

Figure 2.17.- (a) Apparent viscosity (η_{app}) versus shear rate ($\dot{\gamma}$) for concentrated β20 ternary inks before (circles) and after (squares) the addition of APA. (b) The corresponding plots of their shear elastic modulus (G') versus shear stress (τ). Discontinuous lines mark equilibrium moduli (G'_{eq}) and yield stress (τ_y).

Regarding the maximum solids volume fraction achievable in the pastes (Table 2.2), while keeping the desired rheological behavior, an evident relation with the grain size of the starting powders is drawn: whereas it is similar (~0.44) for the β7 and β20 compositions, it is drastically reduced (~0.32) in the case of the N20. Therefore, the green densities of the N20 scaffolds are expected to be reduced by ~25 - 30%, which can limit the full densification of the specimens during the subsequent sintering process.

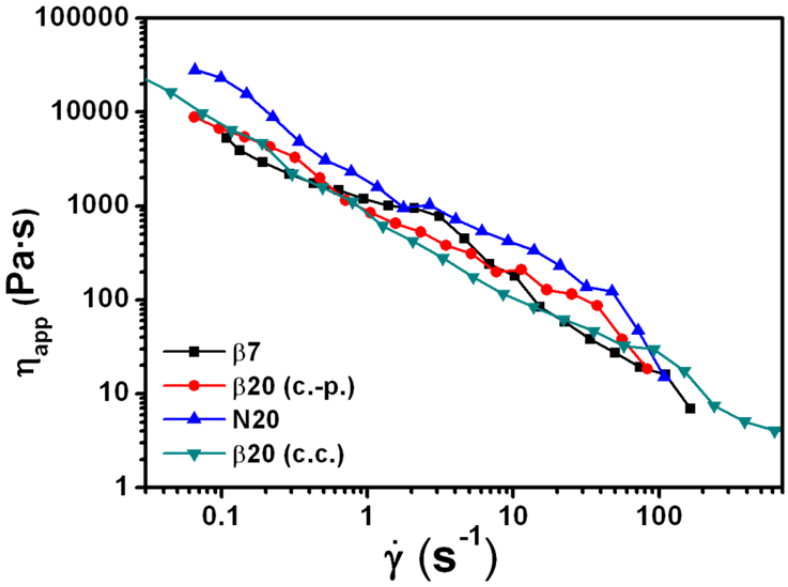

Figure 2.18.- Log-log plot of apparent viscosity (η_{app}) versus shear rate ($\dot{\gamma}$) for the three SiC inks formulated according to Table 2.2, measured with the cone-plate system (shown values of the β20 ink measured with concentric cylinders for comparison).

2.2.2.- Graphene-ceramic inks

By following the same processing route as for the purely ceramic compositions based on the dispersion of the powder particles with PEI, graphene/SiC compositions, with 5, 10 and 20 vol.% of GNPs were prepared, as shown in Table 2.3.

The β7 ceramic composition was used in this case to eventually form the ceramic matrix, and commercially available GNPs (A.2.1) were used as the graphene source. For the preparation of compositions with GNPs (described in detail in the A.2.2), the platelets were sonicated in isopropyl alcohol in an ultrasonic bath to ensure the good dispersion and the disaggregation of agglomerates. Simultaneously, a slurry of the β7 composition was prepared in alcohol using an attrition miller. The ceramic slurry and GNPs suspension were then mixed and sonicated to obtain a homogeneous blend of the all the components, which was followed by the evaporation of the solvent.

Apparent viscosity data for the highly concentrated, flocculated GNPs-SiC pastes with GNPs are shown in Fig. 2.19. The rheology of the formulated GNPs-SiC pastes is highly shear thinning, with similar slopes in the η_{app} *vs.* $\dot{\gamma}$ log-log plots for the studied range of shear rates. As it occurred for the GNPs-free SiC suspensions (Fig. 2.18), low viscosity values (20-100 Pa·s) at $\dot{\gamma}$ = 30-70 s^{-1} and a high viscosity (> 2000 Pa·s)

at low shear rates were attained. An increase in the slope of the log (η_{app}) – log ($\dot{\gamma}$) curves is detected in all compositions at a certain value of $\dot{\gamma}$ ($\dot{\gamma}_c$) that is slightly affected by the GNPs addition. Both the transition interval and $\dot{\gamma}_c$ increase with the amount of GNPs ($\dot{\gamma}_c$ varies from 3 s^{-1} for the GNPs-free ink to 20 s^{-1} for the ink with 20% of GNPs), probably because at high shear rates some charge concentration is induced at the platelet edges that favors face-to-edge interactions between platelets and contribute to disorder, as in the well-known case of kaolin.[83]

Table 2.3.- Ink composition and formulations of the GNPs-SiC inks.

Material		**SiC monolithic**	**5 vol.% GNPs**	**10 vol.% GNPs**	**20 vol.% GNPs**
Powder composition	β-SiC (wt.%)	93	89.83	86.55	79.65
	Al_2O_3 (wt.%)	2	1.93	1.86	1.71
	Y_2O_3 (wt.%)	5	4.83	4.65	4.28
	GNPs (wt.%)	0	3.41	6.94	14.36
	Specific surface ($m^2 \cdot g^{-1}$)	16.1 ± 0.2	17.3 ± 0.2	16.5 ± 0.2	15.0 ± 0.2
Ink composition	Solids loading (wt.%)	71.4	71.1	71.1	68.6
	Solids loading (vol.%)	42.5	43.8	44.4	42.1
	H-PEI, 100% organics (wt.%)	2.6	2.8	2.4	3.5
	L-PEI, 55% organics (wt.%)	2.8	3.1	3.0	3.5
	APA, 40% organics (wt.%)	0.3	0.2	0.2	0.3
	MC, 5% organics (wt.%)	4.8	5.7	5.4	5.0
	Total additives (wt.%) with/ without water	10.5/4.5	11.8/4.9	11.0/4.4	12.3/5.8

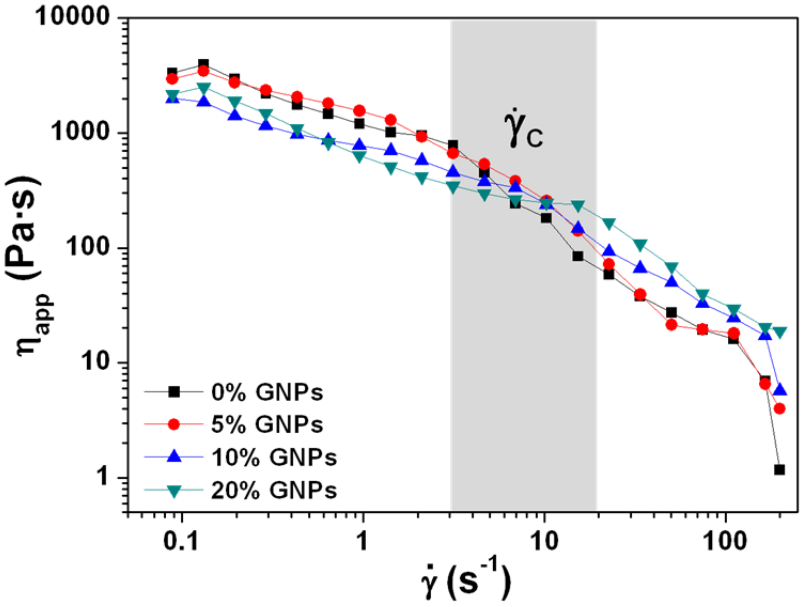

Figure 2.19.- Apparent viscosity (η_{app}) data as a function of the shear rate ($\dot{\gamma}$) for concentrated GNPs-SiC pastes with 0, 5, 10 and 20 vol.% GNPs in the powder compositions, using a cone-plate system. Pre-shearing and equilibration times were applied before the measurement of each series. Points represent experimental data linked by solid lines as a guide to the eye.

2.3.- Robocasting of computer designed architectures from SiC and GNPs-SiC inks

2.3.1.- Fabrication of robocast structures

The main goal of using RC, regarding the possible complex structures that are enabled for fabrication by this technique, is the potential to obtain scaffolds or cellular materials with controlled porosity channels, pore size and morphology. Accordingly, cylindrical and cuboid periodic lattices have been designed with custom software (RoboCAD 4.0) and printed with a custom three-axis Robocasting (A3200) system at room temperature. An example of one of the CAD structures is shown in Fig. 2.20.

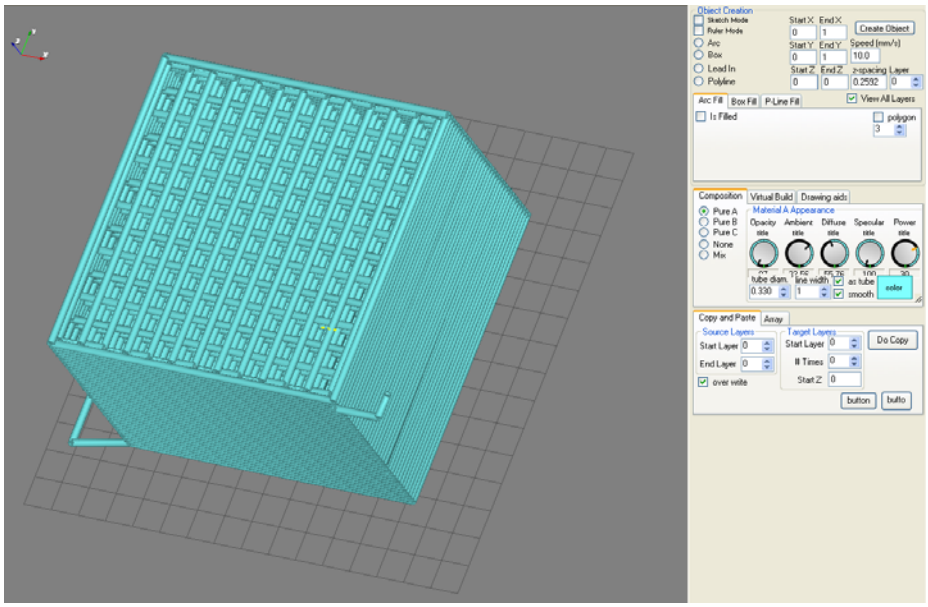

Figure 2.20.- Cuboid periodic lattice designed by RoboCAD 4.0.

Square and rectangular lattices were designed by creating a linear array of parallel filaments in the x-y plane such that they are orthogonal in adjacent layers (Fig. 2.21). Cylindrical lattices were designed in two ways: either by creating concentric circles in one x-y layer, while radial rods are patterned in the adjacent layers (so that graded radial porosity is obtained) or, similarly as for the square lattices, cylinders with layers of perpendicular filaments. In the layer-by-layer construction, either in the case of cuboid scaffolds or for cylindrical structures, special care is taken when designing so that each layer commences to be printed right up the point where the previous layer was finished, to obtain a continuous process of extrusion as shown in Fig. 2.20. Finally, in order to assure a good contact between the green filaments in adjacent layers, a certain penetration of the filaments of each layer was forced into those of the underlying stratum in such a way that the distance between layers in the z-direction is lower than the rod diameter, Ø. Particularly, the selected distance between layers was 0.25π Ø.

The colloidal gels are first loaded into a syringe (barrel diameter=9.5 mm, volume=3cc; EFD Inc., East Providence, RI) and placed into the syringe holder of the robocaster. The ink is extruded in the working shear rate region of 30 to 70 s^{-1} through nozzles[84] (Precision Tips; EFD Inc.) with different diameters, ranging 150—610 μm, onto an alumina substrate, typically using a low-viscosity paraffin oil bath to avoid drying of samples during printing and associated clogging phenomena. In Fig. 2.22, an image of commonly used tips for the extrusion process is shown.

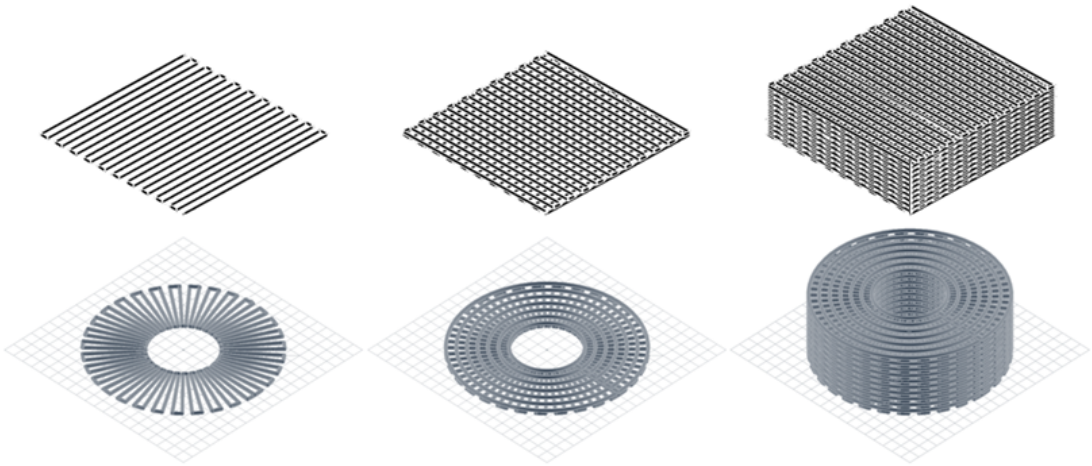

Figure 2.21.- Schematic CAD designs of the lattices with 1, 2, and N layers in cuboid and cylindrical shapes.

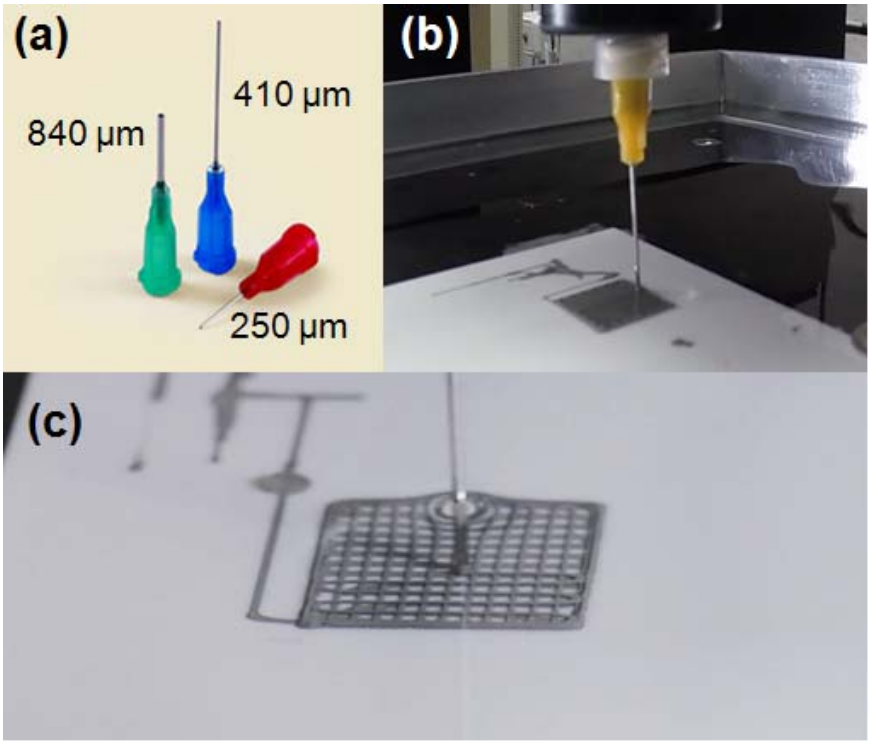

Figure 2.22.- a) Commercial precision tips of different inner diameters (included in the figure) used as nozzles for the extrusion process. b) and c) images corresponding to the printing process.

The extrusion speed of ink was controlled by an automatic feed system at a constant volumetric flow rate of $0.25\pi D^2u$, where D is the inner diameter of nozzles and u is the constant x-y table speed (normally 10 $mm \cdot s^{-1}$ in this PhD Thesis). By way of

example, for a nozzle with an inner diameter of 330 μm, volumetric flow rate is estimated in $8.6x10^{-16}$ $m^3 \cdot s^{-1}$.

Square, rectangular and cylindrical lattices are robocast with dimensions ranging from 8-20 mm in length for the x and y sides, whereas the height is typically of 5-10 mm with 20-30 layers (Fig. 2.23). After printing, the scaffolds are removed from the oil bath and dried at room temperature.

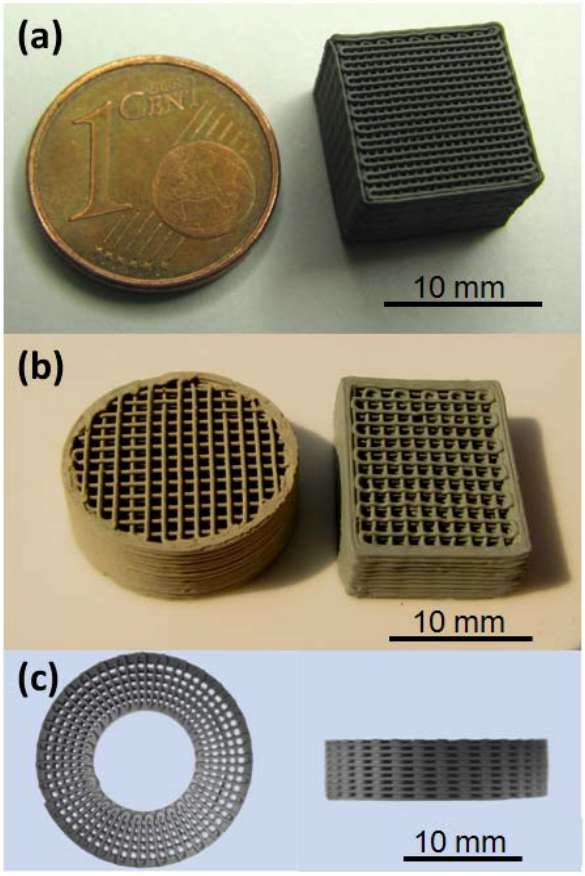

Figure 2.23.- Optical micrographs of (a) a green 10 vol.% GNPs/SiC structure, (b) structures corresponding to the β7 (cylindrical) and N20 (rectangular) SiC-based compositions, and (c) top and side views of a green cylindrical lattice of the β20 composition.

Neither bending nor cracking were detected after printing the inks and forming the 3D structures (Fig. 2.23) and, therefore, the structures were sufficiently strong to retain the shape of the extruded filaments and the overall geometry once deposited, even for the N20 powders composition of significantly lower solids contents.

As for the pore geometry, different shapes have been designed with square, triangle, rhombus or rectangle-like morphologies (Fig. 2.24 illustrates these different pore patterns). This confirms that appropriate rheological properties have been obtained,

allowing the structures to maintain their shape during the deposition and drying processes. Diameters ~12–15 % lower than that of the extrusion nozzle were measured for the green rods; this shrinkage is associated with drying. Further shrinkage occurs during sintering, which will the subject of analysis in the next Chapter; in this process the shrinkage is strongly dependent on the green density and the ceramic composition.

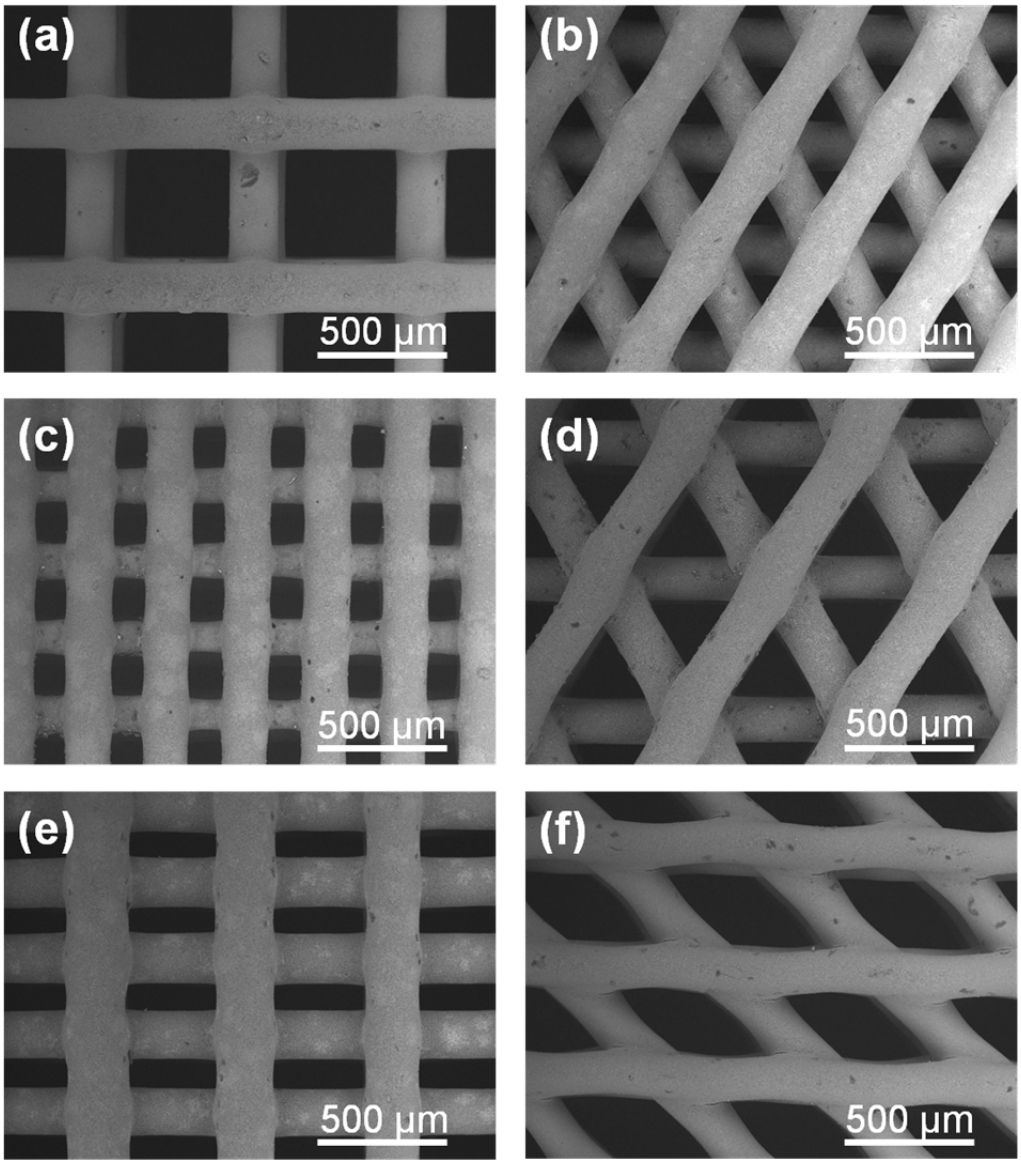

Figure 2.24.- SEM images of sintered structures of the β7 composition extruded through a nozzle of 250 µm in diameter and different pore patterns.

2.3.2.- Polymers burn-out process

Once the structures have been deposited by RC, a last step in the manufacturing process must be accomplished before sintering. The SiC-based pastes contain organic additives (PEI, APA and MC) that should be removed before sintering, as they represent an undesired source of carbon that would eventually obstruct the sintering process and affect the final properties of the scaffolds.

A thermogravimetric-differential thermal analysis (TGA-DTA) was carried out in an air atmosphere, from room temperature to 1000 ºC, to determine the decomposition temperature of the different organic additives used to prepare the SiC-based scaffolds and the associated total weight loss; in Fig. 2.25, TGA-DTA results for a dried green β7 scaffold are shown as a case example.

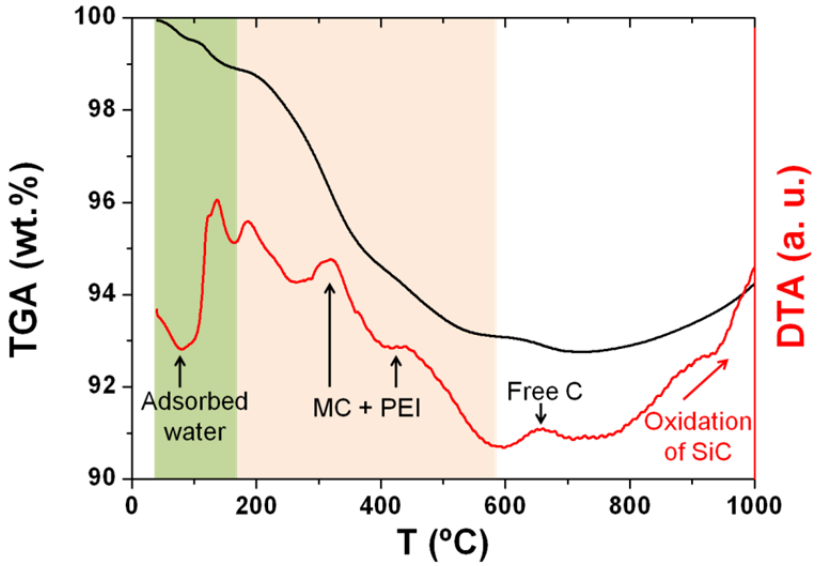

Figure 2.25.- (a) TGA-DTA analysis carried out on a dried green β7 scaffold between room temperature and 1000ºC at 3 ºC·min^{-1}.

Different peaks are observed which can be associated to the removal of the organics employed to fabricate the inks. Below 100 ºC, the endothermic peak observed is linked to removal of the physically absorbed water in the green structures, followed by an exothermic peak at 140 ºC associated to the residual paraffin-oil burn out process. Both processes represent a weight loss of ~1.2 %. Between 180 and 590 ºC, several exothermic and endothermic peaks are observed, being related to the crystallization, melting, oxidation and decomposition of the organic additives which occur above ~140, 220 and 250 ºC for APA, MC and PEI, respectively, amounting a total weight loss of 5.3%. This value fits well with the total amount of additives used (Table 2.2). There is still a final exothermic peak at 655 ºC with an additional weight loss of 0.32%

between 600 and 730 ºC that may be linked to the reaction of impurities (specifically, free carbon) always present in the β-SiC raw powders with oxygen. Above 730 ºC, oxidation of SiC starts and the corresponding weight gain and exothermic peak were observed. According to these results, the conditions for the burn-out process were established as 600 ºC for 2 h, using a heating rate of 3 ºC·min^{-1}.

In the case of the green structures containing GNPs, the samples must be heat-treated at temperatures lower than 500 ºC to avoid GNPs removal as deduced from the DTA-TGA analysis for the pristine GNPs (Fig. 2.26). A heat treatment at 415 ºC in air for 2 h was chosen as a good balance between maximum organics removal and minimum GNPs degradation. A TGA done after this treatment for the GNPs-free β7-SiC scaffold (Fig. 2.27) demonstrates that remaining organics are accountable for a weight loss of ~0.7 wt.% up to 600 ºC which, compared to the total loss of 5.3 wt.% for the untreated β7-SiC sample (Fig. 2.25), implies that a majority of organics was eliminated. In the calcined scaffold, 0.2% of weight loss associated to the free carbon was also observed above 600 ºC.

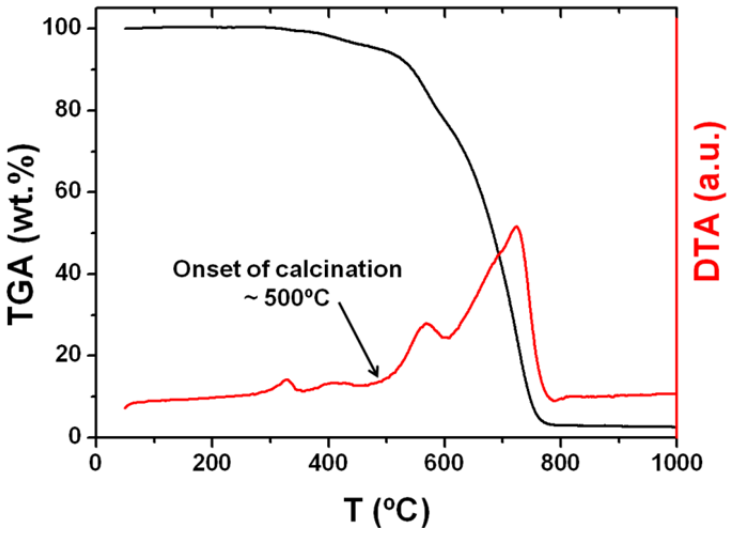

Figure 2.26.- TGA of the pristine GNPs measured at a heating rate of 3 ºC·min^{-1}.

A similar analysis could not be performed for the GNPs-containing scaffolds (shown in Fig. 2.27, the case of 20 vol.% GNPs-containing scaffold is shown as an example) because of the weight gain associated to the quick oxidation of the SiC particles, which counterbalances the weight loss. It is important to notice the higher rate of oxidation of SiC in the scaffold containing GNPs compared to the free-GNPs β7-SiC sacffold. This enhanced kinetics of oxidation can be attributed to both a locally increased temperature due to GNPs combustion and the associated reducing atmosphere created by the CO (g) and CO_2 (g) liberated during reaction of GNPs with

oxygen, which changes oxidation mechanisms of SiC from passive to active, i.e. the surface silica layer is continuously removed.[85]

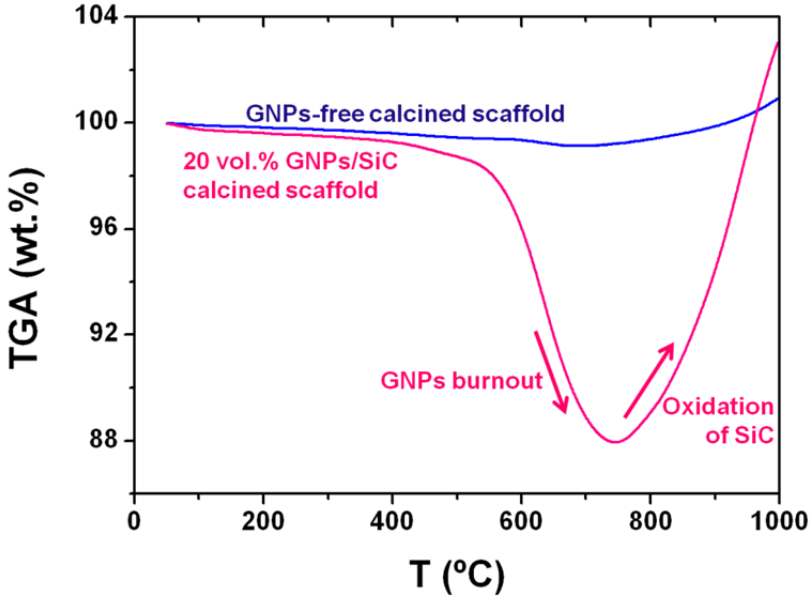

Figure 2.27.- TGA of SiC and GNP-SiC green scaffolds, both for the β7 composition, before and after polymers burn-out processes at 415 ºC; all curves were measured at a heating rate of 3 ºC·min^{-1}.

2.4.- Conclusions

i) SiC- and GNPs/SiC-based colloidal inks suitable for complex 3D deposition by RC, with high solids loadings of up to 44 wt.% and pseudoplastic rheology, have successfully been produced.

ii) The solids volume fraction highly depends on the SiC grain size, decreasing for nanosized SiC powders

iii) The addition of GNPs up to 20 vol.% does not significantly limit the achieved solids volume fraction.

iv) A direct relationship between the amount of organic additives and the specific surface area of the ceramic mixtures has been established for the development of the colloidal pastes.

v) 3D square, rectangular and cylindrical lattices with different pore morphologies have been printed by RC. The shape of the extruded filaments and the overall geometry of the deposited lattice structures is retained in all cases, even when using nanometric SiC powders.

vi) A heat treatment of 600 ºC in air for 2 h is proved effective for the organics removal in the green ceramic bodies without oxidizing SiC powders, whereas a treatment at 415 ºC in air for 2 h allows maximum organics burn-out with minimum GNPs degradation in the GNPs-containing specimens.

2.5.- References

1. Klocke, F. Modern approaches for the production of ceramic components. J Eur Ceram Soc 1997; 17(2): 457-65.
2. Kruth JP, Leu MC, Nakagawa T. Progress in additive manufacturing and rapid prototyping. CIRP Ann-Manuf Techn 1998; 47(2): 525-40.
3. Gibson I, Rosen DW, Stucker B. Additive Manufacturing technologies (pp. 1-8). New York: Springer. 2010.
4. Rosen DW. Computer-aided design for additive manufacturing of cellular structures. Comput Aided Design Appl 2007; 4(5): 585-94.
5. Travitzky N, Bonet A, Dermeik B, Fey T, Filbert-Demut I, Schlier L, Schlordt T, Greil P. Additive Manufacturing of Ceramic-Based Materials. Adv Eng Mater 2014; *16*(6): 729-54.
6. Zhao X, Evans JRG, Edirisinghe MJ, Direct Ink-Jet Printing of Vertical Walls. J Am Ceram Soc 2002; 85: 2113–5.
7. Song JH, Edirisinghe MJ, Evans JRG. Formulation and Multilayer Jet Printing of Ceramic Inks. J Am Ceram Soc 1999; 82: 3374–80.
8. Teng WD, Edirisinghe MJ, Evans JRG. Optimization of Dispersion and Viscosity of a Ceramic Jet Printing Ink. J Am Ceram Soc 1997; 80, 486-94.
9. Sachs E, Cima M, Williams P, Brancazio D, Cornie J. 3-Dimensional Printing—Rapid Tooling and Prototypes Directly from a Cad Model. J Eng Ind—Trans ASME 1992; 114: 481–8.
10. Sachs E, Cima M, Bredt J, Curodeau A, Fan T, Brancazio D. CADCasting: Direct Fabrication of Ceramic Shells and Cores by Three Dimensional Printing. Manuf Rev 1992; 5: 117–26.

11. Moon J, Grau JE, Knezevic V, Cima MJ, Sachs EM. Ink-Jet Printing of Binders for Ceramic Components. J Am Ceram Soc 2002; 85: 755–62.
12. Reis N, Ainsley C, Derby B. Viscosity and Acoustic Behavior of Ceramic Suspensions Optimized for Phase-Change Ink-Jet Printing. J Am Ceram Soc 2005; 88: 802–8.
13. Wang T, Derby B. Ink-Jet Printing and Sintering of PZT. J Am Ceram Soc 2005; 88: 2053–8.
14. Lee DH, Derby B. Preparation of PZT Suspensions for Direct Ink Jet Printing. J Eur Ceram Soc 2004; 24: 1069–72.
15. Seerden KAM, Reis N, Evans JRG, Grant PS, Halloran JW, Derby B. Ink-Jet Printing of Wax-Based Alumina Suspensions. J Am Ceram Soc 2001; 84: 2514–20.
16. Teng WD, Edirisinghe MJ. Development of Ceramic Inks for Direct Continuous Jet Printing. J Am Ceram Soc 1998; 81: 1033–6.
17. Bhatti AR, Mott M, Evans JRG, Edirisinghe MJ. PZT Pillars for 1–3 Composites Prepared by Ink-Jet Printing. J Mater Sci Lett 2001; 20, 1245–8.
18. Melcher R, Martins S, Travitzky N, Greil P. Fabrication of Al_2O_3-based composites by indirect 3D-printing. Mater Lett 2006; 60(4): 572-5.
19. Özkol E, Ebert J, Uibel K, Wätjen AM, Telle R. Development of high solid content aqueous 3Y-TZP suspensions for direct inkjet printing using a thermal inkjet printer. J Eur Ceram Soc 2009; 29 (3):403–9.
20. Özkol E, Ebert J, Telle R. An experimental analysis of the influence of the ink properties on the drop formation for direct thermal inkjet printing of high solid content aqueous 3Y-TZP suspensions. J Eur Ceram Soc 2010; 30 (7):1669–78
21. Cappi B, Özkol E, Ebert J, Telle R. Direct inkjet printing of Si_3N_4: Characterization of ink, green bodies and microstructure. J Eur Ceram Soc 2008; 28(13): 2625-8.
22. Travitzky N, Zimmermann K, Melcher R, Greil P. From polysaccharides to SiSiC composites by 3D printing. Eds.: NP Bansal, JP Singh, WM Kriven: Advances in Ceramic Matrix Composites XI, S, 37-45. 2012.
23. Schlier L, Zhang W, Travitzky N, Greil P, Cypris J, Weclas M. Macro-Cellular Silicon carbide Reactors for Nonstationary Combustion Under Piston Engine-Like Conditions. Int J Appl Ceram Techn 2011, 8(5), 1237-45.
24. Fu Z, Schlier L, Travitzky N, Greil P. Three-dimensional printing of SiSiC lattice truss structures. Mater Sci Eng A 2013; 560: 851-6.

25. Hosseini-Zori M, Soleimani-Gorgani A. Ink-jet printing of micro-emulsion TiO_2 nano-particles ink on the surface of glass. J Eur Ceram Soc 2012; 32(16): 4271-7.
26. Fierz FC, Beckmann F, Huser M, Irsen SH, Leukers B, Witte F, Degistirici Ö, Andronache A, Thie M, Müller B. The morphology of anisotropic 3D-printed hydroxyapatite scaffolds. Biomaterials 2008, 29(28), 3799-806.
27. Winkel A, Meszaros R, Reinsch S, Müller R, Travitzky N, Fey T, Greil P, Wondraczek L. Sintering of 3D-Printed Glass/HAp Composites. J Am Ceram Soc 2012; 95(11): 3387-93.
28. Will J, Melcher R, Treul C, Travitzky N, Kneser U, Polykandriotis E, Horch R, Greil P. Porous ceramic bone scaffolds for vascularized bone tissue regeneration. J Mater Sci-Mater M 2008; 19(8): 2781-90.
29. Butscher A, Bohner M, Roth C, Ernstberger A, Heuberger R, Doebelin N, von Rohr PR, Müller R. Printability of calcium phosphate powders for three-dimensional printing of tissue engineering scaffolds. Acta Biomater 2012; 8(1): 373-85.
30. Butscher A, Bohner M, Doebelin N, Galea L, Loeffel O, Müller R. Moisture based three-dimensional printing of calcium phosphate structures for scaffold engineering. Acta Biomater 2013; 9(2): 5369-78.
31. Beaman JJ, Deckard CR. U.S. Patent No. 4,938,816. Washington, DC: U.S. Patent and Trademark Office. 1990.
32. Kruth JP, Mercelis P, Van Vaerenbergh J, Froyen L, Rombouts M. Binding mechanisms in selective laser sintering and selective laser melting. Rapid Prototyping J 2005; 11(1): 26-36.
33. Waetjen AM, Polsakiewicz DA, Kuhl I, Telle R, Fischer H. Slurry deposition by airbrush for selective laser sintering of ceramic components. J Eur Ceram Soc 2009; 29(1): 1-6.
34. Tang HH, Chiu ML, Yen HC. Slurry-based selective laser sintering of polymer-coated ceramic powders to fabricate high strength alumina parts. J Eur Ceram Soc 2011; 31(8): 1383-8.
35. Gahler A, Heinrich JG, Guenster J. Direct Laser Sintering of Al_2O_3–SiO_2 Dental Ceramic Components by Layer-Wise Slurry Deposition. J Am Ceram Soc 2006; 89(10): 3076-80.
36. Bertrand P, Bayle F, Combe C, Gœuriot P, Smurov I. Ceramic components manufacturing by selective laser sintering. Appl Surf Sci 2007; 254(4): 989-92.

37. Tan KH, Chua CK, Leong KF, Cheah CM, Gui WS, Tan WS, Wiria FE. Selective laser sintering of biocompatible polymers for applications in tissue engineering. Biomed Mater Eng 2005; *15*(1): 113-24.
38. Ko SH, Pan H, Grigoropoulos CP, Luscombe CK, Fréchet JM, Poulikakos D. All-inkjet-printed flexible electronics fabrication on a polymer substrate by low-temperature high-resolution selective laser sintering of metal nanoparticles. Nanotechnology 2007;18(34): 345202.
39. Das S. Physical aspects of process control in selective laser sintering of metals. Adv Eng Mater 2003; *5*(10): 701-11.
40. Agarwala M, Bandyopadhyay A, van Weewn R, Safari A, Danforth SC, Langrana NA, Jamalabad VR, Whalen PJ. FDC, Rapid Fabrication of Structural Components. Am Ceram Soc Bull 1996; 75: 60–6.
41. Allahverdi M, Danforth SC, Jafari M, Safari A. Processing of Advanced Electroceramic Components by Fused Deposition Technique. J Eur Ceram Soc 2001; 21: 1485–90.
42. Rangarajan S, Qi G, Venkataraman N, Safari A, Danforth SC. Powder Processing, Rheology, and Mechanical Properties of Feedstock for Fused Deposition of Si_3N_4 Ceramics. J Am Ceram Soc 2000; 83: 1663–9.
43. Crump SS. Modeling apparatus for three-dimensional objects. 5340433, 1994.
44. Dai C, Qi G, Rangarajan S, Wu S, Langrana NA, Safari A, Danforth SC. High quality, fully dense ceramic components manufactured using fused deposition of ceramics (FDC). In Proceedings Solid Freeform Fabrication Symposium. University of Texas at Austin. 1997.
45. McNulty TF, Shanefield DJ, Danforth SC, Safari A. Dispersion of lead zirconate titanate for fused deposition of ceramics. J Am Ceram Soc 1999; 82(7): 1757-60.
46. Atisivan R, Bose S, Bandyopadhyay A. Porous mullite preforms via fused deposition. J Am Ceram Soc 2001; 84(1): 221-3.
47. Cesarano J III. A Review of Robocasting Technology. Presented at Symposium on Solid Freeform and Additive Fabrication, Boston, MA, 1999.
48. Cesarano J III, Calvert PD. U.S. Patent No. 6,027,326. Washington, DC: U.S. Patent and Trademark Office. 2000.
49. Cesarano J III, Segalman R, Calvert PD. Robocasting Provides Moldless Fabrication from Slurry Deposition. Ceram Ind 1998; 148: 94–102.
50. Smay JE, Gratson GM, Shepherd RF, Cesarano J III, Lewis JA. Directed colloidal assembly of 3D periodic structures. Adv Mater 2002; 14: 1279-83.

51. Lewis JA. Direct write assembly of ceramics from colloidal inks. Curr Opin Solid St M 2002; 6: 245-50.
52. Therriault D, Shepherd RF, White SR, Lewis JA. Fugitive Inks for Direct-Write Assembly of Three-Dimensional Microvascular Networks. Adv Mater 2005; 17(4): 395-9.
53. Schlordt T, Schwanke S, Keppner F, Fey T, Travitzky N, Greil P. Robocasting of alumina hollow filament lattice structures. J Eur Ceram Soc 2013; 33(15): 3243-8.
54. Silva NR, Witek L, Coelho PG, Thompson VP, Rekow ED, Smay J. Additive CAD/CAM process for dental prostheses. J Prosthodont 2011; 20(2): 93-6.
55. He G, Hirschfeld DA, Cesarano III J, Stuecker JN. Robocasting and cofiring of functionally graded Si_3N_4-W materials. In Twenty-fifth Annual Conference on Composites, Advanced Ceramics, Materials, and Structures 2001; 22(3): 119. American Ceramic Society.
56. Stuecker JN, Cesarano J, Hirschfeld DA. Control of the viscous behavior of highly concentrated mullite suspensions for robocasting. J Mater Process Tech 2003; 142(2): 318-25.
57. Nadkarni SS, Smay JE. Concentrated barium titanate colloidal gels prepared by bridging flocculation for use in solid freeform fabrication. J Am Ceram Soc 2006; 89(1): 96-103.
58. Smay JE, Cesarano J, Tuttle BA, Lewis JA. Directed colloidal assembly of linear and annular lead zirconate titanate arrays. J Am Ceram Soc 2004; 87(2): 293-5.
59. Saiz E, Gremillard L, Menendez G, Miranda P, Gryn K, Tomsia AP. Preparation of porous hydroxyapatite scaffolds. Mat Sci Eng C 2007; 27(3): 546-50.
60. Miranda P, Saiz E, Gryn K, Tomsia AP. Sintering and robocasting of β-tricalcium phosphate scaffolds for orthopaedic applications. Acta Biomater 2006; 2(4): 457-66.
61. Eqtesadi S, Motealleh A, Miranda P, Pajares A, Lemos A, Ferreira JM. Robocasting of 45S5 bioactive glass scaffolds for bone tissue engineering. J Eur Ceram Soc 2014; 34(1): 107-18.
62. Scheithauer U, Schwarzer E, Richter HJ, Moritz T. Thermoplastic 3D Printing—An AM Method for Producing Dense Ceramics. Int J Appl Ceram Tech 2015; 12(1): 26-31.

63. Scheithauer U, Bergner A, Schwarzer E, Richter HJ, Moritz T. Studies on thermoplastic 3D printing of steel–zirconia composites. J Mater Res 2014; 29(17):1931-40.
64. Hull CW. Apparatus for production of three-dimensional objects by stereolithography. U.S. Patent No. 4,575,330. Washington, DC: U.S. Patent and Trademark Office. 1986.
65. Ikuta K, Hirowatari K. Real three-dimensional microfabrication using stereolithography and metal molding. In Proceedings of the IEEE international Workshop on Microelectromechanical Systems. MEMS ’93: 42–47. 1993.
66. Shoji S, Smith N, Kawata S. Photofabrication of a photonic crystal using interference of a UV laser. Proc SPIE 1999; 3740: 541–4
67. Straub M, Ventura M, Gu M. Multiple higher-order stop gaps in infrared polymer photonic crystals. Phys Rev Lett 2003; 91:043901
68. Griffith ML, Halloran JW. Freeform fabrication of ceramics via stereolithography. J Am Ceram Soc 1996; 79: 2601-8.
69. Chartier T, Duterte C, Delhote N, Baillargeat D, Verdeyme S, Delage C, Chaput C. Fabrication of Millimeter Wave Components Via Ceramic Stereo- and Microstereolithography Processes. J Am Ceram Soc 2008; 91(8): 2469-74.
70. Greco A, Licciulli A, Maffezzoli A. Stereolitography of ceramic suspensions. J Mater Sci 2001; 36: 99-105.
71. Zhang X, Jiang XN, Sun C. Micro-stereolithography of polymeric and ceramic microstructures. Sensor Actuact A-Phys 1999; 77: 149-56.
72. Bertsch A, Jiguet S, Renaud P. Microfabrication of ceramic components by microstereolithography. J Micromech Microeng 2004; 14:197.
73. Pham TA, Kim DP, Lim TW, Park SH, Yang DY, Lee KS. Three-dimensional SiCN ceramic microstructures via nano-stereolithography of inorganic polymer photoresists. Adv Func Mater 2006; 16(9): 1235-41.
74. Griffin EA, Mumm DR, Marshall DB. Rapid prototyping of functional ceramic composites. Am Ceram Soc Bull 1996; 75(7): 65-8.
75. Zhang Y, He X, Du S, Zhang J. Al_2O_3 ceramics preparation by LOM (laminated object manufacturing). Int J Adv Manuf Tech 2001; 17(7), 531-4.
76. Rodrigues S, Chartoff RP, Klosterman DA, Agarwala M, Hecht N. Solid Freeform Symposium Proceedings, University of Texas, Austin, TX, 2000.

77. Löschau W, Lenk R, Scharek S, Teichgraber M, Nowotny S, Richter C. Prototyping of complex-shaped parts and tools of Si/SiC-ceramics by selective laser sintering. Adv Sci Tech 1999; B567-73.
78. Friedel T, Travitzky N, Niebling F, Scheffler M, Greil P. Fabrication of polymer derived ceramic parts by selective laser curing. J Eur Ceram Soc 2005; 25(2): 193-7.
79. Tian X, Zhang W, Li D, Heinrich JG. Reaction-bonded SiC derived from resin precursors by Stereolithography. Ceram Int 2012; 38(1): 589-97.
80. Windsheimer H, Travitzky N, Hofenauer A, Greil, P. Laminated Object Manufacturing of Preceramic-Paper-Derived Si-SiC Composites. Adv Mater 2007; 19(24): 4515-9.
81. Klosterman D, Chartoff R, Graves G, Osborne N, Priore B. Interfacial characteristics of composites fabricated by laminated object manufacturing. Compos Part A-Appl S 1998; 29(9): 1165-74.
82. Hunter RJ. Zeta potential in colloid science: principles and applications (Vol 2). Academic Press. 1981.
83. Johnson SB, Russell AS, Scales PJ. Volume fraction effects in shear rheology and electroacoustic studies of concentrated alumina and kaolin suspensions. Colloid Surface A 1998;141(1):119-30.
84. Smay JE, Cesarano J, Lewis JA. Colloidal inks for directed assembly of 3-D periodic structures. Langmuir 2002; 18(14), 5429-37.
85. Aparicio M, Durán A. Materiales compuestos C/SiC para aplicaciones estructurales de alta temperatura. Parte I: estabilidad termodinámica y química. Bol Soc Esp Ceram V 2000; 39(6): 687-98.

Chapter 3

The Spark Plasma Sintering of SiC-based materials

The achievement of fully dense SiC-based ceramics as structural materials is always a challenge considering the elevated sintering temperatures and times required for densification. Regarding these shortcomings, the sintering conditions for SiC ceramics have been widely analyzed for conventional sintering processes such as pressureless sintering or hot pressing. However, the analysis devoted to the comprehension of the sintering of SiC ceramics by the use of more modern sintering techniques is still being put forward. In particular, SPS stands out as one of the most modern sintering techniques and requires deep research to elucidate the densification mechanisms for SiC. In Chapter 1, a concise review on the works published related to the SPS process and, in particular, the SPS applied to SiC ceramics was done.

Moreover, the advent of graphene has promoted the use of GNPs as fillers for ceramics. Nonetheless, the extreme conditions required for the sintering of SiC set hurdles in the possibility of using these fillers in the case of SiC matrices. Thus, a study on the preservation of the structural integrity of graphene within SiC is also necessary for the appropriate development of composites by SPS.

Finally, the application of pressure during sintering has been a common method to assist either conventional or more modern sintering processes, as SPS, but it must be avoided when a green cellular structure is intended for densification –as in the case of robocast ceramic scaffolds. Distinctively, a novel punch/die device within the SPS furnaces to accomplish this purpose is required.

Considering these precedents, the scope of this PhD Thesis regarding the SPS process of SiC was to obtain dense bulk SiC materials resulting from different starting powders of SiC, which show different grain sizes and crystalline phases, and simultaneously improving the efficiency of the SPS process by modifying the electric current paths of the SPS during the sintering process. Also, the densification of SiC-based ceramic composites with GNPs contents of up to 20 vol.% and, finally, the sintering by SPS of cellular 3D-structures based on analogous compositions to the bulk materials are among the main objectives of the proposed work for this chapter.

3.1.- Bulk SiC-based ceramics by SPS

3.1.1.- In-situ growth of graphene during the SPS of SiC

The different powder compositions prepared for this PhD Thesis, as explained in A.2.2, have been processed for the achievement, by SPS, of various ceramic materials based on SiC. Most particularly, starting powders batches of three different types of SiC powders, i.e. α-SiC, β-SiC, and nano-β-SiC, with additive amounts of 7 wt.%, have been employed. The powder compositions are placed within the set-up comprised by the graphite SPS die and punches (see diagram in Fig. 3.1) in the middle, according to a standard configuration in such a way that the symmetry of the set-up is maintained. Graphite foil pieces were always used to ensure good contact for electric current flow and heat transfer between the different components (in particular, between the powders compact and the graphite elements), as well as to avoid possible reactions; a graphite fiber blanket surrounding the graphite die was also employed to prevent energy losses by radiation during sintering. Graphite die and punches with standard inner diameters of 20 mm were chosen. Next, the powder compacts were pressed under loads of 2 MPa, and the whole set-up with the powders inside was symmetrically aligned with the graphite spacers and the electrodes within the SPS chamber. Lastly, before the sintering cycles start, a load of 20 MPa was applied by the SPS system onto the powders compact. After that, vacuum was induced to get ~1 Pa, keeping then a constant value of 4-6 Pa during the SPS test.

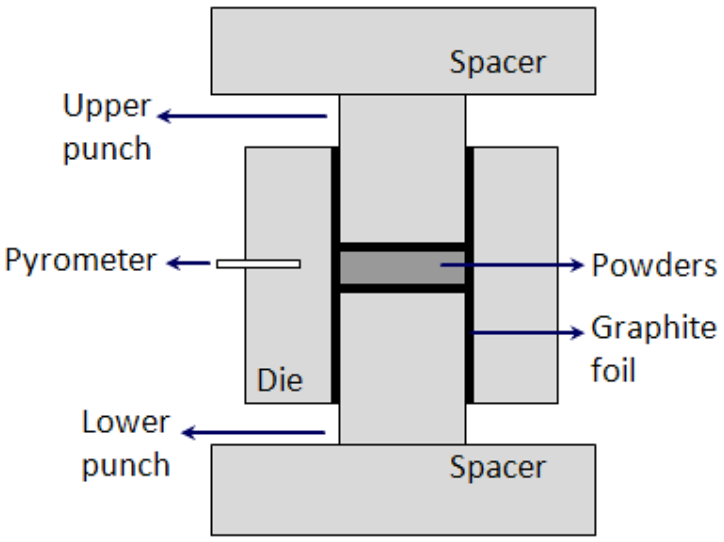

Figure 3.1.- Diagram of a standard graphite die and punches configuration of the SPS system.

Typically, for all the tests involving SiC bulk samples, a load of 50 MPa was linearly attained during the first minute of the test and, then, held constant until the cooling step starts, decreasing the mechanical pressure down to 20 MPa. For the preliminary experiments, temperature was varied within the range from 1650 to 1950 ºC to eventually determine the appropriate densification conditions for SiC. The temperature was measured with a pyrometer focalized on a small hole drilled in the middle of the graphite die whose depth reaches half the thickness of the die wall. The heating rates employed were of 133 °C·min^{-1} up to 1400 ºC, then were progressively decreased until the final temperature was reached in each case. Specifically, being T_s the set-point sintering temperature, heating rates were reduced to 65 °C·min^{-1} in the temperature range (T_s-250 to T_s-120), 45 °C·min^{-1} in the temperature range (T_s-120 to T_s-30), 25 °C·min^{-1} in the temperature range (T_s-30 to T_s-5), and 1 °C·min^{-1} in the last 5 minutes of the SPS test to finally reach T_s, which determines the end of the experiment. Afterwards, electrical current fluxes were stopped to let the cooling down process commences. In Fig. 3.2, a case example where a sintering process where a maximum temperature of 1800 ºC was attained is depicted for pressure and temperature programs. For all the sintering tests, the pulsing relationship was 12:2 between active/non-active pulses, being 3.3 s the duration of pulses. Parameters of electric current/voltage, temperature, vacuum pressure, and displacement along the pressing axis were registered as a function of time in every sintering test. In this way, specimens consisting of ceramic disks of SiC (20 mm diameter, 3 mm height) have been obtained.

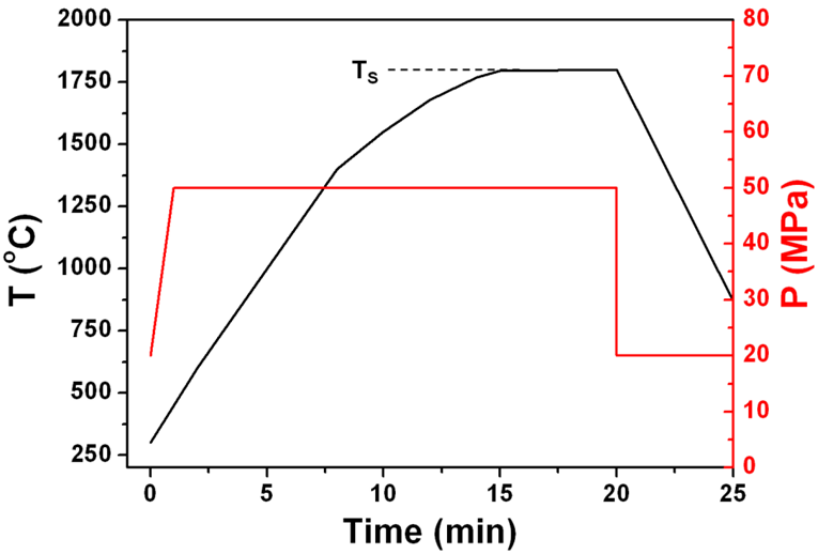

Figure 3.2.- Programmed temperature (T) and pressure (P) of the SPS as a function of time for a case example where the set-point temperature (T_S) was 1800 ºC.

The density (ρ) of the SiC specimens, measured by the Archimedes' method is shown in Fig. 3.3 as a function of the sintering temperature. Samples obtained for sintering temperatures below 1700 ºC exhibit density values lower than 3.20 $g \cdot cm^{-3}$, whereas for temperatures above 1800 ºC, a limit ρ value of ~3.25 $g \cdot cm^{-3}$ was reached for α-SiC and β-SiC materials, which represents a 98.9% of the theoretical density (ρ_{th}), assuming a value of 3.29 $g \cdot cm^{-3}$ for SiC ceramics with the given sintering additives. However, as it will be explained below, the theoretical density is lower and, hence, the specimens SPSed at $T_s \geq 1800$ ºC can be considered as fully dense bodies. On the other hand, specimens obtained from nano-β-SiC showed much lower maximum densities, in particular, a maximum value of 3.17 $g \cdot cm^{-3}$ that corresponds to 96.6% of ρ_{th}; this material shows a decrease in density at 1950 ºC that should be related to decompositions occurring at high temperatures. Considering these results, 1800 ºC was established as the standard temperature for the achievement of highly dense bulk SiC ceramics.

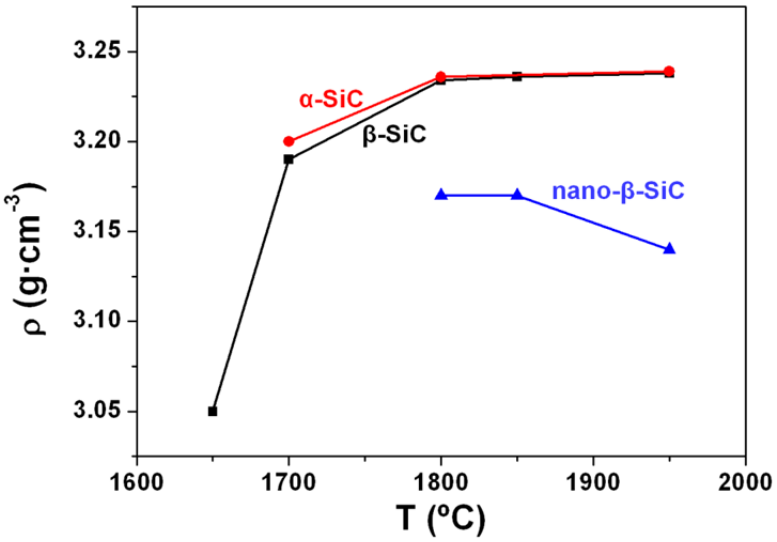

Figure 3.3.- Density (ρ) values of bulk β-SiC ceramics as a function of the sintering temperature.

X-ray diffraction (XRD) analyses were developed in SiC specimens for an investigation of the crystalline phases of the sintered ceramics, with especial attention to those sintered at 1800 ºC as it is considered the lowest temperature for full densification. According to the XRD patterns shown in Fig. 3.4, it can be firstly stated that almost no β→α-SiC transformation occurs in the present materials, as it is usually reported to be induced by temperatures above 2000 ºC.[1-5] As for the nano-β-SiC, only the peaks related to the 3C-SiC polytype (β-SiC) are detected. Some small peaks related to α-SiC polytypes (4H and 6H) are observed in the case of the β-SiC samples, but proved to be already present in the starting β-SiC powders. Finally, α-

SiC samples show the same polytypes as the starting powders (Fig. A.2.3), being comprised by important amounts of the 6H-SiC polytype, together with minor amounts of 4H-SiC and 15R-SiC. It is remarkable that the secondary phase in α-SiC and β-SiC ceramics crystallized as YAG or $YAlO_3$ (YAP) -it was not possible to discern between these two body-centered cubic phases- but remained amorphous in nano-β-SiC. This is explained in terms of its higher oxygen content, as compared to α-SiC or β-SiC, associated to the passivating layer of SiO_2 covering the raw nano-β-SiC powder particles. This SiO_2 would combine with the Al_2O_3 and Y_2O_3 sintering aids modifying the composition of the secondary phase at the SiC grain boundaries. The oxygen contents were determined by elemental analysis (A.2.6) for the three SiC powders (Table 3.1). Results show that the oxygen content increases as the SiC grain size decreases, being 1.2, 1.9 and 4.1 wt.% for α-SiC, β-SiC and nano-β-SiC, respectively. Therefore, the formation of native SiO_2 is obviously related to the surface area exposed to oxidation. To calculate the amount and composition of the secondary phase, the oxygen was converted to SiO_2 (Table 3.1). Based on this, a higher content of secondary phase was estimated for nano-β-SiC (14.2 wt.%) as compared to α-SiC (9.1 wt.%) and β-SiC (10.2 wt.%), which shifts the secondary phase composition towards the difficult-to-crystallize field of the corresponding Al_2O_3-Y_2O_3-SiO_2 phase equilibrium diagram (Fig. 3.5).[6] Considering the estimated amount of secondary phases, theoretical densities for the SiC samples are recalculated as shown in Table 3.1 using the following values: 3.22, 3.97 and 5.01 $g \cdot cm^{-3}$, for SiC, Al_2O_3 and Y_2O_3, respectively.

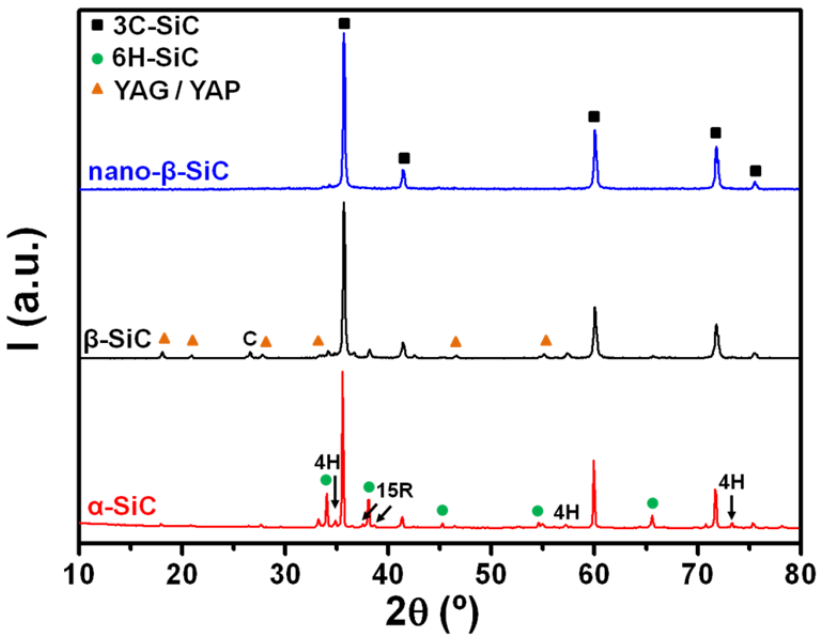

Figure 3.4.- XRD patterns of the reference SiC materials SPSed at 1800ºC.

Table 3.1.- Oxygen and carbon contents for the different SiC starting powders, contents and composition of the secondary phases for the three SiC powders, and estimation of the theoretical density (ρ_{th}) assuming that the oxygen is forming SiO_2.

	α-SiC	β-SiC	nano-β-SiC
Oxygen (wt.%)	1.2 ± 0.1	1.9 ± 0.1	4.1 ± 0.2
Calculated amount of secondary phase (wt.%)	9.1	10.2	14.2
Composition of the secondary phase (wt.%)			
Y_2O_3	54.1	47.8	34.0
Al_2O_3	21.6	19.1	13.6
SiO_2	24.3	33.1	52.4
Estimated ρ_{th} for the secondary phase ($g \cdot cm^{-3}$)	3.67	3.40	2.94
ρ_{th} calculated considering the SiO_2 content ($g \cdot cm^{-3}$)	3.26	3.24	3.18

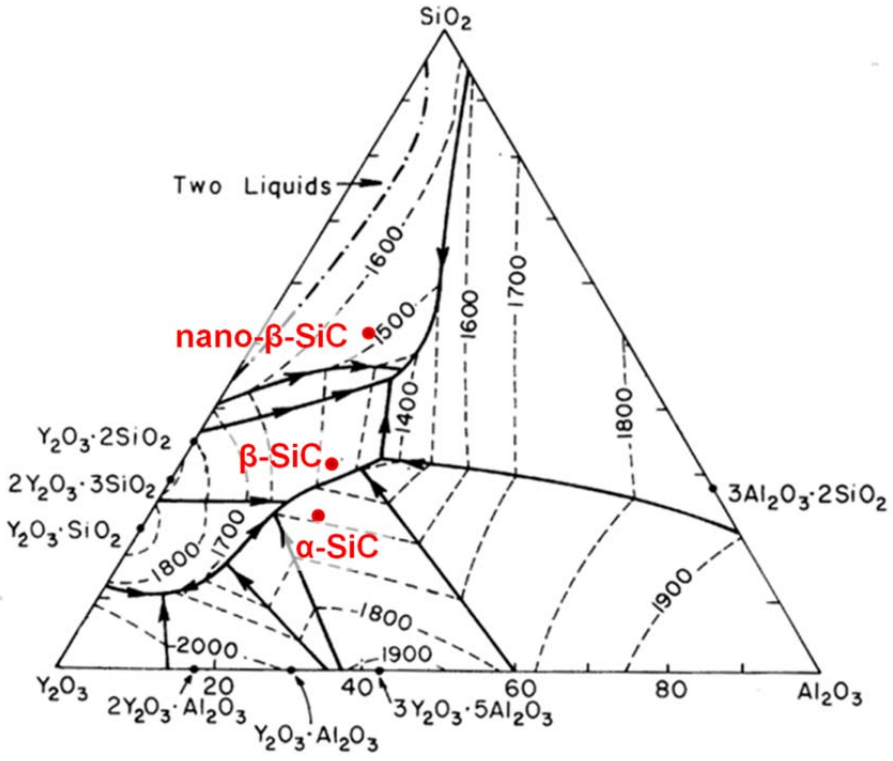

Figure 3.5.- Ternary phase diagram of the system SiO_2-Al_2O_3-Y_2O_3, where the estimated compositions of the secondary phases for each SiC powder have been included.[6]

The presence of the SiO_2 native layer covering the surface of SiC powders is important to understand the kinetics of the SPS process for the three different powder compositions. In Fig. 3.6a, the time evolution of the shrinkage (d_z) of the powder compacts during SPS at 1800 ºC has been depicted for the three compositions. The d_z increases with decreasing grain size of the starting powders probably because of the poorer level of compaction obtained during the pre-pressing cycle prior to the sintering. More interestingly, the maximum shrinkage rate also occurs at different temperatures of the SPS cycle, as it is seen in Fig. 3.6b where the time derivative of d_z is plotted as a function of time for the three materials. Both α-SiC and β-SiC compositions show similar sintering kinetics, with a maximum shrinkage rates at ~1625 ºC and ~1665 ºC, respectively, attributable to the solution-precipitation stage of liquid phase sintering. The shoulder observed at lower temperatures (above 1130 ºC), more visible in the case of β-SiC than in that of α-SiC, can be ascribed to particle rearrangement occurring as a consequence of the applied load when approaching the eutectic temperature of the SiO_2-Al_2O_3-Y_2O_3 system, reached at ~1380 ºC. This temperature is the lowest invariant point of the system (Fig. 3.5). As SPS is an extremely dynamic process and the temperature is measured at the graphite die surface, the true specimen temperature could be quite different from the measured, and local liquid formation can occur at nominally lower temperatures than those measured and predicted by the phase equilibrium diagram.

Conversely, the case of the nano-β-SiC is remarkably different due to the larger amount of secondary phase (Table 3.1) and the more reactive nature of nanosized powders. Firstly, the more intense peak linked to particle rearrangement is explained on account of the more reduced level of compaction of the nanosized powders. Secondly, the maximum shrinkage rate corresponding to the solution-precipitation process shifts to temperatures of at least 75 ºC lower than those of submicronsized SiC powders, owing to the larger amount of liquid phase formed in the nano-β-SiC material.

To complete the investigation of the crystalline phases, micro-Raman spectra and maps of the SiC-based ceramics have been acquired on the polished surfaces of the cross-sections of representative samples of α-SiC, β-SiC and nano-β-SiC. As a first approach, average spectra obtained in such regions of 10 x 10 μm^2 have been plotted in Fig. 3.7. In these spectra, two facts are particularly of interest. Firstly, α-SiC and β-SiC specimens develop Raman peaks associated to SiC polytypes appearing in the 100-1000 cm^{-1} range,[7] specifically the most characteristic vibrational optical modes of

the crystalline lattice, namely the transverse optical mode (TO) at 796 cm^{-1} and the longitudinal optical mode (LO) at ~976 cm^{-1}.

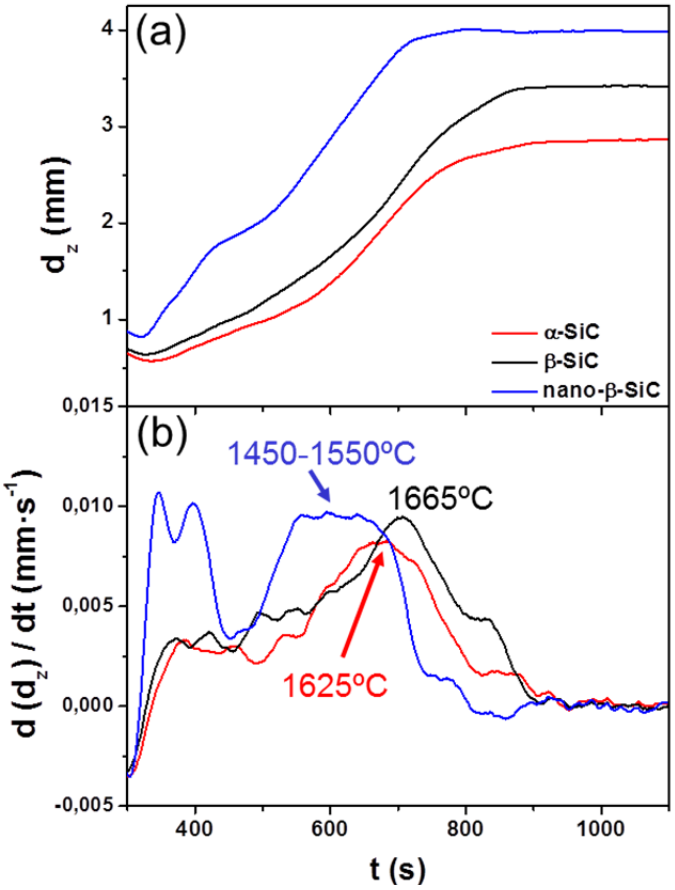

Figure 3.6.- (a) Shrinkage (d_z) and (b) shrinkage rate ($d(d_z)/dt$) curves versus sintering time of α-SiC, β-SiC and nano-β-SiC, obtained for similar SPS cycles at 1800 ºC.

In Table 3.2, a summary of the main Raman features (TO- and LO-band positions (P), full width at half maximum (FWHM) of the TO band, and I_{LO}/I_{TO} ratio) for the three SiC ceramics SPSed at 1800 ºC is collected. As shown, the intensity ratio between the LO and TO peaks (I_{LO}/I_{TO}) is lower for β-SiC (~0.3) than for α-SiC (~0.4), being the TO peaks often blue-shifted up to values of ~801 cm^{-1} for β-SiC. Samples corresponding to the nano-β-SiC composition mainly show a sharp TO peak located at ~804 cm^{-1}, the LO-peak being not detected. The LO mode typically disappears in doped-SiC and the TO mode is overlapped with a characteristic small shoulder at Raman shifts above 800 cm^{-1}. Therefore, in the nano-β-SiC, the absence of the LO vibrational mode should be attributed to a high level of doping of the SiC grains[7] most likely due to the solubility of species such as Al atoms (present in the sintering additives) in the SiC lattice by a solution-precipitation process during the liquid phase SPS.

Table 3.2.- TO- and LO-band positions (P), full width at half maximum (FWHM) of the TO band, and I_{LO}/I_{TO} ratio for averaged Raman spectra of the different materials SPSed at 1800 ºC.

Sample	P (TO) (cm^{-1})	FWHM (TO) (cm^{-1})	P (LO) (cm^{-1})	I_{LO}/I_{TO}
α-SiC	796	13	976	0.4
β-SiC	801	16	976	0.3
nano-β-SiC	804	15	-	-

Secondly, in the range from 1000 to 3000 cm^{-1}, three bands linked to graphitic species[8] are clearly observed: i) the D-band (~1360 cm^{-1}) which arises due to breaks in the translational symmetry of the hexagonal lattice, hence its intensity is very sensitive to the presence of structural defects in the species; ii) the G-band (~1595 cm^{-1}), related to the C-C tangential vibrational mode of graphene; and iii) the 2D-band, at a variable position depending on the nature of graphene layers (~2890-2720 cm^{-1}), originated from a double resonance process. The noticeable intensity of the 2D peaks in the spectra reveals the presence of few-layered graphitic (FLG) domains.

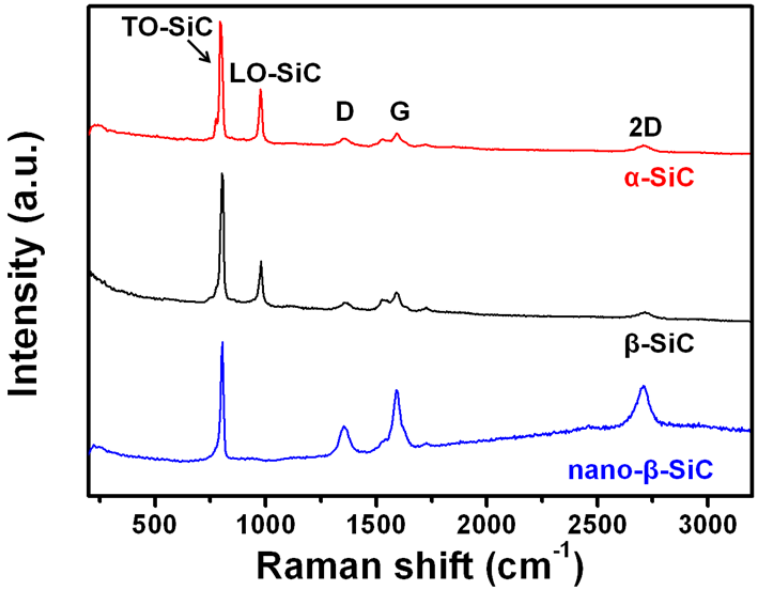

Figure 3.7.- Averaged Raman spectra acquired over 10 x 10 μm^2 regions on polished cross sections of α-SiC, β-SiC and nano-β-SiC samples sintered at 1800 ºC. 60 x 60 pixels and one spectrum per pixel were recorded, using 20 ms of acquisition time for each spectrum.

The Raman maps of the intensity of the G-band (I_G) and the intensity ratio of the 2D- and G-bands (I_{2D}/I_G) for the different SiC specimens, presented in Fig. 3.8, show both the presence of carbonaceous species, related to bright areas with high I_G, and also

the existence of FLG given by a high I_{2D}/I_G. These Raman maps confirm the uniform distribution of graphitic materials within the SiC matrix. The three Raman spectra shown in Fig. 3.8 for each SiC specimen are representative examples obtained on different areas of the produced composites. Raman spectra at positions 1, 2 and 3 correspond to areas in which the I_{2D}/I_G value is higher than 1.5, ~1, and <1, respectively; spectra also show SiC-related peaks. The center of the G- and 2D-bands, the FWHM, and I_{2D}/I_G ratios for averaged Raman spectra are summarized in Table 3.3.

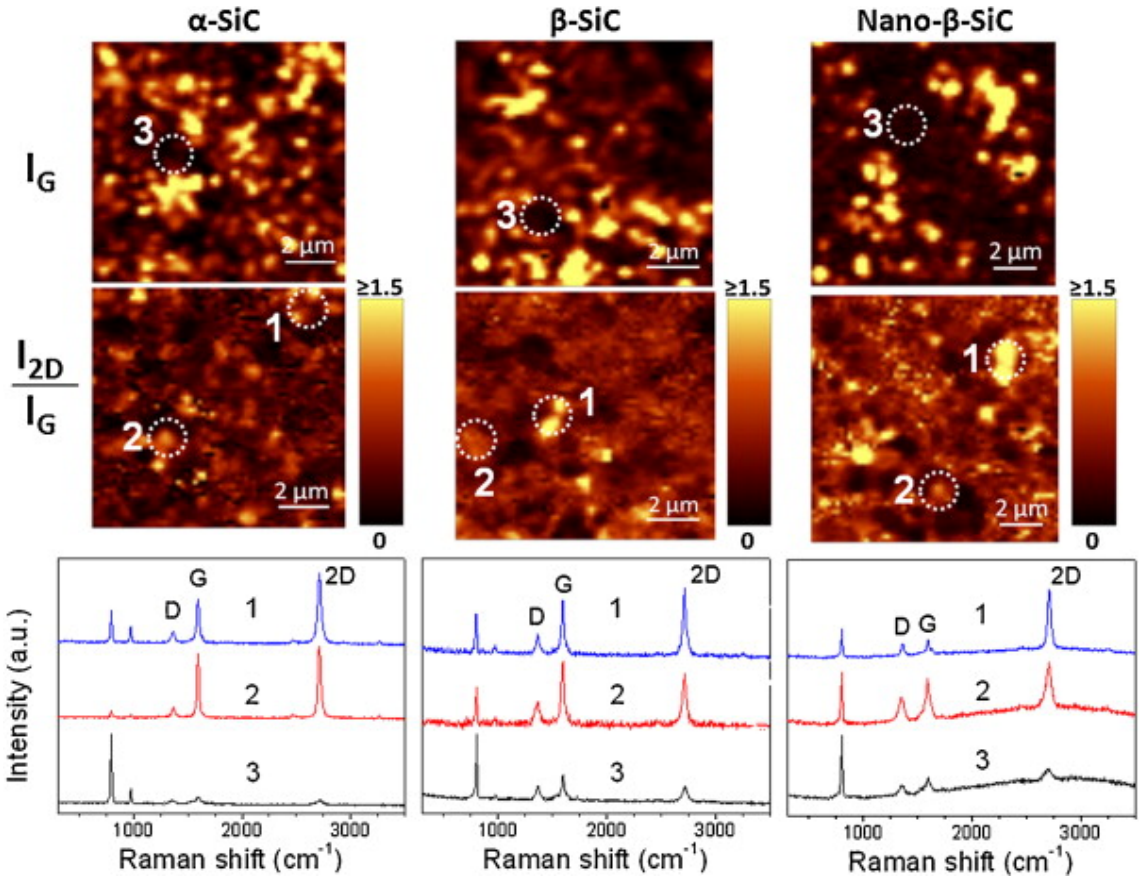

Figure 3.8.- Raman spectroscopy mappings of the intensity of the D band (I_G) and the intensity ratio of the 2D- and G-bands (I_{2D}/I_G) for the different SiC specimens on scanned areas of 10 µm × 10 µm and single spectra collected at the different positions (circled areas). Bright areas in I_G maps are associated to graphite-like structures whereas dark ones correspond to the SiC matrix. The I_{2D}/I_G maps of the same regions indicate the presence of FLG as bright areas. Adscription of the different graphene bands, D, G and 2D, is also shown in one of the spectra; the rest of the peaks correspond to the SiC polytypes. The total color/bright scale (0-1.5 and higher) is the same in all the I_{2D}/I_G maps.

Table 3.3.- G- and 2D-band positions (P), full width at half maximum (FWHM), and I_{2D}/I_G and I_D/I_G ratios for averaged Raman spectra of the different materials SPSed at 1800 ºC.

Sample	P(G) (cm^{-1})	FWHM(G) (cm^{-1})	P(2D) (cm^{-1})	FWHM (2D) (cm^{-1})	I_{2D}/I_G (area)	I_D/I_G (area)
α-SiC	1595	46	2707	74	0.8	0.8
β-SiC	1592	35	2711	78	0.8	0.6
Nano-β-SiC	1597	42	2710	78	1.5	1.0

The I_{2D}/I_G value for the spectrum at position 1 in the nano-β-SiC sample (i.e. 3.4) is significantly higher than the values observed for α-SiC and β-SiC (~ 1.7-1.6). These values agree with those generally reported for epitaxial graphene (EG), which are within the range of 0.5–2.0,[9] being lower than those for micro-mechanically cleft graphene (MG). However, this ratio is not considered an indicator for estimating the number of layers in EG.[9-11] Furthermore, for EG grown on the C-face of SiC $(000\bar{1})$, larger I_{2D}/I_G numbers (1.5-2.5) than those of graphene grown on Si-terminated SiC (0001) surface have been reported, which has been linked to the decoupling of the graphene layers in the former.[12] In general, EG is characterized by disordered (turbostratic) or non-Bernal stacking when grown on the C-face of SiC $(000\bar{1})$, in contrast to EG grown on Si-terminated SiC (0001) surface that is mainly Bernal-stacked.[13] However, the emergence of non-Bernal stacking has also been reported on Si-faces associated to extremely fast and cooling rates.[10] In this way, the higher I_{2D}/I_G value of the nano-β-SiC composite implies a larger amount of disordered stacking as compared to the other two materials.

Another feature observed in the Raman spectra of Fig. 3.8 is the lack of any obvious shoulder in the 2D peak (it is a symmetric signal), with FWHM values of 74-78 cm^{-1} for averaged spectra (Table 3.3), and around 35 cm^{-1} for the FLG single spectrum of Fig. 3.8. Again, these data resemble those of EG grown on the C-face of SiC $(000\bar{1})$ with narrow single Lorentzian 2D-bands (FWHM < 40 cm^{-1}) originating from rotationally faulted multilayers caused by the decrease in interlayer interactions.[11,12] In addition, a blue-shift of the G-band position, P(G), (~1593—1597 cm^{-1}) is observed when compared to multilayered graphene and graphite, both exhibiting P(G) at ~1587 cm^{-1}, which could be attributed to a compressive strain induced by the SiC matrix or a charge doping from the SiC substrate.

The graphene content for each SiC material was estimated from the intensity of the characteristics graphene peaks (I_G and I_{2D}/I_G) in the micro-Raman maps using the following criteria: (i) area fraction on random cross sections directly correlates to the graphene volume fraction, (ii) the brightest areas in the Raman maps correspond to topmost surface graphene, and (iii) these areas were quantified as those pixels with maximum Raman intensity discarding any signal from graphene located beneath the surface. Calculations give volume fractions of ~0.03 from I_G and I_{2D}/I_G maps for the three different materials, although the nano-β-SiC material exhibits a significantly higher value of I_{2D}/I_G (~ 1.5).

FESEM observations of plasma etched polished surfaces (Fig. 3.9) do not allow the identification of the FLGs as they are degraded by the etching process. As shown, the microstructure of the three materials essentially consists of fine SiC grains together with a homogeneously-distributed secondary phase. In particular, α-SiC has larger grain size (i.e., 1.11 μm with aspect ratio of 1.4) than β-SiC (i.e., 0.54 μm with aspect ratio of 1.4) and nano-β-SiC (i.e., 0.44 μm with aspect ratio of 1.7).

FESEM observation of fracture surfaces allows depicting graphene sheets formed during sintering (Fig. 3.10), although it is an inadequate technique to identify monolayer graphene. Whatever the case, few- and multi-layer graphene platelets of different sizes and thicknesses have been observed. Extensive areas of grown graphene were found in α-SiC and β-SiC SPSed at 1800 ºC (Fig. 3.10a,d), not shown in the case of nano-β-SiC because of the difficulty to depict flakes of smaller sizes owing to the fact that they should scale with the starting SiC grain size. In addition, some representative examples of multi-layered graphene flakes are also shown in Fig. 3.10. In this context, EG layers attached to an α-SiC grain are clearly distinguished (Fig. 3.10c), whereas stacked graphene layers at an initial growth stage are observed following a SiC flat terrace pattern (Fig. 3.10f) that resembles those reported by other authors for the epitaxial growth of graphene on SiC substrates.[10,14] In the present case, the terraces would be produced by the surface oxide cleaning of the SiC particles induced by the low pressure, the high temperatures and the enhanced local electric field at the particle interfaces produced during the SPS process.

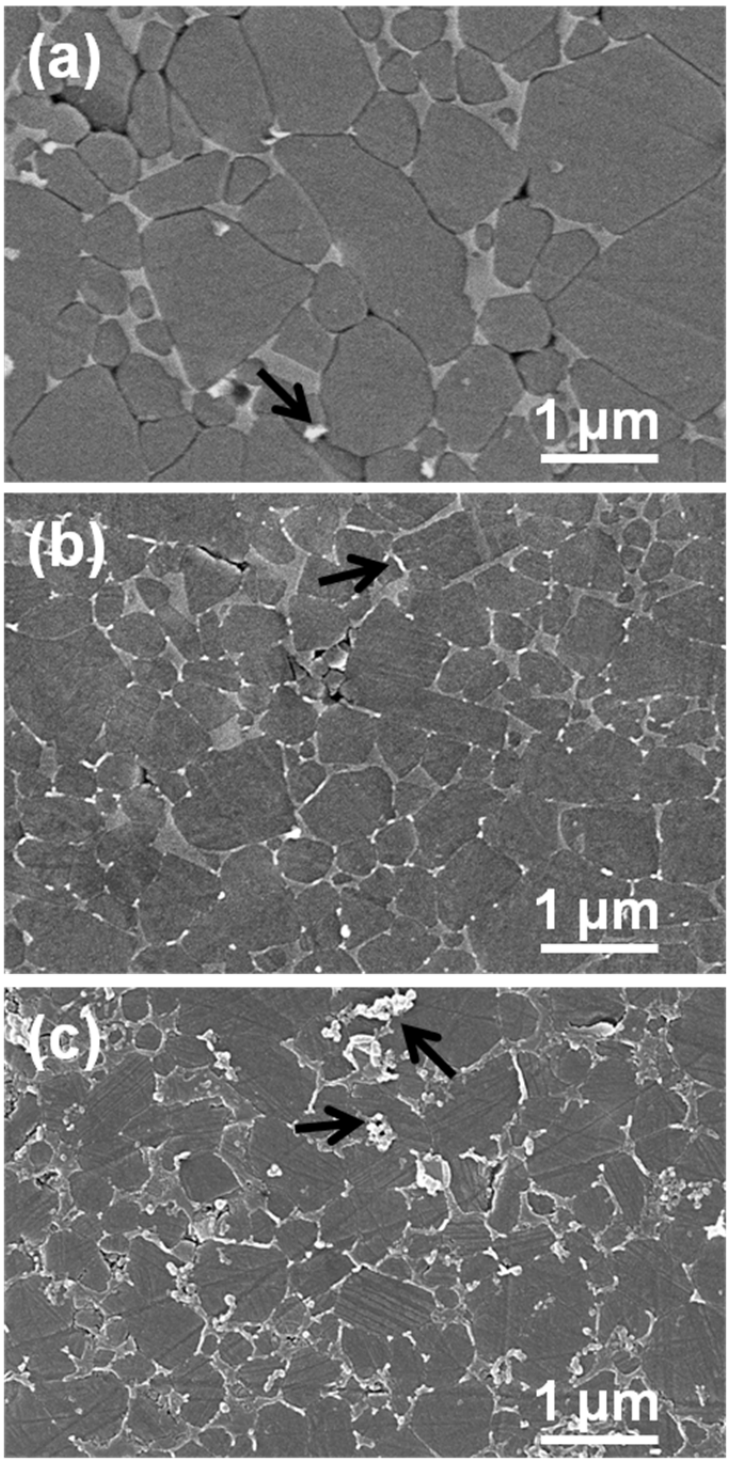

Figure 3.9.- FESEM micrographs of polished and plasma etched surfaces of (a) α-SiC, (b) β-SiC, and (c) nano-β-SiC. Black arrows point to damaged graphene flakes after the plasma-etching process.

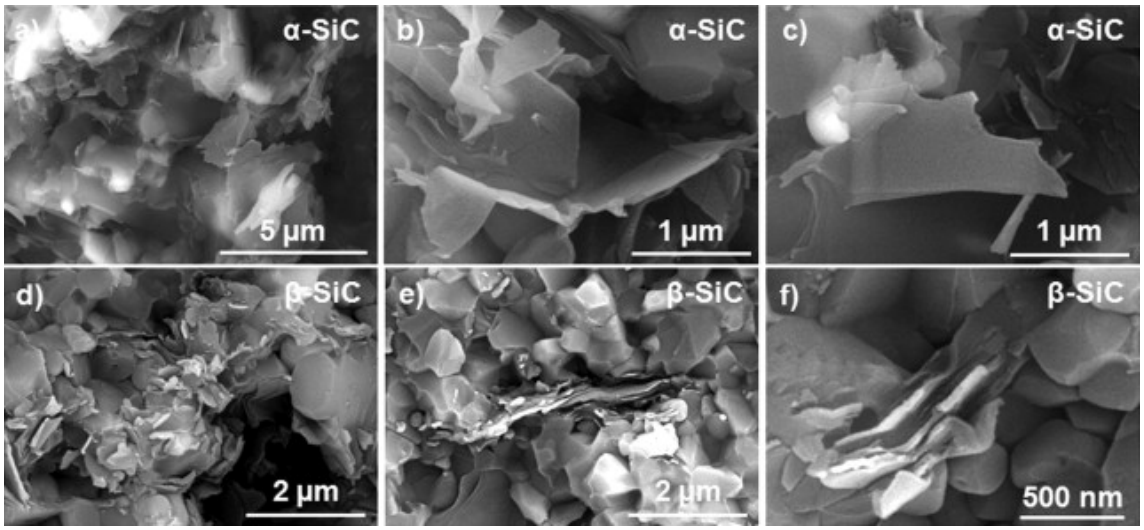

Figure 3.10.- FESEM micrographs of the fracture surfaces for dense α-SiC (a, b, c), and β-SiC (d, e, f) specimens. Representative images of multi-layered graphene flakes are shown bending along grain boundaries (images b,c), protruding from a SiC grain (c) and at an embryonic growth stage following a SiC flat terrace pattern (f). Small lateral size flakes are observed in the β-SiC material (d).

The presence of FLG in the SiC bulk materials was further confirmed by High Resolution Transmission Electron Microscopy (HRTEM, Fig. 3.11). Although Electron Energy Loss Spectroscopy (EELS) is very sensitive to the bonding state and chemical environment of carbon atoms,[15-17] the complexity of the present samples (both in composition and crystal orientation) requires finding regions where the FLG sheets are partially or completely exposed (P1 position in Fig. 3.11a). This condition is necessary to minimize the interference (or overlapping) of the EELS signal, corresponding to the sp^2 hybridized carbon, with the signal coming from the sp^3 carbon located at the SiC grain core. The carbon K-edge of graphene-like materials is associated with transitions from the 1s state to empty π* and σ* anti-bonding orbitals. These peaks were unambiguously observed in the EELS spectra from regions in the samples, with abundant sp^2 hybridized carbon atoms (Fig. 3.11e at P1 position). In addition, EELS from SiC grains showed a completely different carbon K-edge (Fig. 3.11e at P2 position). However, even in this case, small shoulders corresponding to the π* and σ* peaks were observed (vertical blue dashed lines in Fig. 3.11e). The presence of these shoulders suggests that the EELS signal, although coming from a region with abundant sp^3 carbon, also contains a small proportion of sp^2 carbon that could be originated inside a grain boundary oriented perpendicular to the electron beam.

Higher magnification images from P1 region (Fig. 3.11b) reveal parallel lines with dark contrast that resemble the cross-sections of FLG (2L, 3L and 5L). In fact, the measured spacing between these lines ranges between 3.4 and 3.8 Å, which is in agreement with the interlayer spacing between graphene layers in graphite.

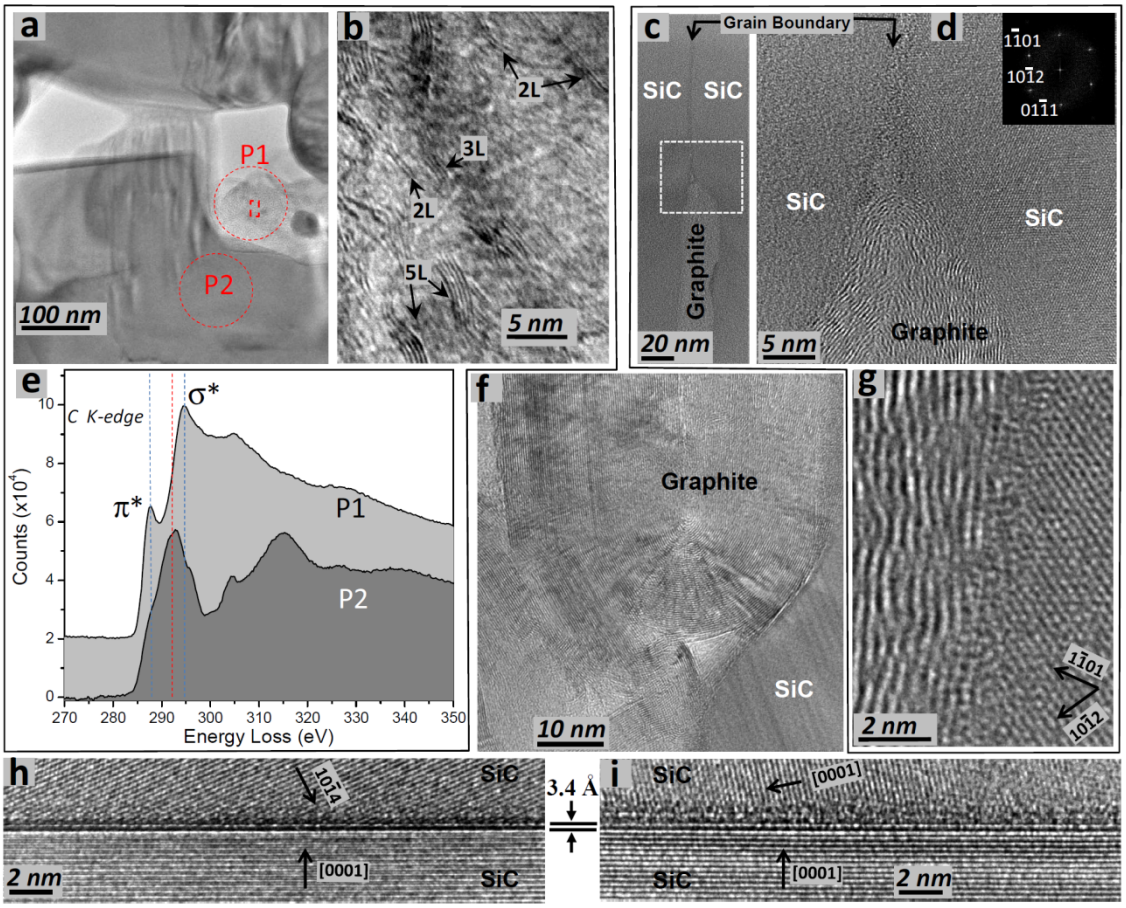

Figure 3.11.- TEM examination of the α-SiC composite sample, showing several regions with different number of graphene layers. *Region 1*: (a) low magnification TEM image of the region of interest. (b) is a higher magnification image of the P1 region (inside the highlighted rectangular region) which is rich in sp^2 carbon, showing different cross-section views of few-layers graphene flakes (2L, 3L and 5L); the spacing between dark contrast lines is consistent with the spacing between graphene sheets. (e) are EELS spectra (after multiple-scattering background removal) of the carbon K edge at positions P1 and P2, respectively. *Region 2*: (c) low magnification TEM image of a grain boundary with formation of a graphite island, (d, g) high-resolution TEM images of the same region, the inset is the FT of the right side SiC grain. *Region 3*: (f) graphitic formation of several tens of nanometers. *Region 4*: (h and i) two different grain boundaries presenting bi-layer graphene.

The region P1 is also carbon-rich as confirmed by the Energy-dispersive X-ray Spectroscopy (EDS) spectrum (not shown), indicating that the contributions to the EELS signal originated by SiC is very small. Grain boundaries exhibiting different number of graphene layers sandwiched in between grains were also found (shown in Fig. 3.11d,f–i). Previous reports on epitaxial graphene formed by the sublimation of Si from SiC substrates at high temperatures[18] have demonstrated that FLG formed on $(1\bar{1}0n)$ planes (known as terrace step edges) are significantly thicker than those formed on (0001) terraces. Apparently, the reduced bonding coordination facilitates graphene formation. Although the present experiments take place under different conditions, a grain boundary in which a graphene layer is sandwiched between two different surfaces that do not have the same crystalline orientation was observed. These observations are in agreement with the findings reported by Robinson et al.[18] Indeed, in this case, the smaller number of graphene layers have been observed at grain boundaries with at least one of the grains surfaces terminated with (0001) terraces (Fig. 3.11h,i). When the grain surfaces display any other crystalline orientation (i.e. Fig. 3.11d,f), the graphitic formations contain several tens of graphene layers. Because the crystalline orientation seems to govern the number of graphene layers formed at the grain interface, the graphene formation is not homogeneous along the entire grain boundary (Fig. 3.11c,d).

This in-situ graphene growth within different bulk SiC ceramics must be mainly caused by the SPS process as other densification methods, such as HP, which also take place under an enriched carbon atmosphere and even at higher temperatures, do not show this effect. The SPS technique uses high pulsed dc currents (~3000 A) and a low voltage (~4 V). The current passes through the crucible/powder/punches system and the sample experiences densification mainly by Joule heating. Therefore, the *dc* current flowing in the SPS system, in conjunction with the residual vacuum, must play a key role in the graphene formation within the SiC ceramics. It is important to note that highly crystalline graphene sheets with atomically smooth edges can be produced via Joule heating in graphitic nanoribbons.[19] Therefore, SPS appears to be an efficient and unique technique able to produce highly crystalline graphene, and the experiment described here is no exception. In this way, during SPS, extreme temperatures may locally happen at regions that intercept the percolation path. In fact, increased electric strength at the interface of neighboring particles of up to 40 times the applied field has been modeled for the SPS.[20] The low pressure (4 Pa) and the high local temperatures at the particle interfaces will favour the formation of highly crystalline graphene domains by decomposition of the $SiOC/SiO_2$ coating covering

the SiC particles. Sublimation of SiO under the vacuum and high temperature conditions,[21] presumably leaves a carbonaceous residue and exposes the underneath SiC layers for further thermal decomposition. The proposed mechanism is illustrated in Fig. 3.12.

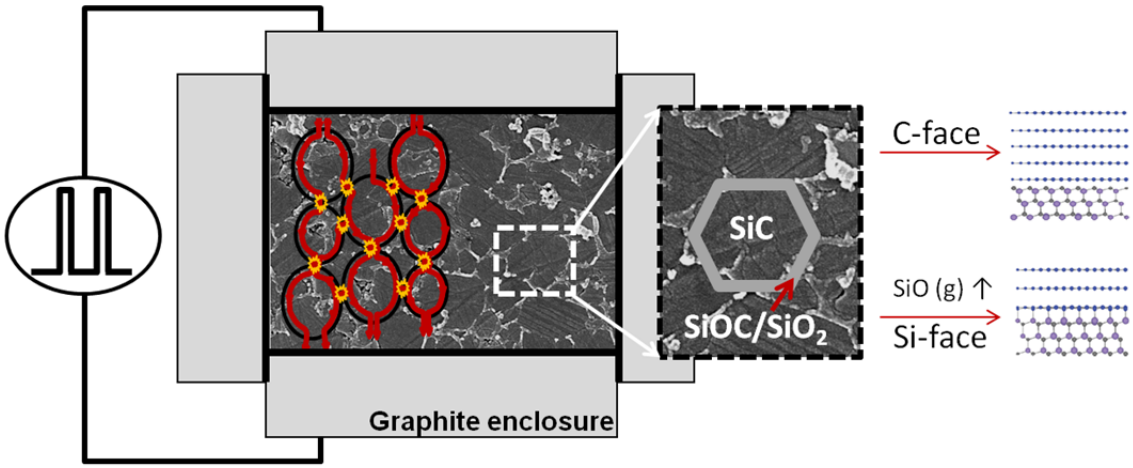

Figure 3.12.- Schematic illustration of the in-situ graphene growth process.

Raman studies done on nano-β-SiC composites sintered at low SPS temperatures show that a highly defective carbonaceous phase forms at 1200 ºC, probably coming from decomposition of the $SiOC/SiO_2$ coating, evolving to crystalline graphitic nanodomains at temperatures above 1300 ºC (Fig. 3.13). Carbon contamination from the graphite tooling was discarded as a source of carbon for the formation of graphene; in fact, graphitic nanodomains formed during the SiC thermal decomposition were confirmed as the graphene source as the carbon content in nano-β-SiC sintered samples is quite similar (25.3 wt.%) to that of the starting powders (25.1 wt.%, recalculated from data in Table 3.1 by considering 7 wt.% of oxide sintering additives).

Considering the effect of ~3 vol.% of the in-situ grown graphene content in the density of the specimens, the values collected in Table 3.4 are predicted assuming a density for the graphene of ρ ~2.2 $g \cdot cm^{-3}$. The calculated values are slightly lower than those experimentally measured for α-SiC and β-SiC (3.24 $g \cdot cm^{-3}$) and for the nano-β-SiC composite (3.17 $g \cdot cm^{-3}$), which could be due to either a partial volatilization of the secondary phases or to an overestimation of the SiO_2 content.

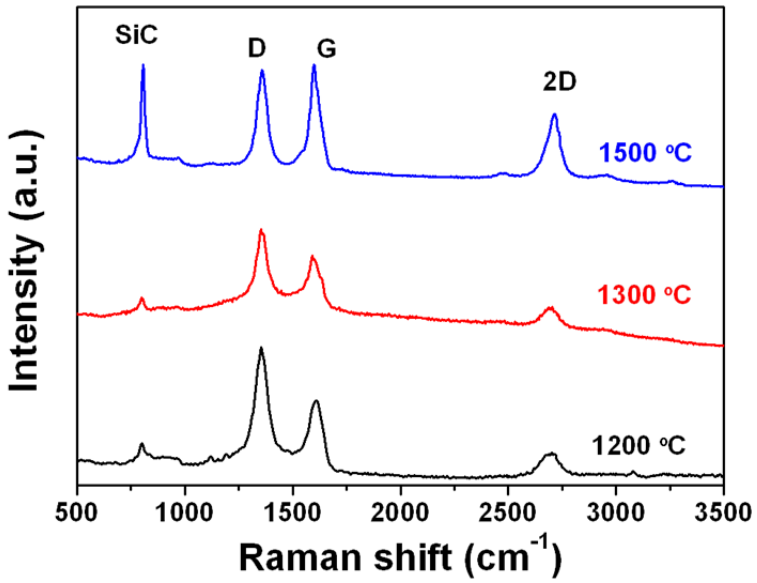

Figure 3.13.- Micro-Raman average spectra of the spark plasma sintered nano-β-SiC materials at different SPS temperatures. Conditions used: 60 x 60 pixels and one spectrum per pixel using 20 ms of acquisition time for each spectrum.

As it can be seen in Table 3.5, these materials present different mechanical properties as consequence of their different microstructural features. Thus, the nano-β-SiC is slightly softer (19.0 ± 0.1 GPa) than the other two ceramics (~21.0 - 22.6 GPa), attributable to the higher content of secondary phase, which is mainly amorphous (Table 3.1 and Fig. 3.4) and, then of lower hardness (~7 GPa)[22] than YAG (15 GPa),[23] as the grain sizes in the three materials are too large (i.e., in the range 0.44-1.11 μm) to exhibit a size effect hardening. The same reason is valid for the reduced elastic modulus of the nano-β-SiC. As for the fracture toughness, β-SiC and nano-β-SiC show slightly higher K_{IC} values than the α-SiC material. This is unexpected in the case of nano-β-SiC regarding the higher content of amorphous secondary phase. However, an increased effectiveness of crack-bridging mechanisms would be expected in this material associated to the slightly greater aspect ratio of the SiC grains and the slightly higher number of graphene flakes at the grain boundaries. This larger number of graphene flakes is simply attributed to the fact that the size of the graphene flakes scales with the starting SiC grain sizes.

Table 3.4. Theoretical density (ρ_{th}) of the three materials considering the initial compositions, and the estimations corresponding to the assumptions that O contents form SiO_2, and that 3 vol.% FLG is formed in-situ. Measured values are also included (ρ_{exp}).

Densities	α-SiC	β-SiC	nano-β-SiC
ρ_{th}	3.29	3. 29	3. 29
ρ_{th} recalculated considering the SiO_2 content ($g \cdot cm^{-3}$)	3.26	3.24	3.18
ρ_{th} recalculated considering the SiO_2 graphene content ($g \cdot cm^{-3}$)	3.22	3.21	3.15
ρ_{exp}	3.24	3.24	3.17

Table 3.5.- Elastic modulus (E), hardness (H) and toughness (K_{Ic}) measured by indentation at a force of 49 N on the different SiC materials SPSed at 1800 ºC.

Sample	H (GPa)	E (GPa)	K_{Ic} ($MPa \cdot m^{1/2}$)
α-SiC	21.0 ± 0.7	392 ± 16	3.8 ± 0.4
β-SiC	22.6 ± 0.7	430 ± 25	4.7 ± 0.2
Nano-β-SiC	19.0 ± 0.1	350 ± 7	4.0 ± 0.1

3.1.2.- Effects of current confinement on the SPS of SiC

Despite the variety of studies on the SPS of SiC powders, a significant lack of fundamental research about the effects of the electrical current distribution on the sintering process of SiC ceramics with Y_2O_3–Al_2O_3 additives is detected. As it was stated in Chapter 1, several attempts have been done for the energy-efficient sintering of different ceramics (such as Al_2O_3, HfB_2–SiC, ZrB_2, and $MoSi_2$) by SPS, inducing electric current flow isolation by using highly resistive films.[24,25] In this PhD Thesis, the effect of the electric current confinement on the sintering of SiC materials by SPS, and thus, on the microstructure and properties, has been analyzed using two different configurations of the SPS tools: i) the standard symmetric system (Fig. 3.1), as for the ordinary samples fabricated so far, using the common graphite tooling

setup, namely SYM, and ii) a set-up –also symmetric- where a BN powdered coating of ~100 μm thickness was sprayed onto the inner walls of the cylindrical graphite die (Fig. 3.14), namely SYM-BN. This insulating coating electrically detaches the graphite foil and the specimen from the graphite die, thus inducing current confinement around the sample. The effect of these distinct current pathways on the SPS parameters (voltage, current, temperature), the whole electrical resistance of the system, and the energy consumption, as compared to the standard sintering process, were analyzed. In both systems, three grams of the β-SiC composition were placed in the middle of the graphite arrangement preserving axial symmetry.

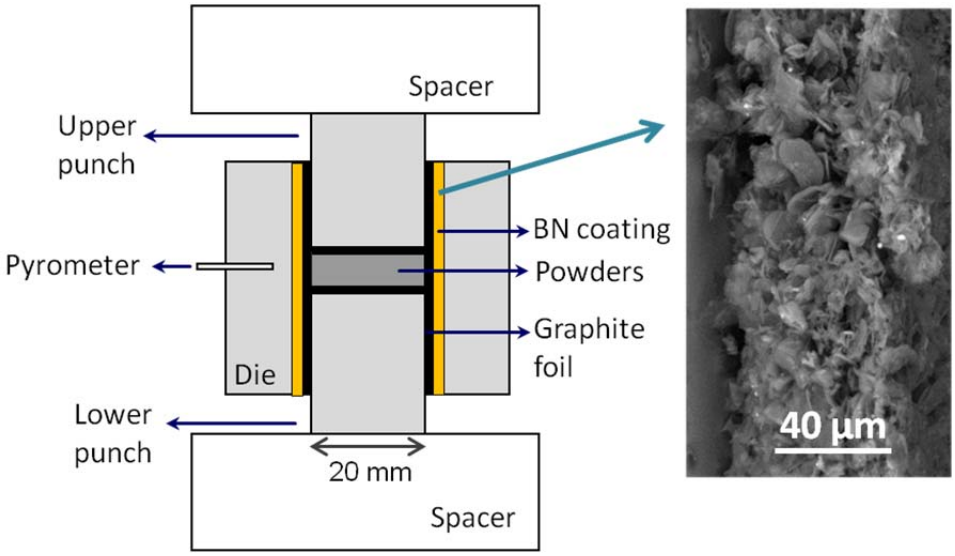

Figure 3.14.- Schematic illustration of the SYM-BN assembly, including a SEM micrograph of the BN layer between the graphite foil and die.

As a first approach to the sintering efficiency in both SPS set-ups, the degree of densification of SiC ceramics was measured. The apparent density of β-SiC specimens SPSed using SYM and SYM-BN arrangements, for different T_s but same sintering conditions (atmosphere, dwelling time, heating rate, etc.), is plotted in Fig. 3.15a. As it was previously described, $T_s \geq 1800$ °C were required to reach fully dense bodies for the SYM configuration. Interestingly, for similar densities, a shift to lower T_s temperatures is observed for the SYM-BN configuration, for which almost full densification (3.22 $g \cdot cm^{-3}$, 99.4% ρ_{th}) is achieved at a T_s of 1575 °C, 225 °C lower than for the SYM specimen.

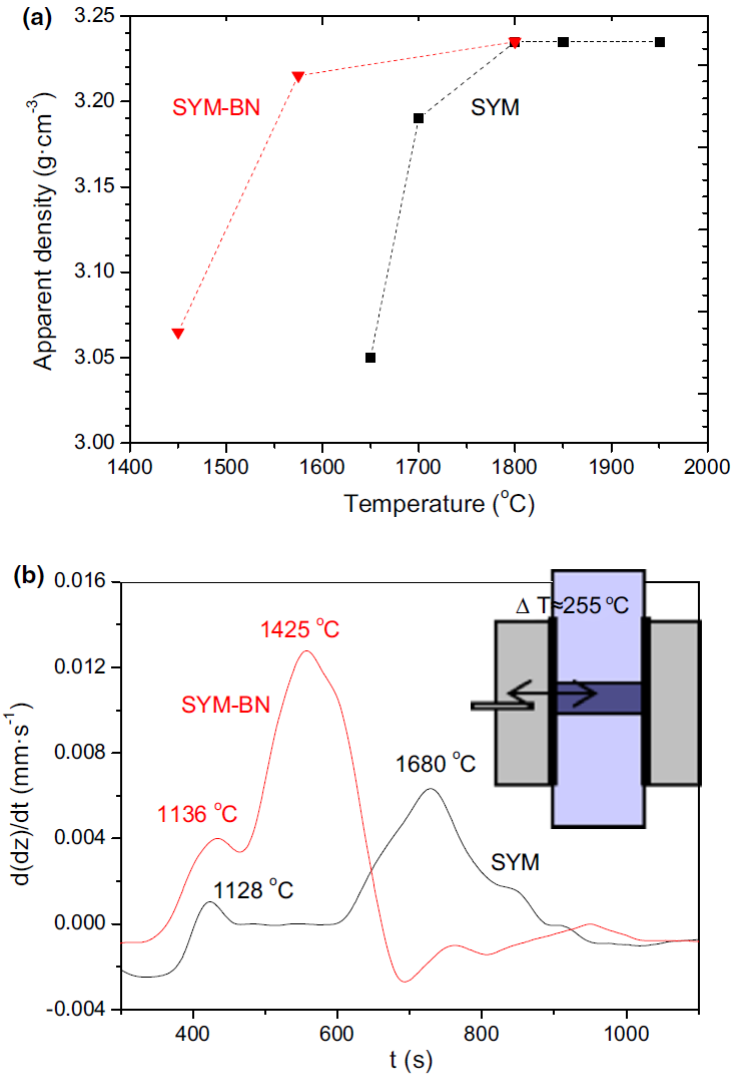

Figure 3.15.- (a) Apparent density versus set-point temperature and (b) displacement rate [d(dz)/dt] at 1800°C versus sintering time for β-SiC specimens SPSed using SYM and SYM-BN configurations.

For a deeper understanding of the densification processes, the derivative of the specimens shrinkage as a function of time was plotted in Fig. 3.15b for T_s = 1800 °C, using the same heating rate ramps and both SYM and SYM-BN settings. At this temperature, both materials exhibit similar densities Fig. 3.15a. Shrinkage was obtained from the vertical displacement along the z axis (dz) of the system frame digitally recorded by the SPS device. Similarly as in the case of the sintering kinetics of SPSed Si_3N_4 ceramics using the same additive system,[26] two peaks in the shrinkage rate curves associated to the particle rearrangement (lower temperature peak) and solution-precipitation (higher temperature peak) stages of liquid phase sintering were also observed. The first peak at ~1130 ºC (Fig. 3.15b) then

corresponds to the particle rearrangement rate enhancement when approaching the eutectic temperature of the additive SiO_2–Al_2O_3–Y_2O_3 system.

The densification kinetics would be further accelerated with increasing temperature aided by the solution-precipitation process, which corresponds to the most intense peak in Fig. 3.15b. As shown, the maximum shrinkage rate is higher (0.13 $mm \cdot s^{-1}$) and takes place at a lower temperature (1425 °C) for the SYM-BN than for the SYM set-up (0.06 $mm \cdot s^{-1}$ and 1680 °C, respectively), the temperature shifting (255 °C below) being comparable to that observed for reaching maximum densification which was ~225 °C, Fig. 3.15a. As the real temperature for complete densification must be the same irrespective of the SPS arrangement, the apparent temperature reduction observed for the SYM-BN specimen should be related to disparity between the true sample temperature and the pyrometer read-out. In this way, it can be ascertained that the BN die coating induces a real temperature between 225 °C and 255 °C higher in the samples, possibly because the electrical current is mostly driven through the graphite foil covering the powdered specimen, avoiding the direct Joule heating of the graphite die; also, the outward heat flow is somewhat prevented by the sprayed BN layer.

To prove this statement, electrical data as a function of time during SPS runs at a set-point temperature of 1800 °C for both SYM and SYM-BN settings, as well as for a SYM-BN specimen sintered at the hypothetically real temperature of 1800 °C, i.e. a T_s=1575 °C, 225 °C below the T_s of the SYM configuration, were comparatively analyzed. As observed in Fig. 3.16a, there is an initial stage before the pyrometer starts to control the heating schedule during which the current intensity, I, remains constant (~360 A) and, therefore, the voltage, V, drops (Fig. 3.16b) following the system resistance, R, shown in Fig. 3.16c, which is significantly higher for the SYM-BN configuration than that of the SYM. Throughout the initial phase (0-100 s), the dissipated power (P), calculated from the equation $P = I \cdot V$, is also higher for the SYM-BN arrangement as shown in Fig. 3.16d, and thus the programmed temperature is reached much earlier, at about half the time required for the SYM run (100s vs. 200s). After this first stage, the electrical conditions drastically change to power controlled stage and a much lower current (Fig. 3.16a) is detected for the SYM-BN specimens, consequently resulting in an overall lower power consumption compared to SYM configuration. The slight decrease in the current detected in Fig. 3.16a at 900 s (i.e., at the beginning of the holding time) for the SYM-BN could be explained by the thermal stabilization with the die, which is at a lower temperature of ~200 °C than the sample.

The energy consumed during the SPS run, E_C, calculated by integrating the P(t) outline in Fig. 3.16c over the sintering cycle, varies considerably between the different settings (see Table enclosed in Fig. 3.16d). Thus, the BN insulating layer reduces around 30% the consumed power for SPS runs at the same set point temperature of 1800 °C, namely from 7.71 MJ to 5.34 MJ, and the reduction was even larger (~60%, E_C = 3.06 MJ) for the test carried out at the same real temperature, that is, for SYM-BN at 1575 °C. The reduction in P and the increase in the system resistance for SYM-BN setup are both directly related to the electrical current confinement through a smaller volume of higher electrical resistance.

Instead of the SiC powders, a cylindrical graphite specimen (the same material type used for the furnace tools) was used as reference to elucidate the current paths for both settings. In this way, two runs, SYM at 1800 °C and SYM-BN at 1575 °C, that is, at the same real temperature, were performed. The same trends of resistance with time (Fig. 3.17) are observed during these SPS runs although 1 mΩ higher R values were attained when using the BN coating. From the resistivity of graphite given by the suppliers (1.00×10^{-5} and 1.14×10^{-5} Ω·m for the in-plane graphite foil and the bulk graphite die and punches, respectively) and the dimensions of the different components of the assembly, the R values of the different graphite components are calculated as shown in Table 3.6; considering that the graphite foil has a significantly higher resistance (30.30 Ω at 25 °C) than the denser graphite die (0.28 Ω) and punches (0.67 Ω), electrical current can be assumed to mainly flow through the central, highly conducting graphite parts for the SYM-BN configuration.

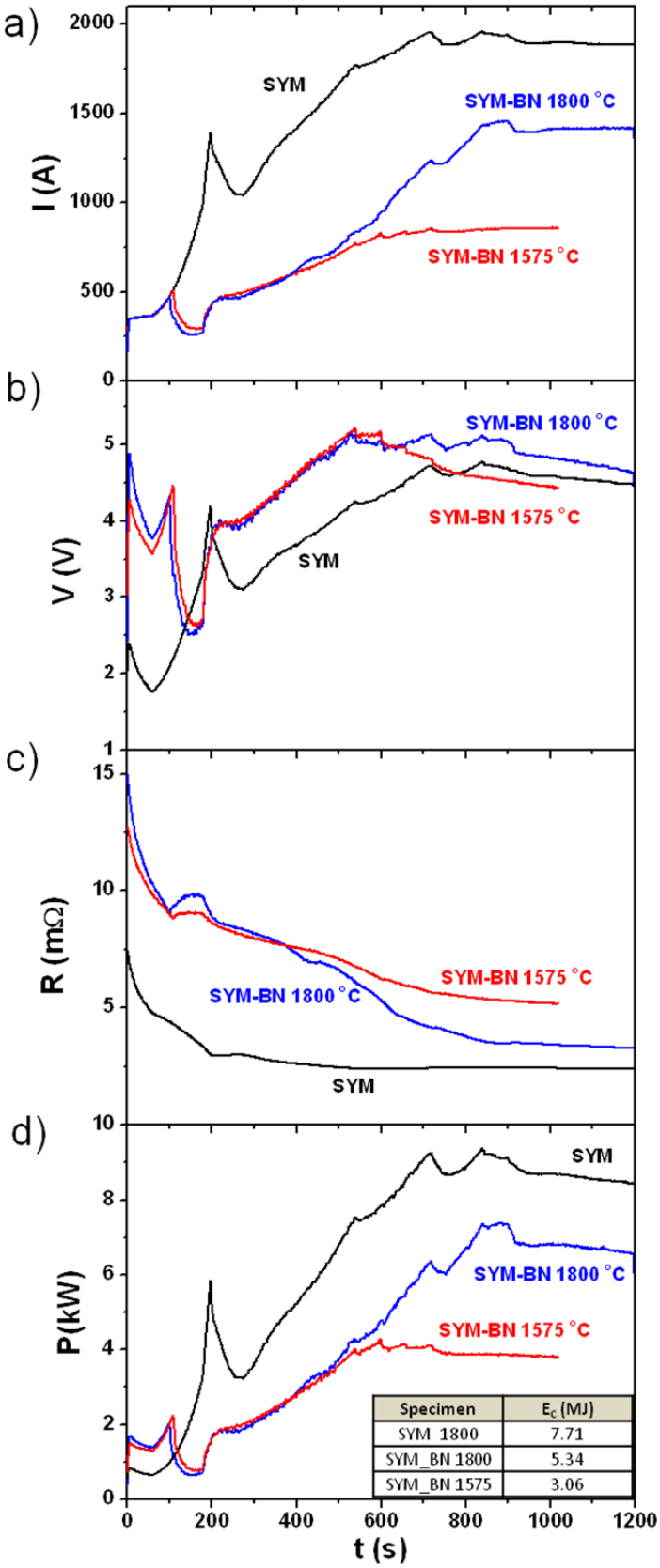

Figure 3.16.- (a) Current intensity, I, (b) voltage, V, (c) electrical resistance, R, and (d) dissipated power, P, as a function of time for different SPS runs using both the SYM and the SYM-BN assemblies. The Table on (d) collects the energy consumption, E_C, of the sintering tests.

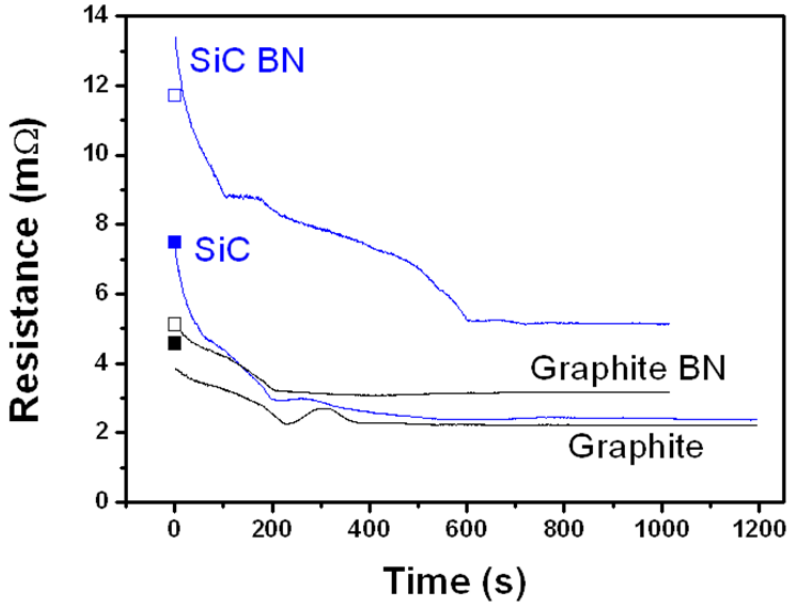

Figure 3.17.- Electrical resistance plots as a function of time measured for different SPS runs using both a graphite disk and a SiC powdered compact, with the SYM and the SYM-BN assemblies, where the predicted room temperature resistances are plotted as square dots.

Table 3.6.- Table summarizing the resistances of the graphite elements of the circuits in Fig. 3.18b,c, calculated from the resistivity of the graphite punches, die and foil (given by the supplier) and the dimensions of the different components of the assembly.

Resistive element	$R_{top}=R_{bot}$	R_{mid} (graphite)	$R_{sysT}=R_{sysB}$	R_{die}	R_{GFm}	R_{GFb}	R_c (punch/GF)	R_c (BN)
Resistance (mΩ)	0.67	0.11	1.89	0.14	2.27	14	~2.53	>150

In this way, the equivalent circuit shown in Fig. 3.18b was assumed for this case, in which the top (sysT) and bottom (sysB) parts of the assembly are separately considered, and those of the punches have been divided into top (top) and bottom (bot). R_{mid}, R_{die}, and R_c represent the resistances associated to the sample (graphite, in this case), die and contacts, respectively. From data in Table 3.6, and the resistance experimentally measured (R_{exp}) for the reference run with BN, the system resistance in Fig. 3.18, R_{sys}, is estimated as 1.89 mΩ assuming a higher contact resistance (R_c) than 150 mΩ, using the following expression:

$$R_{sysT} = R_{sysB} = (R_{exp} - R_{top} - R_{mid} - R_{bot})/2 \quad (1)$$

Those estimated values are used for modeling the resistance for the SYM, without BN, in which a part of the current passes through the die, which would be equivalent to add the parallel dashed circuit in Fig. 3.18b.

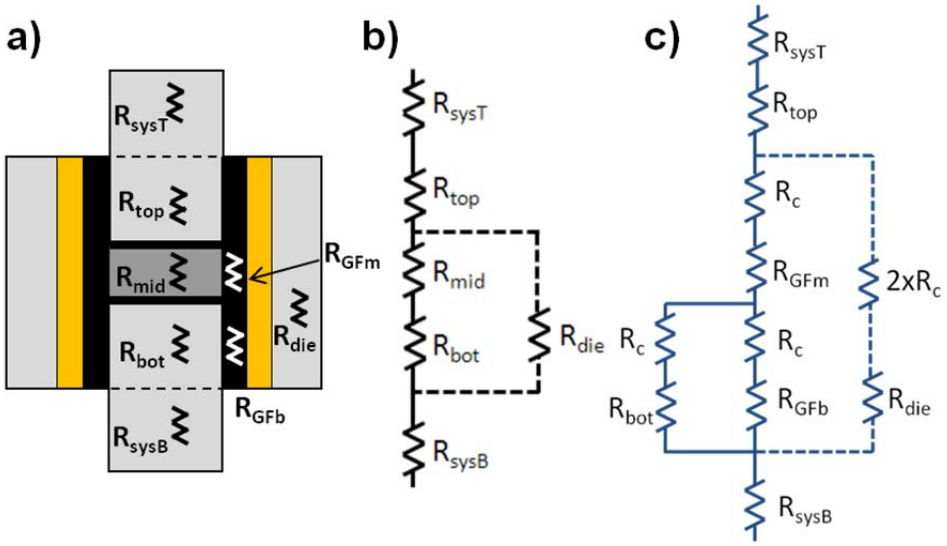

Figure 3.18.- (a) Schematic pattern of the elements, and their associated resistances, of the SPS setting. (b) Equivalent patterned circuit of (a) when a graphite sample is placed in the center of the system; the dashed branch only operates in the absence of the BN layer. (c) Equivalent patterned circuit of (a) when a ceramic powdered compact is placed in the center of the system; in the presence of a BN layer, the dashed branch is suppressed. Resistance (R) subscripts nomenclature is: “sysT” and “sysB” for top and bottom parts of the assembly; “top” and “bot” for top and bottom punches; “mid,” “die,” and “c” for sample, die and contacts, respectively; “GFm” and “GFb” for graphite foils in contact with the sample (middle) and the bottom punch.

Resistance data in Table 3.6 are also employed to model the resistance of the assembly during the sintering of a SiC powdered specimen. Due to its much higher electrical resistance (e.g., the R of dense SYM SiC materials is ~10^4–10^5 times that of graphite, see Chapter 5), it is assumed that the current path deviates when reaching the sample to the graphite foil—with BN—and also to the die—without BN— (as shown in the equivalent circuits in Fig. 3.18c). The deduced R values, plotted as squared dots in Fig. 3.17 fit quite well with the experimental data (lines in Fig. 3.17) at the very beginning of the tests. Results show that the contact resistance linked to the BN coating produces current confinement through the graphite foil provided that it is above a certain threshold resistance (in this case, higher than 150 mΩ), irrespective of the BN layer thickness (at least above a coating thickness threshold of ~100 μm). In this way, electrical current would flow around the specimen in the SYM-BN

assembly, whereas it mainly flows through the dense graphite die of much lower electrical resistivity in the SYM setting. The confinement of the electrical current around the specimen leads to local energy dissipation by Joule effect, which appears as a successful method for a faster and more efficient heating of present materials. This reduction in the power consumption is especially remarkable when facing a large-scale production.

In Fig. 3.19, representative FESEM micrographs at the top and bottom regions of the cross-sectioned SiC specimens sintered at 1800 °C are collected, using the SYM (Fig. 3.19a,b) and SYM-BN (in Fig. 3.19e,f) configurations, as well as a SYM-BN sample sintered at 1575 °C (Fig. 3.19c,d).

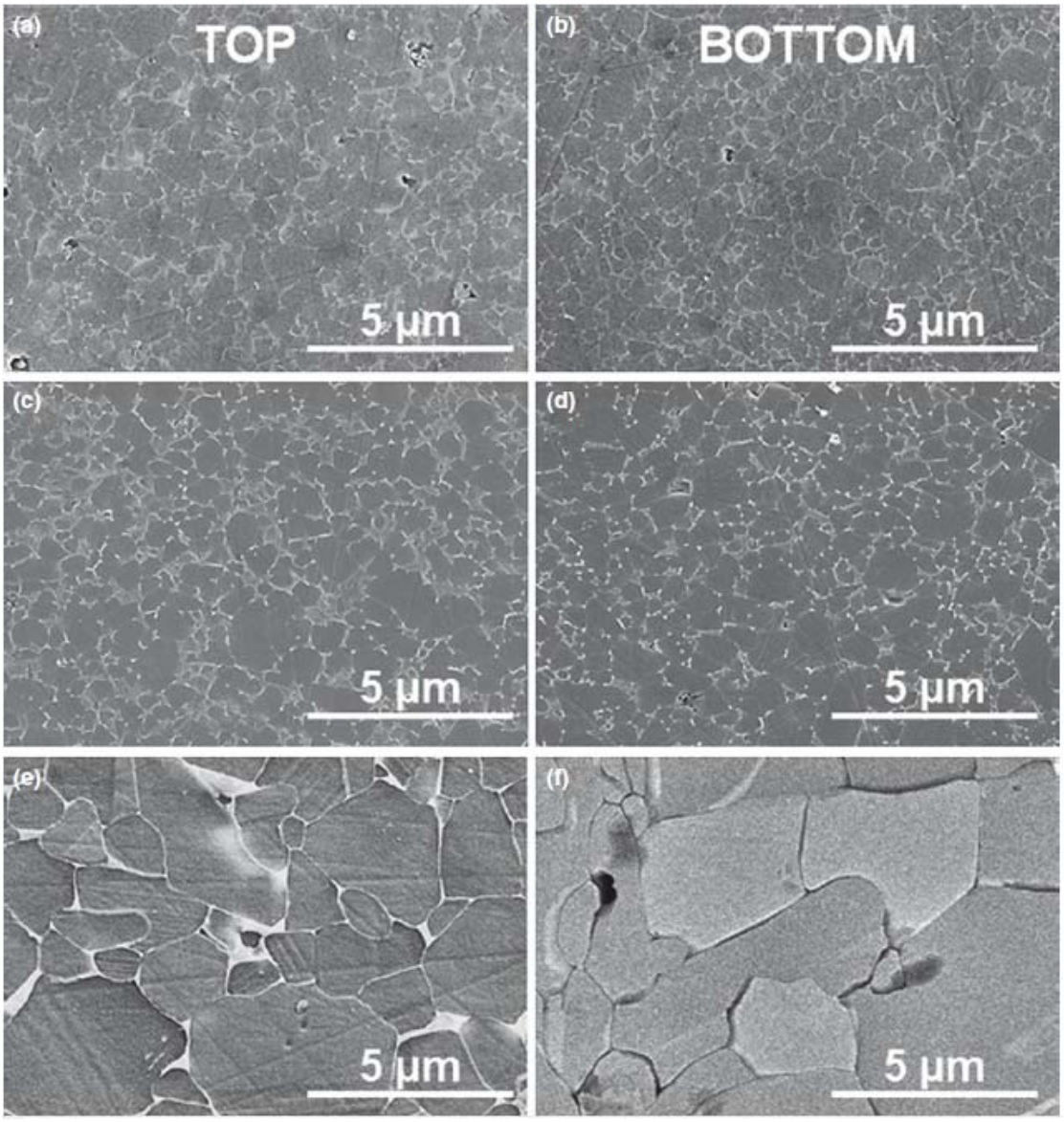

Figure 3.19.- FESEM micrographs at the top (a,c,e) and bottom (b,d,f) parts for SYM (a,b) and SYM-BN specimens SPSed at 1575 °C (c,d) and 1800 °C (e,f).

All these SiC materials show microstructures with mostly equiaxed SiC grains surrounded by a homogeneously distributed secondary phase (light gray color in the micrographs). Several statements can be drawn from these microstructures and their corresponding grain size and aspect ratio quantification (Fig. 3.20):

(i) grain size for SYM-BN specimen SPSed at 1800 °C (Fig. 3.19e,f) is up to six times coarser and contains a higher percentage, about 50%, of elongated grains (Aspect Ratio (AR) >> 1) than for SYM samples (Fig. 3.20a,b), which is linked to the higher real sintering temperature attained in the former material (i.e., ~2050 °C) that would promote grain growth;

(ii) the microstructure of the SYM-BN sample SPSed at 1575 °C (Fig. 3.19c,d) is very similar to that of SYM -similar grain size distributions and d_{50} and median AR (AR_{50}) values (0.53-0.61 μm and 1.5, respectively)- confirming that the assumed difference in real SPS temperatures of 225 ºC is correct;

(iii) SYM-BN specimen SPSed at 1800 °C exhibits a significant gradient in the axial direction in particular the bottom region shows coarser and longer grains (d_{50} = 3.86 μm, AR_{50} = 2.1) than the top one (d_{50} = 2.38 μm, AR_{50} = 1.5); conversely, the other two materials do not show relevant differences between both end regions,

(iv) the amount of grain-boundary phase decreases as grain size increases, especially at the bottom part of the SYM-BN specimen SPSed at 1800 °C. These observations are also confirmed by microstructure quantification, as shown by the grain size and aspect ratio cumulative area fraction distributions of Fig. 3.20, and the corresponding d_{50} and AR_{50} specified in Table 3.7.

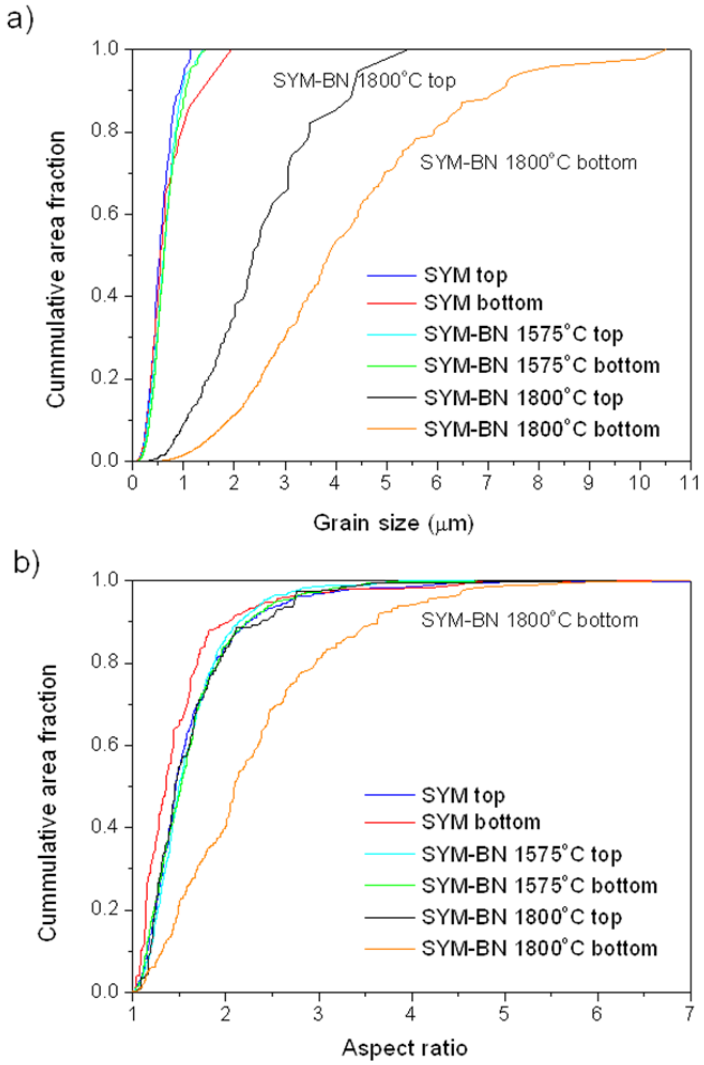

Figure 3.20. (a) Grain size and (b) aspect ratio cumulative area fraction plots for the SYM and SYM-BN specimens at the top and bottom regions.

Tabla 3.7.- Basic microstructural parameters and values for the elastic modulus (E), hardness (H), and toughness (K_{IC}) of the SYM and SYM-BN specimens SPSed at 1575°C and 1800°C. Data at the Top and Bottom regions are shown, obtained by Vickers indentation with applied loads of 50N.

SPS Set-up	T_{SPS} (ºC)	Sample region	d_{50} (μm)	AR_{50}	E (GPa)	H (GPa)	K_{IC} (MPa·m$^{1/2}$)
SYM	1800	Top	0.53	1.5	432 ± 17	20.7 ± 0.5	4.8 ± 0.2
		Bottom	0.54	1.4	430 ± 25	22.6 ± 0.7	4.7 ± 0.2
SYM-BN	1575	Top	0.61	1.5	409 ± 37	25.4 ± 1.3	4.2 ± 0.1
		Bottom	0.61	1.5	433 ± 25	27.5 ± 1.7	4.4 ± 0.2
SYM-BN	1800	Top	2.38	1.5	420 ± 18	19.0 ± 1.2	4.9 ± 0.2
		Bottom	3.86	2.1	437 ± 48	19.6 ± 0.8	5.4 ± 0.2

According to the XRD patterns shown in Fig. 3.21, the secondary phase only crystallized at the bottom of the SYM 1800 °C (Fig. 3.21a) and SYM-BN 1575 °C (Fig. 3.21b) specimens, as YAP or YAG in the former specimen and a mixture of YAP and YAM in the latter, which are the expected phases according to the formulated sintering additive composition.[27] Interestingly, SYM-BN SPSed at 1800 °C showed no crystalline secondary species at the bottom, probably due to the complete vaporization of SiO_x species at the high sintering temperatures attained (nominal value 1800 °C but real value of ~2050 °C) under pressures beneath the atmospheric (~6 Pa). Actually, the absence of that secondary phase surrounding SiC grains was confirmed by FESEM observations at the bottom part, just as shown in Fig. 3.19f. Besides, a low β→α-SiC transformation ratio was observed at both sides of the SYM sample at 1800 °C (Fig. 3.21a) and SYM-BN at 1575 °C (Fig. 3.21b) specimens, evidenced by the low intensity of the peaks ascribed to 6H and 4H polytypes of α-SiC phase in the XRD patterns. Conversely, the signal for these polytypes noticeably increased in the SYM-BN specimen SPSed at 1800 °C (Fig. 3.21c), especially at the bottom region with a considerable decrease in the intensity of the β-SiC phase peaks (3C polytype) and the occurrence of highly intense peaks mostly linked to the 4H-SiC polytype. The high degree of the β→α-SiC transformation and the huge volatilization of the secondary phase at the bottom part of the SYM-BN SPSed at 1800 °C specimen suggest a higher temperature in this zone.

Average Raman spectra taken at the bottom of the SYM and SYM-BN specimens (Fig. 3.22) established the presence of both cubic and hexagonal α-SiC polytypes, with Raman bands associated to the TO and LO vibrational modes. Although the identification of the different hexagonal polytypes was not possible due to the weak signal of the Raman bands, the SYM-BN specimen SPSed at 1800 °C showed larger contribution of the hexagonal phases due to the higher sintering temperature attained as well as a high level of doping; the latter was inferred from the spectrum of this specimen, as bands at 964.5 and 969.8 cm^{-1} of undoped α-SiC, corresponding to the axial and planar coupled modes, respectively, were broadened and slightly shifted to higher frequencies.[7] In addition, the three main D, G, and 2D characteristic peaks of graphitic species associated to the FLG sheets in-situ formed at the SiC grain boundaries during the SPS were clearly observed for SYM material. However, the formation of these FLG was considerably lower for current SYM-BN samples, especially for that SPSed at 1800 °C. In fact, the intensity ratio between the G peak and the most intense band of SiC (TO band at 796 cm^{-1}) for each spectrum, which approximately relates to the graphitic species content within these SiC ceramics, was

0.27 for the SYM specimen and nearly the half (0.15) for the SYM-BN SPSed at 1575°C. This ratio was negligible for the SYM-BN SPSed at 1800 °C.

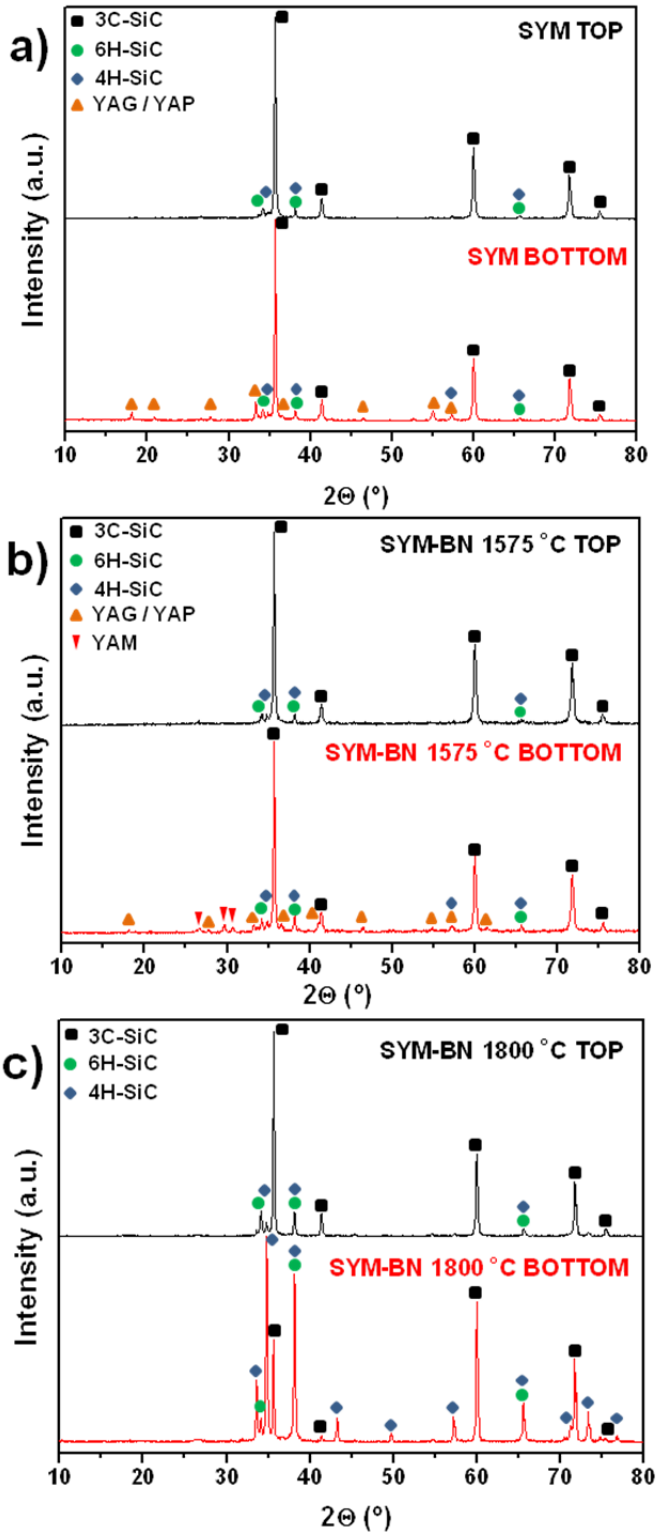

Figure 3.21.- XRD patterns recorded on the top and bottom regions of the SYM (a) and SYM-BN specimens SPSed at 1575°C (b) and 1800°C (c).

The content of FLG was estimated quantifying the relative number of pixels with highest intensity in Raman images constructed by mapping the intensity of the G band. As a result, a content of FLG ~0.6 vol.% was determined for the SYM-BN specimen SPSed at 1575 °C, in contrast to ~3.0 vol.% of the SYM one, calculated in the same way. The amount of the graphene domains was almost negligible for SYM-BN SPSed at 1800 °C. Therefore, the faster heating rate developed for the SYM-BN configuration limited the in-situ synthesis of graphene-like structures, and even vanished for the highest SPS temperature.

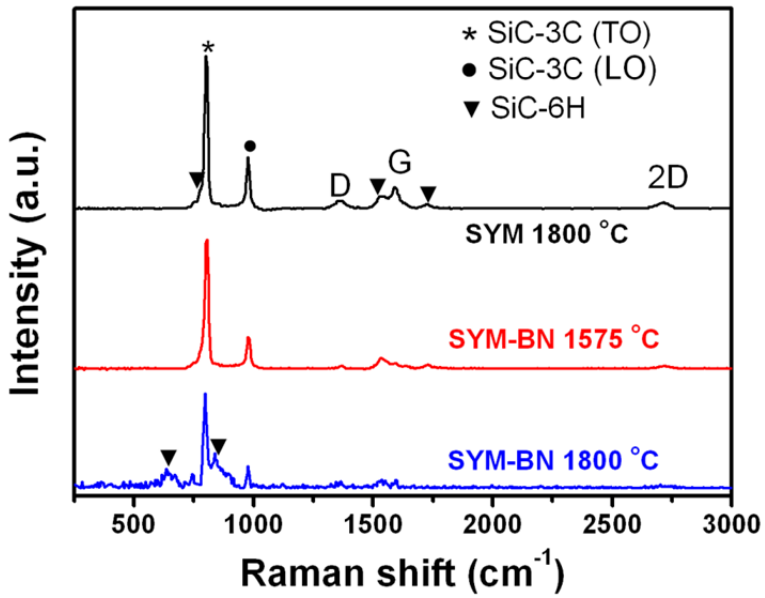

Figure 3.22.- Micro-Raman average spectra corresponding to the bottom region of the SYM and SYM-BN specimens. Conditions used: 60 x 60 pixels and one spectrum per pixel using 20 ms of acquisition time for each spectrum.

It has been proved that control of the silicon vapor density is essential for uniform growth of epitaxial graphene layers on SiC on both the Si- and the C-faces.[28] In this context, the rapid heating of the SiC powders in the SYM-BN assembly may increase the sublimation rate of silicon. Taking into account the real amount of graphene in the specimens, ρ_{th} and the corresponding relative density (ρ_{rel}) were recalculated for SYM-BN specimens SPSed at 1575 °C and 1800 °C, resulting in values of 3.27 and 3.28 $g \cdot cm^{-3}$, for ρ_{th} and 98.2% and 98.6% for ρ_{rel}, respectively; for comparison, the SYM material had a ρ_{th} of 3.24 $g \cdot cm^{-3}$ representing 99.9% of the theoretical density.

The observed coarser microstructure and the lack of secondary phases at the bottom part of the SYM-BN specimen sintered at 1800 °C can be explained by the thermoelectric character of SiC.[29,30] Computer simulations and experiments on highly p-doped silicon nanoparticles have clearly demonstrated that SPS is very sensitive to

the Peltier effect, which leads to a significant redistribution of heat within the sample during the densification with a higher temperature on the cathode side.[31] Considering that the SYM-BN specimen sintered at 1800 °C is highly doped (Fig. 3.22) probably by Al coming from the sintering additives (i.e., p-type), this sample could achieve during sintering much higher electrical conductivity than undoped SiC when reaching complete densification and doping, thus competing with the graphite foil path. This fact is confirmed by a further reduction in the system resistance (up to ~37%) above 600 s (~1700 °C in the sample) and up to 800 s (~2000 ºC) only observed for the SYM-BN assembly at set temperature of 1800 °C (Fig. 3.16c). In this way, the current across the specimen would be of same order of magnitude as the current measured (10^3 A) and, therefore, the current density (j) for the 20 mm diameter sample could then be calculated as ~3 x 10^2 A·cm^{-2}. On the other hand, the Seebeck coefficient (S) for SiC ceramics strongly depends on their doping level, significantly increasing with temperature,[29] with reported absolute values around 100 to 400 μV·K^{-1} at 1300 K. Considering this range of values for S, and being T = 2300 K (i.e., the real holding temperature) in this sample, the Peltier coefficient (Π =T·S) would vary between 0.2 and 0.9 V. The thermal power density ($\dot{q}$) can be then predicted, following a similar analysis to that proposed by Becker et al. for highly doped Si,[31] from $\dot{q}$ = Π · j, as ~60–270 W·cm^{-2}. This thermoelectric effect would cause extra-heating at the bottom part of the sample (cathode side). The temperature difference (∆T) between the top and bottom parts is then estimated as 50–225 K using the heat Fourier's law:

$$\dot{q} = -K_T \nabla T \rightarrow q_z = -K_T \frac{\Delta T}{\Delta z} \quad (2)$$

where ∆z is the sample thickness (2.5 mm in the present case) and K_T is the thermal conductivity of the specimen at 2300 K, assumed as 30 W·m^{-1}·K^{-1}, which is the conductivity of these type of materials at ~ 800 ºC (Chapter 5.1). The lack of secondary phases at the bottom part of the specimen can also be explained because this higher temperature favors partial volatilization of species from the grain-boundary phase.

As shown in Table 3.7, these distinct microstructural features affect the mechanical parameters. In this way, the hardest material was the SYM-BN specimen SPSed at 1575 °C, in particular at the bottom part (27.5 GPa), showing increments of 23-40% with respect to the other materials. On the other hand, the partial volatilization of the secondary phase that occurred in the SYM-BN specimen SPSed at 1800 °C would weaken the interface between the SiC grains (Fig. 3.19e,f) leading to the softest material. Furthermore, the presence of a larger amount of in-situ synthesized

graphene-like species in the SYM material (~3 vol.%), compared to SYM-BN SPSed at 1575 °C (~0.6 vol.%), would soften the first material too, as it has been widely reported in graphene/ceramic composites.[32,33] Finally, the slightly higher hardness at the bottom part of the specimens, particularly for the SYM-BN at 1575 °C, compared to the top region is due to the crystallization events in the secondary glassy phase that preferentially took place in the bottom side.

Regarding fracture toughness data, the highest K_{IC} values were attained at the bottom part of the SYM-BN specimen SPSed at 1800 °C (5.4 $MPa \cdot m^{1/2}$), which gave improvements of 15% and 22% with respect to the SYM and SYM-BN at 1575 °C, respectively, when comparing the same regions within the specimens. This enhancement was due to the coarser microstructure and elongated grains of SYM-BN specimen SPSed at 1800 °C (Table 3.7) that would induce toughening mechanisms such as bridging and deflection.[34] The slight K_{IC} gradient across this material (10%) should be linked to the observed variations of d_{50} and AR_{50}. Even though SYM and SYM-BN samples SPSed at 1575 °C exhibited similar features, K_{IC} values were higher for the SYM specimen (up to 14%). In this particular case, the existence of the graphene-like structures would produce additional bridging and pullout mechanisms.[35] Therefore, the mechanical characteristics of these SiC materials were controlled by several parameters: the crystalline character of the secondary phase, the SiC grain size, and the in-situ synthesis of graphene-like species.

3.2.- Bulk graphene/SiC composites

GNPs emerge as a natural filler candidate for SiC ceramics which, furthermore, would increase the electrical conductivity of these structural ceramics as a key factor for potential applications that require static charge dissipation or using the electro-discharge machining (EDM) technique.[36-38] Different GNPs/SiC composites were prepared with GNPs additions of 0, 5, 10, and 20 vol.% by following a similar method to that of monolithic SiC-based ceramic compositions (A.2.2). For the preparation of these composites, the GNPs were first dispersed in isopropyl alcohol in an ultrasonic bath. Meanwhile, a β-SiC ceramic slurry containing 7 wt.% of sintering additives was prepared (A.2.2). This slurry was mixed with the GNPs suspension and, then, stirred and sonicated for 1 h to obtain a homogeneous mixing of all components, followed by the solvent evaporation in a rotary-evaporator. Table 3.8 summarizes the starting composition for each GNPs/ceramic material.

The SPS process was identical to the case of SiC-based samples with no GNPs additions using a standard SPS setting, i.e. 1800 ºC for 5 min under vacuum atmosphere of ~4 Pa, and applying an uniaxial pressure of 50 MPa.

Table 3.8. Starting composition and microstructural characteristics of the prepared composites.

GNPs content (vol.%)	SiC:Y_2O_3:Al_2O_3:GNPs composition (wt.%)	ρ_{th} ($g \cdot cm^{-3}$)	ρ_{rel} (%)	d_{50} (μm)	AR_{50}
0	93 : 5 : 2 : 0	3.24	99.9	0.6	1.4
5	89.79 : 4.83 : 1.93 : 3.45	3.19	99.9	0.6	1.4
10	86.47 : 4.65 : 1.86 : 7.02	3.13	99.9	0.7	1.4
20	79.51 : 4.27 : 1.71 : 14.51	3.03	99.0	0.6	1.4

The theoretical density for the different materials was estimated from the values of the SiC matrix (3.24 $g \cdot cm^{-3}$ as the monolithic material) and the added GNPs (2.2 $g \cdot cm^{-3}$), which led to 3.19, 3.13 and 3.03 $g \cdot cm^{-3}$ for the composites containing 5, 10 and 20 vol.% GNPs, respectively (Table 3.8). Fully dense GNPs/SiC composites were obtained (Table 3.8), although the material containing 20 vol.% GNPs was somewhat less dense (99.0% ρ_{th}) due to the large GNPs network that partially hinders the densification of the matrix.

The observation of the fracture surfaces (Fig. 3.23) shows the homogeneous distribution of GNPs within the fine ceramic matrix, with no visible platelet agglomerates even in the case of the highest amount of GNPs (Fig. 3.23d). For the monolithic material, in-situ grown graphene flakes are detected with lateral sizes ranging from ~ 70 nm to 3 μm. In the case of the flakes with lateral sizes larger than the SiC grains (Fig. 3.23a), their main plane seems to be preferentially oriented along the plane perpendicular to the SPS pressing axis. This orientation is even more clearly observed for the added GNPs (Fig. 3.23b-d), and it is the natural consequence of their large size (between 5 and 10 times the grain size of the ceramic phase) and the application of uniaxial pressure. This effect has been previously reported for the closely related GNPs/Si_3N_4 composites.[39-40] The median SiC grain sizes of all the composites were in the range 0.6—0.7 μm (Table 3.8), with a median aspect ratio of ~1.4, which implies small grain growth during sintering as the raw powder had a median size of 0.5 μm (A.2.1).

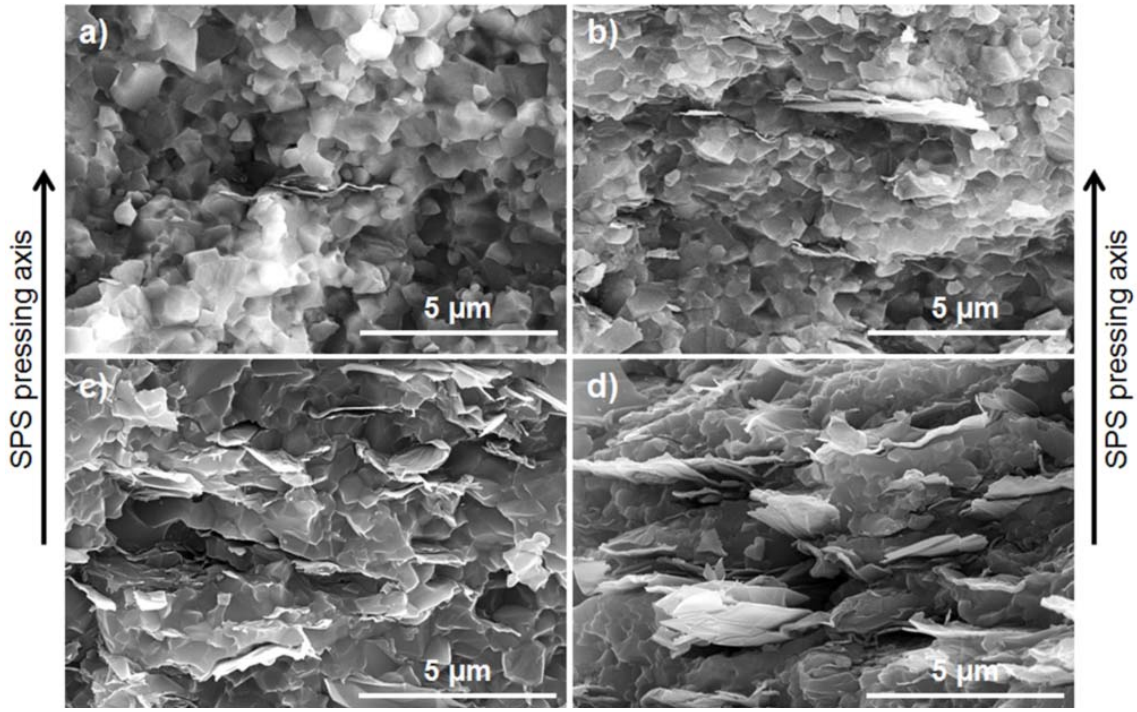

Figure 3.23.- FESEM micrographs of the fracture surfaces of the SiC-based composites containing GNPs additions: (a) 0 vol.%, (b) 5 vol.%, (c) 10 vol.% and (d) 20 vol.%.

XRD analyses (Fig. 3.24) confirmed that the 3C-SiC polytype was the majority phase in all materials, showing low intense peaks that could be clearly assigned to the polycrystalline 6H-SiC phase, and traces of the 4H-SiC phase. Therefore, only a slight degree of β → α-SiC transformation occurred due to the relatively low sintering temperatures and short sintering times. As the GNPs contents increased, the peak associated to graphite proportionally increased. Considering that the content of sintering additives (5 vol.% - or 7 wt.%) with respect to SiC remained constant for all composites, the total amounts of Al_2O_3 and Y_2O_3 ready to form YAG or YAP diminished as the GNPs content augmented in the composite, being ~4 vol.% (~6 wt.%) for the sample with 20 vol.% GNPs. As a consequence, the intensity of the XRD peaks associated to the secondary phase diminishes with the amount of GNPs.

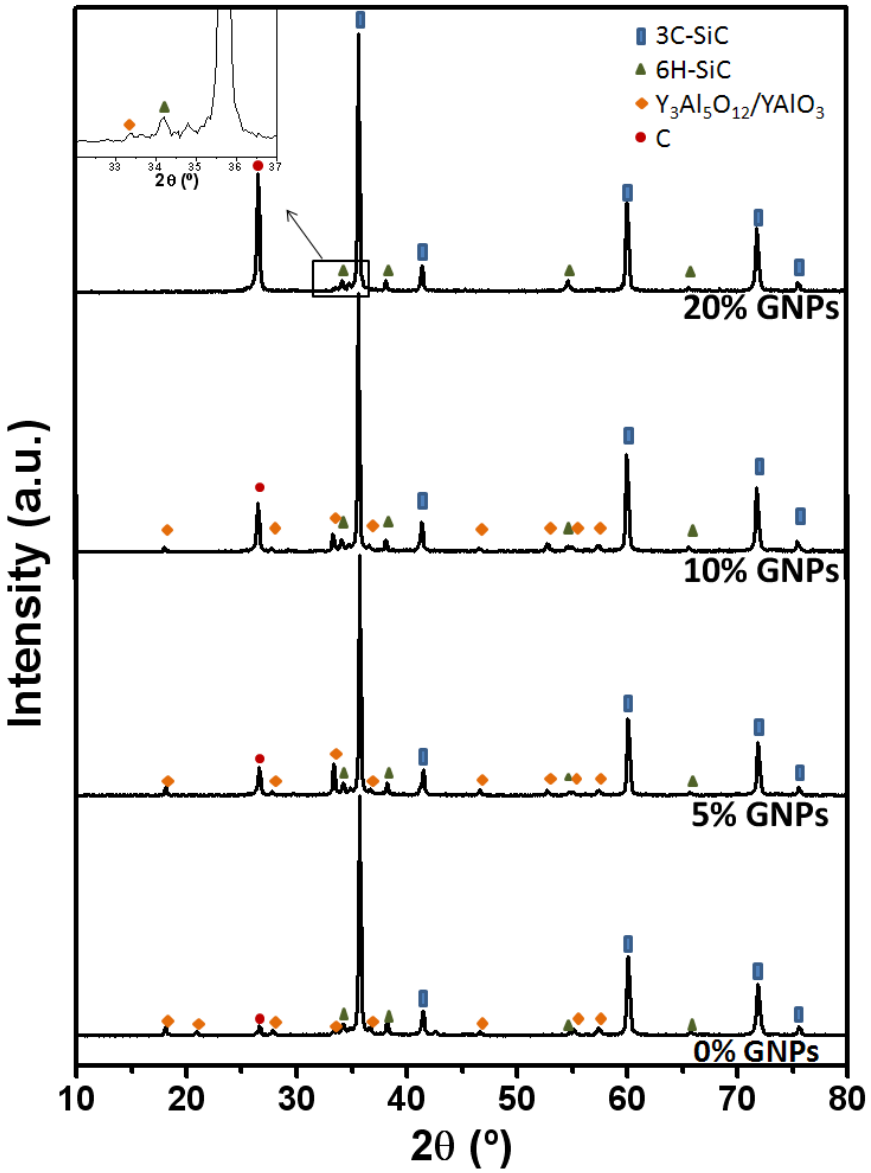

Figure 3.24.- XRD patterns of all the GNPs/SiC composites.

Average spectra collected over an area of 10 × 10 μm^2 of the polished surfaces of the various samples are shown in Fig. 3.25 Apart from the TO and LO bands associated to SiC, the D-, G- and 2D-bands corresponding to the graphite-like network can be clearly distinguished in the composites. The composites present a clear asymmetric 2D-band with FWHM in the range 81-86 cm^{-1} (Table 3.9), very similar to that of the pristine GNPs, deconvoluted into the D_1 and D_2 components (Fig. A.2.2). The slightly higher I_D/I_G ratio observed in the composites as compared to the pristine GNPs (in the 0.25-0.33 range vs. 0.21) seems to indicate that GNPs become slightly more defective after the processing and sintering steps (Table 3.9). The increase in the D-band in the composites may be also associated to a major contribution of the exposed platelets edges.[41] Nonetheless, GNPs still preserve very high structural quality after the SPS runs, comparable to that of the pristine state. The ratio I_{2D}/I_G is

kept between 0.9 and 1.1, which compared to 1.7 of the pristine GNPs (Fig. A.2.2) and confirms the graphene-like nature of these platelets. Moreover, the D-, G- and 2D-bands appeared in all composites at the same positions (1361 ± 2, 1592 ± 2 and 2716 ± 3 cm^{-1}, respectively). The slight blue-shift of the G-band position, as compared to multilayered graphene and graphite (in both cases centred at ~1587 cm^{-1}, see Table 3.9), can be attributed to a compressive strain induced during cooling by the SiC matrix on the basal *ab*-plane of the GNPs. This would be the result of the much higher thermal expansion coefficient of SiC (~4.9x10^{-6} K^{-1} from room temperature to 800 ºC)[42] than that for the ab plane of graphite or GNPs (~1x10^{-6} K^{-1} beween room temperature and 800 ºC).[43] It is noteworthy to mention that the thermal expansion coefficient of graphene and graphite in the *c* direction (~30x10^{-6} K^{-1}) is much higher than for the ab-plane, and higher than for pure SiC, inducing a tensile stress in the thickness direction, which does not affect the position of the G peak.

Table 3.9.- Averaged Raman data corresponding to the D-, G- and 2D-bands of graphene[8] of the 10 μm × 10 μm maps obtained on the polished surfaces of the composites, as well as that for the corresponding pristine GNPs.

GNPs content (vol.%)	**Center G (cm^{-1})**	**FWHM 2D (cm^{-1})**	**I_D/I_G**	**I_{2D}/I_G**
0	1592 ± 2	75 ± 6	0.58 ± 0.03	0.8 ± 0.1
5	1592 ± 2	83 ± 2	0.25 ± 0.03	0.9 ± 0.1
10	1592 ± 2	81 ± 1	0.29 ± 0.02	0.9 ± 0.1
20	1591 ± 3	86 ± 3	0.33 ± 0.04	1.1 ± 0.2
Pristine GNPs	1587 ± 2	77 ± 2	0.21 ± 0.02	1.7 ± 0.1

It should be noticed that graphitic peaks can also be seen in the Raman spectrum of the monolithic material without GNP additions, which correspond to the graphene flakes grown in-situ at the grain boundaries of SiC. Data in Table 3.9 suggest a narrower 2D-band for monolithic SiC than for the composites containing GNPs, which was associated to a turbostratic stacked epitaxial growth of graphene. Also, the highest I_D/I_G value of the monolithic materials (0.58) is explained by the smaller size of the formed graphene flakes, where the numerous edges greatly contribute to increase the intensity of the D-band.

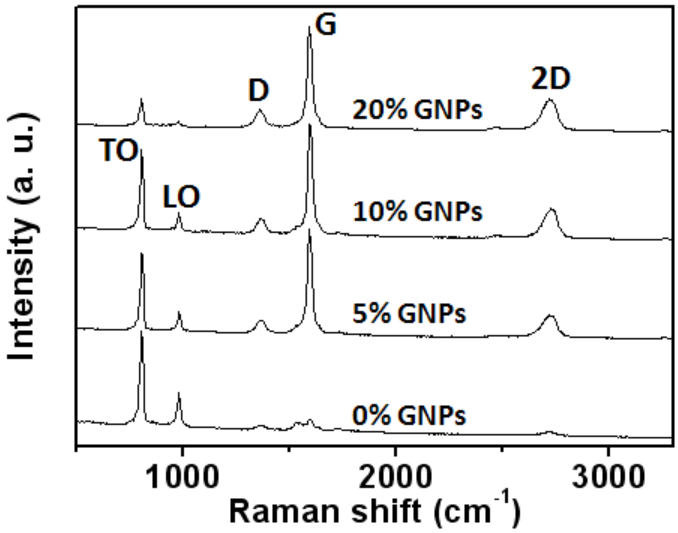

Figure 3.25.- Raman spectra of representative 10 × 10 μm^2 surface regions of the different composites, calculated as the average of 60 × 60 pixels with an acquisition time of 20 ms each.

The differences between the Raman spectra of the in-situ grown graphene and the added GNPs are a helpful tool to elucidate the formation of graphene flakes by SiC decomposition also in the composites with added GNPs. By way of example, a Raman study performed for the composite with 20 vol.% GNPs is presented in Fig. 3.26. The false-colour Raman map shown in Fig. 3.26b (corresponding to the optical image in Fig. 3.26a) was constructed by merging maps of the integrated intensity of the 2D-band (~2710 cm^{-1}) of GNPs (red), its FWHM (yellow corresponds to the areas with narrowest peaks) and the intensity of the 796 cm^{-1} band of SiC (blue). Spectra representative of the three distinct coloured regions are given in Fig. 3.26c. The D-, G- and 2D-bands are observed even in the SiC regions (region 3), probably because of the higher Raman sensitivity of GNPs as compared to SiC. The narrow, single graphene 2D-band centred at ~2709 cm^{-1} appearing in the spectra collected in region 1 can be ascribed to the graphene formed in-situ (Fig. 3.26b). In contrast, the spectrum of the GNPs corresponding to the red region 2 can be deconvoluted into the D_1 and D_2 components (see Fig. 3.26d), with centres at 2699 and 2732 cm^{-1}, just as for pristine GNPs. The above results definitely confirm the in-situ formation of graphene by SiC decomposition also in the presence of added GNPs.

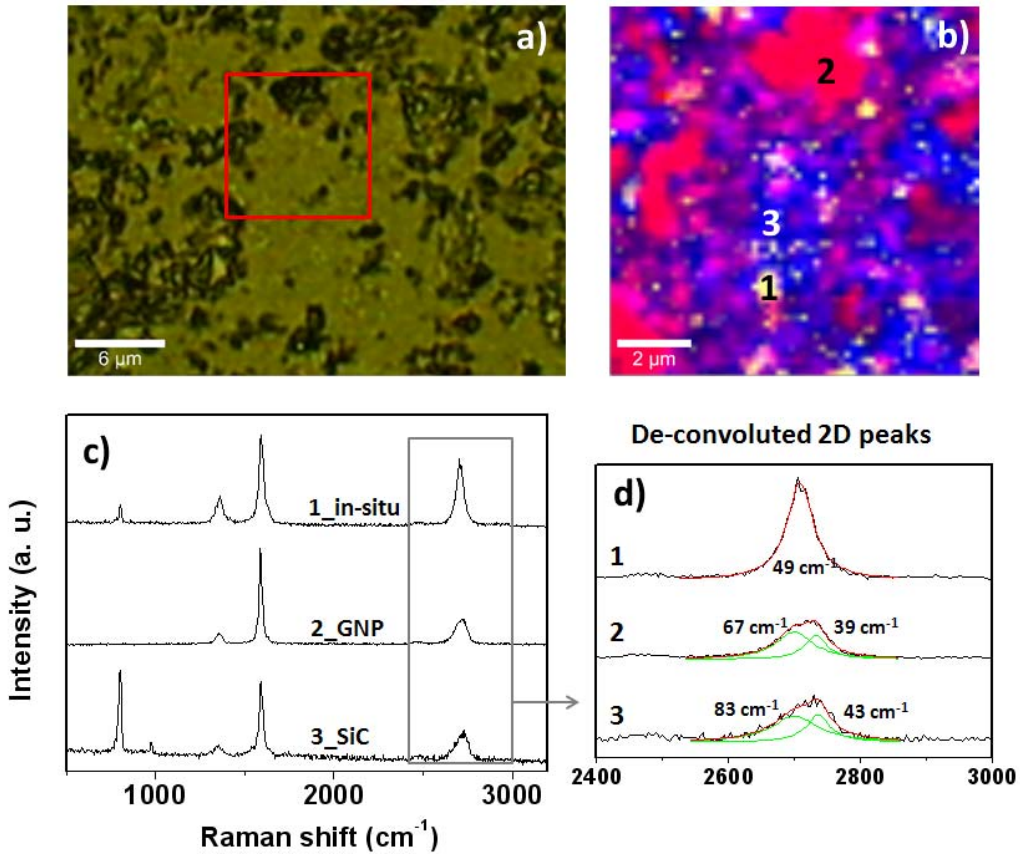

Figure 3.26.- (a) Optical image of a polished surface of a 20 vol.% GNPs/SiC and (b) false-colours Raman spectral image of the area marked in (a), constructed by merging the maps of the 2D-band intensity (~2710 cm^{-1}) of GNPs (red), its FWHM (yellow corresponds to the areas with narrowest peaks), and the intensity of the 796 cm^{-1} band of SiC (blue). (c) Single Raman spectra corresponding to areas marked with 1, 2 and 3 in (b) representing in-situ grown graphene, GNPs and SiC, respectively. (d) High magnification plot of the 2D-peak for the three spectra showing FWHM of each band from the corresponding fitting.

As for the mechanical properties, Table 3.10 collects the data for the different materials. Monolithic SiC exhibited higher *E* and *H* values than the composites, a trend previously observed in other graphene-based ceramic composites[33,44] that is related to the sliding of the graphene layers within the flakes under shear stresses, helped by the waviness of the platelets following the boundaries of the matrix grains (Fig. 3.23). Actually, both *E* and *H* decreased with increasing amounts of GNPs. K_{IC} is expected to increase for the graphene-based composites when compared to SiC due to the development of crack shielding mechanisms associated to the graphene flakes;[33] however, the development of multiple lateral cracks in Vickers scars for GNPs-containing composites and, most predominantly, for high graphene contents,

precludes K_{IC} determination by this method. Consequently, low loads (10N) were employed for the characterization of *E* and *H* to minimize this effect on the as-obtained data.

Table 3.10.- Elastic modulus (E) and hardness (H) obtained by Vickers indentation at 50N loads for the case of monolithic SiC, and at 10N for the composites.

Material	E (GPa)	H (GPa)
SiC	430 ± 25	22.6 ± 0.7
5 vol.%GNPs/SiC	310 ± 23	24.3 ± 2.1
10 vol.%GNPs/SiC	233 ± 38	14.8 ± 3.1
20 vol.%GNPs/SiC	120 ± 28	9.8 ± 1.1

3.3.- Robocast SiC-based ceramic scaffolds

SiC-based scaffolds with different patterned morphologies, as described in Chapter 2, have been formed by the Robocasting technique for β-SiC and nano-β-SiC and different amounts of sintering additives. The subsequent challenge towards the achievement of the final cellular materials was the densification of the as-produced structures.

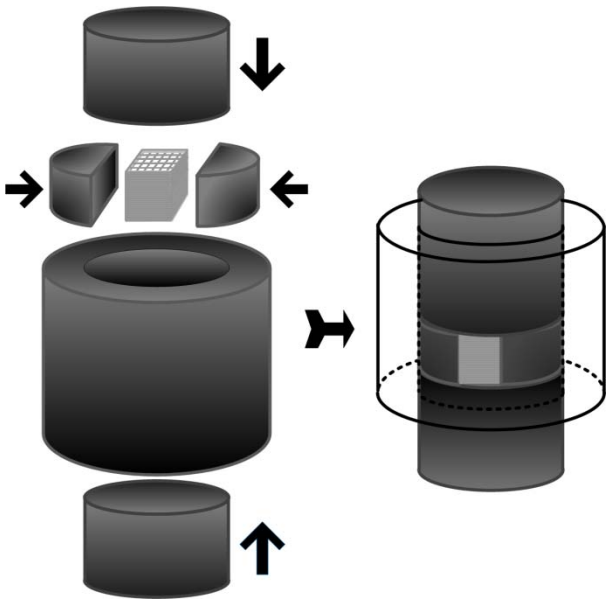

Figure 3.27.- Schematic illustration of graphite dies used in SPS process. Two graphite chocks with the same height of the sample are designed to stand the applied pressure.

An especial die assembly for the SPS was designed to enhance the sinterability of the SiC ceramic scaffolds assuring electrical contact with the punches but avoiding mechanical loads on the sample, thus preventing damage or cracking of the cellular specimens (Fig. 3.27). It should be pointed out that, once the specimen starts to shrink, the current flow through the sample is not assured as the close contact with the upper graphite die is lost. However, as shown farther on in this Chapter, this peculiarity did not affect the sintering as full-dense SiC skeletons can be produced.

SPS tests were done at different temperatures (in the range 1700-1800 ºC) using a similar heating rate ramp as described for bulk materials. In this particular case, an argon (Ar) atmosphere (P_{Ar} ~10 kPa) within the chamber of the SPS was chosen. The reason for dismissing the vacuum atmosphere was to avoid the SiC crystal growth on the rod surface in contact with the lower punch by a vaporization–condensation–recrystallization process. In Fig. 3.28, examples of these SiC crystals (typically hexagonal) grown when using vacuum are shown.

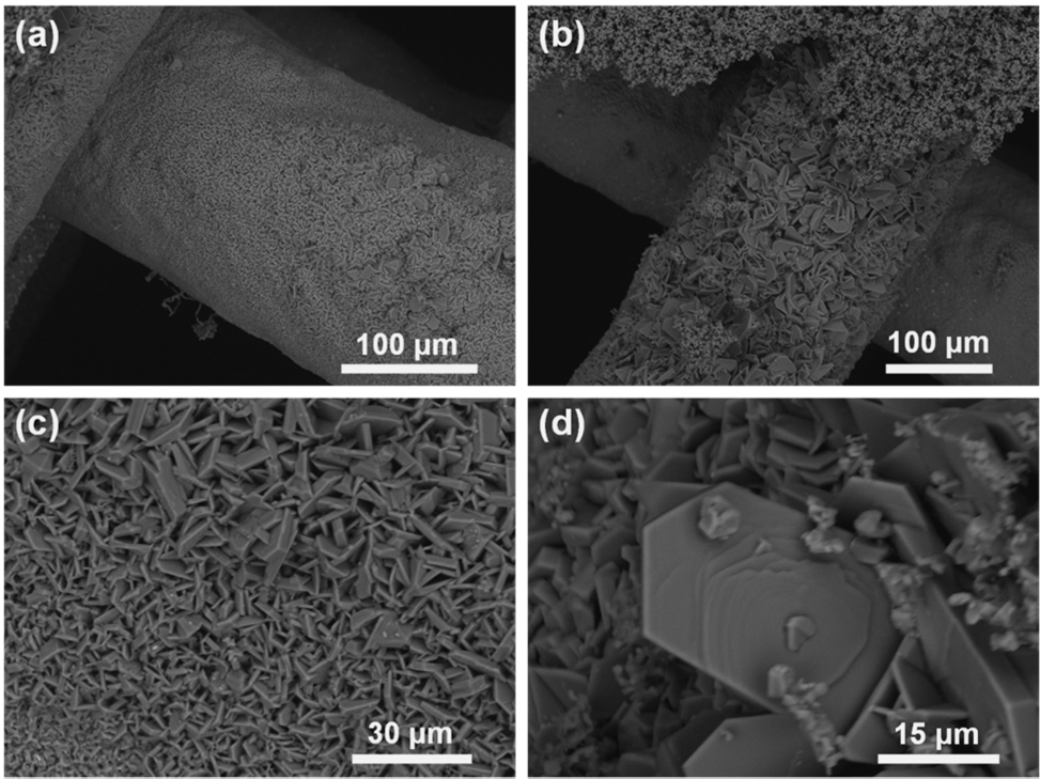

Figure 3.28.- (a-d) FESEM images at different magnifications of SiC crystals locally formed as a consequence of the vaporization–condensation–recrystallization of SiC onto the scaffolds rods in contact with the lower punch of a β20 sample SPSed at 1700 ºC in vacuum.

The SPS temperatures shown in Table 3.10 were selected based on the previous results obtained for the corresponding bulk materials. In this way, a temperature of 1700 ºC was chosen for the composition β20, and increased up to 1800 ºC for β7, according to a reduction in the sintering aids from 20 to 7 wt.%. In the case of the N20 structures, a temperature of 1750 ºC (50 ºC above that used for β20) was selected due to its lower degree of compaction associated to the lower solids loading of this ink. During the SPS process, the SiC scaffolds and the lattice rods experienced significant isotropic shrinkage (Table 3.10). Comparing lattices for the two compositions with similar amount of additives (20 wt.%), shrinkage was larger for the N20 (28%) than for the β20 (23%) scaffolds, due to the lower density in the green state of the former (the solids volume fraction of the corresponding inks was 0.32 and 0.44 for N20 and β20, respectively, as shown in Table 3.11). The smaller shrinkage observed for the β7 scaffolds (19%) compared to the β20 scaffold may be attributed to an insufficient amount of liquid phase formed during the sintering process, which would limit the full densification of the SiC skeleton under pressureless conditions.

Table 3.11.- Sintering parameters of the SPSed SiC scaffolds.

Material	**β20**	**N20**	**β7**
Sintering temperature (ºC)	1700	1750	1800
Linear shrinkage (%)	23	28	19
Apparent density ($g \cdot cm^{-3}$)	3.34	3.31	3.23
Weight loss (%)	8.4	11.6	11.1

As for the theoretical densities, the values for the β7 and β20 compositions were calculated by the rule of mixtures (3.29 and 3.44 $g \cdot cm^{-3}$, respectively) using the proportion of SiC and additives and their theoretical densities. By employing the water immersion method (in boiling water to eliminate bubbles), relative densities of 98-99% were obtained. It should be remarked that the water immersion method was not valuable for the estimation of apparent densities in the case of N20 scaffolds as open porosity was partially present. The porosity fraction measured on the SiC rods by image analysis results in values of 0.9, 1.6 and 9.5% for β20, β7 and N20, respectively. Despite the temperature raise (from 1700 to 1750 ºC) and the higher shrinkage of the N20 scaffold, the porosity level was by far the largest, which emphasizes the significance of achieving a high solids loading in the printing ink. During the SPS process, a weight loss (Table 3.11) of 8, 12 and 11 wt.% was measured for the β20, N20 and β7 scaffolds, respectively, which should be attributable to decomposition or volatilization processes of the more unstable ceramic

phases, since the organic additives present in the structures were eliminated in the pre-heat treatment in air at 600 ºC (with a weight loss of ~5.5 wt.%, as shown in Chapter 2). Actually, Si and Al were detected by EDX on the graphite wrapping in the furnace surrounding the samples, which implies some SiC and Al_2O_3 decomposition or volatilization during the SPS process, additionally confirmed by XRD patterns for these graphite wrappings showing the formation of α-SiC (6H polytype) on the inner surface. This volatilization, in the preliminary vacuum SPS tests, was larger.

As seen in Fig. 3.29, the sintering additives (bright phase in the images) are well distributed within the SiC matrix for the three compositions.

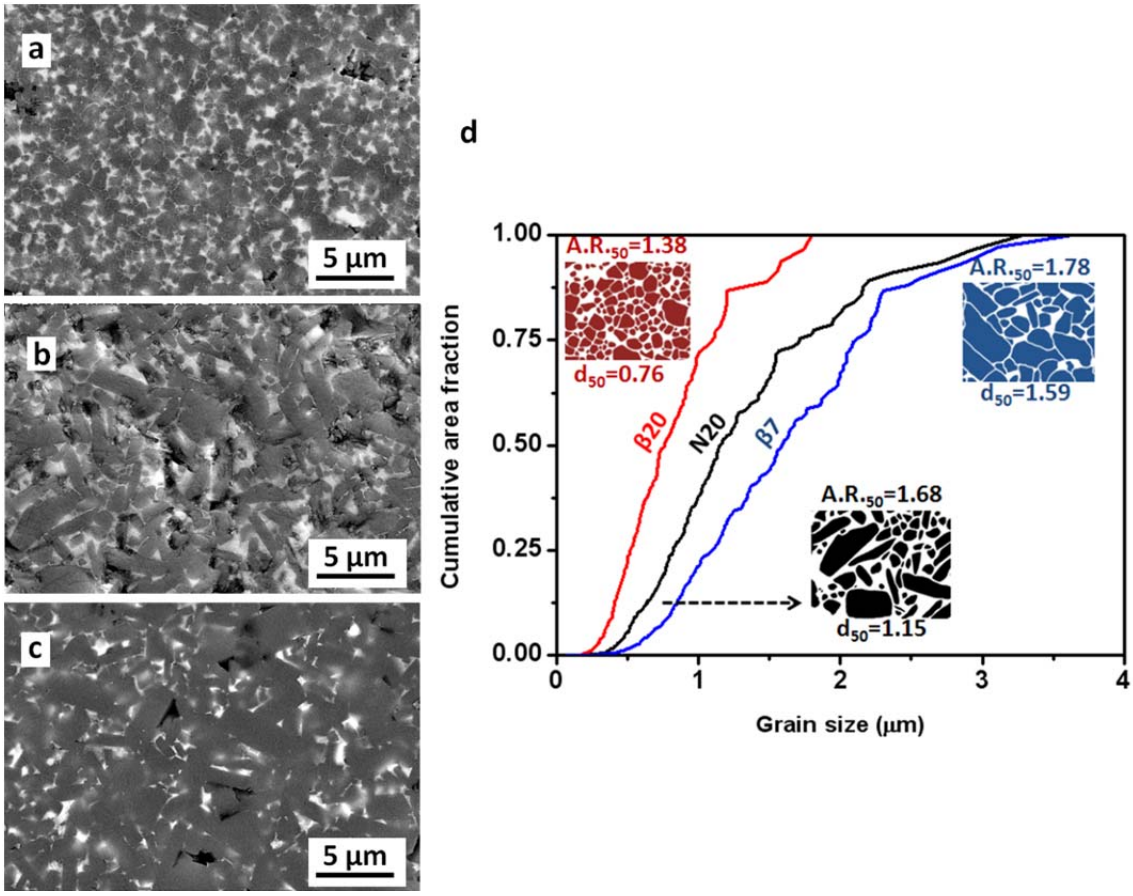

Figure 3.29.- FESEM micrographs of the polished and CF_4/O_2 plasma etched cross-sections of the sintered scaffold rods for (a) β20, (b) N20 and (c) β7. (d) Corresponding SiC cumulative grain size distributions measured by image analysis on FESEM images. The median grain size (d_{50}) and aspect ratio (AR_{50}) data are also included in the figure.

In this figure, important differences in the grain size are observed, which are mainly related to the SPS temperature, as expected. For the same amount of sintering additives, the quantitative image analysis confirms that the N20 scaffold have a

median grain size (1.15 μm) 1.5 times higher than that of β20 (0.76 μm), developing also more elongated SiC grains of AR_{50} = 1.68 as compared to 1.38 for β20 (as shown in Fig. 3.29d). This fact relates to the higher sintering temperature (1750 ºC versus 1700 ºC), as well as to the more reactive character and higher oxygen content of the nano-β-SiC powder that would lead to a faster sintering and grain growth kinetics. Finally, the highest grain size was observed in the rods of the β7 lattice (d_{50} = 1.59 μm and AR_{50} = 1.78), which was densified at the highest SPS temperature.

Comparing with a bulk SiC material of the same composition as β7 (Fig. 3.30), also densified by SPS at 1800 ºC in Ar under a uniaxial pressure of 50 MPa, the robocast specimens have significantly higher values (~3 and ~1.5 times higher for d_{50} and AR_{50}, respectively), which is an indication that the robocast specimens withstood temperatures above those measured by the controlling pyrometer.

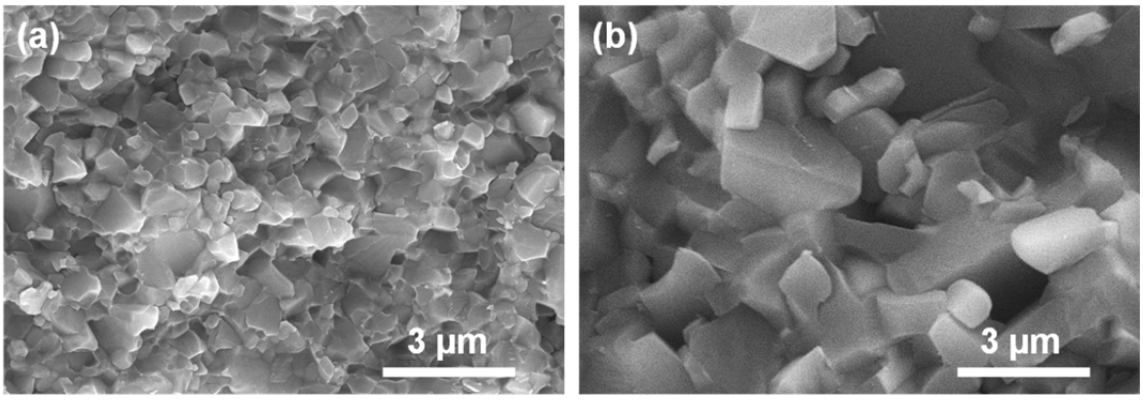

Figure 3.30.- FESEM images of the fracture surfaces: (a) a standard bulk β7 specimen, and (b) a β7 scaffold rod, both sintered at 1800 ºC.

As seen in Fig. 3.31, slightly higher electrical power was dissipated during the SPS tests in the case of robocast SiC (8.2 MJ by integrating on time) than in the runs of bulk SiC specimens of the β7 composition (7.6 MJ), both at 1800 ºC in Ar. Due to the macroporous nature of the scaffolds, radiation phenomena within the graphite chamber contribute to a faster self-heating of the lattice structure. These high temperatures directly should affect the crystalline phases formed in the SiC ceramic skeletons.

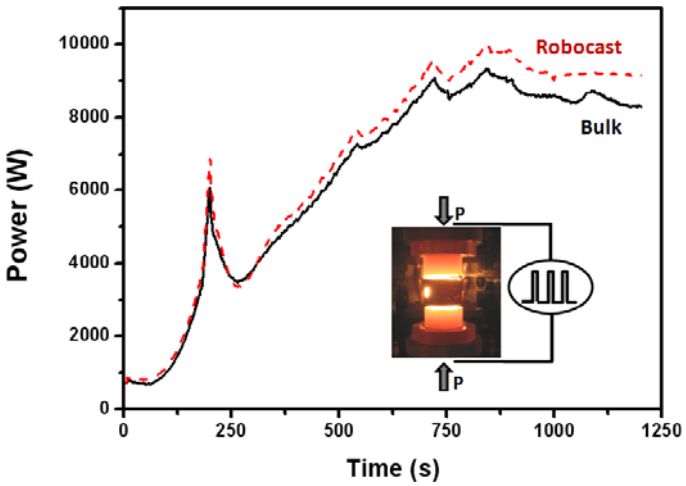

Figure 3.31.- Power versus time during SPS of a β7 bulk SiC and a β7 robocast specimen sintered in Ar at 1800 ºC.

In fact, whereas very low of degree of β→α-SiC phase transformation is observed for bulk materials sintered at 1800 ºC, the N20 and β7 scaffolds pressureless SPS at 1750 and 1800 ºC show high transformation (Figs. 3.32 and 3.33), with peaks associated to different hexagonal and rhombohedral polytypes, more stable at these high temperatures, as observed in Fig. 3.32a for a β7 specimen. A high transformation degree is also observed for the N20 samples, mainly showing 6H-SiC and 4H-SiC polytypes (Fig. 3.33a). The elongation of grains taking place for the N20 sample is clearly observed in the Raman map (Fig. 3.33b), where the SiC grains are depicted as the blue features. Raman spectra for SiC in the two specimens also show the high level of doping of SiC scaffolds owing to the absence of the LO-band of SiC. Secondary phases and additional peaks ascribed to a cubic aluminum yttrium carbide phase were detected in the β7 specimen, and the YAM phase in both β7 and N20. The presence of such high-temperature-related phases was confirmed by Raman spectroscopy. As shown in Figs. 3.32b and 3.33b, three different phases are observed in Raman images constructed by mapping the intensity of the 796 cm^{-1} band of SiC, the G-band at 1575 cm^{-1} of any carbonaceous species, and a 630 cm^{-1} band, which is ascribed to either the $AlY_3C_{0.5}$ reaction product or $YAlO_3$, according to the XRD pattern. The spectra at the position where maximum intensity of each of these bands is recorded are also shown in the Figs. 3.32c and 3.33c. The high temperatures developed during SPS of robocast specimens then favor grain growth and SiC decomposition, and the reaction of carbon with the sintering additives.

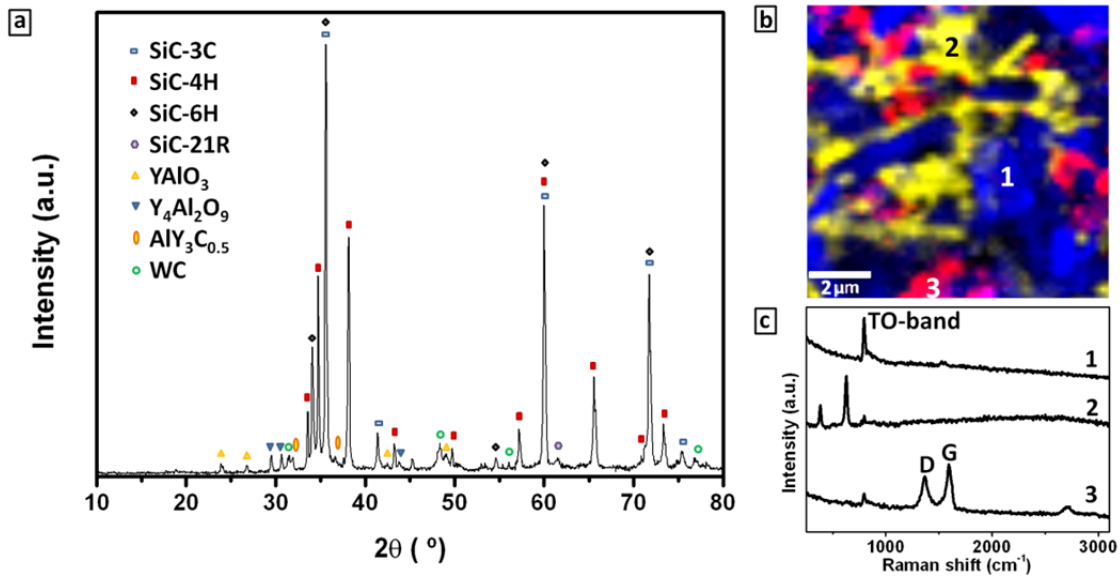

Figure 3.32.- Analysis of the crystalline phases in the β7 robocast specimen: (a) XRD pattern of a powdered specimen (WC contamination comes from the mechanical miller); (b) Raman image (in false colours) constructed by mapping the intensity of the 796 cm^{-1} band of SiC (1), the 630 cm^{-1} band of the grain boundary phases, either $AlY_3C_{0.5}$ or $YAlO_3$ (2) and the G-band at 1575 cm^{-1} of carbonaceous species (3); and (c) single spectra of each of these phases marked with numbers on the map.

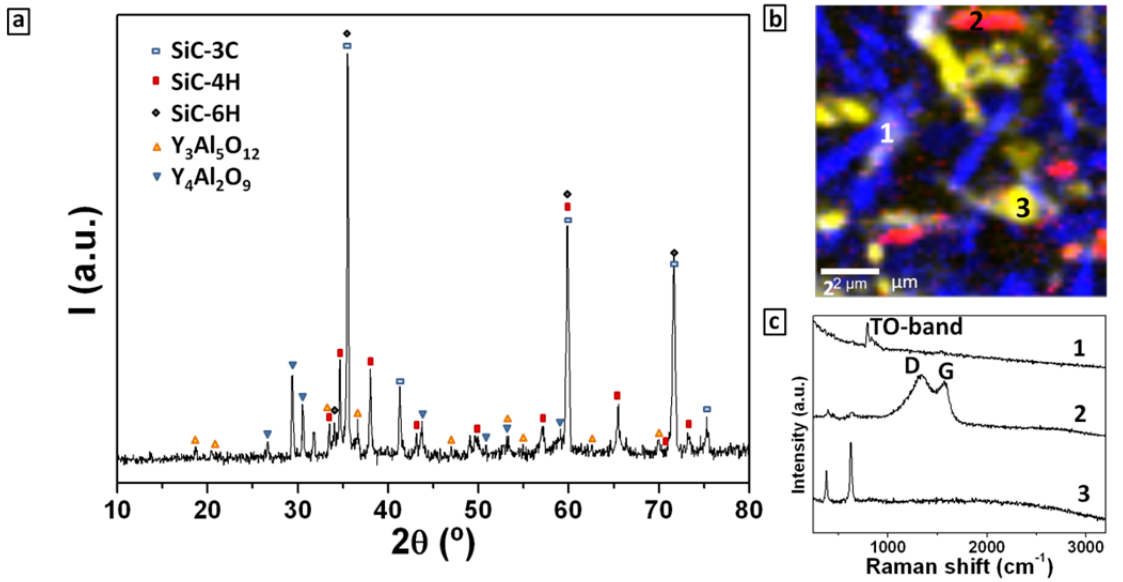

Figure 3.33.- Analysis of the crystalline phases in the N20 robocast specimen: (a) XRD pattern of a powdered specimen. (b) Raman image (in false colours) constructed by mapping the intensity of the 796 cm^{-1} band of SiC (1), the G-band at 1575 cm^{-1} of carbonaceous species (2) and the 630 cm^{-1} band of the grain boundary phases, either $AlY_3C_{0.5}$ or $YAlO_3$ (3); and (c) single spectra of each of these phases marked with numbers on the map.

For a mechanical characterization on hardness and elastic modulus at room temperature, a depth sensing indentation method with a Vickers pyramidal indenter at two different loads (0.5 and 10 N) was employed on the polished cross sections of the SiC rods forming the scaffolds (see example in Fig. 3.34a) after being embedded in a resin. The loading-unloading curves of the force vs. indentation depth at 10 N for β7 and β20 samples are shown in Fig. 3.34b, demonstrating the more compliant behavior of the latter due to its higher content of sintering additives and smaller grain size. As shown in the Table 3.12, E of the β20 and N20 rods were lower than that for β7 rods (exhibiting ~13-17% increase), at both of the tested loads, thus enabling to produce SiC scaffolds with tailored stiffness by varying the amount of sintering aids. It should be noted that the elastic modulus values at 10 N were significantly lower than those measured at 0.5 N for all the scaffolds.

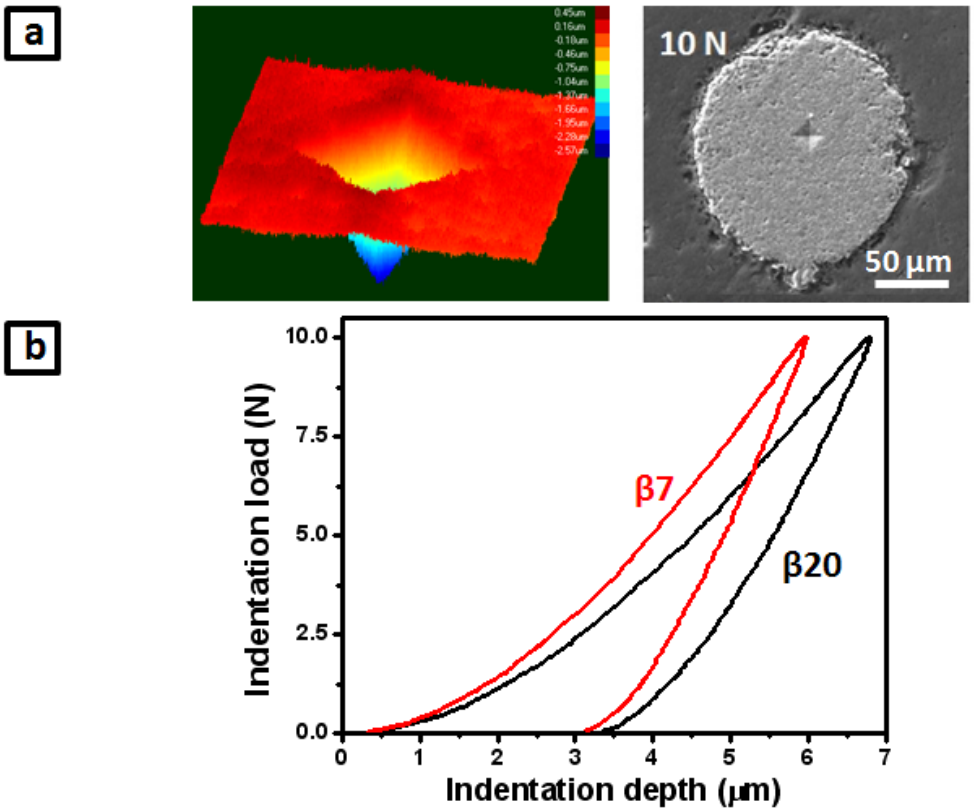

Figure 3.34.- (a) 3D profilometry plot and FESEM image of a 10 N indentation performed on the cross section of a rod belonging to N20 skeleton. (b) Indentation load vs. depth of two representative 10 N indentations on β7 and β20 structures.

Table 3.12.- Summary of the values for elastic modulus (E) and hardness (H) of the three different SiC ceramic materials.

Material	E (GPa)		H (GPa)	
	10 N	0.5 N	10 N	0.5 N
β20	194 ± 25	315 ± 26	20.8 ± 0.5	22.9 ± 2.2
N20	200 ± 29	299 ± 23	19.8 ± 0.9	22.3 ± 3.1
β7	245 ± 16	360 ± 17	21.9 ± 1.3	24.6 ± 2.9

Conversely, the E value observed in the case of the β7 bulk specimen (406 ± 13 GPa) at 0.5 N is similar to that reported for higher indentation loads (430 ± 25 GPa, as shown in Chapter 4). A possible explanation for this may be related to the compliance of the resin in which the specimens are embedded for the indentation tests, which is especially remarkable for the robocast rods of ~220 μm diameter than for the larger bulk specimens (3 mm x 20 mm). Therefore, more realistic E values for robocast rods are those measured using 0.5 N, which are around 300 GPa for 20 wt.% additives and 360 GPa for 7 wt.%. The lower E value of the β7 scaffold as compared to that of the bulk β7 specimen (360 vs 406 GPa) may be partially due to its small remaining porosity and the observed differences in crystalline phases. Data for the averaged hardness of the different SiC rods is also reported for both of the indentation loads used. H values were slightly lower for the N20 and β20 than for the β7 scaffolds, clearly associated to their higher amount of sintering additives. All of them are in the range of ~ 20–22 GPa for 10 N and, as it could be expected, they are slightly higher (22.3-24.6 GPa) for 0.5 N (Table 3.12). The H value measured at low loads (0.5 N) for β7 scaffold is again lower than that of the bulk β7 (29.6 ± 0.7 GPa), because of differences in porosity and crystalline phases.

3.4.- Robocast graphene/SiC composite scaffolds

Graphene/SiC scaffolds (consisting in amounts of 5, 10 and 20 vol.% GNPs using the β7 composition for the ceramic matrix) were pressureless SPSed at 1800 °C for 5 min, in an Ar atmosphere of ~ 10 kPa, with the same sintering conditions as for the standard β7 scaffolds.

The water immersion method has not been valid for the density measurements of these cellular ceramic composites due to the elevated porosity of the skeletons. Consequently, the relative linear shrinkage data ($\Delta L/Lo$) of the structures during

sintering, averaged over the three respective spatial dimensions, and the green densities (ρ_{green}), have been used to estimate the density of the ceramic skeletons:

$$\rho = \rho_{green}/(1-\frac{\Delta L}{L_o})^3 \quad (3)$$

The same green density was assumed for all the rods of each scaffold, estimated as 47% from Eq. (3) considering a porosity value of 1.6 vol.% for the sintered GNPs-free SiC-skeleton from the image analysis. The porosity of the skeletons was then estimated using the corresponding ρ_{th} of each composite, in particular, 3.24, 3.19, 3.13 and 3.03 g·cm^{-3} for 0, 5, 10 and 20 vol.% of GNPs, respectively. The maximum relative shrinkage during sintering steadily decreases with the GNPs content, from 22% for the monolithic SiC scaffold to just 5% in the 20 vol.% GNPs/SiC scaffold (as shown in Fig. 3.35a) and, in parallel, the porosity content in the skeletons increases from 1.6% for the monolithic SiC to 43% for the composite containing 20 vol.% GNPs (Fig. 3.35b). This reduced densification, typical of bimodal sintering, is due to the development of sintering backstresses within the compact as a consequence of the presence of the non-sinterable GNPs fillers.

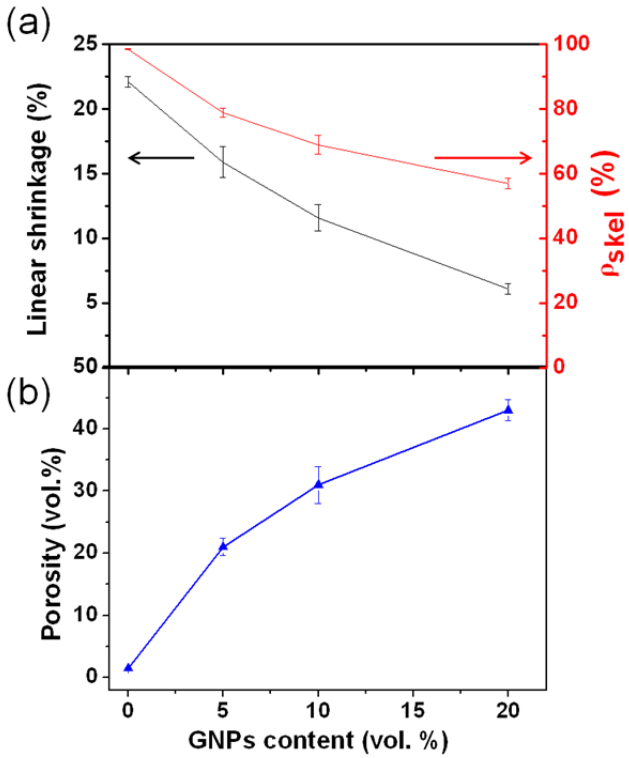

Figure 3.35.- (a) Linear shrinkage of structures upon sintering as a function of the GNPs content, estimated from their length change averaged over the three spatial dimensions and the corresponding relative density of the ceramic skeleton estimated from Eq. (3). (b) Porosity of the ceramic skeletons versus graphene content.

There is a clear preferential orientation of the GNPs within the rods (Fig. 3.36), where the platelets protrude (white arrows in Fig. 3.36) with the GNPs plane parallel oriented to the rod axis.

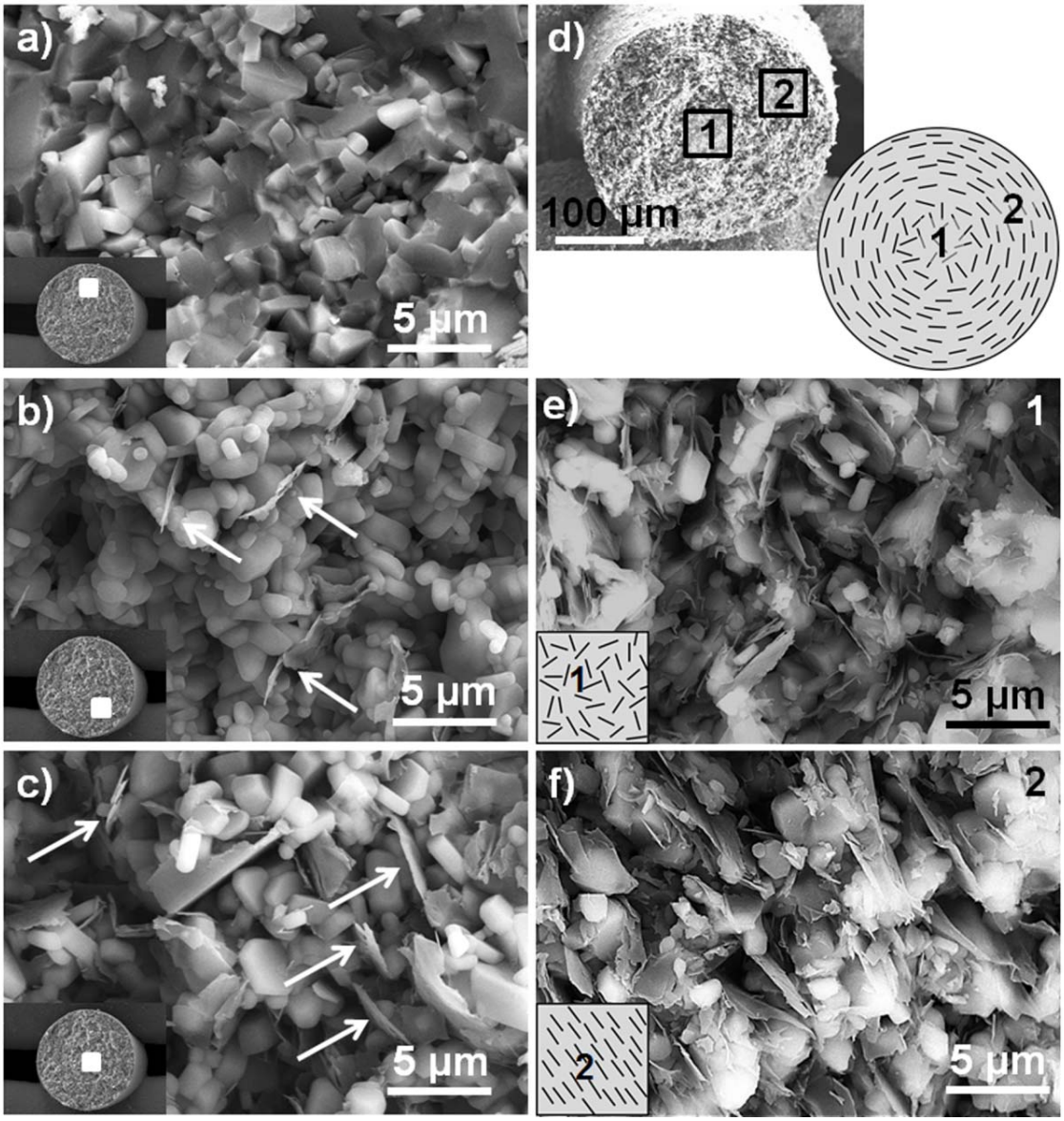

Figure 3.36.- Representative FESEM micrographs of the fracture surfaces of sintered rods belonging to GNPs/SiC cellular composites containing a) 0, b) 5 and c) 10 vol.% GNPs (indicated by white arrows). The white dots on the insets mark the observation area for the high magnification images. d) FESEM micrograph of the fracture surface of a sintered rod in the 20 vol.% GNPs cellular composite with a schematic illustration of the core-shell structure of GNPs. e) and f) Higher magnification images of the areas marked in d) with numbers 1 and 2, respectively. The insets in e) and f) show illustrations of the GNPs distribution in different zones of the rod.

A remarkable core/shell structure is perceived in the rod transverse plane, where the GNPs exhibit parallel alignment with the rod outer cylindrical wall along the rod shell, (Fig. 3.36f) whereas a random radial orientation is observed in the rod core (Fig. 3.36e). The shear thinning behavior of the inks and the radially varying shear stress lead to the occurrence of a slip layer, a yielded shell and a solid core,[45] thus inducing the GNPs self-orientation along the extrusion direction in the yielded shell by reproducing the ink fluxes during extrusion.

A representative example of the micro-Raman spectroscopy analysis is presented in Fig. 3.37 for the scaffold with 10 vol.% GNPs. Two spectra are detected in the SiC matrix, labeled as 1 and 2 in Fig. 3.37c and attributed to undoped and doped SiC, respectively. Undoped SiC plainly exhibits the most characteristic vibrational optical modes of the crystalline lattice, namely TO and LO bands, whereas the LO mode disappears in highly doped-SiC and the TO mode is overlapped with a characteristic shoulder at Raman shifts above 800 cm^{-1}. As shown in the Raman image of Fig. 3.37b, most of the SiC grains are doped probably because of the high temperatures reached during sintering in the SPS furnace (at least 100 °C above the set point temperature based on the SiC grain sizes), which destabilizes the Al_2O_3 additive into Al atoms that dissolve into the SiC lattice.[46] Another phase showing three distinctive Raman bands at 128, 378 and 632 cm^{-1} is detected –see spectrum 3 in Fig. 3.37c- with a minor presence as shown in the Raman map of Fig. 3.37b, which is tentatively ascribed to either $AlY_3C_{0.5}$ or $YAlO_3$ according to the XRD results (Fig. 3.38).

Apart from the spectra associated to the ceramic matrix phases, three distinct carbonaceous-related spectra were recorded as well. The first corresponds to the characteristic spectrum of graphene/graphite clearly showing the D-, G- and 2D-bands (number 4 in Fig. 3.37d). The other two spectra marked as 5 and 6 in Fig. 3.37d appear sparsely distributed in the Raman maps. Spectrum 5 presents the typical ethylenic band with peak at 1503 cm^{-1} and a band in the C-C fingerprint region peaked at 1127 cm^{-1}.[47] Spectrum 6 is due to amorphous carbon. These two spectra are observed in all the samples and therefore should be associated to organic residues left within the structures by the polymeric additives used for the ink formulations (~1 wt.% according to the TG analysis, as shown in Fig. 2.27).

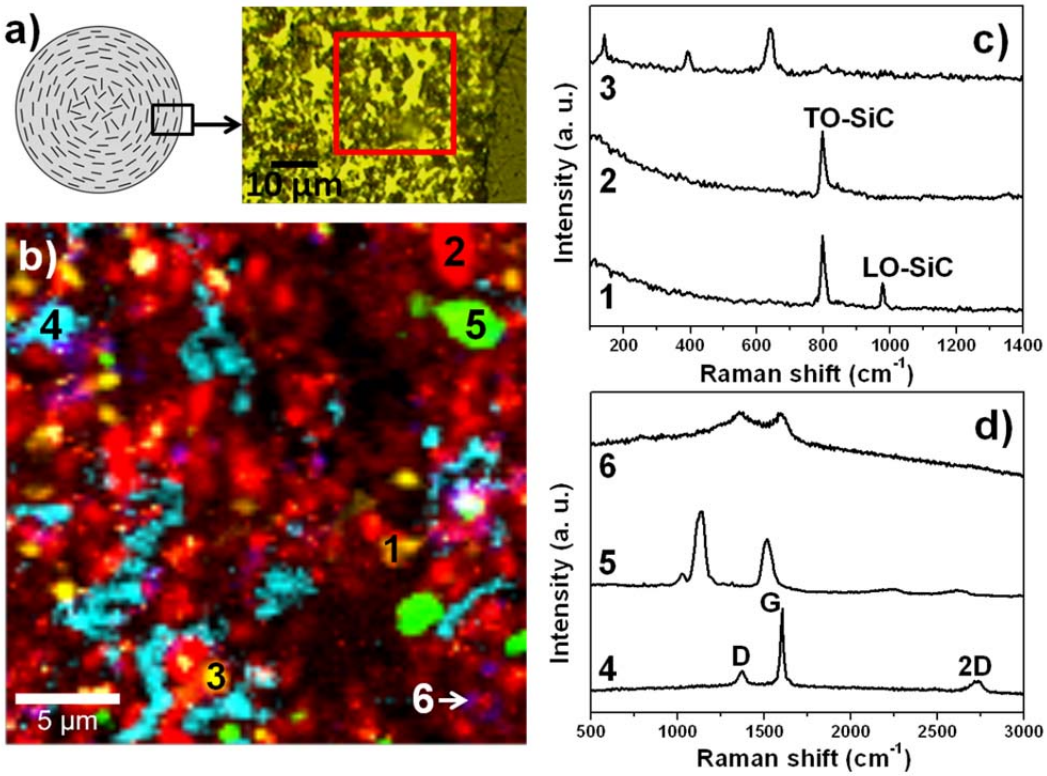

Figure 3.37.- (a) Optical image of a polished surface of the graphene/SiC scaffold with 10 vol.% GNPs, (b) false-color image of the area marked in (a) constructed by merging six individual intensity maps of different Raman bands associated to the single spectra shown in c) and d): 1) orange, the 978 cm^{-1} band of SiC (LO-SiC); 2) red, the 796 cm^{-1} band of SiC (TO-SiC); 3) yellow, the 628 cm^{-1} band of the grain boundary phase; 4) light blue, the 2D band (~2716 cm^{-1}) of GNPs; 5) green, the 1136 cm^{-1} band of the remaining organic phase; 6) purple, the D band (~1359 cm^{-1}) of amorphous carbon.

The spectrum 4 in Fig. 3.37d presents a slight blue-shift in the position of the G-band of graphene and graphite from 1587 to 1590 cm^{-1}. A similar shift was also observed for bulk GNPs/SiC materials (Table 3.9), and would indicate the development of a compressive strain on the basal ab-plane of the platelets induced by the surrounding ceramic matrix. The intensity ratio of the D and G bands (I_D/I_G) decreases with increasing GNPs content (I_D/I_G = 0.84, 0.67 and 0.31 for 5, 10 and 20 vol.% GNPs, respectively), in all cases higher than that for the pristine GNPs (I_D/I_G = 0.21). This may be explained by the fact that those Raman maps were recorded on the rod cross-sections where there is a higher contribution of the more defective GNPs edges,[48] even though some contribution of the amorphous carbon to the intensity of the D-band in spectrum 4 cannot be disregarded.

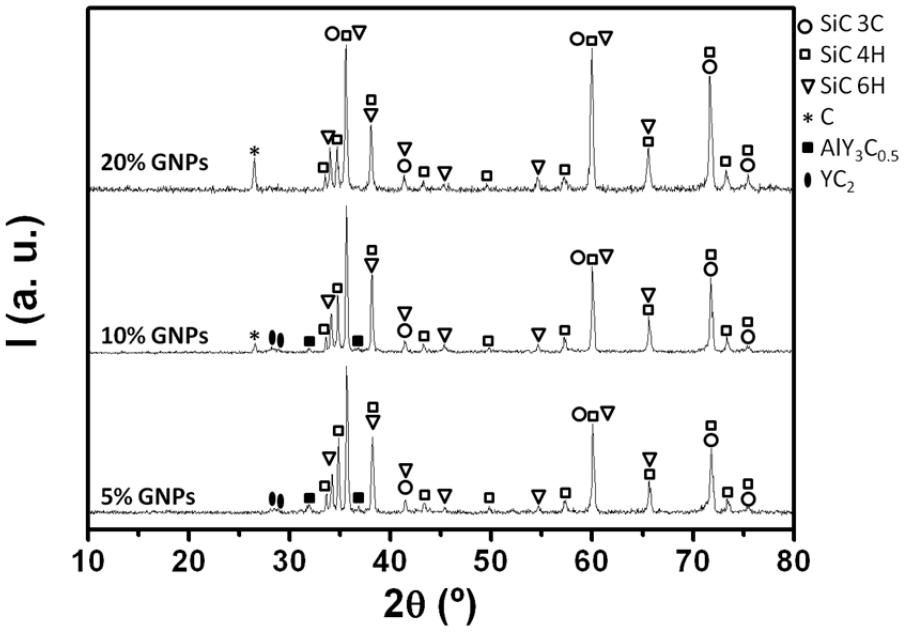

Figure 3.38.- XRD patterns of the robocast GNPs/SiC composites. The starting 3C-SiC powders, as well as transformed 4H- and 6H-SiC polytypes were detected, evidently affected by the high temperatures of the SPS process. Secondary phases were tentatively ascribed to $AlY_3C_{0.5}$ and YC_2.

3.5.- Conclusions

i) Dense SiC-based bulk ceramics with very different microstructures, containing 3-4 vol.% of well dispersed graphene flakes in–situ grown at the grain boundaries, can be fabricated by SPS at temperatures of as low as 1800 ºC using SiC powders with different grain size and polytypes.

ii) The mechanism for the in-situ formation of graphene flakes during the SiC densification is proposed to be due to the simultaneous actions of the high temperature, the electric current passing through the graphite dies and specimen and the partial vacuum, all of them involved in the SPS process.

iii) The use of an electrically insulating coating of BN on the inner surface of the graphite die induces the current confinement, which enhances the shrinkage rate of the SiC materials due to localized dissipation of heat, and prompts the full densification at shorter times than those required for the standard SPS set-up, with

energy savings of up to 60% when compared to the standard SPS cycle. The use of thick BN coatings makes the SPS process more energetically profitable and has been proved a fast and effective method for the densification of SiC-based ceramics.

iv) The mechanical characteristics of SPSed SiC materials are controlled by the crystalline character of the secondary phase, the SiC grain size, and the in-situ synthesis of graphene-like species.

v) Dense and homogeneous GNPs/SiC composites with up to 20 vol.% GNPs additions can be fabricated by SPS preserving the structural integrity of graphene. The uniaxial pressure applied during SPS and the large size of the GNPs as compared to the SiC grains resulted in a major orientation of GNPs in the plane perpendicular to the pressing axis.

vi) Robocast structures have successfully been pressureless SPSed, retaining in all cases the shapes of the extruded filaments and the overall geometry of the structures. In the case of GNP/SiC composites, robust and relatively lightweight (0.9 - 1.3 $g \cdot cm^{-3}$) 3D structures containing up to 20 vol.% of GNPs have been developed.

vii) Temperatures reached in the SPS graphite die tool during the pressureless SPS of the scaffolds seem to be above those measured by the controlling pyrometer, producing a noticeable SiC grain growth and causing reactions between SiC and sintering additives, when compared with bulk specimens sintered alike.

viii) The total shrinkage of the GNPs-free SiC structures depends on the size of starting SiC powders which affects the inks solid content and therefore the skeleton green density. That is not the case of the GNP/SiC structures where the presence of non-sinterable GNPs limits densification.

3.6.- References

1. Izhevskyi VA, Bressianiw AHA, Bressiani JC. Effect of Liquid Phase Sintering on Microstructure and Mechanical Properties of Yb_2O_3-AlN Containing SiC-Based Ceramics. J Am Ceram Soc 2005; 88(5): 1115–21.
2. Lee SK, Kim CH. Effects of a-SiC Versus b-SiC Starting Powders on Microstructure and Fracture Toughness of Sic Sintered With Al_2O_3-Y_2O_3 Additives. J Am Ceram Soc 1994; 77(6): 1655–8.

3. Cao JJ, MoberlyChen WJ, De Jonghe LC, Gilbert CJ, Ritchie RO. In Situ Toughened Silicon Carbide with Al-B-C Additions. J Am Ceram Soc 1996; 79(2): 461–9.
4. Nader M, Aldinger F, Hoffmann MJ. Influence of the a/b-SiC Phase Transformation on Microstructural Development and Mechanical Properties of Liquid Phase Sintered Silicon Carbide. J Mater Sci 1999; 34, 1197–204.
5. Kim YW, Mitomo M, Hirotsuru H. Microstructural Development of Silicon Carbide Containing Large Seed Grains. J Am Ceram Soc 1997; 80(1): 99–105.
6. Bondar IA, Galakhov FY. Phase equilibria in the system Y_2O_3-Al_2O_3-SiO_2. Russ Chem Bull 1964; 13(7): 1231-2.
7. Nakashima S, Harima H. Raman investigation of SiC polytypes. Physica status solidi (a) 1997; 162(1): 39-64.
8. Ferrari AC, Meyer JC, Scardaci V, Casiraghi C, Lazzeri M, Mauri F, Piscanec S, Jiang D, Novoselov KS, Roth S, Geim AK. Raman spectrum of graphene and graphene layers. Phys Rev Lett 2006; 97: 187401–4.
9. Lee DS, Riedl C, Krauss B, von Klitzing K, Starke U, Smet JH. Raman spectra of epitaxial graphene on SiC and of epitaxial graphene transferred to SiO_2. Nano Lett 2008; 8: 4320–5.
10. Yannopoulos SN, Siokou A, Nasikas NK, Dracopoulos V, Ravani F, Papatheodorou GN. CO_2-laser-induced growth of epitaxial graphene on 6H-SiC (0001). Adv Funct Mater 2012; 22: 113–20.
11. Faugeras C, Nerriere A, Potemski M, Mahmood A, Dujardin E, Berger C, de Heer WA. Few-layer graphene on SiC, pyrolytic graphite, and graphene: a Raman scattering study. Appl Phys Lett 2008; 92: 011914.
12. Hu H, Ruammaitree A, Nakahara H, Asaka K, Saito Y. Few-layer epitaxial graphene with large domains on C-terminated 6H-SiC. Surf Interface Anal 2012; 44: 793–6.
13. Hass J, de Heer WA, Conrad EH. The growth and morphology of epitaxial multilayer graphene. J Phys Condens Matter 2008; 20: 323202.
14. Emtsev KV, Bostwick A, Horn K, Jobst J, Kellogg GL, Ley L, McChesney JL, Ohta T, Reshanov SA, Röhrl J, Rotenberg E, Schmid AK, Waldmann D, Weber HB, Seyller T. Towards wafer-size graphene layers by atmospheric pressure graphitization of silicon carbide. Nat Mater 2009; 8: 203–7.
15. Xie W, Möbus G, Zhang S. Carbon nanotube to SiC nanorod conversion in molten salt studied by EELS and aberration corrected HRTEM. J Phys Conf Ser 2010; 241(1): 012093. IOP Publishing.

16. Fu X, Jiang J, Hu X, Yuan J, Zhang Y, Han X, Zhang Z. The microstructure origin of large strain plastically deformed SiC nanowires. J Phys Conf Ser 2008; 126(1): 012072. IOP Publishing.
17. Muller DA, Tzou Y, Raj R, Silcox J. Mapping sp^2 and sp^3 states of carbon at sub-nanometre spatial resolution. Nature 1993; 366(6457): 725-7.
18. Robinson JA, LaBella III M, Trumbull KA, Weng X, Cavelero R, Daniels T, Hughes Z, Hollander M, Fanton M, Snyder D. Epitaxial graphene materials integration: effects of dielectric overlayers on structural and electronic properties. ACS Nano 2010, 4(5), 2667-72.
19. Jia X, Hofmann M, Meunier V, Sumpter BG, Campos-Delgado J, Romo-Herrera JM, Son H, Hsieh Y-P, Reina A, Kong J, Terrones M, Dresselhaus MS. Controlled formation of sharp zigzag and armchair edges in graphitic nanoribbons. Science 2009; 323(5922): 1701-5.
20. Holland TB, Anselmi-Tamburini U, Quach DV, Tran TB, Mukherjee AK. Local field strengths during early stage field assisted sintering (FAST) of dielectric materials. J Eur Ceram Soc 2012; 32(14): 3659-66.
21. Shimoo T, Takeuchi H, Okamura K. Thermal Stability of Polycarbosilane-Derived Silicon Carbide Fibers under Reduced Pressures. J Am Ceram Soc 2001; 84(3): 566-70.
22. Sainz MA, Miranzo P, Osendi MI. Sintering behaviour and properties of YAlSiO and YAlSiON glass-ceramics. Ceram Int 2011; 37(5): 1485-92.
23. de With G, Parren JED. Translucent $Y_3Al_5O_{12}$ ceramics: Mechanical properties. Solid State Ionics 1985; 16: 87-93.
24. Carney CM, Mah TI. Current Isolation in Spark Plasma Sintering of Conductive and Nonconductive Ceramics. J Am Ceram Soc 2008; 91(10): 3448–50.
25. Zapata-Solvas E, Gomez-Garcia D, Dominguez-Rodriguez A, Todd RI. Ultrafast and Energy Efficient Sintering of Ceramics by Electric Current Concentration. Sci Rep 2015; 5: 8513 (2015)
26. Miranzo P, González-Julián J, Osendi MI, Belmonte M. Enhanced Particle Rearrangement During Liquid Phase Spark Plasma Sintering of Silicon Nitride-Based Ceramics. Ceram Int 2011; 37(1): 159–66.
27. Lysenko VA, Voronin GF. System Al_2O_3-Y_2O_3. Calculated, Temperature Composition Melting Equilibria. Vestn Mosk Univ, Khim 1990; 31(1): 30–4.
28. de Heer WA, Berger C, Ruan M, Sprinkle M, Li X, Hu Y, Zhang B, Hankinson J, Conrad E. Large Area and Structured Epitaxial Graphene Produced by Confinement Controlled Sublimation of Silicon Carbide. P Natl Acad Sci 2011; 108(41): 16900–5.

29. Koumoto K, Shimohigoshi M, TakedaS, Yanagida H. Thermoelectric Energy Conversion by Porous SiC Ceramics. J Mater Sci Lett 1987; 6(12): 1453–5.
30. Wei W, Li JW, Zhang HT, Cao X-M, Tiana C, Zhang J-S. Macrostructural Influence on the Thermoelectric Properties of SiC Ceramics. Scripta Mater 2007; 57(12): 1081–4.
31. Becker A, Angst S, Schmitz A, Engenhorst M, Stoetzel J, Gautam D, Wiggers H, Wolf DE, Schierning G, Schmechel R. The Effect of Peltier Heat During Current Activated Densification. App Phys Lett 2012; 101: 013113.
32. Liu J, Yan H, Jiang K. Mechanical Properties of Graphene Platelet-Reinforced Alumina Ceramic Composites. Ceram Int 2013; 39(6): 6215–21.
33. Ramirez C, Miranzo P, Belmonte M, Osendi MI, Poza P, Vega-Diaz SM, Terrones M. Extraordinary Toughening Enhancement and Flexural Strength in Si_3N_4 Composites Using Graphene Sheets. J Eur Ceram Soc 2014; 34(2): 161–9.
34. Padture NP. In Situ-Toughened Silicon Carbide. J Am Ceram Soc 1994; 77(2): 519–23.
35. Ramirez C, Osendi MI. Toughening in Ceramics Containing Graphene Fillers. Ceram Int 2014; 40(7): 11187–92.
36. Martin C, Cales B, Vivier P, Mathieu P. Electrical discharge machinable ceramic composites. Mater Sci Eng 1989; A109 :351-6.
37. Malek O, González-Julián J, Vleugels J, Vanderauwer W, Lauwers B, Belmonte M. Carbon nanofillers for machining insulating ceramics. Materials Today 2011; 14:496-501.
38. Lauwers B, Kruth JP, Liu W, Eeraerts W, Schacht B, Bleys P. Investigation of material removal mechanisms in EDM of composite ceramic materials. Journal of Materials Processing Technology 2004; 149(1): 347-52.
39. Ramírez C, Figueiredo FM, Miranzo P, Poza P, Osendi MI. Graphene nanoplatelet / silicon nitride composites with high electrical conductivity. Carbon 2012; 50: 3607-15.
40. Ramírez C, Vega-Díaz SM, Morelos-Gómez A, Figueiredo FM, Terrones M, Osendi MI, Belmonte M, Miranzo P. Synthesis of conducting graphene/Si_3N_4 composites by spark plasma sintering. Carbon 2013; 57:425-32.
41. Ramírez C, Osendi MI. Characterization of graphene nanoplatelets-Si_3N_4 composites by Raman spectroscopy. J Eur Ceram Soc 2013; 33(3): 471-7.
42. Li Z, Bradt RC. Thermal expansion and thermal expansion anisotropy of SiC polytypes. J Am Ceram Soc 1987; 70(7):445-8.
43. Tsang DKL, Marsden BJ, Fok SL, Hall G. Graphite thermal expansion relationship for different temperature ranges. Carbon 2005; 43(14): 2902-6.

44. Walker LS, Marotto VR, Rafiee MA, Koratkar N, Corral EL. Toughening in graphene ceramic composites. ACS Nano 2011; 5(4): 3182-90.
45. Smay JE, Cesarano III J, Lewis JA. Colloidal inks for directed assembly of 3-D periodic structures. Langmuir 2002; 18: 5429-37.
46. Kim YW, Lim KY, Kim KJ. Electrical resistivity of silicon carbide ceramics sintered with 1wt% aluminum nitride and rare earth oxide. J Eur Ceram Soc 2012; 32: 4427-34.
47. Wang C, Tauber MJ. High-yield singlet fission in a zeaxanthin aggregate observed by picosecond resonance Raman spectroscopy. J Am Chem Soc 2010; 132: 13988-91.
48. Casiraghi C, Hartschuh A, Qian H, Piscanec S, Georgi C, Fasoli A, Novoselov KS, Basko DM, Ferrari AC. Raman spectroscopy of graphene edges. Nano Lett 2009;9(4):1433-41.

Chapter 4

Properties of in-situ grown graphene/SiC ceramic nanocomposites

As shown in the Chapter 3, in-situ grown graphene/SiC nanocomposites have been developed by liquid-phase SPS. The presence of graphene within the SiC matrix can modify the mechanical performance of these ceramics and, hence, in the present Chapter, a study of the contact-mechanical properties through Hertzian indentation tests has been carried out at medium and elevated temperatures as a function of the SiC starting material, i.e., α-SiC, β-SiC and nano-β-SiC. In addition, considering the conductive nature of graphene, the electrical conductivity of the in-situ grown graphene/SiC nanocomposites has been analyzed, including the use of nano-scale scanning probes to demonstrate the formation of a conducting graphene percolated network.

4.1.- Contact-mechanical properties at medium and elevated temperatures

Contact mechanics supplies important data for the efficient design of mechanical systems and for the assessment of tribological properties and indentation hardness. Indentation mechanics is lengthily used in the analysis and characterization of fracture and deformation of materials, most particularly, brittle ceramics[1] as indentation damage provides knowledge on other mechanical properties, such as strength or toughness. In fact, contact damage is known to be a major limiting factor in the durability of materials in engineering applications, like bearings or engine components.[2] Indentation testing is normally characterized by its experimental simplicity, often being the only realistic means of acquiring essential data on damage modes in ceramics, particularly the quasi-plastic mode. The main benefit of spherical indenters is the possibility to evaluate damage modes progressively evolving from low loads (elastic regime) to high loads (plastic regime).

Hertzian indentation is especially appropriate for ceramics or brittle materials. The stress fields created by spherical indenters initially induce deformations within the elastic regime and, therefore, ceramic plane surfaces recover their shape after the removal of the load. After the elastic regime, increases in the applied loads result in the formation of elasto-plastic fields. As in many other types of tests, materials undergo plastic flow beneath the contact above a certain yield point. Defining the uniaxial compression yield stress as Y, the plastic flow initiates at pressure values of $p_Y \approx 1.1Y$.[3,4] Deviations from linearity in the stress-strain plots are the indication of the commencement of the plastic behavior which, should be, in each material, determined by different microstructural parameters.

Two main damage modes have been found to appear in monolithic ceramics. The first one is the brittle mode, or Hertzian fracture, which commonly begins as a surface cone crack outside the contact area with the sphere; the spreading of cracks propagates underneath the contact surface with a truncated-cone shape. Actually, some initial investigations on this topic date back to 1891, when it was experimentally proved that there is a linear relation between the critical load for the cone crack initiation and the sphere size; this relation is referred to as the Auerbach's law. The analysis of the initiation of ring/cone cracking phenomena is indeed a subject of Hertzian indentation techniques. The second damage mode is quasiplasticity, or the quasi-plastic damage, based on the formation of a zone of disseminated shear-driven defects and microcracks in the subsurface, very common in tough ceramics where the coalescence of microcracks remarkably impairs their performance for fatigue or wear applications.[5,6] That is the case of heterogeneous ceramics with weak internal interfaces, large and elongate grains, and high internal residual stresses, etc. with the peculiarity that some positive aspects in the microstructures that prevent the propagation of long cracks are, conversely, negative for short crack propagation. In this sense, extensive work has been done in the particular case of LPSed SiC ceramics, both fine brittle and coarse tough materials, processed by conventional sintering methods, such as pressureless sintering and hot pressing.[7-10] Nonetheless, almost no research is known on the mechanical behavior LPSed SiC ceramics obtained by rapid sintering techniques like SPS, which could be of great interest especially because of the in-situ formation of graphene flakes at the SiC grain boundaries that can play a very significant role on the contact mechanical behavior of the materials.

The Hertzian contact tests (A.2.15) for SiC were performed in air in the 25-850 °C temperature range. Then, the indentations were observed and measured by optical microscopy; in the case of low loads (elastic regime), a circular scar was visible as a consequence of the sputter-coated metallic layer, which is inevitably used to determine the contact radii between the indenter and the polished surface of the SiC specimens. At increasing loads, different forms of scars can be detected around the indentation prints. Initial cracks were typically incomplete, growing bigger and more ring-shaped as applied loads increased. As an example, the indentations created in the three different studied SiC materials at the same load of 1250 N and temperature of 400 ºC are shown in Fig. 4.1. Especially in the case of α-SiC and β-SiC ceramics (Fig. 4.1a,b), evidence of brittle damage is shown by the concentric circles appearing

during the application of the loads, a typical attribute of brittle solids. Damage is, thus, confined within a hemispherical deformation zone below the circular scar.

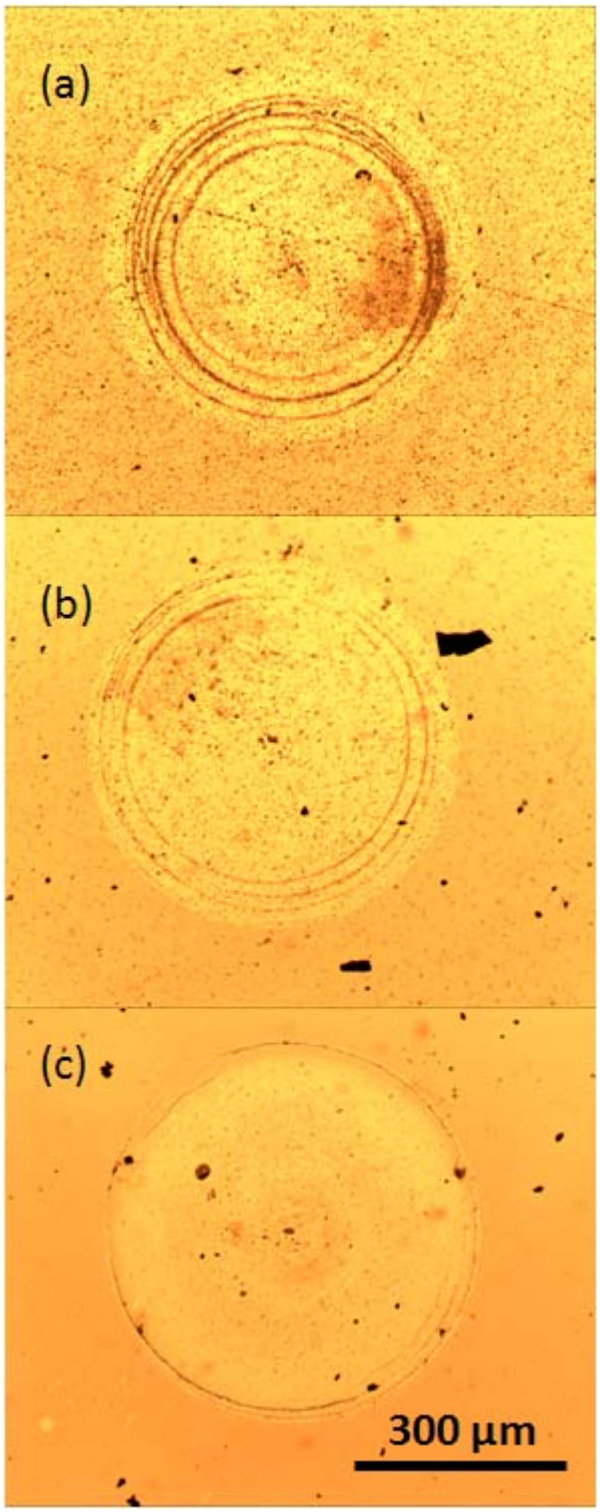

Figure 4.1.- Optical images of the contact scars induced by loads of 1250 N at 400 ºC in the case of: (a) α-SiC, (b) β-SiC, and (c) nano-β-SiC samples.

Indentation stress-strain curves were constructed by plotting the mean contact pressure, p_0 ($p_0=F/\pi a^2$), exerted on the sample below the indenter, versus the strain represented by the normalized radius of the printed circle (a/r). Elastic modulus was then measured from the linear stretch of each indentation curve using the Hertzian relation for elastic contacts[1] as stated before (applicable when $p_0 < 1.1Y$):[1,11]

$$p_0 = \frac{4/3\pi}{(1-v^2)/E+(1-v'^2)/E'}\frac{a}{r} \quad (1)$$

where v is Poisson's ratio, and the primes indicate indenter properties. The error in *E* was calculated by the error propagation in the expression.

Fig. 4.2 shows the Hertzian indentation stress–strain curves for α-SiC, β-SiC, and nano-β-SiC at various temperatures, from 25 to 850 °C. The shape of the curves is the typical of a polycrystalline ceramic,[11-15] that is, an initial linear stretch attributable to the elastic deformation regime, followed by a nonlinear stretch associated to the quasi-plastic deformation regime.

It is observed that the slope of the linear stretch and the contact pressure for the deviation of the linearity decrease with increasing temperature. The particular details are, however, different for the three different SiC ceramics, as discussed next. Fig. 4.3a shows the evolution of the elastic moduli on the temperature, slowly decaying in the tested temperature range. This is indeed the type of trend previously observed in other polycrystalline ceramics.[16-18] As a general consideration, a theory of the dependence of elastic constants with temperature was first proposed by Max Born in 1954 in his book Dynamical theory of crystal lattices.[19] In essence, this dependence was claimed to arise from the variations of the lattice potential energy, showing dependence of T^{-1} at temperature range studied here. Later on, these factors have been subjected to debate and corrected in works published by Wachtman[20] or Varshni[21] back in 1970, among others.

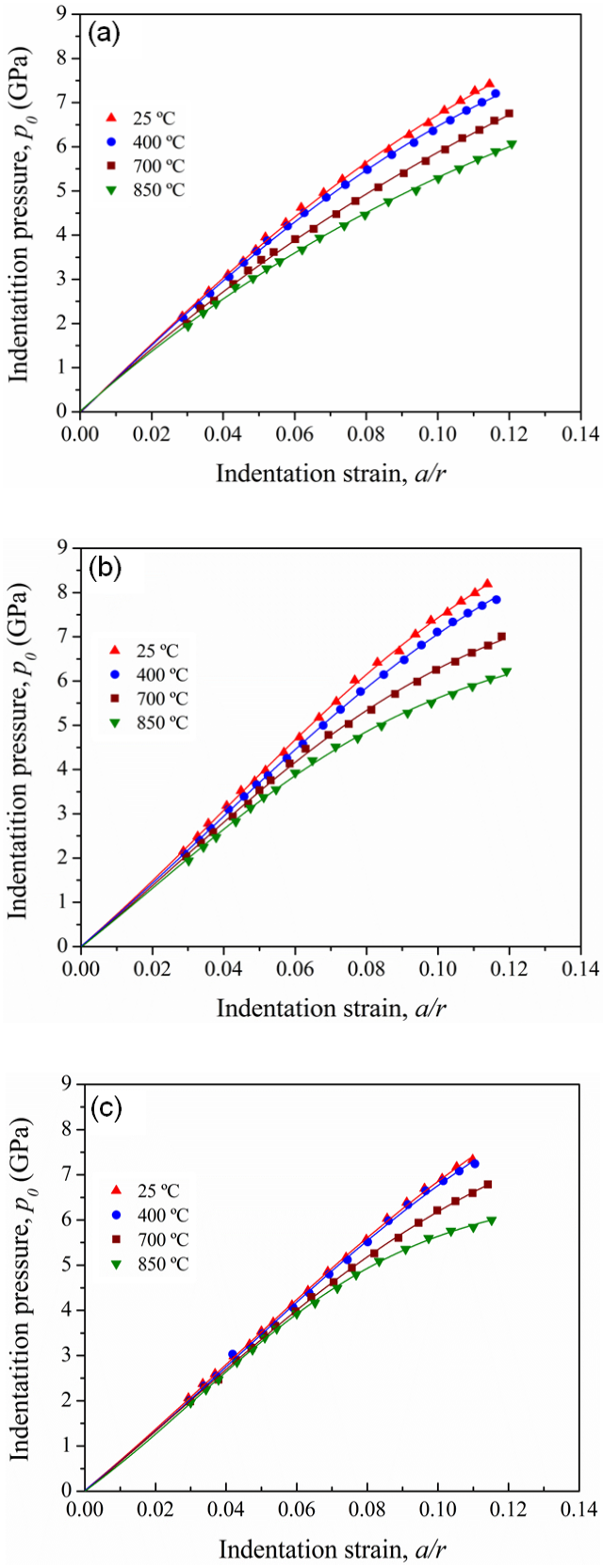

Figure 4.2.- Indentation stress-strain curves of (a) α-SiC, (b) β-SiC, and (c) nano-β-SiC at temperatures in the range 25-850 °C. The points are experimental data, and the solid curves are guides to the eye. The error bars are lower than the point size.

For α-SiC and β-SiC ceramics, both *E* values at room temperature (390-425 GPa) and their decay with temperature are similar to those observed for pressureless LPSed α-SiC with comparable amounts of sintering additives additives.[13] In that work, an α-SiC based ceramic with 5 wt.% of sintering additives (Al_2O_3:Y_2O_3) mostly forming YAG, with an average particle size for SiC of 1.9 μm, showed E ~400 GPa. However, in the case of the nano-β-SiC, E is lower and remains practically constant up to 700 °C (E~335 GPa). At 850 °C, E becomes similar for the three materials, which suggests the activation and relevance of the reversible grain-boundary sliding.[16,17] It is also seen in Fig. 4.3a that β-SiC is slightly stiffer than α-SiC, which agrees with data for pure single crystals where E varied, depending on the crystallographic direction, from 280 to 510 GPa and from 340 to 510 GPa, for α-SiC and β-SiC, respectively.[22] Even though nano-β-SiC specimens are only comprised of β-SiC grains, it is nevertheless less stiff than α-SiC due to its higher content of compliant secondary phase (14.2 wt.% for nano-β-SiC and 9.1 wt.% for α-SiC, Table 3.1). Note that E measured by instrumented Vickers indentation at 50 N (Table 3.5) at room temperature were 392 ± 16, 430 ± 25, and 350 ± 7 GPa for α-SiC, β-SiC, and nano-β-SiC, respectively, which lends strong credence to those determined by Hertzian indentation.

It is observed in Fig. 4.3b that for the three materials the yield stress decreases progressively with increasing temperature. This is a reasonable tendency because quasi-plasticity in LPSed SiC generally occurs by shear-faulting along the weak interfaces facilitated by the increased thermal energy.[13] α-SiC systematically exhibits much lower yield stress than the other two finer-grained ceramics, β-SiC and nano-β-SiC, of similar grain sizes, d_{50} = 0.54 and 0.44 μm (Chapter 3), respectively, which is then attributable to a higher tendency to undergo shear faulting because of its coarser microstructure (d_{50} = 1.1 μm);[8,9] indeed, shear faulting phenomena are more prone to occur in the presence of slip planes and weaker interfaces, both of which are more likely to occur in the case of microstructures showing larger grain sizes. In addition, α-SiC shows a yield stress temperature decay similar to coarse pressureless LPSed SiC;[13] specifically, a decay of approximately 0.1 GPa over each 100 ºC for T < 800 ºC in both the pressureless-sintered and the SPSed SiC materials is observed. On the other hand, the finer-grained β-SiC and nano-β-SiC show a faster decay in the yield stress with temperature due to the grain-boundary weakening, apart from similar yield stress values themselves despite the latter having a 5 wt.% higher amount of secondary phase. Therefore, the grain size seems to play the dominant role in the

yield stress of the present LPSPSed SiC ceramics, with differences in secondary phase content of 5 wt.% just playing a minor role.

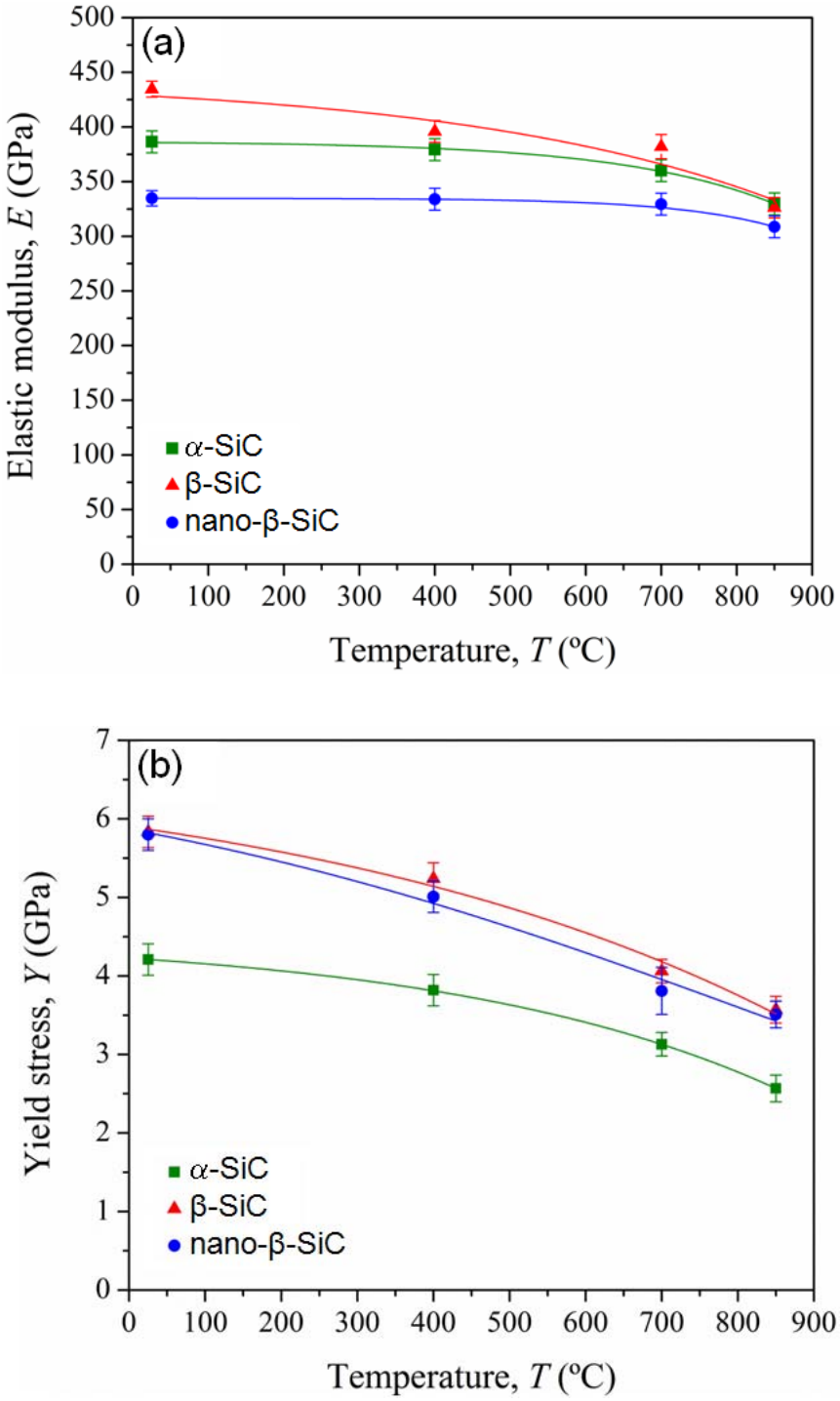

Figure 4.3.- Dependence of the (a) elastic modulus and (b) yield stress of α-SiC, β-SiC, and nano-β-SiC with the temperature in the range 25-850 °C. The points are the experimental data, and the solid curves are guides to the eye.

The critical loads for the initiation of quasi-plasticity were calculated from the *Y* values experimentally determined, using the relation derived for the Hertzian mechanical contact:[1,3]

$$P_Y = \frac{9}{16}\left(\frac{1-\nu^2}{E} + \frac{1-\nu'^2}{E'}\right)^2 (\pi 1.1Y)^3 r^2 \quad (2)$$

where *Y* is in turn calculated from the contact pressure at which the experimental indentation curve deviates from linearity (p_Y) using the expression $p_Y \approx 1.1\ Y$; again, the error in P_Y was calculated by error propagation in the expression.

On the other hand, the critical loads for the onset of fracture in the form of ring/cone cracking (P_C) were taken as the lowest applied load at which such damage was observed during the post-test observation of the specimens; the error in P_C was considered to be the difference between that load and the preceding one in the test sequence (i.e., error bars plotted only in the minus direction).

Fig. 4.4a shows the critical loads for the initiation of quasi-plasticity and fracture (specifically ring/cone cracking) in α-SiC, β-SiC, and nano-β-SiC as a function of temperature. Logically, P_Y decreases with increasing temperature because it is computed analytically from the experimentally-measured *E* and *Y* values according to the functional dependence $Y^3 \cdot E^{-2}$, as inferred from Eq. (3), thus resembling the temperature dependence of *Y.* On the other hand, as shown in Fig. 4.4b, nano-β-SiC is the least prone among the three ceramics to ring/cone cracking. Indeed, apart from these higher critical loads, nano-β-SiC always exhibited less ring/cone cracks than α-SiC or β-SiC under the same applied load and, in addition, they were normally incomplete. Considering that P_C satisfies the expression of Eq. (3) defined by Lawn:[1]

$$P_C = 8.63 \cdot 10^3 \cdot K_{IC}^2 \cdot r \cdot E^{-1} \quad (3)$$

this behavior could be explained by the lower E (Fig 4.3a) of nano-β-SiC as well as a higher toughness. In fact, as it is also shown in Fig. 4.4b, the toughness values calculated from P_C using Eq. (3) increase as the particle size of starting SiC particles decreases. The higher toughness of the nano-β-SiC can be is attributed to the slightly greater aspect ratio of the SiC grains and the higher number of graphene flakes at grain boundaries that would increase the effectiveness of the crack-bridging mechanisms. For the three ceramics, the critical loads for ring/cone cracking decrease appreciably with increasing temperature above 400 °C, a trend that indeed reflects the evolution of the toughness. This fall in toughness above 400 °C may be

related with a slight increase of defects in the multilayered graphene flakes located at grain boundaries, inferred from the observed increase in the intensity ratio of the D to G Raman bands of graphene on the surface of the nano-β-SiC specimen after the Herztian test. This ratio is 0.55 up to 400 °C, but increased up to 0.65 at temperatures above 700 °C (Fig. 4.5).

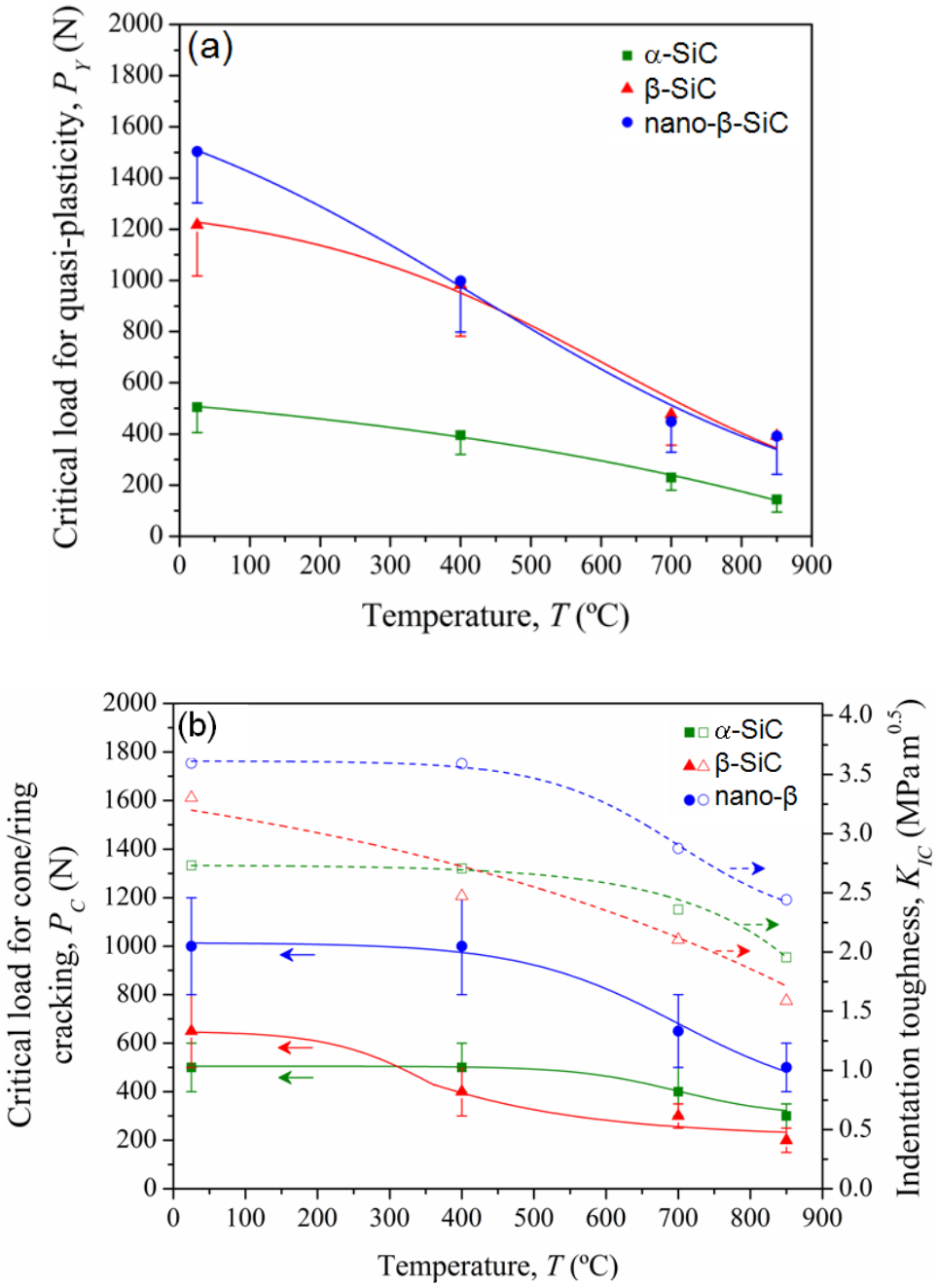

Figure 4.4.- Dependence of the critical load for the initiation of (a) quasi-plasticity and (b) ring/cone cracking in α-SiC, β-SiC, and nano-β-SiC with the temperature in the range 25-850 °C. Points are experimental data, and solid curves are guides to the eye. Also in (b) the toughness calculated from the critical loads for ring/cone cracking.

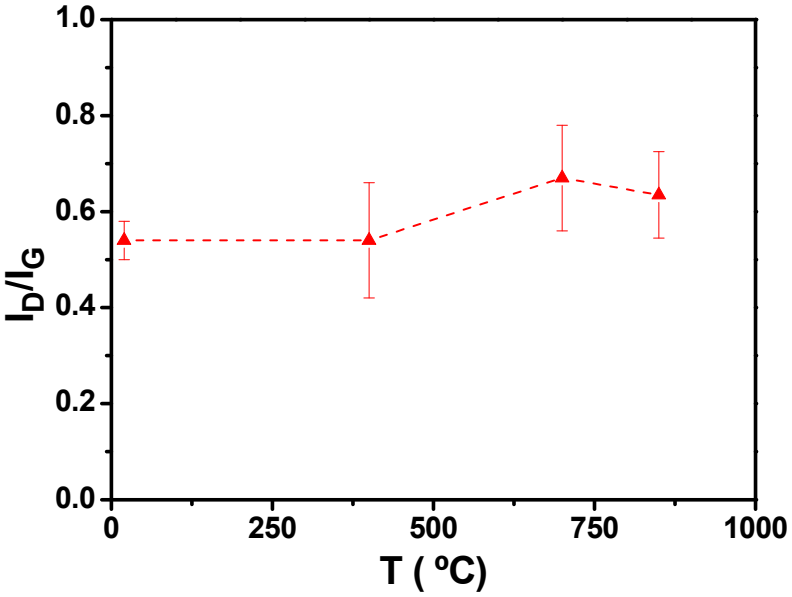

Figure 4.5.- Ratio between the Raman intensity of the D and G bands (I_D/I_G) of graphene (in area) as a function of the testing temperature for the Raman analyses done on the surface of the nano-β-SiC specimen after the Herztian tests.

Toughness of α-SiC decays slower with temperature compared to the other two finer-grained ceramics because of the slightly lower amount of secondary phase and the larger size of the graphene flakes that leads to a lesser abundance of interfaces; therefore, an attribute that makes it less tough at room-temperature could contribute to toughen it at high-temperatures. Interestingly, nano-β-SiC exhibits a brittle-to-ductile transition at ~400 °C, when $P_C > P_Y$ occurs, with fracture no longer being the first damage mode above that temperature. β-SiC and α-SiC are however brittle in the entire temperature range investigated in the present study, with cone/ring cracking occurring always at lower critical loads than quasi-plasticity. SPSed SiC materials present generally much finer microstructures than their conventionally sintered counterparts; this microstructural refinement implies a tendency to brittleness being different from what has been reported for pressureless LPSed SiC ceramics, which have been found to be “ductile” under high-temperature Hertzian indentation.[13]

4.2.- Electrical properties at the micro- and the macro-scales

Increasing the electrical conductivity of structural ceramics is fundamental in many technological issues, for instance for applications that require static charge dissipation in mechanical devices or for manufacturing miniaturized complex components using the electro-discharge machining (EDM) technique.[23-25]

There are two main facts that can affect the electrical conductivity of present SiC materials sintered by SPS. One is the in-situ growth of graphene flakes at the SiC grain boundaries and the other is the possible doping of SiC grains, both simultanerously occurring during sintering. From the electrical conduction viewpoint, SiC is a semiconductor with fairly large band gap energies ranging from ~2.4 to 3.4 eV, depending on the structural polytype,[26,27] thus exhibiting low electrical conductivity (σ). However, SiC-based ceramics can be tailored to display very diverse σ values within a range from 10^{-9} to 10^{5} S m^{-1},[28-36] depending on the type of doping, often resulting from sintering additives. In this sense, the case of sintering additives containing nitrogen (N) is especially significant, since N atoms can be incorporated into the SiC lattice substituting for carbon (C) during sintering,[37] creating a donor level within the bandgap. The highest σ reported for N-doped SiC (3×10^{4} S m^{-1}) was obtained using 19 wt.% yttrium nitrate ($Y(NO_3)_3 \cdot 4H_2O$) as sintering aid.[29] High conductivities are also obtained with additive systems based on AlN (*e.g.* 2×10^{3} S·m^{-1} for AlN–RE_2O_3, RE = Y, Er).[30,31] Comparatively lower σ values (in the range 10^{-9}-10^{-1} S·m^{-1}) were reported when employing only oxide additives such as Y_2O_3 and Al_2O_3,[28,32-34] depending on the dopant concentration and nature, location and thickness of grain boundaries.

As shown in Fig. 4.6, the *dc* electrical conductivity, measured at room temperature, is affected by the type of starting SiC powders, ranging from 6.4×10^{-4} S·m^{-1} for the α-SiC material up to a 6 orders of magnitude higher value (σ = 33 S·m^{-1}) for the nano-β-SiC material, all of them SPSed at the same temperature of 1800 ºC. All these samples are fully dense ceramics, so no variations in their final electrical conductivity can be inferred owing to effects of porosity; besides, all these specimens are comprised of a similar amount of in-situ grown graphene flakes (~3 vol.%), as it was previously described in Chapter 3. Therefore, the significant increase in the electrical conductivity observed for the β-SiC and the nano-β-SiC materials should be explained in terms of the smaller flake size of graphene in the case of their more refined microstructures, which would facilitate the percolation for electrical transport, as well

as the most possible doping of SiC grains by Al atoms from the grain boundary phase occurring during grain growth by solution precipitation processes.[38,39]

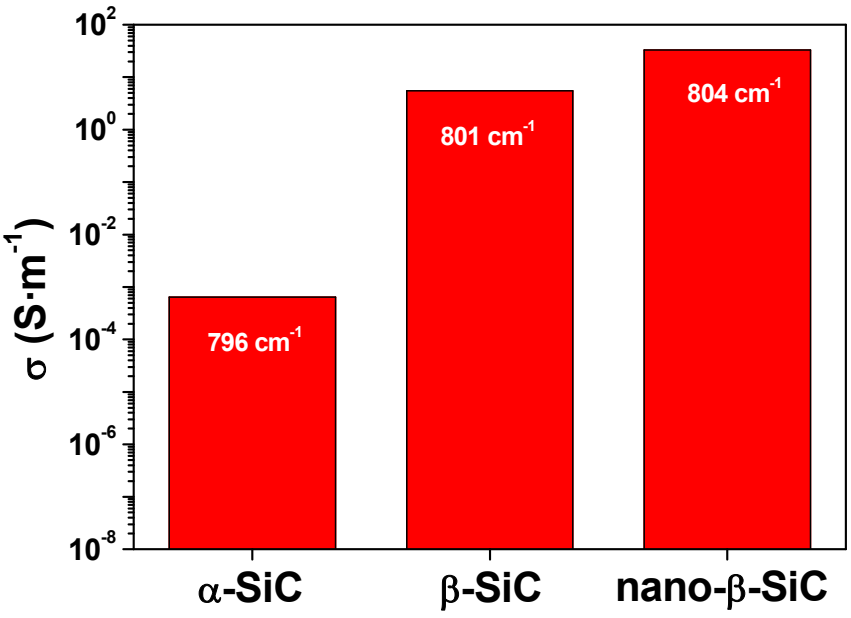

Figure 4.6.- Electrical conductivity (σ) for the three SiC materials SPSed at 1800 ºC. The Raman shift value of the the TO band is also included within the columns.

Undoped SiC plainly exhibits characteristic vibrational optical Raman modes, namely the transverse mode (TO) at 796 cm^{-1} and the longitudinal mode (LO) at ~978 cm^{-1}. However, the intensity of the LO mode decreases in doped-SiC and the TO mode is overlapped with a characteristic shoulder at Raman shifts above 800 cm^{-1} (as discussed for Fig. 3.22). As it is shown in the average Raman spectra of the three samples, shown in Fig. 3.7, the nano-β-SiC material is clearly doped because the LO mode almost disappears; this higher doping level is attributed to the more elevated amount of liquid phase associated with its higher oxygen content (Table 3.1) and the improved reactivity of nanosized powders, which enhance its sintering and grain growth kinetics by promoting solution-precipitation processes. A certain level of doping for the β-SiC can also be inferred from the lower intensity ratio between the LO and TO bands (0.3), calculated in Table 3.2, compared to the α-SiC material (0.4).

Considering that SiC grains may result doped during sintering due to the presence of elements like Al at sintering temperatures of as high as 1800ºC, identifying the conducting phases of these ceramics is of paramount relevance. With the aid of atomic force microscopy (AFM) in its conventional topographic and conducting (C-AFM) modes, it has been confirmed that the conduction path occurs along the percolated network of few-layered graphene located at intergranular positions in the case of the low doped α-SiC material. Simultaneous topographic images $z(x,y)$ and current maps $I(x,y)$ taken over the same region at a fixed voltage permitted the correlation between the morphological features and the conducting response even at large scales. This procedure allowed ascribing flat low regions to the SiC matrix, and areas of obviously conductive character with varying sizes to FLG emerging between the matrix grains. According to the employed configuration, in which the current must flow between tip and a millimeters apart macroscopic counter-electrode, the fact of measuring electronic current implies the existence of a conductive path within the composite that makes it electrically conducting. As a revealing example, a couple of FLG flakes are shown in Fig. 4.7. The layered morphology of the FLG can be seen in the lower piece of Fig. 4.7a (see arrow), exhibiting a strikingly homogeneous conductive response (Fig. 4.7b). The flake thickness estimated for the isolated FLG shown in Fig. 4.7c is approximately 4 nm (Fig. 4.7d), but a variety of flakes with thickness ranging between 1 and 10 nm were found in agreement with the Raman data and FESEM and HRTEM images presented in Chapter 3. The linear *I-V* curves recorded at such FLGs (Fig. 4.7e) confirmed the presence of an interconnected 3D network of conductive FLG throughout the entire SiC composite and explains its higher electrical conductivity compared to similar materials sintered by conventional methods,[33] which are below 10^{-7} S m^{-1} in the case of undoped SiC ceramics.[28]

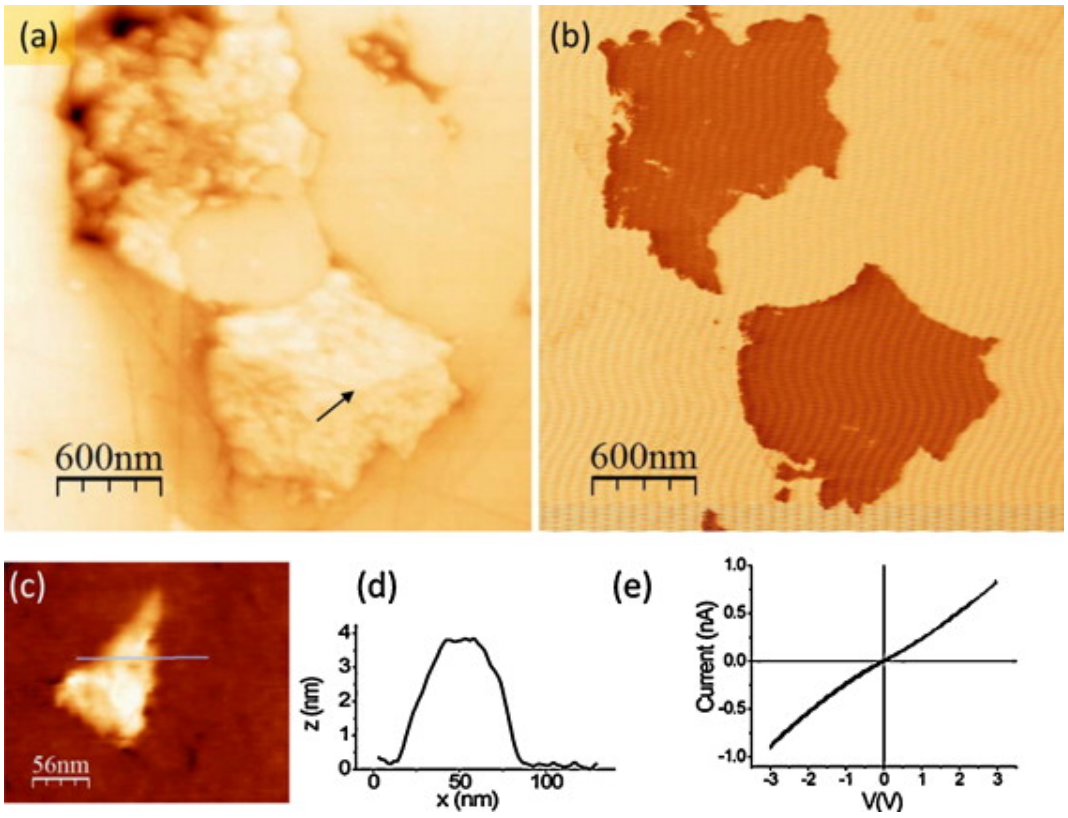

Figure 4.7.- AFM and C-AFM on α-SiC: (a) topographic image showing the inter-grain location of two epitaxial graphene flakes. The total color scale (dark for low and bright for high values) spans 20 nm. (b) The simultaneously measured current map, obtained at V_{tip} = −1.5 V, shows a clear correlation between FLG and conducting regions (I_{max} = −40 pA). Note that because of I < 0 for V_{tip} < 0, conducting FLG appear as dark patches (negative values) in the current map. (c) Topographic image of a triangular shaped FLG with lateral size ~70 nm and thickness lower than 4 nm (d). (e) *I-V* curve obtained after averaging 20 curves taken at different conducting FLGs.

Similar measurements done on β-SiC and nano-β-SiC samples indicate that I-V curves taken at the β-SiC grains (Fig. 4.8) show slightly more current for positive than for negative voltages (p-type doping). Even though presenting different resistivity most SiC grains do conduct at the applied voltage (-2V) in the nano-β-SiC material except some percentage of smaller grains. These resistive grains probably correspond to original β-SiC particles whereas larger ones have grown during sintering by a solution-precipitation process favoring Al atoms entering in solid solution within the SiC grains, explaining their p-type doping. Despite there is not a significant increase in the mean grain size (i.e. 0.54 μm vs. d_{50}=0.50μm for the starting powder) in the β-SiC composite, there is a 25% increase in the number of

grains above 1 μm which confirms the occurrence of solution-precipitation processes and the subsequent doping also in this material.

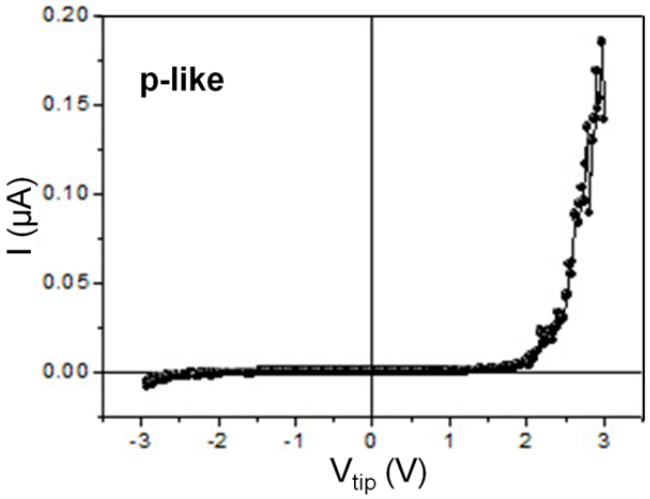

Figure 4.8.- Characteristic IV curve obtained on the surface of a matrix grain of the nano-β-SiC sample.

Considering the ease doping of the nano-β-SiC, new SPS tests were performed at increasing set-point temperatures, up to 1950 ºC. Interestingly, an increment on the SPS temperature of 150 ºC, keeping constant the rest of the SPS parameters, led to a remarkable σ value of 935 $S \cdot m^{-1}$ that corresponds to an improvement on this parameter of ~2700% as compared to the material SPSed at 1800 ºC (Fig. 4.9). Besides, it seems that this improvement follows a linear temperature dependence in the logarithmic scale, as pointed out by the plot in Fig. 4.9. This increment in σ can be explained mainly by SiC doping promoted by the high temperature attained, although the in-situ FLG content also increases from 2.9 vol.% at 1800 ºC to 3.6 vol.% at 1950 ºC. These consuctivity values are significantly higher than those obtained for Al-doped SiC ceramics LPSed with the same additives system, which are in the range of ~10^{-3}-10^{-4} $S \cdot m^{-1}$, being ~ 5 orders of magnitude lower than the doped nano-β-SiC materials.[33] In the case of the present undoped α-SiC material, the graphene network resulted in σ values close to those for conventional sintered Al-doped α-SiC.[28,33]

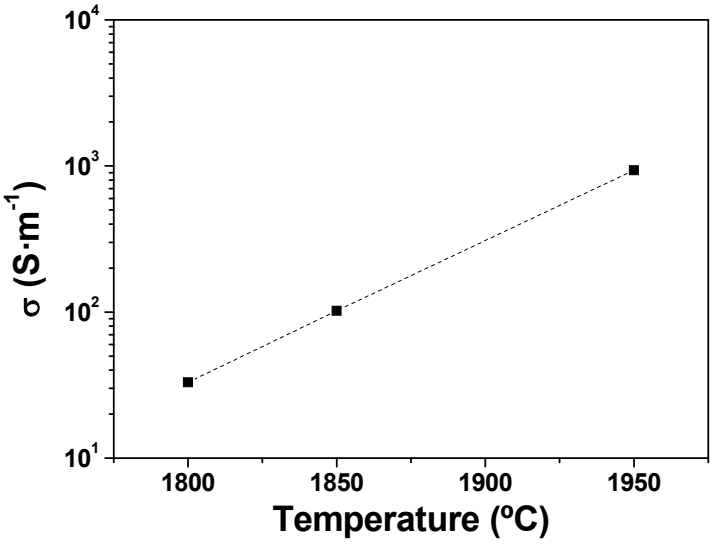

Fig. 4.8. Electrical conductivity (σ) for nano-β-SiC specimens as a function of the SPS temperature.

4.3.- Conclusions

i) Hertzian indentation tests have shown significant differences on the pre-creep contact mechanical properties of LPSPSed graphene/SiC composites prepared in-situ from different SiC powders. α-SiC and β-SiC materials show brittle cone-crack damage in the whole temperature range studied, but nano-β-SiC materials show a brittle-to-ductile transition below 700 ºC.

ii) The yield stress and the resistance to quasi-plasticity increase with the microstructural refinement, whereas the presence of multilayered graphene at the grain boundaries significantly increases the resistance to cone/ring cracking and the toughness.

iii) The formation of an in-situ graphene-like conducting network within the SiC matrix is inferred using a combination of macro (dc electrical conductivity) and micro (c-SFM) characterization techniques.

iv) The in-situ grown graphene/SiC ceramic nanocomposites exhibit electrical conductivity values of 935 S·m^{-1}, larger than those obtained for similar SiC ceramics fabricated by conventional sintering techniques.

v) P-doping during sintering highly contributes to the electrical conductivity enhancement of composites SPSed from β-SiC powders, especially for nanosized starting powders.

4.4.- References

1. Lawn BR. Indentation of ceramics with spheres: a century after Hertz. J Am Ceram Soc 1998; 81(8): 1977–94.
2. Katz RN, Hannoosh JG. Ceramics for High-Performance Rolling Element Bearings: A Review and Assessment. Int J High Technol Ceram 1985; 1: 69–79.
3. Johnson KL. Contact mechanics. Cambridge, 1985. Cambridge University Press.
4. Tabor D. Hardness of Metals. Clarendon, Oxford, UK. 1951.
5. Kim DK, Jung YG, Peterson IM, Lawn BR. Cyclic fatigue of intrinsically brittle ceramics in contact with spheres. Acta Mater 1999; 47(18): 4711-25.
6. Jung YG, Peterson IM, Kim DK, Lawn BR. Lifetime-limiting strength degradation from contact fatigue in dental ceramics. J Dent Res 2000; 79(2): 722-31.
7. Roebben G, Duan RG, Sciti D, Van der Biest O. Assessment of the high temperature elastic and damping properties of silicon nitrides and carbides with the impulse excitation technique. J Eur Ceram Soc 2002; 22(14–15): 2501-9.
8. Padture NP, Lawn BR. Toughness properties of a silicon carbide with in situ-induced heterogeneous grain structure. J Am Ceram Soc 1994; 77(10): 2518-22.
9. Padture NP, Lawn BR. Contact fatigue of a silicon carbide with a heterogeneous grain structure. J Am Ceram Soc 1995; 78(6): 1431-8.
10. Jensen RP, Luecke WE, Padture NP, Wiederhorn SM. High-temperature properties of liquid-phase-sintered alpha-SiC. Mater Sci Eng A: Struct Mater Prop Microstruct Process 2000; 282(1–2):109-14.
11. Sánchez-González E, Miranda P, Guiberteau F, Pajares A. Effect of temperature on the pre-creep mechanical properties of silicon nitride. J Eur Ceram Soc 2009; 29(12): 2635–41.
12. Sánchez-González E, Meléndez-Martínez JJ, Pajares A, Miranda P, Guiberteau F, Lawn BR. Application of Hertzian tests to measure stress–strain

characteristics of ceramics at elevated temperatures. J Am Ceram Soc 2007; 90(1): 149-53.

13. Sánchez-González E, Miranda P, Guiberteau F, Pajares A. Effect of microstructure on the mechanical properties of liquid-phase-sintered silicon carbide at pre-creep temperatures. J Eur Ceram Soc 2011; 31(6): 1131-9.
14. Sánchez-González E, Miranda P, Meléndez-Martínez JJ, Guiberteau F, Pajares A. Temperature dependence of mechanical properties of alumina up to the onset of creep. J Eur Ceram Soc 2007; 27(11): 3345-9.
15. Sánchez-González, Miranda P, Meléndez-Martínez JJ, Guiberteau F, Pajares A. Contact properties of yttria partially stabilized zirconia up to 1000ºC. J Am Ceram Soc 2007; 90(11): 3572-7.
16. Wachtman JB Jr, Lam DG Jr. Young's modulus of various refractory materials as a function of temperature. J Am Ceram Soc 1959; 42(5): 254-60.
17. Bruls RJ, Hintzen HT, deWith G, Metselaar R. The temperature dependence of the Young's modulus of $MgSiN_2$, AlN and Si_3N_4. J Eur Ceram Soc 2001; 21(3): 263-8.
18. Osendi MI, Baudin C. Mechanical properties of mullite materials. J Eur Ceram Soc 1996; 16(2): 217-4.
19. Born M, Huang K. Dynamical theory of crystal lattices. Oxford University Press 1954.
20. Wachtman JB Jr, Tefft WE, Lam DG Jr, Apstein CS. Exponential temperature dependence of Young's modulus for several oxides. Phys Rev 1961; 122(6): 1754.
21. Varshni YP. Temperature dependence of the elastic constants. Phys Rev B 1970; 2(10): 3952.
22. Paquin RA. Metal Mirrors. In: Ahmad A, editor. Handbook of optomechanical engineering, New York 1997: 89-110. CRC Press LLC.
23. Martin C, Cales B, Vivier P, Mathieu P. Electrical discharge machinable ceramic composites. Mater Sci Eng 1989; A109 :351-6.
24. Malek O, González-Julián J, Vleugels J, Vanderauwer W, Lauwers B, Belmonte M. Carbon nanofillers for machining insulating ceramics. Mater Today 2011; 14:496-501.
25. Lauwers B, Kruth JP, Liu W, Eeraerts W, Schacht B, Bleys P. Investigation of material removal mechanisms in EDM of composite ceramic materials. J Mater Proc Tech 2004; 149(1): 347-52.
26. Irmscher K. Electrical properties of SiC: characterization of bulk crystals and epilayers. Mater Sci Eng 2002; B,91: 358-66.

27. Persson C, Lindefelt U, Relativistic Band Structure Calculation of Cubic and Hexagonal SiC Polytypes. J Appl Phys 1997; 82: 5496–508.
28. Sauti G, Can A, McLachlan DS, Herrmann M. The AC Conductivity of Liquid-Phase-Sintered Silicon Carbide. J Am Ceram Soc 2007; 90(8): 2446-53.
29. Kim YW, Kim KJ, Kim HC, Cho NH, Lim KY. Electrodischarge-machinable silicon carbide ceramics sintered with yttrium nitrate. J Am Ceram Soc 2011; 94: 991-3.
30. Lim KY, Kim YW, Kim KJ, Yu JH. Effect of in situ-synthesized nano-size SiC addition on density and electrical resistivity of liquid-phase sintered silicon carbide ceramics. J Ceram Soc Jpn 2011; 119: 965-67.
31. Kim YW, Lim KY, Kim KJ. Electrical resistivity of silicon carbide ceramics sintered with 1wt% aluminum nitride and rare earth oxide. J Eur Ceram Soc 2012; 32(16): 4427-34.
32. Can A, McLachlan DS, Sauti G, Herrmann M. Relationships between microstructure and electrical properties of liquid-phase sintered silicon carbide materials using impedance spectroscopy. J Eur Ceram Soc 2007; 27: 1361-3.
33. Sánchez-González J, Ortiz AL, Guiberteau F, Pascual C. Complex impedance spectroscopy study of a liquid-phase-sintered α-SiC ceramic. J Eur Ceram Soc 2007; 27: 3935–9.
34. Kusunose T, Sekino T. Increasing resistivity of electrically conductive ceramics by insulating grain boundary phase. ACS Appl Mater & Interfaces 2014; 6(4): 2759-63.
35. Kim KJ, Lim KY, Kim YW, Lee MJ, Seo WS. Electrical resistivity of α-SiC ceramics sintered with Al2O3 or AlN additives. J Eur Ceram Soc 2014; 34: 1695-701.
36. Siegelin F, Kleebe HJ, Sigl LS. Interface characteristics affecting electrical properties of Y-doped SiC. J Mater Res 2003; 18: 2608-17.
37. Persson C, Lindefelt U, Sernelius BE. Doping-induced effects on the band structure in n-type 3C-, 2H-, 4H-, 6H-SiC, and Si. Phys Rev B 1999; 60(24): 16479.
38. Sciti D, Bellosi A. Effects of additives on densification, microstructure and properties of liquid-phase sintered silicon carbide. J Mater Sci 2000; 35(15): 3849-55.
39. Sigl LS, Kleebe HJ. Core/Rim Structure of Liquid-Phase-Sintered Silicon Carbide. J Am Ceram Soc 1993; 76(3): 773-6.

Chapter 5

Transport properties of bulk graphene/SiC ceramic composites

As briefly explained in Chapter 1, graphene is known to exhibit outstanding transport properties. In particular, thermal and electrical conductivities of pure single-layer graphene have been reported to achieve exceptionally elevated figures in its basal ab plane, reaching 5000 $W \cdot m^{-1} \cdot K^{-1}$ for the thermal conductivity, and an electron mobility of $2x10^5$ $cm^2 \cdot V^{-1} \cdot s^{-1}$. Even so, in the case of multilayered graphene flakes, these figures tend to be impaired due to boundary scattering phenomena, especially for the thermal conductivity, as well as the most likely presence of defects, leading to values that resemble more those of graphite. Regardless of this deterioration of transport phenomena as compared to pure graphene, GNPs have already come into sight as appealing fillers for the thermal and electrical functionalization of ceramic materials.

The present Chapter is, hence, devoted to the analysis of the thermal and electrical transport mechanisms of bulk GNPs/SiC composites. The study has been performed as a function of temperature and GNPs content, where the orientation of the nanoplatelets was taken into account for parallel and perpendicular measurements. Besides, models for the conduction mechanisms have also been proposed.

5.1.- Thermal properties of graphene/SiC composites

SiC ceramics can be classified as thermally conductive, since monocrystalline pure SiC exhibits a room temperature thermal conductivity of 490 $W \cdot m^{-1} \cdot K^{-1}$.[1] However, their polycrystalline nature and the presence of grain boundary phases and solid solutions associated to the use of sintering additives diminish their effective capability to transport heat fluxes due to increased phonon scattering processes. In fact, the highest values reported for SiC ceramics at room temperature are within the range 252-270 $W \cdot m^{-1} \cdot K^{-1}$ using BeO as a sintering aid;[2,3] whereas lower values, in the range between 30-90 $W \cdot m^{-1} \cdot K^{-1}$, are usually reported for LPS-SiC ceramics when using Al-containing sintering aids[4-6] since Al atoms easily penetrate in the SiC lattice[7,8] forming a solid solution that impairs thermal transport.

Due to the high thermal conductivity of graphene, GNPs and rGOs have been used for the thermal functionalization of ceramic materials, as shown in Subsection 1.5.2 in Chapter 1 of the present PhD Thesis where a review was given. It is noteworthy to point out that, in those reported works, the preferential orientation of the nanoplatelets during pressure-assisted sintering processes induced a high degree of thermal anisotropy. Consequently, in this thesis, the thermal properties of the bulk GNPs/SiC composites sintered by SPS will be analyzed in the directions parallel and

perpendicular to the SPS pressing axis. Besides, the temperature dependence on the thermal conductivity in the parallel direction will be assessed.

The α data of the specimens were first measured in the directions parallel and perpendicular to the SPS pressing axis (Fig. 5.1) by the laser-flash method (A.2.9). Thermal diffusivity in the through-thickness direction, parallel to the SPS pressing axis ($\alpha^{\parallel}$), was measured in an Ar atmosphere as a function of temperature, from 298 to 1073 K; whereas measurements in the in-plane direction, perpendicular to the SPS pressing axis ($\alpha^{\perp}$), were developed only at room temperature, due to limitations of the equipment, using a special arrangement (Fig. A.2.5).

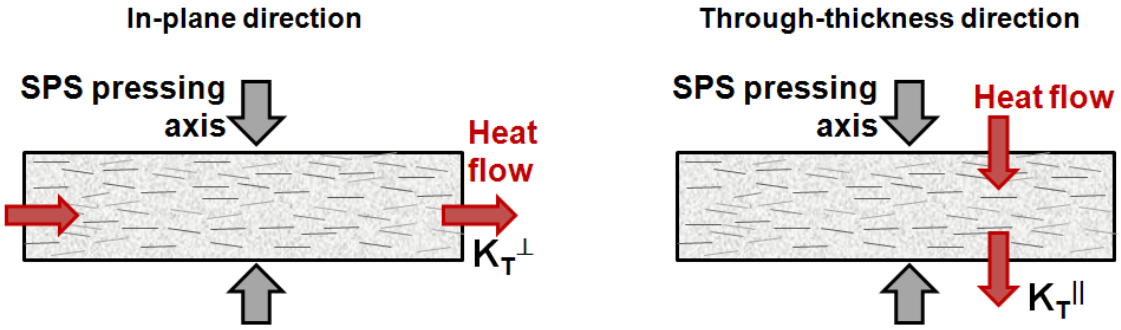

Figure 5.1.- Diagram of the arrangements used for thermal diffusivity measurements in the directions perpendicular ($\alpha^{\perp}$) and parallel ($\alpha^{\parallel}$) to the pressing axis of the SPS, also referred to as the in-plane and through-thickness, respectively

Then, K_T is calculated from α, ρ and the specific heat (C_P) of the materials using the following expression:

$$K_T = \alpha \cdot \rho \cdot C_p \qquad (1)$$

The thermal diffusivity values at room temperature for the graphene/SiC composites as a function of the GNPs content (0, 5, 10 and 20 vol.%) are displayed on Fig. 5.2. The α behavior is clearly anisotropic, with increasing values of the rate $\alpha^{\perp}/\alpha^{\parallel}$ as a function of the GNPs content from 1.5 to 3.5. The in-plane thermal diffusivity increases from 0.30 $cm^2 \cdot s^{-1}$, for the monolithic material, to ~0.42 $cm^2 \cdot s^{-1}$, for composites containing 20 vol.% GNPs; whereas the corresponding through-thickness thermal diffusivity decreases from 0.20 to 0.12 $cm^2 \cdot s^{-1}$. Significantly, even the monolithic SiC material exhibits anisotropic propagation of heat.

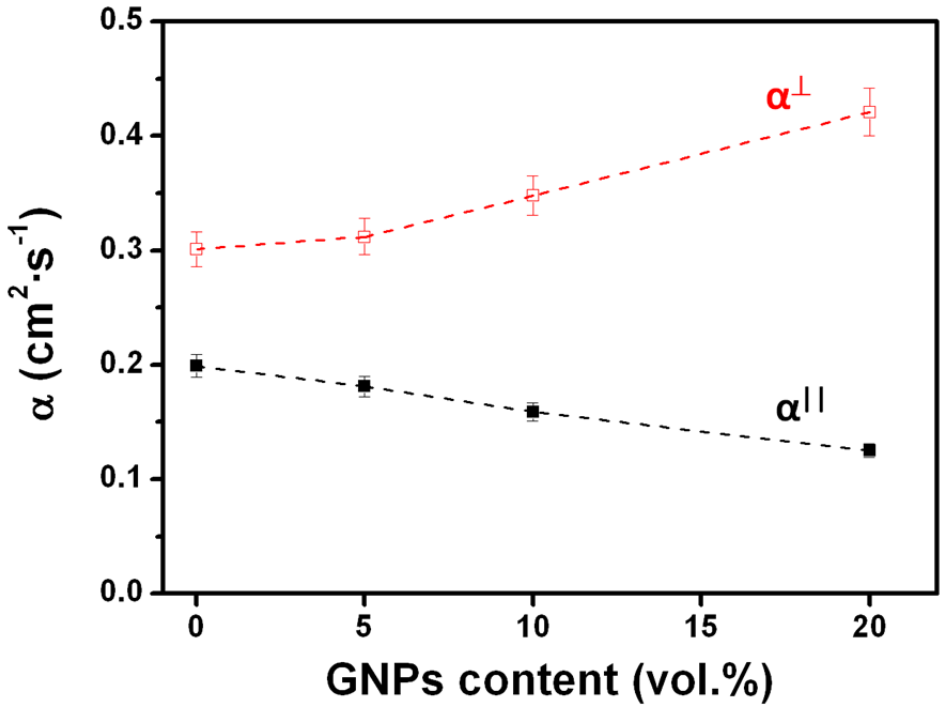

Figure 5.2.- Room temperature α values for the different composites considering the through-thickness ($\alpha^{\parallel}$) and in-plane ($\alpha^{\perp}$) directions. Errors represent the estimated accuracy of the laser flash technique being ~5% for parallel diffusivity data and the standard deviation of the values for the perpendicular diffusivity.

The specific heat of the composites as a function of temperature was calculated by the rule of mixtures from the chemical composition and the heat capacity data of each phase using the HSC Outokumpu database.[9] For the GNPs, values taken for C_p into the rule of mixtures were well approximated by those of graphite, as measurements were done above room temperatures (differences in the C_p between graphene and graphite arise at much lower temperatures).[10] In Fig. 5.3, results for the C_p calculations corresponding to the monolithic SiC material and the composites containing 5, 10 and 20 vol.% of GNPs (3.40, 6.95, and 14.30 wt.%, respectively) are plotted as a function of temperature. It can be seen that C_p increases with temperature and the amount of GNPs, the latter becoming especially significant above 500 K. Lines in Fig. 5.3 represent the fittings justified by the Bose-Einstein distribution, whose quality factor is above 99.93% in all cases, according to Eq. (2):

$$Cp \sim A \cdot \exp(-C/T) \qquad (2)$$

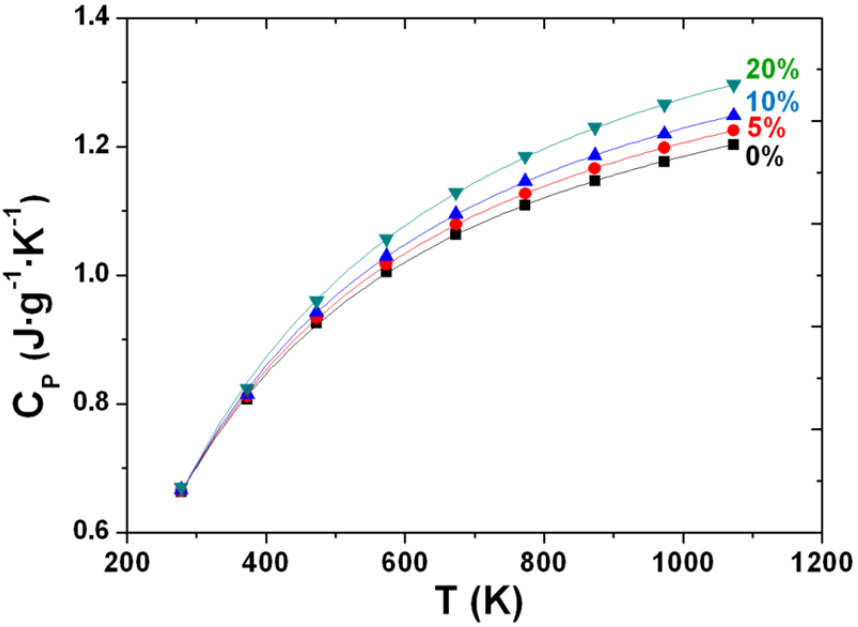

Figure 5.3.- C_p values of the GNPs/SiC composites as a function of the GNPs content calculated from the chemical composition and the heat capacity data.[9] Curves represent the fittings according to a Cp ~ A · exp (-C/T) model.

The room temperature thermal conductivity values of the different materials, calculated from Eq. (1), for the through-thickness ($K_T^{\parallel}$) and the in-plane ($K_T^{\perp}$) directions are shown in Fig. 5.4. $K_T^{\perp}$ values augment with increasing amounts of GNPs from ~65 W·m^{-1}·K^{-1}, for the monolithic material, to ~84 W·m^{-1}·K^{-1}, for composites containing 20 vol.% GNPs, which corresponds to a ~29% increase. However, an opposite trend was observed for $K_T^{\parallel}$ measurements, ranging from ~43 to ~25 W·m^{-1}·K^{-1} (0 and 20 vol.% GNPs specimens, respectively).

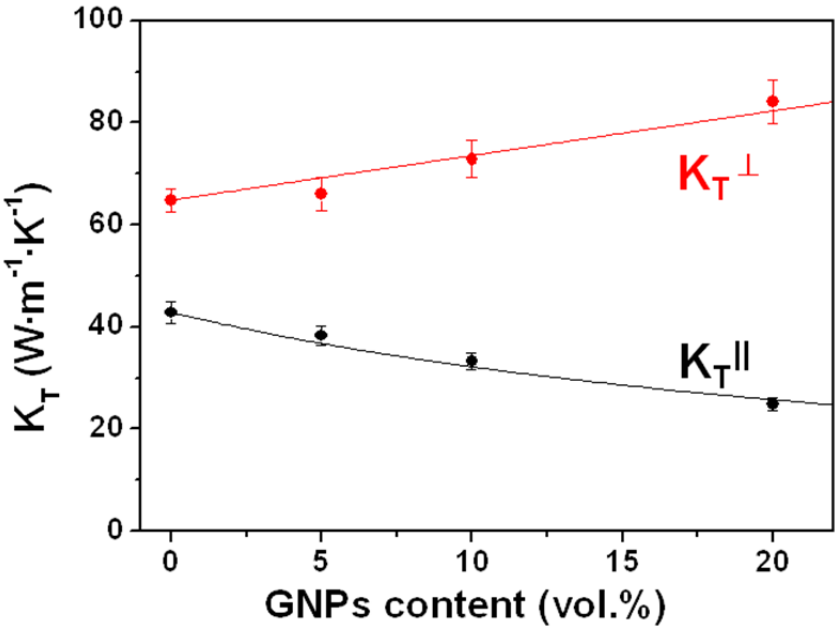

Figure 5.4.- Room temperature thermal conductivity (K_T) of the composites plotted as a function of the GNPs content for the through-thickness ($K_T^{\parallel}$) and in-plane ($K_T^{\perp}$) directions. Lines correspond to the model predictions according to Eqs. (7) and (8).

A wide range of K_T values, between 30 and 270 W·m^{-1}·K^{-1}, can be found in the literature for SiC-based materials,[2-6,8,11-17] depending mainly on the nature of the grain boundary phases and the solid solutions within the SiC lattice. To theoretically explain K_T values, phonons are assumed to be responsible for thermal conduction of SiC ceramics, as the electronic contribution (estimated with the Wiedemann-Franz law and the electrical conductivity) is negligible even in the case of the most electrically conductive ceramics. The lattice thermal conductivity can be expressed according to the kinetic theory of gases as:[18]

$$K_T = \frac{1}{3}\int_0^{f_M} C_v(\omega)\cdot\lambda\,(\omega)\cdot v(\omega)\,df \qquad (3)$$

where C_v is the heat capacity per unit volume, v is the phonon group velocity of acoustic phonons (speed of sound in the material), λ is the phonon mean free path, and ω is the phonon frequency considering that the phonon gas is vibrating in a range between 0 and the Debye frequency. There are generally three main types of phonon scattering: boundary (b), impurity (i), and phonon–phonon (p-p) interactions and, additionally, phonon-electron (p-e) interactions as in doped SiC. The effective mean free path, λ_{eff}, can then be expressed as:

$$\frac{1}{\lambda_{eff}(\omega,T)} = \frac{1}{\lambda_b(\omega,T)} + \frac{1}{\lambda_i(\omega,T)} + \frac{1}{\lambda_{p-p}(\omega,T)} + \frac{1}{\lambda_{p-e}(\omega,T)} \quad (4)$$

being the inverse sum of the different effective mean free paths associated to the different scattering processes. At very low temperatures, much lower than the Debye temperature, boundary scattering dominates over other processes and the phonon mean free path is constant and limited by the crystal boundary. Impurity scattering is highly frequency-dependent and dominates at intermediate temperatures, in the range where the thermal conductivity reaches a maximum, usually at approximately 1/10 of the Debye temperature. Substitutional solute atoms scatter phonons as a result of differences in atomic masses, in atomic binding forces, and lattice distortion introduced by the presence of the solute. However, its effect on the thermal conductivity diminishes at higher temperatures because phonon-defect scattering is almost independent of the temperature, becoming less important as compared to phonon-phonon scattering, which increases with temperature.

In this way, the thermal conductivity of SiC materials is usually reduced in the case of LPSed-SiC ceramics as a consequence of the creation of a complex distribution of defects introduced by variable SiO_2 amounts present in the native oxide layer of SiC powders or Al_2O_3 (currently used in the sintering additive system formulation). According to the models proposed by Zhou et al.,[8] SiO_2 and Al_2O_3 would induce the following defect reactions when dissolving into SiC:

$SiO_2 \rightarrow Si_{Si} + 2\ O_C + V_{Si}$

$Al_2O_3 \rightarrow 2\ Al_{Si} + 3\ O_C + V_{Si}$

producing defects such as aluminum in a silicon site (Al_{Si}), silicon vacancies (V_{Si}), or oxygen in carbon sites (O_C). Abeles,[19] back in 1963, analyzed the effect of phonon-defect scattering on K_T obtaining, at room and intermediate temperatures, a temperature dependence of the type:

$$K_T = \frac{1}{A\sqrt{\Gamma T} + BT} \quad (5)$$

where A and B are constants, and Γ is the scattering cross section which strongly depends on the local mass difference ($\Delta M/M$) and lattice mismatch ($\Delta\delta/\delta$) produced by a certain fraction (X) of lattice sites occupied by the impurity:

$$\Gamma = X(1-X)\left[\left(\frac{\Delta M}{M}\right)^2 + \epsilon\left(\frac{\Delta\delta}{\delta}\right)^2\right] \quad (6)$$

In the case of vacancies, the term (ΔM/M) is especially significant.

Moreover, the secondary phase at the grain boundaries (~5 vol.%) would also limit the heat transport as it forms a continuous grain boundary phase (see example cases in Fig. 5.5) consisting of a mixture of low thermal conductivity phases, i.e. YAG/YAP (~ 9 $W \cdot m^{-1} \cdot K^{-1}$)[20] and amorphous phases (~1.2 $W \cdot m^{-1} \cdot K^{-1}$)[21].

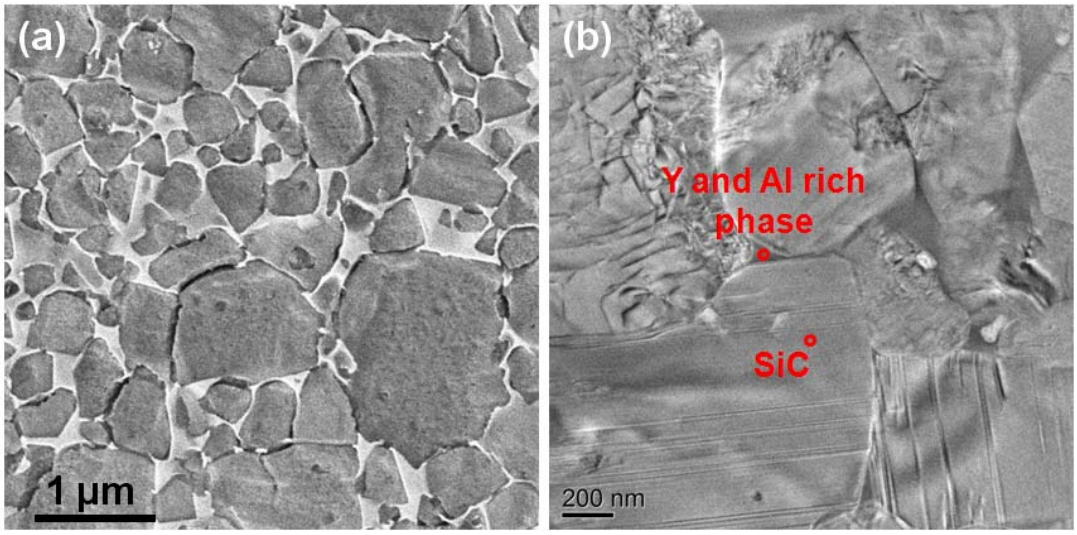

Figure 5.5.- (a) FESEM micrograph of the ceramic matrix of a 5 vol.% GNPs/SiC composite and (b) HRTEM micrograph of a GNPs-free SiC sample where a grain boundary phase containing Y and Al, and SiC were identified by EDS. In both cases, a continuous grain boundary phase is observed.

As for the effect of aligned GNPs, measurements performed in other ceramic matrices reproduce quite well a similar anisotropic behavior to that observed for SiC. In the case of Si_3N_4-based ceramics, increases in thermal conductivity in the in-plane direction from 40 to 61 $W \cdot m^{-1} \cdot K^{-1}$ (~52% increase, from 0 to 10 wt.% GNPs)[22] and from 20 to 38 $W \cdot m^{-1} \cdot K^{-1}$ (~90% increase, from 0 to 16.7 vol.% GNPs),[23] for HPed with AlN-Y_2O_3 and SPSed with Al_2O_3-Y_2O_3 samples, respectively, were recorded. These increases were higher than in the present case of SiC (~29%), probably because the absolute values for the monolithic ceramics were already higher in the case of SiC. In the direction parallel to the pressing axis, analogous decreases in thermal conductivity have been reported for 10 wt.%-containing SPSed Al_2O_3 composites (with a ~38% decrease from 31.6 to 19.7 $W \cdot m^{-1} \cdot K^{-1}$),[24] and for 10 wt.% containing GNPs/Si_3N_4 (20-30%, from ~28 to ~20 $W \cdot m^{-1} \cdot K^{-1}$ for HPed composites,[22] or from ~18 to ~14.5 $W \cdot m^{-1} \cdot K^{-1}$ for SPSed composites).[23] This decrease for the present case of SiC is ~40%.

The $K_T^{\perp}/K_T^{\parallel}$ ratio was employed for the evaluation of the thermal anisotropy of the GNPs/SiC composites. As for thermal diffusivity, a high degree of anisotropy is indeed observed, presenting a $K_T^{\perp}/K_T^{\parallel}$ ratio that evolves from ~1.5, in the case of the monolithic material, to ~3.4, for the composite with 20 vol.% GNPs (Fig. 5.6), thus increasing with the GNPs contents linked to their orientation with respect to the pressing axis (Fig. 3.23). These ratios are significantly lower than the intrinsic ratio for highly-ordered graphite (comparable to GNPs), which is between 200 and 300.[25] The higher $K_T^{\perp}/K_T^{\parallel}$ ratio at high contents for SiC compared to similar Si_3N_4 composites (plotted by a dashed line in Fig. 5.6) is believed to be due to the bigger size, and also aspect ratio, of the GNPs used in the present PhD Thesis (10-20 nm thickness, and 14 μm in the basal plane) as compared to that work (~1 nm thickness, and 0.2 μm in the basal plane).

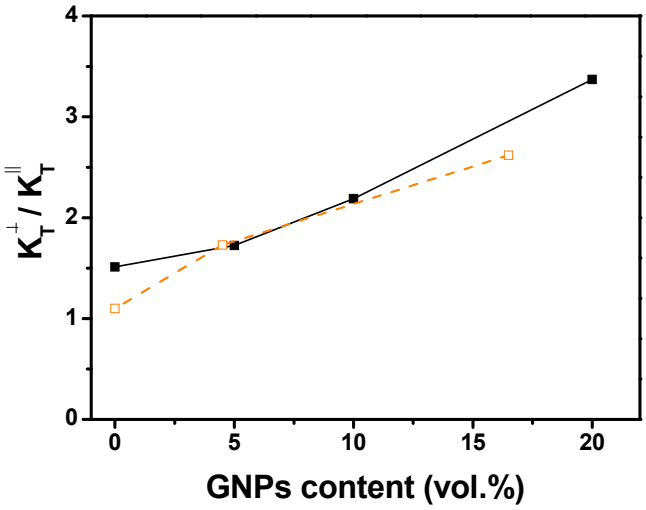

Figure 5.6.- $K_T^{\perp}/K_T^{\parallel}$ ratio as a function of the GNPs content. Unfilled squares linked by a dashed orange line represent the corresponding values for GNPs/Si_3N_4 composites with a similar Al_2O_3-Y_2O_3 system.[23]

The anisotropy of the monolithic composite could be attributed to both the formation of in-situ grown graphene flakes at the SiC grain boundaries as well as possible directional growth of the SiC grains during SPS due to the application of uniaxial mechanical pressure (50 MPa). Compared to the anisotropy of similar GNPs/Si_3N_4 composites, also plotted in Fig. 5.6,[23] the presence of in-situ grown graphene in SiC matrices induces a slightly larger anisotropy in the case of the monolithic materials.

Considering the elevated degree of anisotropy, a simple model of thermal resistances is proposed for the interpretation of the in-plane and through-thickness conductivities of the composites. In this way, the structure of these composites can be regarded as two distinct phases, the ceramic matrix and the dispersed GNPs, arranged as series or parallel thermal resistances for the heat flow when measuring in the through-thickness and in-plane directions, respectively. Thus, being V_{GNP} the volume fraction of GNPs, and $K_{GNP}^{||}$, $K_{GNP}^{\perp}$, $K_{cm}^{||}$ and $K_{cm}^{\perp}$ the intrinsic thermal conductivities of the GNPs and the ceramic matrix (cm) in the through-thickness ($^{||}$) and in-plane ($^{\perp}$) directions, the following relationships in Eqs. (7) and (8) are proposed:

$$K_T^{||^{-1}} = V_{GNP} {K_{GNP}^{||}}^{-1} + (1 - V_{GNP}) {K_{cm}^{||}}^{-1} = A^{||^{-1}} V_{GNP} + B^{||^{-1}} \quad (7)$$

$$K_T^{\perp} = V_{GNP} K_{GNP}^{\perp} + (1 - V_{GNP}) K_{cm}^{\perp} = A^{\perp} V_{GNP} + B^{\perp} \quad (8)$$

being the A constants the fitted parameters, equivalent to:

$$A^{||^{-1}} = {K_{GNP}^{||}}^{-1} - {K_{cm}^{||}}^{-1} \quad (9)$$

$$A^{\perp} = K_{GNP}^{\perp} - K_{cm}^{\perp} \quad (10)$$

and the B constants fixed parameters depending on the thermal conductivity of the ceramic matrix ($K_{cm}^{||}$ = 43 W·m^{-1}·K^{-1} and $K_{cm}^{\perp}$ = 65 W·m^{-1}·K^{-1}), defined as:

$$B^{||} = K_{cm}^{||} \quad (11)$$

$$B^{\perp} = K_{cm}^{\perp} \quad (12)$$

Consequently, $K_{GNP}^{||}$ and $K_{GNP}^{\perp}$ remain as unknown variables to be deduced from the K_T data fittings. These equations model the approximation of the case where totally parallel or totally series equivalent thermal resistances are simulated for the two phases. This is a reasonable choice grounded in previous patterns[26] for flat-plate-like dispersed phases, as GNPs, also assuming that an interfacial thermal barrier resistance between GNPs and the ceramic matrix is coupled to $K_{GNP}^{||}$. The GNPs are often bent and twisted, therefore, the GNP-SiC interfaces represent significant thermal barriers that might contribute to reduce the mean free path of phonons propagating within the composite in the parallel direction. In this way the value deduced for $K_{GNP}^{||}$ is underestimated.

Table 5.1.- Results of the fitting of the conductivity data in Fig 5.4 according to Eqs. (7) and (8).

Fitting	A ($W \cdot m^{-1} \cdot K^{-1}$)	B ($W \cdot m^{-1} \cdot K^{-1}$)	K_{GNP} ($W \cdot m^{-1} \cdot K^{-1}$)	Fit quality (%)
$K_T^{\parallel}$ [Eq. (7)]	12.9 ± 0.6	43	9.9 ± 0.6	94
$K_T^{\perp}$ [Eq. (8)]	87 ± 11	65	152 ± 11	98

The parameters resolved from the fitting are collected in Table 5.1. The fitting curves from the proposed model are displayed in Fig. 5.4 showing a reasonably adequate fitting. From the values of the fitted parameters ($A^{\perp}$ and $A^{\parallel}$), $K_{GNP}^{\perp}$ =152 ± 11 $W \cdot m^{-1} \cdot K^{-1}$ and $K_{GNP}^{\parallel}$= 9.9 ± 0.6 $W \cdot m^{-1} \cdot K^{-1}$ are inferred. Similar values of 133 and 6.9 $W \cdot m^{-1} \cdot K^{-1}$ for $K_{GNP}^{\perp}$ and $K_{GNP}^{\parallel}$ in the case of GNPs embedded within a Si_3N_4-matrix were obtained in a previous study.[27] The slightly larger conductivity values predicted in both directions of anisotropy for the present GNPs according to the proposed models is attributed to the bigger size, and also aspect ratio, of the GNPs used in the present study. The present multilayered GNPs within the ceramic composites show similar thermal behavior to graphite but not to graphene (see Fig. 5.7 for a reference). In fact, topmost conductivities were reported for suspended graphene monolayers with $K_T^{\perp}$ values from 5000 to 2000 $W \cdot m^{-1} \cdot K^{-1}$,[28,29] which coincide with computed estimations (~2000 $W \cdot m^{-1} \cdot K^{-1}$),[30] but tending to be smaller in the case of supported graphene (graphene supported on SiO_2 exhibited ~600 $W \cdot m^{-1} \cdot K^{-1}$).[31] As seen in Fig. 5.7, the value deduced for the in-plane thermal conductivity is very close to those of polycrystalline graphite (~200 $W \cdot m^{-1} \cdot K^{-1}$) at room temperature,[25,28,32] almost one order of magnitude lower than highly oriented pyrolytic graphite (HOPG), which exhibits a $K_T^{\perp}$ value at room temperature of ~2000 $W \cdot m^{-1} \cdot K^{-1}$,[33] which can be explained because GNPs present defects, being twisted and bent within the composite.

On the other hand, cross-plane conductivity of the pyrolytic graphite is 2-3 orders of magnitude smaller than in the in-plane direction (~6-7 $W \cdot m^{-1} \cdot K^{-1}$) at room temperature,[25] being close to the deduced value for $K_{GNP}^{\parallel}$ (9.9 $W \cdot m^{-1} \cdot K^{-1}$).

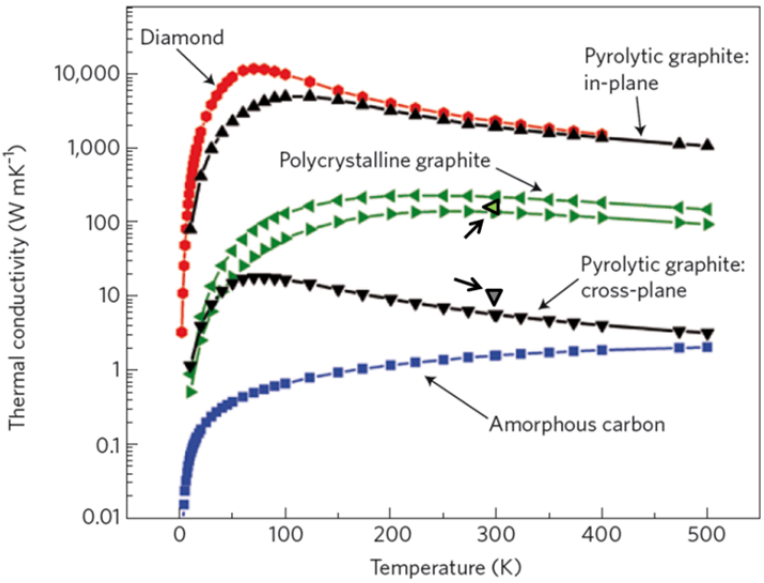

Figure 5.7.- K_T of different bulk carbon allotropes as a function of temperature. Plots are based on commonly accepted values from reference 25, represented by Balandin.[28] Arrows indicate the room temperature values obtained for the present for $K_{GNP}^{\perp}$ and $K_{GNP}^{||}$.

It should be pointed out that the model predictions for the 5 vol.% GNPs/SiC composite slightly deviate from the experimental data in both measuring directions, which are closer than predicted to the monolithic figures. These deviations may be attributed to a weak connectivity of the GNPs network for such low GNPs. In fact, more accurate values (68 and 40 $W \cdot m^{-1}K^{-1}$ for the effective in-plane and through-thickness thermal conductivities as compared to the obtained 66 and 38 $W \cdot m^{-1}K^{-1}$, respectively) are calculated for this material using the expression developed by Eucken (Eq. (13)),[34] which is an extension of the Maxwell equation, for dilute dispersed particles:

$$\frac{K_{eff}}{K_{cm}} = \frac{1+2r-2V_{GNP}(r-1)}{1+2r+V_{GNP}(r-1)} \qquad (13)$$

where r is the K_{cm}/K_{GNP} ratio.

In order to expand the comprehension of the thermal behavior of these composites above room temperature, $\alpha^{||}$ measurements were carried out up to temperatures of ~800 ºC (1073 K), as shown in Fig. 5.8, taking into account that the laser flash system is unable to perform measurements in-plane at temperatures higher than room temperature.

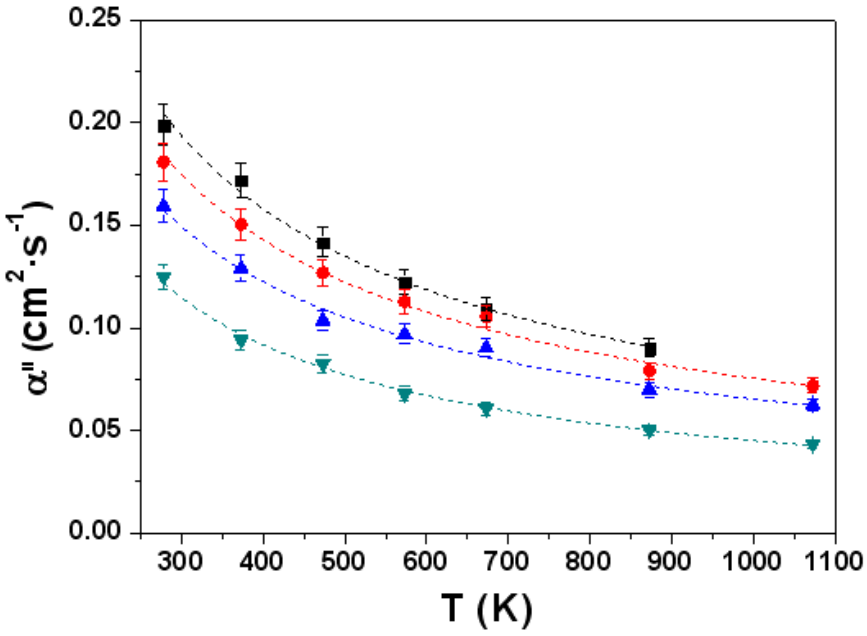

Figure 5.8.- Through-thickness thermal diffusivity, $\alpha^{\parallel}$, of GNPs/SiC composites as a function of temperature and GNPs content. Dotted curves are the fits to the data of each composite according to an $\alpha \sim A \cdot T^{-B}$ model.

As it usually occurs for dielectric materials, diffusivity decreases monotonically with temperature in all of the composites (Fig. 5.8). At room temperature the phonon mean free path is mainly limited by impurity/defect scattering and phonon scattering processes, including three-phonon scattering and Umklapp processes; the latter become the limiting processes with increasing temperature.[35] In this way, the allometric $\alpha \sim A \cdot T^{-B}$ approximation, with B usually lower than 1, is reasonable for patterning the effective decrease of diffusivity in dielectric materials.[36] Actually, the fits for $\alpha^{\parallel}$ shown in Fig. 5.8 ($A \cdot T^{-B}$ model fits drawn as dotted lines) reveal that composites ranging 0-10 vol.% GNPs exhibit similar dependence with temperature with B values ~0.70 ± 0.03, whereas the composites containing 20 vol.% GNPs exhibit a slightly more rapid decay (B ~ 0.78 ± 0.02).

The experimental $\alpha^{\parallel}$ (T) and the calculated C_p (T) data for the composites are used in Eq. (14) to calculate $K_T^{\parallel}$ as a function of temperature, giving the values plotted in Fig. 5.9. According to that equation, and introducing the corresponding temperature dependences of Cp (T) (well modelled by Eq. (2)) and $\alpha^{\parallel}$ (T) (fitting the allometric relationship $A \cdot T^{-B}$), the following prediction for the dependence of the thermal conductivity on temperature can be inferred:

$$K_T \sim A \cdot T^{-B} \cdot \exp(-\theta/T) \qquad (14)$$

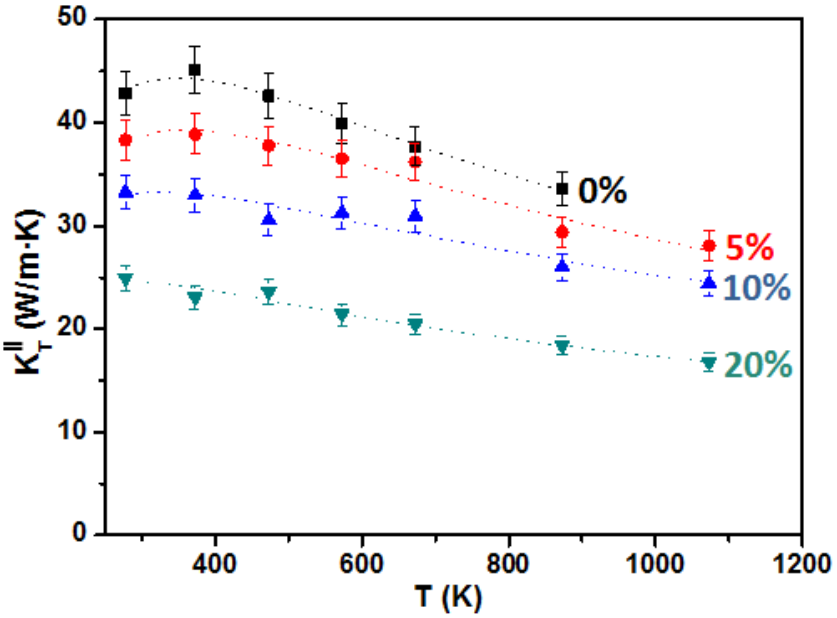

Figure 5.9.- Through-thickness thermal conductivity, K_T^{II}, of GNPs/SiC composites as a function of temperature and GNPs content. Dotted curves are the fits to the data of each composite according to the model in Eq. (14).

The dependence of the density with temperature is estimated by extrapolating the values at room temperature (ρ_0) with the relation:

$$\rho(T) = \rho_0 / (1 + 3\alpha\Delta T) \qquad (15)$$

where *α is* the thermal expansion coefficient of the composites. The thermal expansion coefficient was calculated from the slope of the expansion curves (Fig. 5.10) for different GNPs/SiC composites, measured in the in-plane direction. As shown, in the temperature range 200-800 ºC, it is very similar, 4.3 x 10^{-6} K^{-1} for 0 and 10 vol.% of GNPs, and slightly higher for 20 vol.% of GNPs (4.5 x 10^{-6} K^{-1}). Considering these values, ρ/ρ_0 can be well approximated as constant with temperature and equal to 1.

Table 5.2 shows the results of the fitting for the four materials. The fittings corresponding to Eq. (14) are plotted as dotted lines in Fig. 5.9, showing good agreement with the experimentally determined thermal conductivity data. The strong dependence of $C_p(T)$ with temperature (Fig. 5.3) in these SiC-based composites is very slowly counterbalanced by the weak temperature evolution of α^{II} (Fig. 5.9). As K_T in the through thickness direction decreases with increasing amounts of GNPs both fitting parameters B and θ become smaller with increasing GNPs content.

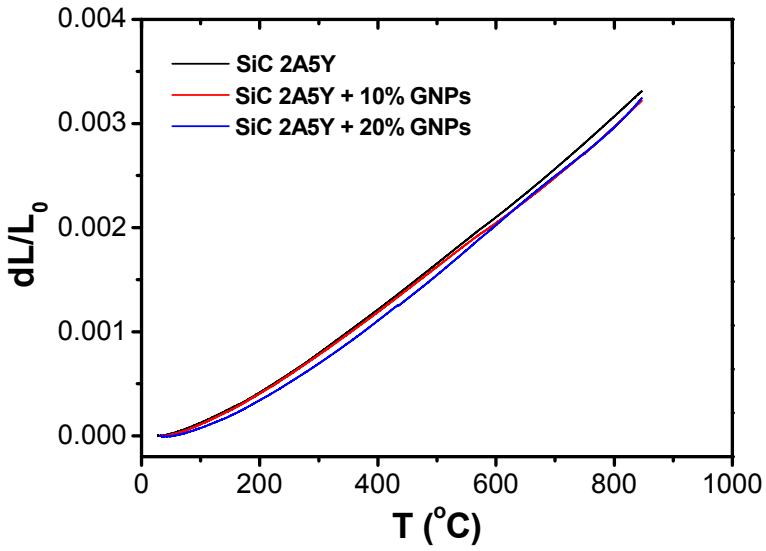

Figure 5.10.- Thermal expansion curves (dL/L_0) for the 0, 10 and 20 vol.% GNPs/SiC composites as a function of temperature.

Table 5.2.- Results of the fit for the through thickness thermal conductivity (K_T^{II}) according to the model $K_T \sim A \cdot T^{-B} \cdot \exp(-\theta/T)$ (Eq. 14).

GNPs content (vol.%)	Fit Quality (%)	B	θ (K)
0	98.3	0.91 ± 0.09	318 ± 42
5	93.6	0.83 ± 0.16	300 ± 78
10	89.1	0.62 ± 0.18	202 ± 89
20	96.6	0.61 ± 0.12	164 ± 59

It is possible to estimate the effective mean free path of the lattice vibrations in each material from Eq. (3) introducing the group velocity, estimated from $\nu = \sqrt{E/\rho}$, where E and ρ represent the elastic modulus and the density at room temperature of each composite, respectively (E values were taken from Table 3.10). The resulting curves, plotted for the parallel and perpendicular direction in Fig. 5.11, show almost no

dependence of λ^{II} with increasing amounts of GNPs, implying almost no contribution of GNPs to the K_T^{II}. Considering average values of ~10 nm for the GNPs thickness, an increment in the effective mean free path of the composites is not expected. In the in-plane direction $\lambda^{\perp}$ is significantly increased showing, again, the anisotropic contribution of GNPs to the thermal conduction, and the possible connectivity between GNPs especially above 10 vol.% GNPs contents.

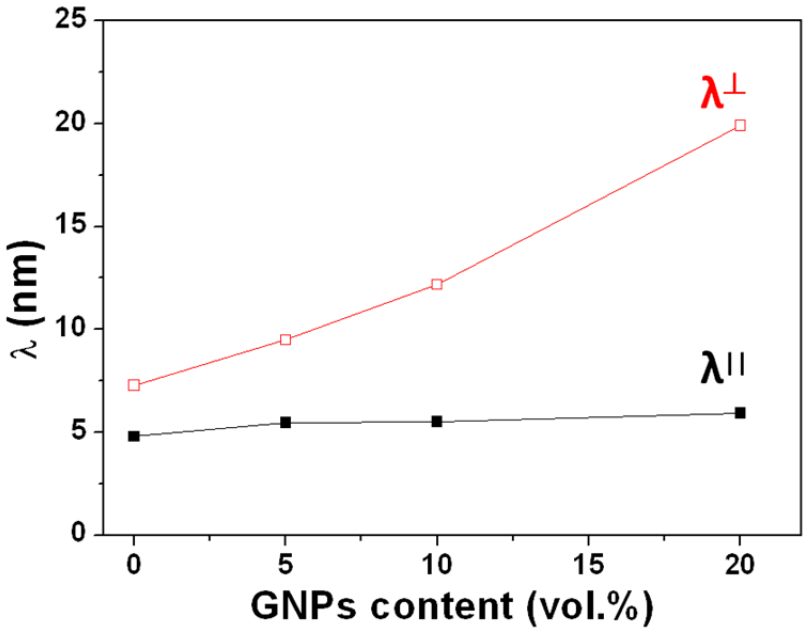

Figure 5.11.- Estimation for the effective mean free path of phonons (λ), obtained with the elastic moduli of materials at room temperature, as a function of the GNPs contents for in-plane ($\lambda^{\perp}$) and through-thickness (λ^{II}) directions.

5.2.- Electrical properties of graphene/SiC composites

In Subsection 4.2 in Chapter 4, the works published on the electrical conductivity of monolithic SiC-based ceramics were reviewed, concluding that σ values oscillated within the wide range from 10^{-9} to 10^{5} $S \cdot m^{-1}$, mainly as a function of the type of doping that often result from the sintering additives employed for the densification process. Also, a succinct review on GNPs and rGOs employed for the electrical functionalization of ceramic composite materials was shown in Subsection 1.5.2, Chapter 1, of the present PhD Thesis. Most significantly, increments in the electrical conductivity of up to 14 orders of magnitude for insulating ceramic matrices have been reached when adding graphene-based sources, defining thresholds of percolation for these GNPs/ceramic composites below 10 vol.% GNPs.

As a clear lack is detected in the literature for SiC, a similar study to that carried out for thermal conductivity has been attempted for the electrical conductivity of the GNPs/SiC composites. For the electrical characterization, measurements were performed under variable temperature (278-523 K) in an air atmosphere, in the directions parallel ($\sigma^{||}$) and perpendicular ($\sigma^{\perp}$) to the SPS pressing axis (Fig. A.2.7). For more details on the measuring system, see A.2.10. The room temperature electrical conductivity of the GNPs/SiC composites as a function of the GNPs content measured for the sample directions parallel ($\sigma^{||}$) and perpendicular ($\sigma^{\perp}$) to the SPS pressing axis is shown in Fig. 5.12.

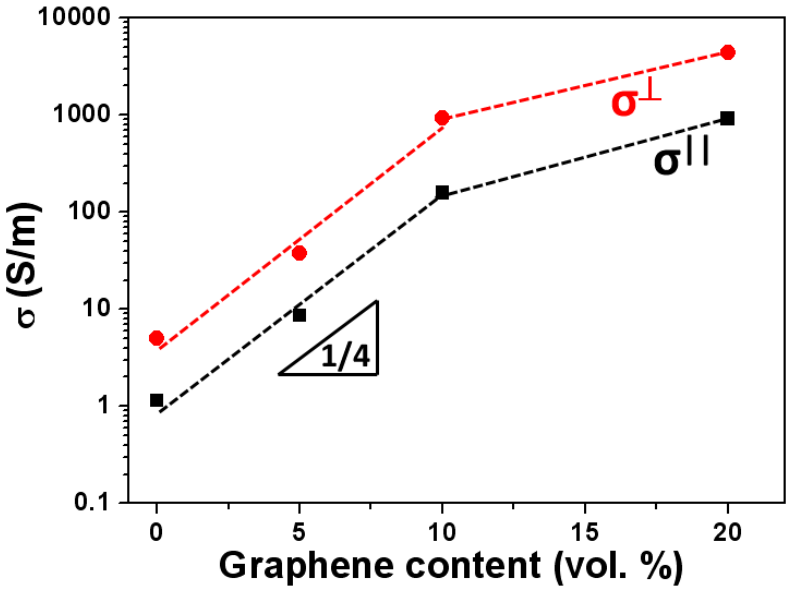

Figure 5.12.- Room temperature electrical conductivity of the GNPs/SiC composites plotted as a function of the GNPs content for directions parallel ($\sigma^{||}$) and perpendicular ($\sigma^{\perp}$) to the SPS pressing axis. Note the linear trend with slope ~¼ for GNPs contents lower than 10 vol.%.

Both $\sigma^{||}$ and $\sigma^{\perp}$ increase up to three orders of magnitude by addition of up to 20 vol.% GNPs in comparison to the monolithic SiC sample, confirming the expected effect of the GNPs of enhancing the electrical conductivity of the composites. The σ values in the direction perpendicular to the pressing axis (e.g. $\sigma^{\perp}$ of 922 $S \cdot m^{-1}$ and 4378 $S \cdot m^{-1}$ for samples with 10 and 20 vol.% GNPs, respectively, at room temperature) are comparable to those reported in the literature for 10 vol.% GNPs/Al_2O_3 (1300 $S \cdot m^{-1}$)[37] or 24 vol.% GNPs/Si_3N_4 (4100 $S \cdot m^{-1}$) composites.[38] In the case of Si_3N_4 or Al_2O_3 ceramics, which are electrical insulators (<10^{-8} $S \cdot m^{-1}$, at room temperature), the conductivity *vs*. fraction of graphene for the corresponding composites implies a

percolation–type behavior. In contrast, the graphene-like network formed in-situ during the SPS process (see Chapter 3, Section 3.2) and the possible doping of SiC leads to a much higher conductivity ($\sigma^{||}$ = 0.81 S·m^{-1} and $\sigma^{\perp}$ = 5.04 S·m^{-1} at room temperature) than that reported for monolithic SiC ceramics containing similar type and amount of sintering additives ($\sigma < 10^{-7}$ S·m^{-1}).[39] Therefore, instead of the sharp increase of conductivity for a particular fraction of graphene (characteristic of percolation), Fig. 5.12 depicts an approximately linear trend (slope of ~1/4) for $\log_{10}\sigma$ *vs*. GNPs content for up to 10 vol.% GNPs. This trend deviates for higher GNPs content, which indicates a change in the type of phase connectivity as a result of both the nanoplatelet orientation and the increase in GNPs volume fraction. Consequently, the GNPs network dominates the overall behavior. In the case of Si_3N_4 insulating ceramics, a percolation threshold was observed for comparable GNPs contents,[38] indicating a similar change in the connectivity of platelets.

As a first approximation to describe the compositional dependence of the conductivity of the composites, the general mixing rule is considered:[40]

$$\sigma^n = V_{GNP}\sigma_{GNP}^n + (1 - V_{GNP})\sigma_{cm}^n \quad (16)$$

where σ_{GNP} and σ_{cm} are the conductivities of GNPs and the SiC-based matrix, respectively, and V_{GNP} is the volume fraction of GNPs. The exponent n accounts for the phase connectivity mode, being 1 for a parallel arrangement of both phases in the direction of the current flow, and -1 for a series arrangement. These are the two extreme configurations, and intermediate n values correspond to mixed arrangements.

Eq. (16) was thus used to fit the data in Fig. 5.12 in order to gain insight on the electrical behavior of the composites. The conductivity of the sample with 0 vol.% GNPs ($\sigma^{||}$ = 0.81 S·m^{-1} and $\sigma^{\perp}$ = 5.04 S·m^{-1}) is assumed as σ_{cm} and was a fixed parameter in the calculations. This represents the electrical conductivity of a complex three-phase mixture comprising the SiC grains, the secondary phase, and the graphene formed in-situ during the SPS, as shown in Section 3.2 of this PhD Thesis. Since there is no direct measurement of the conductivity of GNPs, σ_{GNPs} is left as a fitting parameter. In fact, σ_{GNP} can vary significantly depending on the defect concentration and the orientation of the GNPs. As starting point for the fitting, and given the multilayered structure of the GNPs used in this PhD Thesis, values of 10^6 and 10^4 S·m^{-1} were assumed for the *ab*-plane and the corresponding normal

direction, respectively, based on data from literature for GNPs or graphite-type materials.[38,41,42]

Table 5.3 lists the results of the fits. The model reproduces the measured conductivities with very small deviations. The estimated σ_{GNP} are roughly constant for the three compositions, and about one order of magnitude higher for the perpendicular direction. The exponent *n* is positive and lower than 0.35 in all cases, which indicates a homogenous distribution of both phases (ceramic matrix and GNPs) ensuring parallel transport paths. On the other hand, the fact that *n* is distinctively smaller for the samples with 5 vol.% GNPs, and is similar for the samples with 10 and 20 vol.%, suggests a change in the phase connectivity mode when the GNPs fraction increases from 5 to 10 vol.%.

Table 5.3. Results of the fitting of the conductivity data in Fig. 5.12 according to the mixing rule expressed by Eq. (16).

	Perpendicular to the pressing axis				**Parallel to the pressing axis**			
Vol.% GNPs	$\sigma^{\perp}$ **(S·m^{-1})**	σ_{GNP} **(S·m^{-1})**	***n***	**error [a] (S·m^{-1})**	$\sigma^{\parallel}$ **(S·m^{-1})**	σ_{GNP} **(S·m^{-1})**	***n***	**error [a] (S·m^{-1})**
5	38.1	1.00×10^{6}	0.19	6.93×10^{-6}	8.66	9.83×10^{4}	0.21	3.76×10^{-5}
10	922	9.92×10^{5}	0.30	3.59×10^{-4}	159	8.89×10^{4}	0.34	7.46×10^{-4}
20	4378	8.96×10^{5}	0.28	4.89×10^{-3}	935	7.94×10^{4}	0.35	4.03×10^{-3}

[a] $error = \sqrt{\left|\sigma^2_{estimate} - \sigma^2_{measure}\right|}$

It is quite remarkable that the factor of electrical anisotropy, i.e. the ratio $\sigma^{\perp}/\sigma^{\parallel}$, does not vary much with the GNPs content (between 4.5 and 6.2), including the monolithic SiC sample with no GNPs addition. This observation is not totally unexpected since the GNPs are oriented regarding the SPS pressing axis and the conductivity is determined, in all cases, by graphitic domains with intrinsic electrical anisotropy. There are, however, important differences that become significant when analyzing the effect of temperature on the conductivity. Data are plotted in Fig. 5.13 according to the variable range hoping (2D-VRH) model:

$$\sigma = \sigma_0 exp\left(-BT^{-1/3}\right) \quad (17)$$

where σ_0 is a pre-factor and *B* is the hopping parameter measuring the energy cost associated to the charge hopping between pristine graphene domains along the ab-plane.[38,43] The hopping parameter *B* is an indirect measurement of the purity degree of graphene. *B* is thus expected to be lower for materials with lower concentration of defects, since there is less energy needed for the charge hopping between the pure graphene domains (where the conduction mechanism is of ballistic-type).

Despite the large difference in the magnitude of the conductivity of the various samples, Fig. 5.13 shows a weak temperature dependence, which is in excellent agreement with Eq. (17) (regression coefficients $r^2 > 0.998$). The observation of two slopes for the high and low temperature ranges is a common feature for several of the present materials, with higher B values at high temperature. The origin for such apparent change in the conduction mechanism is likely to result from the coexistence of two parallel electrical paths, each characterized by a different *B*. It can be easily concluded from this assumption that the path with lower *B* predominates at low temperature, whereas the path with higher B, which eventually dominates the total conductivity above a certain temperature, shows a conductivity that increases at a higher rate with increasing temperature. The volume fraction of GNPs within the ceramic matrix and the conductivity of each electrical path, which are likely to change with increasing GNPs additions, must be considered to explain the existence of both the two regimes and the transition temperature between them.

To continue the analysis, it is useful to separate the case of the composites with and without GNPs additions. In the composites with just the graphene grown in-situ (0 vol.% GNPs), a certain orientation of the graphene flakes with respect to the SPS pressing axis cannot be discarded, and the properties (e.g. domain size and defect concentration) of the crystalline graphitic nanodomains formed during the SPS at the grain boundaries should depend on the percolation path of the pulsed current and the applied pressure (See Fig. 3.23 corresponding to FESEM micrographs of the fracture surface). The higher *B* for $\sigma^{\parallel}$ than for $\sigma^{\perp}$ (Fig. 5.13, 0 vol.% GNPs) suggests a higher defect concentration in the graphene domains located at the grain boundaries parallel to the pressing axis than in the graphene domains of the perpendicular grain boundaries and, thus, $\sigma^{\perp}$ should indeed be higher than $\sigma^{\parallel}$. As both types of grain boundaries co-exist in the material, the two slopes in the $\log(\sigma^{\perp})$ *vs.* $T^{-1/3}$ representation with a larger B value at high temperature suggest an increasing role of the parallel contribution with increasing temperature. Also, the more conductive perpendicular grain boundaries represent a smaller resistance in series with the

highly resistive SiC grains when measuring in the direction parallel to the SPS pressing axis and, thus, the total resistance of the sample in this direction is essentially determined by the less conductive parallel grain boundaries. Indeed, the plot of $\log(\sigma^{\parallel})$ vs.$T^{-1/3}$ displays a single slope for the ceramic matrix (0 vol.% GNPs) in the entire temperature range, featuring the highest *B* value of all materials (31.7 $K^{1/3}$). It should be noticed that the intrinsic electrical anisotropy of the in-situ graphitic nanodomains might also contribute to the observed electrical anisotropy of the ceramic material, assuming that these nanodomains tend to be aligned with their most conductive *ab*-plane perpendicular to the pressing axis. The similarity of the electrical anisotropy ratios ($\sigma^{\perp}/\sigma^{\parallel}$) for all the materials supports this assumption.

The addition of GNPs introduces additional complexity to the previous case. Besides the strong enhancement of $\sigma^{\perp}$, the addition of more than 5 vol.% GNPs leads to one single slope with $B \approx 9.5\ K^{1/3}$ (Fig. 5.13), much smaller than that for the composite without GNPs, indicating that the conduction is determined mostly by these fillers. In fact, the *B* value is equal to that estimated for GNPs/Si_3N_4 ceramic composites with up to 25 vol.% GNPs,[38] where the dielectric nature of the Si_3N_4 matrix ensures that the electrical transport occurs only through the GNPs network. The lower *B* for the two samples with highest GNPs content also indicates a lower defects concentration for the GNPs than for the graphene grown in-situ, in agreement with the higher Raman I_D/I_G intensity ratio for the sample with 0 vol.% GNPs (0.58 vs. 0.25—0.33 for composites containing 5—20 vol.% GNPs, see Chapter 3). The transition from the two-slope to the one-slope temperature dependence observed between 5 and 10 vol.% GNPs correlates well with the increase in the exponent *n* estimated through Eq. (16), also an indication of the change of the connectivity mode where the GNPs network prevails.

A noticeable transition between 5 and 10 vol.% GNPs is also observed on the *B* values measured for $\sigma^{\parallel}$. Contrary to the trend observed for $\sigma^{\perp}$, the composites with 10 and 20 vol.% GNPs display two distinct slopes. At low temperature, with $B \approx 9.5\ K^{1/3}$, the dominant contribution of the GNPs and the conduction along the basal plane of the nanoplatelets is denoted; and another slope at high temperature with higher *B* (~27.9 $K^{1/3}$ and ~23.3 $K^{1/3}$ for the 10 and 20 vol.% GNPs composites, respectively). This second slope may be seen as a hint of a larger contribution of the conduction across the c-axis of the GNPs, or of more defective graphene nanodomains aligned parallel to the pressing axis.

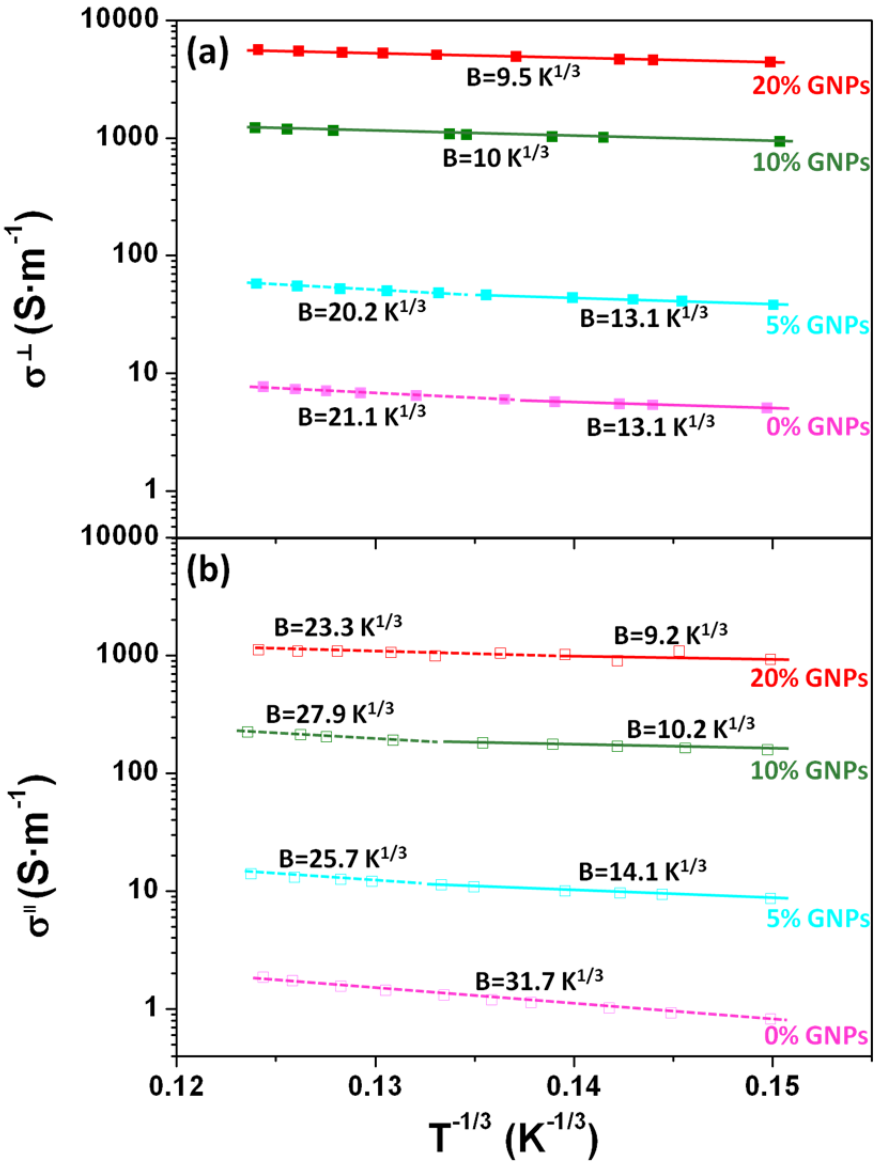

Figure 5.13.- Temperature dependence of the electrical conductivity of the various GNPs/SiC samples plotted according to 2D-VRH model for the (a) perpendicular ($\sigma^{\perp}$) and (b) parallel ($\sigma^{\parallel}$) measuring directions. The lines are linear fits to the high (dashed) and low (solid) temperature ranges of the data, with indication of the corresponding *B* values.

5.3.- Conclusions

i) The major orientation of GNPs within the SiC matrix in the plane perpendicular to the pressing axis provides the composites with markedly anisotropic transport performance, in particular, the thermal conductivity is 1.5 to 3.4 times higher and the electrical conductivity 4 to 6 times higher in the perpendicular direction than in the

parallel direction. However, the GNPs-free composite also show anisotropic behavior, which was explained by a higher defect concentration in the graphene domains formed in-situ at the intergranular regions parallel to the SPS pressing axis

ii) The addition of GNPs to SiC ceramics increases thermal conductivity in the in-plane direction, but reduces the through-thickness thermal conductivity, due to the thermal resistance of the GNPs-SiC interfaces and the low thickness of added GNPs.

iii) A simple model based on an equivalent thermal resistances system is proposed to model the effective through-thickness (series) and in-plane (parallel) thermal conductivities, estimating the K_T value of the GNPs in the basal plane and along the c-axis in 152 and 9.9 $W \cdot m^{-1} \cdot K^{-1}$, respectively.

iv) The GNPs augment the electrical conductivity of the composites in both directions up to three orders of magnitude as compared to the monolithic materials, reaching a maximum value at room temperature of 4380 S m^{-1} for composites with 20 vol.% GNPs. However, no percolation-type conductivity was detected because the monolithic material also exhibits high conductivity. A 2D variable range hopping mechanism is proposed with two competitive parallel conduction paths.

5.4. References

1. Slack GA. Thermal conductivity of pure and impure silicon, silicon carbide, and diamond. J Appl Phys 1964; 35(12): 3460-6.
2. Nakano H, Watari K, Kinemuchi Y, Ishizaki K, Urabe K. Microstructural Characterization of High-Thermal-Conductivity SiC Ceramics, J Eur Ceram Soc 2004; 24: 3685–90.
3. Ogihara S, Maeda K, Yakeda Y, Nakamura K. Effect of Impurity and Carrier Concentrations on Electrical Resistivity and Thermal Conductivity of SiC Ceramics Containing BeO. J Am Ceram Soc 1985; 68(1): C16–8.
4. Sigl LS. Thermal conductivity of liquid phase sintered silicon carbide. J Eur Ceram Soc 2003; 23(7):1115-22.
5. Zhan GD, Mitomo M, Mukherjee AK. Effects of heat treatment and sintering additives on thermal conductivity and electrical resistivity in fine-grained SiC ceramics. J Mat Res 2002; 17(9): 2327-33.

6. Sakai T, Aikawa T. Phase Transformation and Thermal Conductivity of Hot-Pressed Silicon Carbide Containing Alumina and Carbon. J Am Ceram Soc 1988; 71(1): C-7.
7. Tajima Y, Kingery WD. Solid Solubility of Aluminum and Boron in Silicon Carbide. J Am Ceram Soc 1982; 65(2)*:* C27–9.
8. Zhou Y*,* Hirao K*,* Yamauchi Y, Kanzaki S. Effects of Rare-Earth Oxide and Alumina Additives on Thermal Conductivity of Liquid-Phase-Sintered Silicon Carbide. J Mater Res 2003; 18(8): 1854–62.
9. Roine A. Outokumpu HSC Chemistry for Windows V 5.11. Outokumpu Research; Pori, Finland, 2002.
10. Popov VN. Low-temperature specific heat of nanotube systems. Phys Rev B 2002; 66(15): 153408.
11. Watari K*,* Nakano H*,* Sato K*,* Urabe K*,* Ishizaki K*,* Cao S*,* Mori K. Effect of Grain Boundaries on Thermal Conductivity of Silicon Carbide Ceramic at 5 to 1300 K. J Am Ceram Soc 2003; 86(10):1812–4.
12. Kinoshita T, Munekawa S. Effect of Grain Boundary Segregation on Thermal Conductivity of Hot-Pressed Silicon Carbide. Acta Mater 1997*;* 45(5): 2001–12.
13. Kim Y-W, Lim K-Y, Seo W-S. Microstructure and Thermal Conductivity of Silicon Carbide with Yttria and Scandia. J Am Ceram Soc 2014; 97: 923–28.
14. Zhou Y*,* Hirao K*,* Watari K*,* Yamauchi Y*,* Kanzaki S. Thermal Conductivity of Silicon Carbide Densified With Rare-Earth Oxide Additives. J Eur Ceram Soc 2004; 24*:* 265–70.
15. Zhang C, Yao X, Li Y, Liang H, Chen J, Zhang J, Yang J, Li X, Qiu T, Chen Z, Liu X, Huang Z. Effect of AlN addition on the thermal conductivity of pressureless sintered SiC ceramics. Ceram Int 2015; 41(7): 9107-14.
16. Takeda Y. Development of high-thermal-conductive SiC ceramics. Am Ceram Soc Bull 1988; 67(12).
17. Liu DM, Lin BW. Thermal conductivity in hot-pressed silicon carbide. Ceram Int 1996; 22(5): 407-14.
18. Klemens PG. Thermal conductivity and lattice vibrational modes. Solid state physics, 7, 1-98.1958. Ed. F. Seitz and D. Turnbull, Vol 7,P1, Academic Press, New York.
19. Abeles, B. Lattice thermal conductivity of disordered semiconductor alloys at high temperatures. Phys Rev 1963; 131(5): 1906.
20. Padture NP, Klemens PG. Low thermal conductivity in garnets. J Am Ceram Soc 1997; 80(4): 1018-20.

21. Cohn JL, Nolas GS, Fessatidis V, Metcalf TH, Slack GA. Glasslike heat conduction in high-mobility crystalline semiconductors. Phys Rev Lett 1999; 82(4): 779.
22. Rutkowski P, Stobierski L, Górny G. Thermal stability and conductivity of hot-pressed Si_3N_4–graphene composites. J Therm Anal Calorim 2014; 116(1):321-8.
23. Miranzo P, García E, Ramírez C, González-Julián J, Belmonte M, Osendi MI. Anisotropic thermal conductivity of silicon nitride ceramics containing carbon nanostructures. J Eur Ceram Soc 2012; 32(8): 1847-54.
24. Rutkowski P, Klimczyk P, Jaworska L, Stobierski L, Dubiel A. Thermal properties of pressure sintered alumina–graphene composites. J Therm Anal Calorim 2015. Doi: 10.1007/s10973-015-4694-x.
25. Ho CY, Powell RW, Liley PE. Thermal conductivity of the elements. Journal of Physical and Chemical Reference Data 1972; 1(2): 279-421.
26. Hasselman DPH, Johnson LF. Effective thermal conductivity of composites with interfacial thermal barrier resistance. Journal of Composite Materials 1987; 21(6): 508-15.
27. Ramírez Maglione MC. PhD Thesis: Materiales multifuncionales de nitruro de silicio con nanoestructuras reforzanters basadas en grafeno. 2014. http://hdl.handle.net/10486/662461
28. Balandin AA, Ghosh S, Bao W, Calizo I, Teweldebrhan D, Miao F, Lau CN. Superior thermal conductivity of single-layer graphene. Nano letters 2008; 8(3):902-7.
29. Chen S, Moore AL, Cai W, Suk JW, An J, Mishra C, Amos C, Magnuson CW, Kang J, Shi L, Ruoff RS. Raman measurements of thermal transport in suspended monolayer graphene of variable sizes in vacuum and gaseous environments. ACS Nano 2010; 5(1):321-8.
30. Alofi A, Srivastava GP. Thermal conductivity of graphene and graphite. Phys Rev B 2013; 87(11):115421.
31. Seol JH, Jo I, Moore AL, Lindsay L, Aitken ZH, Pettes MT, Li X, Yao Z, Huang R, Broido D, Mingo N, Ruoff RS, Shi L. Two-dimensional phonon transport in supported graphene. Science 2010, 328(5975), 213-6.
32. Woodcraft AL, Barucci M, Hastings PR, Lolli L, Martelli V, Risegari L, Ventura G. Thermal conductivity measurements of pitch-bonded graphites at millikelvin temperatures: finding a replacement for AGOT graphite. Cryogenics 2009; 49(5): 159-164.

33. Dreyfus B, Maynard R. Analyse de la conductibilité thermique du graphite.-II. théorie. J Phys 1967 ; 28(11-12): 955-66.
34. Introduction to ceramics. Kingery WD. John Wiley & Sons. 1976.
35. Watari K, Ishizaki K, Tsuchiya F. Phonon scattering and thermal conduction mechanisms of sintered aluminium nitride ceramics. J Mater Sci 1993; 28(14): 3709-14.
36. Klemens PG. The thermal conductivity of dielectric solids at low temperatures (theoretical). In Proceedings of the Royal Society of London A: Mathematical, Physical and Engineering Sciences 1951; 208 (1092): 108-33. The Royal Society.
37. Fan Y, Wang L, Li J, Li J, Sun S, Chen F, Chen L, Jiang W. Preparation and electrical properties of graphene nanosheet/Al_2O_3 composites. Carbon 2010; 48:1743-9.
38. Ramírez C, Figueiredo FM, Miranzo P, Poza P, Osendi MI. Graphene nanoplatelet / silicon nitride composites with high electrical conductivity. Carbon 2012; 50:3607-15.
39. Sánchez-González J, Ortiz AL, Guiberteau F, Pascual C. Complex impedance spectroscopy study of a liquid-phase-sintered α-SiC ceramic. J Eur Ceram Soc 2007; 27:3935–9.
40. McLachlan DS, Blaszkiewicz M, Newnham RE. Electrical resistivity of composites. J Am Ceram Soc 1990; 73(8): 2187-203.
41. Edman L, Sundqvist B, McRae E, Litvin-Staszewska E. Electrical resistivity of single-crystal graphite under pressure: an anisotropic three-dimensional semimetal. Phys Rev B 1998; 57:6227-30.
42. Celzard A, Mareche JF, Furdin G, Puricelli S. Electrical conductivity of anisotropic expanded graphite-based monoliths. J Phys D: Appl Phys 2000; 33(23):3094.
43. Kaiser AB, Gómez-Navarro C, Sundaram RS, Burghard M, Kern K. Electrical conduction mechanism in chemically derived graphene monolayers. Nano Lett 2009; 9(5): 1787-92.

Chapter 6

Electrical performance of 3D architectured graphene/SiC structures

6.1.- Electrical properties of graphene/SiC ceramic scaffolds

6.1.1.- Introduction: 3D architectures of graphene

As analyzed in the previous Chapter, bulk GNPs/SiC composites exhibited enhanced transport properties as compared to GNPs-free SiC due to the more elevated thermal and electrical conductivities of the GNPs fillers. In addition, 3D architectures of graphene are of interest for a number of applications where high thermal and electrical conductivities are crucial, such as energy storage/conversion systems or supports for electrocatalysis membranes and gas sensors. Therefore, the significance of developing advanced materials that combine the transport properties of GNPs/SiC composites with the low density, high specific surface area or the feasibility of hierarchical designs is addressed in the present Chapter. The electrical conduction of such complex composite structures has been experimentally determined as well as simulated by using both a simple resistors model and the finite-elements method (FEM) to predict the scaffolds conductivity as a function of the GNPs content, the scaffold geometric parameters, the rod-to-rod contact area, and the conductivity of the single rods.

The development of 3D cellular structures/networks of graphene and graphene composites is appreciated for a wide range of emerging applications such as energy storage/conversion,[1-3] due to quite useful characteristics as thermal management capabilities or highly accessible surfaces,[4] which allows the access of electrolytes to the conductive surface exhibiting a fast electron transfer when acting as electrodes.

In 2011, the achievement of graphene foams grown by CVD using Ni sacrificial templates[5,6] blazed a trail towards the fabrication of novel 3D-structured graphene-based materials. 3D macroporous graphene networks have been created ever after by various methods (see a review in ref. 7), among others, direct templating cellular structures using these CVD methods (usually to subsequently anchor metal oxide nanoparticles such as MnO_2[8] or Co_3O_4)[9] by employing SiO_2 aerogels as templates for CVD,[10] self-assembling graphene sheets with a hierarchical structure,[11] and ice templating methods.[12] Robocasting has recently been employed as a 3D printing method for the creation of 3D structured GO microlattices[13-15] of very low density (in the range 31-123 $mg \cdot cm^{-3}$) and electrical conductivity values of 87-278 $S \cdot m^{-1}$.[13,14]

The combination in one material of the robustness and electrical and thermal conductivities of GNPs/SiC composites with the intrinsic characteristics of the macroporous 3D GNPs/SiC structures developed by RC in Chapter 3 are intended to

have several potential advantages with respect to analogous graphene structures, as the ceramics would provide mechanical stability and also protection of graphene from wear damage, corrosion and thermal degradation. No attempts of embedding GNPs within 3D ceramic structures have been reported so far. Only a few tries of using a carbothermic reduction CVD process to grow graphene on Al_2O_3 foams,[16] 3D-structured SiO_2 porous materials,[17] and cordierite substrates[18] are known. These materials were intended as reservoirs with enhanced thermal management for phase change materials.[19]

6.1.2.- Materials processing

Scaffolds corresponding to the β7 composition, containing 0, 5, 10 and 20 vol.% GNPs, whose manufacture was described in Chapters 2 and 3, were employed for the electrical characterization. Cuboid lattices (13 x 13 x 10 mm^3 size) were robocast through nozzles with 330 μm diameter for all compositions according to the computer design of Fig. 6.1a. As shown in Chapter 2, dried green structures were heated to burn-out the organics at 415 ºC for 1h in air. For the present study, even the GNPs-free samples were subjected to those temperatures in order not to introduce variability among the different compositions. Afterwards, the 3D structures were sintered in the SPS furnace at 1800 °C for 5 min using the standard cycle. As usual, sintering runs for scaffolds were done in an Ar atmosphere.

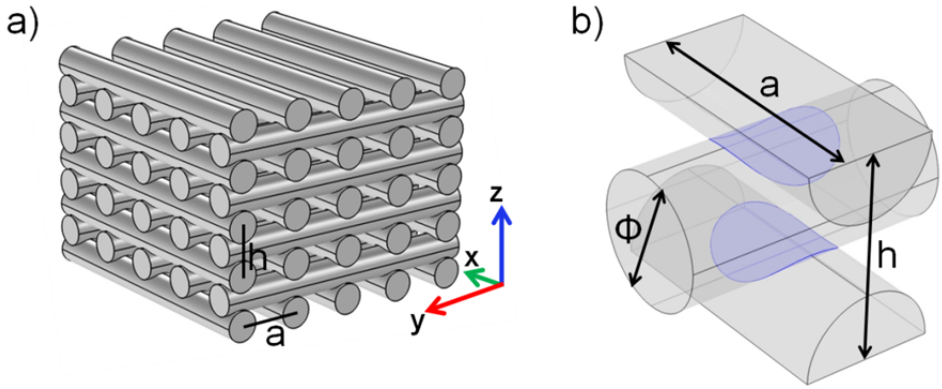

Figure 6.1.- (a) Patterned structure used for the scaffolds designing and (b) scheme of the contact area between two orthogonal rods in a unit cell of the structure, with the structural parameters *h, a*, and *Ø.*

The macro-porosity of the scaffolds (P_{scaf}) was estimated from the void volume of the spanned structures using the characteristic dimensions of the scaffolds –*h, a* and Ø (Fig. 6.1b)- that correspond to the distance between two equivalent layers in the z direction (h), the distance between two adjacent rods (a), and the rod diameter (Ø), respectively:

$$P_{scaf} = 1 - \frac{V_{skel}}{V_T} = 1 - \frac{\pi \cdot \phi^2}{2 \cdot a \cdot h} \quad (1)$$

where V_{skel} and V_T are the (skeleton) solid and (total) structure volumes, respectively.

Values for the macro-porosity of the scaffolds –around 51% for all composites- do not depend on the sintering shrinkage (Fig. 6.2), whereas the total porosity (cells plus the skeleton) augments with increasing GNPs contents, reaching values of 72% for composites containing 20 vol.% GNPs, where the porosity of the skeleton calculated from Eq. (3) of Chapter 3 has been taken into account (Fig. 6.2). In this way, the scaffold density ranges from 1.6 to 0.9 g·cm^{-3} for GNPs contents from 0 to 20 vol.%.

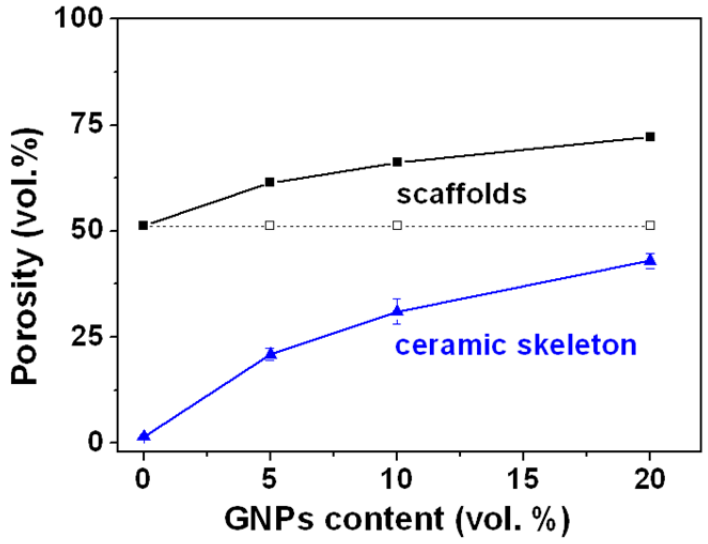

Figure 6.2.- Porosity for the ceramic skeleton versus graphene content, with corresponding macro- (dashed lines) and total (continuous lines) porosities of the scaffolds

The 3D-graphene/SiC structures did not show any noticeable deformation after the sintering process. In Table 6.1, the lattice geometric parameters (*h, a*, and Ø) are given before and after sintering, which will be useful for modelling the electrical behavior of each sample, before and after sintering, and therefore the shrinkage of the sample in the three directions (x, y, z).

Table 6.1. Lattice parameters in the green state and after sintering for the different GNPs/SiC scaffolds. Data dispersion is ± 5 μm for all measurements. S_{eff} is the effective contact area between adjacent orthogonal rods calculated from Eq. (5).

Materials		**h (μm)**	**Ø (μm)**	**a (μm)**	**S_{eff} (μm^2)**
Green state	All	465	295	605	2.91x10^4
Sintered state	0 vol.% GNPs	360	230	475	1.80x10^4
	5 vol.% GNPs	390	250	510	2.15x10^4
	10 vol.% GNPs	410	260	530	2.26x10^4
	20 vol.% GNPs	435	275	570	2.50x10^4

6.1.3.- Electrical characterization

For the electrical conductivity measurements, the GNPs/SiC cuboid scaffolds were machined into rectangular shapes of ~10 × 10 × 7 mm^3. Two silver electrodes, especially conceived for these structures, were attached on opposite faces of the scaffolds using silver paste (Agar 6302) to assure a good electrical contact, and connected to platinum wires to measure the conductivity in the directions longitudinal and transverse to the scaffold rods (see scheme of the setting in Fig. 6.3). In this way, the conductivity along the rod axis within the xy plane (σ_L), and in the transverse direction (σ_T) (xz plane) were measured.

The impedance spectra (Fig. 6.4) display at high frequency the usual inductance due to the electric current in the platinum wires of the holder. At low frequency the impedance tends to a pure ohmic component that corresponds to the resistance of the samples. This resistance was used to calculate the conductivity through application of the geometrical factor corresponding to each configuration.

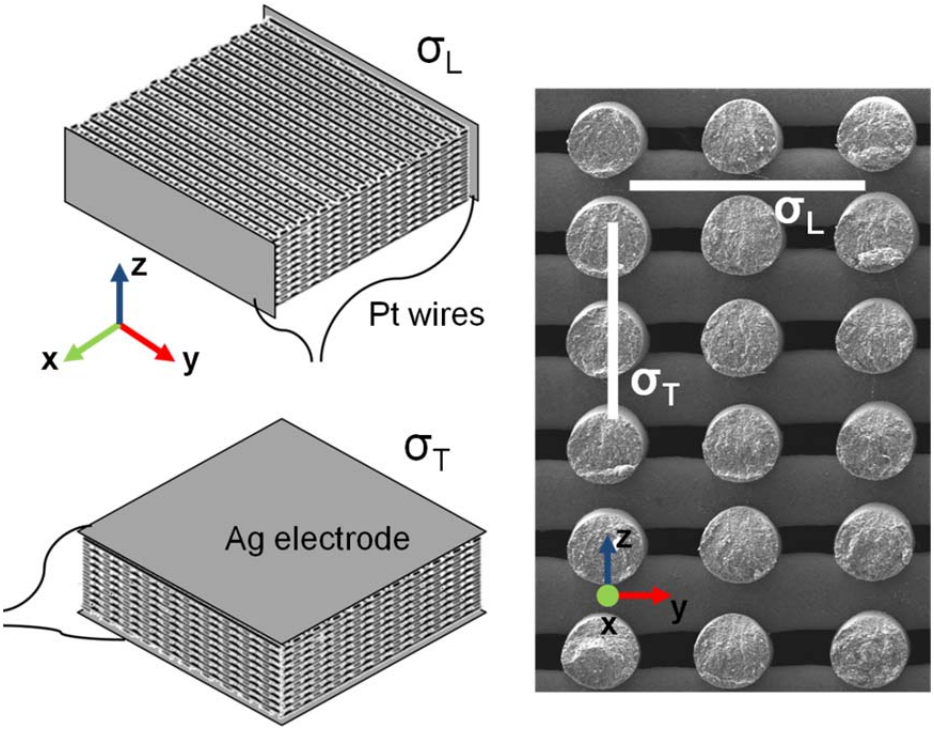

Figure 6.3.- Schematic illustration of the set-ups for σ measurements of the GNPs/SiC scaffolds in the longitudinal (σ_L) and transverse (σ_T) directions, as well as diagram showing the rods arrangement for σ_L and σ_T measurements.

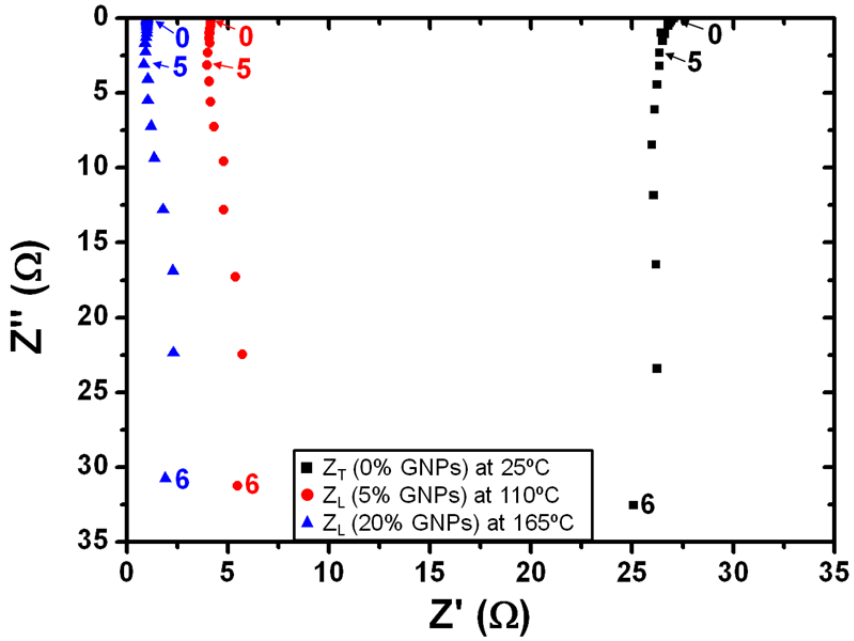

Figure 6.4.- Representative impedance curves corresponding to different samples: i) 0 vol.% GNPs in the transverse orientation at room temperature, ii) 5 vol.% GNPs in the longitudinal orientation at 110 ºC, and iii) 20 vol.% GNPs in the longitudinal orientation at 165 ºC. Numbers in the plot (6,5,0) represent the order of magnitude of the frequency at which each measurement was obtained (exponent in base 10).

Fig. 6.5 shows higher electrical conductivity for the longitudinal orientation (σ_L) than for the transverse direction (σ_T) of the scaffolds. As expected, the electrical conductivity increases with the GNPs content, attaining σ_L and σ_T values in the range of 6-611 $S \cdot m^{-1}$ and 1-273 $S \cdot m^{-1}$, respectively. In agreement also with previous results on the electrical conductivity of GNPs/SiC bulk composites (Chapter 5), these scaffolds do not show any evidence for percolation-type conduction because of the high conductivity of the SiC matrix. The electrical conductivity values of the scaffolds favorably compare with values of 3D graphene aerogels (87-278 $S \cdot m^{-1}$), although aerogels obviously show much lower density.[14] The electrical conductivity of the single rods, σ_{rod}, measured along the longitudinal axis for each composition using a four probe array on a Physical Properties Measurement System (PMMS), follows the same compositional trend as the 3D structures, but it is 5 and 10 times higher than σ_L and σ_T, respectively, with a maximum value of 2306 $S \cdot m^{-1}$ for the 20 vol.% GNPs/SiC rod (Fig. 6.5). The electrical anisotropy of the scaffolds (taken as the σ_L/σ_T ratio) is roughly constant (~ 2-4) and independent of the GNPs content and, thus, of the magnitude of measured conductivity, which varies more than 2 orders of magnitude between the four tested compositions. As σ_{rod} shows a similar trend with the GNPs content as the scaffolds (Fig. 6.5), differences between the conductivity measured in the longitudinal and transverse directions must be due to the different conducting paths for each measuring configuration.

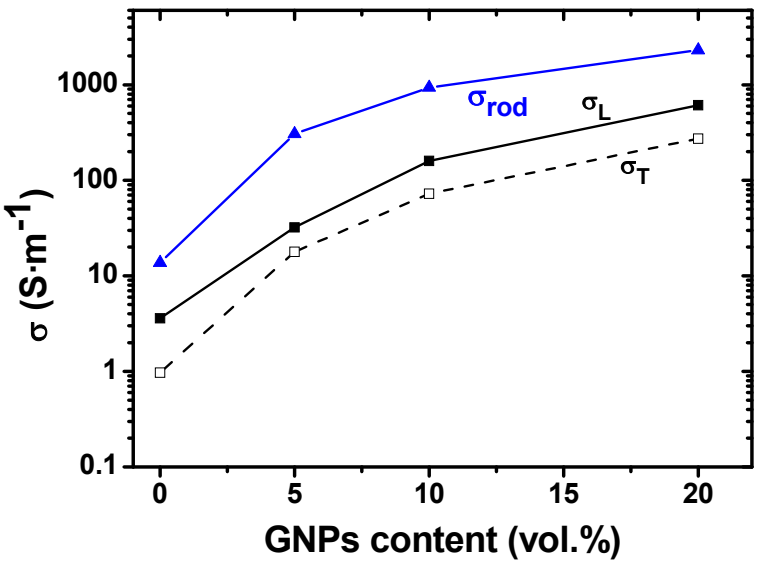

Figure 6.5.- Electrical conductivity (σ) of the scaffolds as a function of the GNPs content for the longitudinal (σ_L) and transverse (σ_T) settings. The electrical conductivity of the single rods (σ_{rod}) from each composition is plotted as well.

It is noteworthy that the conductivity of the GNPs/SiC rods is higher than the values reported for printed, low density reduced graphene oxide filaments (~ 6 mg·cm^{-3}) which is about 40 S·m^{-1}.[13] According to the temperature dependence of the electrical resistivity in the 2.5-370 K interval (Fig. 6.6), the ceramic skeletons exhibit a semiconductor behavior ascribable to a 3D-VRH variable range hopping mechanism. Therefore, this would indicate that charge carriers would move in all directions throughout the entire rods and for each GNPs concentration.

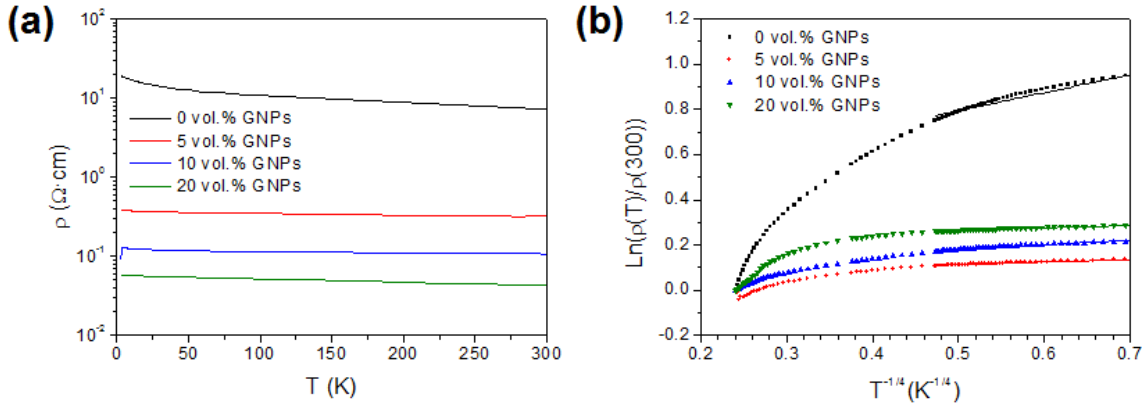

Figure 6.6.- (a) Resistivity (ρ) versus temperature, and (b) variable range hopping (VRH) fitting for 3D-VRH measured in GNPs/SiC rods as a function of the GNPs vol.% content. In (b), points correspond to experimental data and the fittings are represented by lines.

The rod conductivity data are compared with those obtained in the direction perpendicular to the SPS axis for dense bulk specimens of similar composition in Table 6.2. Firstly, the conductivity of the monolithic rod is three times higher than that of the bulk specimens (17.3 versus 5.1 S·m^{-1}), despite it does not show any evidence of in-situ formed graphene, which can be explained by a high level of doping in these structures as demonstrated by Raman spectroscopy (Fig. 3.37). A maximum σ of 4380 S·m^{-1} was achieved for bulk composites containing 20 vol.% GNPs for current flowing along the direction of the preferential alignment of the GNPs. This conductivity is about twice the value of a single rod prepared in this work with the same composition (2306 S·m^{-1}). The difference is, at least partly, due to the much higher porosity of the rod (~43 vol.%) as compared to the bulk composite (virtually dense). In fact, the less porous rods with 10 and 5 vol.% GNPs (30 and 20 vol.% porosity, respectively) show conductivities of 933 and 305 S·m^{-1}, respectively, which are close (for the 10 vol.% GNPs composite) or even higher (in the case of the 5 vol.% GNPs composite) than the values measured for the corresponding dense bulk composites (922 and 38 S·m^{-1}).

As the GNPs are orientated following the extrusion axis within the rods (Fig. 3.36), the model developed in the Chapter 5 (Table 5.3) for the bulk materials in the perpendicular direction can be employed to estimate σ of the GNPs/SiC rods in the longitudinal direction with a SiC matrix of higher conductivity (σ = 17.3 $S \cdot m^{-1}$). In this way, values ranging from 85 to 5342 $S \cdot m^{-1}$ were predicted for dense rods of the different GNPs/SiC compositions (Table 6.2). These values were corrected considering the volume fraction of porosity, P, in each skeleton by using the equation $\sigma_{porous} = \sigma_{dense} \cdot (1 - 3/2 \cdot P)$,[20] showing good agreement for the 20 vol.% GNPs composite but being significantly lower than those experimentally measured by PMMS for 5 and 10 % of GNPs (80% and 30%, respectively). These differences could be ascribed to the presence of a highly conductive annulus in the case of low GNPs content (≤ 10 vol.%) in which the GNPs would be extremely oriented, leading to a PMMS effective electrical conductivity higher than the predicted. This orientation, described in Chapter 3, is a consequence of the radial shear stresses generated during the printing process.

Table 6.2. Electrical conductivity (σ) of bulk GNPs/SiC bulk materials in the perpendicular direction (Chapter 5), and experimental data for the GNPs/SiC rod and estimated values for dense and porous rods. Values for the external rim (RIM) are also included, which were calculated assuming that rods behave as two parallel resistors.

GNPs (vol.%)	**σ ($S \cdot m^{-1}$)**				
	BULK	**ROD**			
		PPMS	**DENSE**	**POROUS**	**RIM**
0	5.1	17.3			
5	38	305	85	59	485
10	922	933	1210	666	1128
20	4380	2306	5342	2137	2430

Furthermore, a more porous core of diameter ~0.60 times the diameter of the rods could be clearly distinguished in the 5 and 10 vol.% of GNPs skeletons while a more homogeneous microstructure is observed for the GNPs-free and the 20 vol.% of GNPs, as shown in Fig. 6.7. The formation of this porous core can also be linked to the disorientation of the GNPs in the core of the specimens (Fig. 3.36) that will lead to a worse particle packing during printing and prevents densification due to the development of sintering backstresses. Meanwhile, the formation of a well-connected

GNPs network clearly occurs in the whole bulk of the rods for high GNPs contents, leading to a more homogenous electrical behavior for the 20 vol.% GNPs composite rods; the same homogenous behavior can be foreseen in the case of the GNPs-free rods. In this way, GNPs/SiC composite rods can be regarded as two concentric cylinders showing the external rim higher electrical conductivity than the core cylinder, being the effective electrical conductivity that experimentally measured for the rod. Assuming that the conductivity of the core is the value estimated for the porous rods (Table 6.2) and rods behave as two parallel resistors, the conductivity of the external rim was calculated. These values are also shown in the Table 6.2 and range between 485 and 2430 $S \cdot m^{-1}$ for composites containing 5-20 vol.% GNPs.

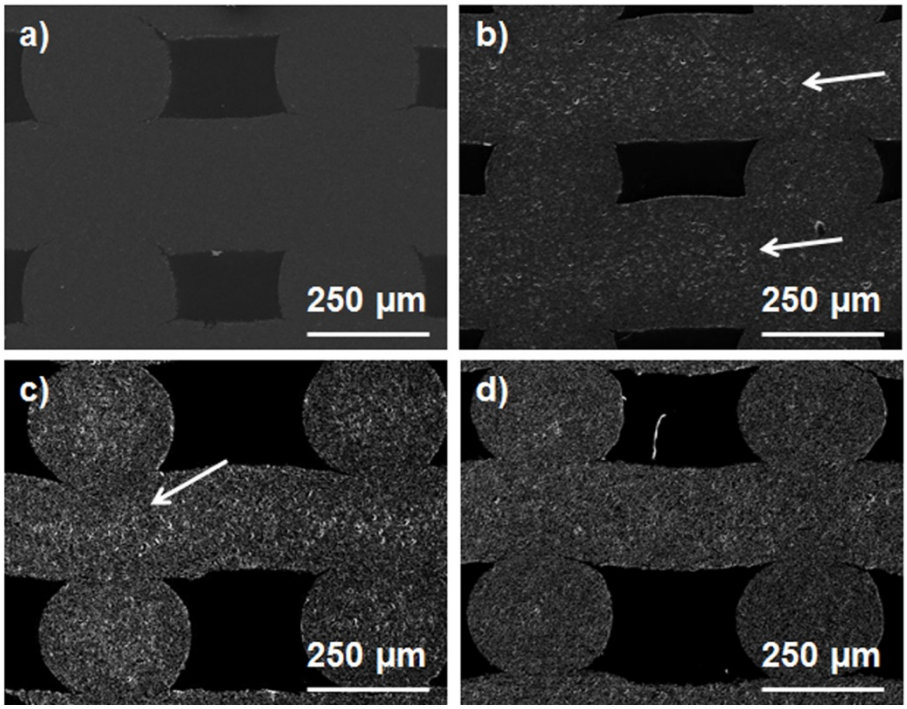

Figure 6.7.- FESEM micrographs of the polished cross-sections corresponding to GNPs/SiC cellular composites containing: a) 0, b) 5, c) 10, and d) 20 vol.% GNPs. The arrows in b) and c) show a more porous core structure.

6.2.- Modelling

6.2.1.- Resistors model

For a scaffold of dimensions X', Y' and Z', the resistance for current flowing in the longitudinal X direction (the same is valid for the Y direction) can be calculated from the resistance of a rod (R_{rod}) as: $R_{X,Y}^{-1} = n_{yz} \cdot R_{rod}^{-1}$, where n_{yz} is the number of rods

perpendicular to the yz plane, i.e. the number of conducting paths along the X direction, which can be geometrically calculated as n_{yz} = Y'Z'/ah. In this way, the conductivity of the scaffold in the X (or Y) direction is:

$$\sigma_{X,Y} = \frac{X'}{Y'Z'} R_{x,y}^{-1} = \frac{X'}{ah} R_{rod}^{-1} \quad (2)$$

The good contact between the green filaments in adjacent layers was achieved by forcing certain penetration of the filaments of each layer into those of the underlying stratum in such a way that h = 0.25π Ø. As shown in Fig. 6.1b, the intersection area of two orthogonal rods has a pringle-like hyperbolic paraboloid shape. Introducing the resistance of the rod (R_{rod} = 4X'/πØ$^2\sigma_{rod}$), and assuming that the overlapping is kept constant after the SPS process, the expression in Eq. (2) can be simplified as:

$$\sigma_{X,Y} = \frac{\phi}{2a} \sigma_{rod} \quad (3)$$

which means that the longitudinal electrical conductivity directly depends on the ratio between the diameter and the separation of the rods. For the conduction in the Z direction, i.e. in the transverse mode, the proposed model considers that the current flows through parallel paths of R_z resistance defined by the intersections of the scaffold rods in adjacent layers. Also, the assumption that the scaffold rods present isotropic electrical conductivity is made in the model ($\sigma_{rod} = \sigma_z$). In this case, similarly to the longitudinal mode, $R_z^{-1} = n_{xy} \cdot R_z^{-1}$, where n_{xy} is the number of rods perpendicular to the xy plane (i.e., $\frac{X'Y'}{a^2}$) and R_z can be expressed as function of the effective contact area between adjacent orthogonal rods, S_{eff}, like $R_z = \frac{1}{\sigma_z}\frac{Z'}{S_{eff}}$. From R_z, the transverse conductivity will be:

$$\sigma_z = R_z^{-1} \frac{Z'}{X'Y'} = \frac{S_{eff}}{a^2} \sigma_{rod} \quad (4)$$

Therefore, S_{eff} acts as limiting factor for the electrical conductivity of the scaffolds in the transverse mode and its accurate estimation is highly desirable. Here, S_{eff} is assumed to be the area projected by the intersection of two orthogonal rods (Fig. 6.1b) on the underlying rod, which is a rectangle with effective area of:

$$S_{eff} = h \cdot \phi \cdot (1 - h/2\phi) \quad (5)$$

and, therefore:

$$\sigma_z = \frac{h \cdot \phi}{a^2}(1 - f) \cdot \sigma_{rod} \quad (6)$$

where f = h/2Ø is the overlapping between adjacent layers. Accordingly, the conductivity of the structure in the Z direction depends upon the intrinsic conductivity of the scaffold rods, the overlapping between adjacent layers, and the spacing between rods normalized to the rod diameter.

The electrical conductivity values estimated using the resistors model are collected in Table 6.3, reproducing the trend observed for the experimental data for both measuring directions. From this model, a σ_L/σ_T ratio of 2.4 is predicted, which is in the range of those experimentally measured (1.8-3.7).

Table 6.3. Comparison of the experimental (Exp) values of longitudinal (σ_L) and transverse (σ_T) electrical conductivity and predictions obtained by the resistors model (Res).

Vol.% GNPs	**σ_L (S·m^{-1})**		**σ_T (S·m^{-1})**	
	Exp	**Res**	**Exp**	**Res**
0	4.2	3.3	0.8	1.7
5	32.1	75	17.8	39.6
10	159.4	229	72.4	117.7
20	610.6	556.3	273	278.9

However, significant differences between the predicted and the experimental values are observed in the case of the 5 and 10 vol.% GNPs scaffolds, as measured values for σ are lower than expected according to the proposed model. Curiously, the rods forming these scaffolds show also important differences between the measured and the estimated electrical conductivities (Table 6.3) attributed to the development of a low conducting porous core and a highly conducting rim where GNPs would be extremely oriented. Consequently, the higher values estimated from the model for the 5 and 10 vol.% GNPs scaffolds should be associated to this layered structure of the rods when they integrate in the scaffold, as the highly conductive rim is strongly affected by the rods overlapping. In this way, rod-rod contacts would act as series

resistors reducing the effective electrical conductivity, which explains the overestimation of the model. This effect is negligible in the case of the more electrically homogeneous rods of the GNPs-free and 20 vol.% GNPs scaffolds.

6.2.2.- Finite-element modelling (FEM)

FEM simulations were performed with COMSOL 4.4.0.0.150 Multiphysics 4.4 solver. For the accomplishment of the model, the input geometrical parameters (a, h and Ø) were those shown in Table 1, according to Fig. 6.1a,b. Considering the symmetry of the scaffolds, the FEM unit cell of $a \times a \times h$ dimensions was designed with a progressively refined mesh until the FEM results –i.e. the estimated electrical resistance- differed by less than 0.5%. The unit cell of the robocast structures (Fig. 6.8) contained approximately 1.5 million tetrahedral elements with sizes ranging from 0.7 μm to 8 μm, and approximately 2 million degrees of freedom.

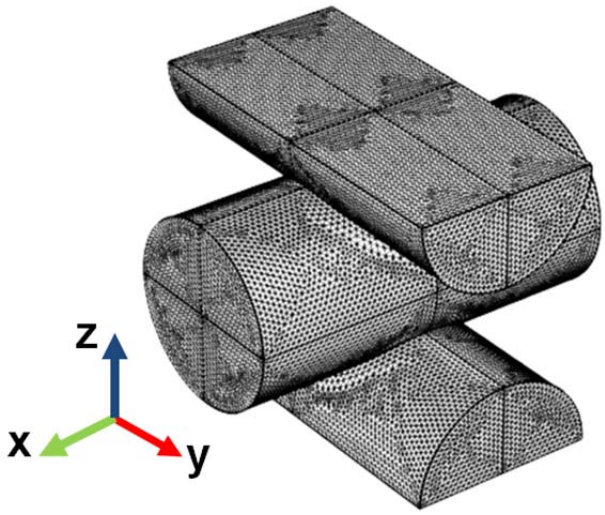

Figure 6.8.- mesh of the unit cell of the robocast structures used for the FEM calculations

The experimental electrical conductivity values for the rods of each GNPs/SiC composition were used in the model as material property. The effective relative permittivity of the composites was calculated by the rule of mixtures using data from the literature: i) 9.72 for SiC,[21] ii) 10.6 for YAG,[22] and iii) in the range 10-15 for graphite,[23] and also considering the skeleton porosity of each composition. The model assumes that current flows along the scaffold rods in the longitudinal mode (x-axis or y-axis in Fig. 6.3), and from rod-to-rod of successive layers through the intersections in the case of the transverse mode (z-axis in Fig. 6.3). In this way, for the FEM

calculations of the longitudinal conductivity, a voltage was simulated in yz plane, while the opposite yz plane was at ground voltage. Likewise, for the transverse conductivity, the voltage was applied to xy plane and the opposite xy plane was at ground voltage.

FEM simulations were performed by using two electrical models based on the use or absence of rod-to-rod contact resistances (R_c). The simplest implementation of the FEM model (without contact resistance) yields figures for the longitudinal direction close to the resistors model, in agreement with the experimental data. However, the predictions of the transverse conductivity are poor (Table 6.4), hence, failing to reproduce the observed electrical anisotropy.

Table 6.4.- Comparison of the experimental (Exp) values of longitudinal (σ_L) and transverse (σ_T) electrical conductivity and the predictions obtained by FEM and the modified FEM with a rod-to-rod contact resistance (FEM_CR).

Vol.% GNPs	**σ_L (S·m^{-1})**			**σ_T (S·m^{-1})**		
	Exp	**FEM**	**FEM_CR**	**Exp**	**FEM**	**FEM_CR**
0	4.2	3.7	3.3	0.8	3.3	0.9
5	32.1	82.9	72.6	17.8	73.3	17.6
10	159.4	253.3	236.2	72.4	224.7	72.3
20	610.6	622.2	567.6	273	549.5	276.5

In fact, as shown in Fig. 6.9a,c, the effective area for current flow is the rod cross-section in the longitudinal direction, coinciding with the resistance model, but in the transverse direction it is much higher than that assumed in the resistors description of the material (Fig. 6.9b,d). Therefore, a rod-to-rod R_c was introduced in a modified FEM model (noted as FEM_CR) forcing the transverse resistance to reproduce the corresponding experimental data. The contact resistances can be used to estimate an area-specific contact conductance ($G_A = R_c^{-1} \cdot S_{eff}^{-1}$). Fig. 6.10 depicts an increase of G_A with increasing GNPs content, which can be explained considering that G_A is as a function of the rod conductivity. In this way, the effective area for current flow in the FEM_CR model becomes significantly lower as shown in Fig. 6.9f. On the other hand,

the introduction of a rod-rod contact resistance does not modify significantly the current flow in the longitudinal direction (Fig. 6.9e and Table 6.4).

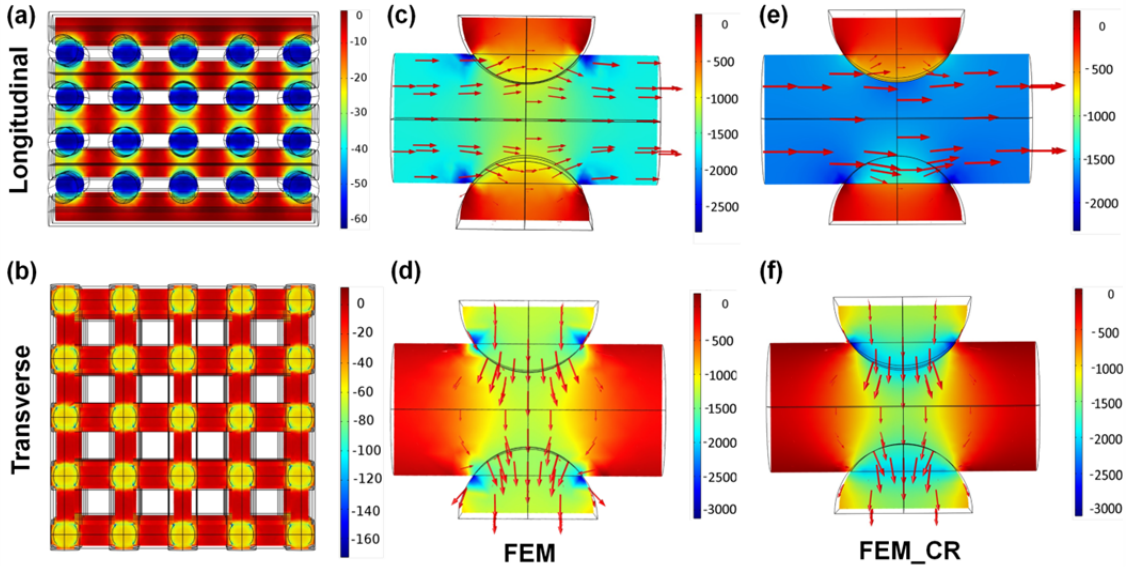

Figure 6.9.- Current density results from the FEM models for the 20 vol.% GNPs/SiC scaffold simulating current flowing in the longitudinal mode (a, c and e) and transverse mode (b, d and f). a) and b) correspond to xz (equivalent to yz) and xy planes, respectively. c) and e) detail of a rod-to-rod contact on the orthogonal yz (equivalent to xz) plane in the longitudinal mode, without (FEM) and with rod-to-rod contact resistance (FEM_CR), respectively. d) and f) detail of a rod-to-rod contact on the yz (similarly xz) plane in the transverse mode, without (FEM) and with rod-rod contact resistance (FEM_CR), respectively. The color coding varies from red to blue for lowest to highest electric current densities, respectively.

The G_A/σ_{rod} ratio should be an indirect measure of the contact geometry, as σ_{rod} includes the effect on the conductivity of other factors such as the GNPs distribution and the porosity. A simple calculation shows that G_A/σ_{rod} varies within the range 3×10^3 – 8×10^3 m^{-1} without any apparent trend with composition (Fig. 6.10). This suggests fairly similar contact geometries for the four composites, in qualitative agreement with the close contact areas estimated from the structure parameters (Table 1). Both results are a good indication of the level of control of the rod contact area achieved by Robocasting, despite the significant differences in porosity and GNPs content of the various composites.

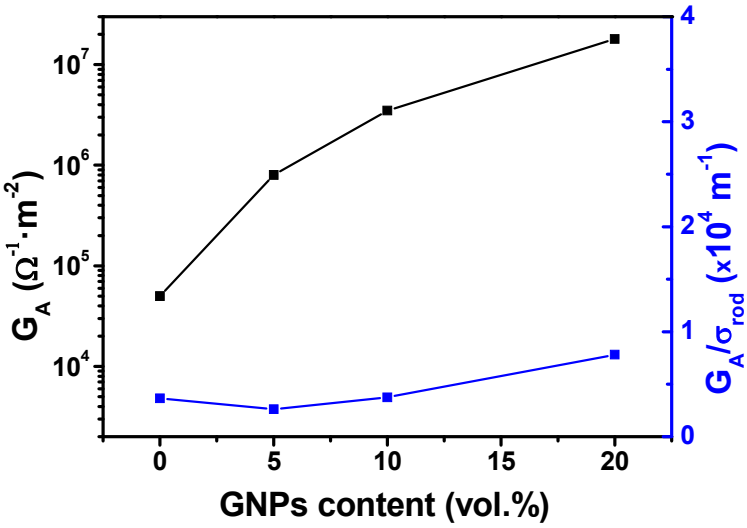

Figure 6.10. Area-specific contact conductance (G_A) figures from the FEM model as a function of the GNPs content and the G_A/σ_{rod} ratio.

6.3.- Conclusions

i) The robocast, relatively lightweight 3D graphene/SiC structures showed anisotropic electrical conductivity.

ii) The individual rods comprising the structures exhibited σ values that increased with the GNPs concentration up to a maximum of ~2300 $S\cdot m^{-1}$ for 20 vol.% graphene contents, resulting in σ values for the present 3D structures that reproduce the same trend of up to 611 $S\cdot m^{-1}$ and 273 $S\cdot m^{-1}$ in the longitudinal and the transverse directions, respectively.

iii) Both an equivalent circuit model and more complex FEM reproduce the conducting behavior of these robocast structures as a function of the rod electrical conductivity, the overlapping between adjacent layers and the spacing between rods normalized to the rod diameter.

iv) The electrical performance of this type of spanned structures can be tailored by tuning the GNPs content, the rod diameter, the separation between rods, and the overlapping between consecutive layers.

v) The developed scaffolds potentially combine in one material the high mechanical stability and electrical and thermal conductivities of graphene-ceramic composites with the intrinsic characteristics of hierarchical designs 3D structures, such as ordered porosity, low specific weight and high specific surface area.

6.4.- References

1. Brownson DA, Kampouris DK, Banks CE. An overview of graphene in energy production and storage applications. J Power Sources 2011; 196(11): 4873-85.

2. Liu C, Yu Z, Neff D, Zhamu A, Jang BZ. Graphene-based supercapacitor with an ultrahigh energy density. Nano Lett 2010; 10(12): 4863-8.

3. Pettes MT, Ji H, Ruoff RS, Shi L. Thermal transport in three-dimensional foam architectures of few-layer graphene and ultrathin graphite. Nano Lett 2012; 12(6): 2959-64.

4. Nardecchia S, Carriazo D, Ferrer ML, Gutiérrez MC, del Monte F. Three dimensional macroporous architectures and aerogels built of carbon nanotubes and/or graphene: synthesis and applications. Chem Soc Rev 2013; 42(2): 794-830.

5. Chen Z, Ren W, Gao L, Liu B, Pei S, Cheng HM. Three-dimensional flexible and conductive interconnected graphene networks grown by chemical vapour deposition. Nat Mater 2011; 10(6):424-8.

6. Cao X, Shi Y, Shi W, Lu G, Huang X, Yan Q, Zhang Q, Zhang H. Preparation of novel 3D graphene networks for supercapacitor applications. Small 2011; 7(22):3163-8.

7. Jiang XF, Wang XB, Dai P, Li X, Weng Q, Wang X et al. High-throughput fabrication of strutted graphene by ammonium-assisted chemical blowing for high performance supercapacitors. Nano Energy 2015;16;81-90

8. Cao X, Zeng Z, Shi W, Yep P, Yan Q, Zhang H. Three-Dimensional Graphene Network Composites for Detection of Hydrogen Peroxide. Small 2013; 9(9-10):1703-7.

9. Dong XC, Xu H, Wang XW, Huang YX, Chan-Park MB, Zhang H, Wang LH, Huang W, Chen P. 3D graphene–cobalt oxide electrode for high-performance supercapacitor and enzymeless glucose detection. ACS Nano 2012; 6(4): 3206-13.

10. Bi H, Chen IW, Lin T, Huang F. A new tubular graphene form of a tetrahedrally connected cellular structure. Adv Mater 2015. doi: 10.1002/adma.201502682

11. Yin S, Zhang Y, Kong J, Zou C, Li CM, Lu X, Ma J, Boey FYC, Chen X. Assembly of graphene sheets into hierarchical structures for high-performance energy storage. ACS Nano 2011; 5(5): 3831-8.

12. Qiu L, Liu JZ, Chang SL, Wu Y, Li D. Biomimetic superelastic graphene-based cellular monoliths. Nat Comm 2012; 3 : 1241.

13. García-Tuñón E, Barg S, Franco J, Bell R, Eslava S, D'Elia E, Maher RC, Guitián F, Saiz E. Printing in Three Dimensions with Graphene. Adv Mater 2015; 27: 1688-93.

14. Zhu C, Han TYJ, Duoss EB, Golobic AM, Kuntz JD, Spadaccini CM, Worsley MA. Highly compressible 3D periodic graphene aerogel microlattices. Nat Comm 2015; 6: 7962.

15. Jakus AE, Secor EB, Rutz AL, Jordan SW, Hersam MC, Shah RN. Three Dimensional Printing of High-Content Graphene Scaffolds for Electronic and Biomedical Applications. ACS Nano 2015; 9(4): 4636-48.

16. Zhou M, Lin T, Huang F, Zhong Y, Wang Z, Tang Y, Bi H, Wan D, Lin J. Highly conductive porous graphene/ceramic composites for heat transfer and thermal energy storage. Adv Funct Mat 2013; 23(18): 2263-9.

17. Huang H, Bi H, Zhou M, Xu F, Lin T, Liu F, Zhang L, Zhang H, Huang F. A three-dimensional elastic macroscopic graphene network for thermal management application. J Mater Chem A 2014; 2(43): 18215-8.

18. Zhou M, Bi H, Lin T, Lü X, Huang F, Lin J. Directional architecture of graphene/ceramic composites with improved thermal conduction for thermal applications. J Mater Chem A 2014; 2(7): 2187-93.

19. Zhou M, Bi H, Lin T, Lü X, Wan D, Huang F, Lin J. Heat transport enhancement of thermal energy storage material using graphene/ceramic composites. Carbon 2014; 75: 314-21.

20. McLachlan DS, Blaszkiewicz M, Newnham RE. Electrical Resistivity of Composites. J Am Ceram Soc 1990; 73(8): 2187-203.

21. Patrick L, Choyke WJ. Static dielectric constant of SiC. Phys Rev B 1970;2;2255-6.

22. Shannon RD, Subramanian MA, Allik TH, Kimura H, Kokta MR, Randles MH, Rossman GR. Dielectric constants of yttrium and rare-earth garnets, the polarizability of gallium oxide, and the oxide additivity rule. J Appl Phys 1990;67;3798-3802.

23. Taft EA, Philipp HR. Optical properties of graphite. Phys Rev 1965;138;A197.

Chapter 7

Future trends and applications of SiC-based materials

7.1. Introduction: future applications of bulk and 3D SiC-based materials

In this PhD Thesis, different SiC-based materials have been developed with potential to be employed in future applications owing to their properties, mainly the electrical conductivity, or to their specific 3D architectures.

One interesting future prospect of the electrically conductive bulk graphene/SiC materials, obtained either through the in-situ formation of graphene flakes within SiC ceramics by SPS or by addition of GNPs to SiC matrices, could be the use of the EDM process for manufacturing complex 3D parts able to be used as microturbines, microreactors, or microelectromechanical systems (MEMS). Actually, one of the limitations facing the accomplishment of end-user applications for structural ceramics is the difficulty to manufacture ceramic parts with both highly complex geometries and a high level of morphological accuracy. Besides, SiC is a hard ceramic material and machining processes using diamond grinding are costly and limited for the production of complex parts of very high added value. EDM is a thermoelectric process that facilitates a relatively inexpensive manufacture of complex components, where the main limiting prerequisite for ceramics is to show sufficient electrical conductivity values (~1 $S \cdot m^{-1}$) to commence the process of erosion (developed by physicochemical interaction of sparks between the tool electrode and the ceramic material). However, the electrical conductivity of SiC is commonly not enough sufficient for EDM, requiring the use of the assisting electrodes and where the ceramic must be electrically coated. The goal is, hence, to analyze the EDM performance of the SiC materials as a function of the GNPs content, i.e., of the electrical conductivity of the composite, looking for the machining of complex SiC parts without the need of using the assisting electrode method. This research has already started in collaboration with Prof. C. Mueller's group at Department of Microsystems Engineering (IMTEK), University of Freiburg (Germany). Preliminary results show that whereas monolithic β-SiC cannot be EDMed in absence of assisting electrode, GNPs composites are successfully machined. Fig. 7.1 illustrates two examples of EDMed GNPs containing materials, in particular, a prismatic pillar of ~50 and ~100 μm of top and bottom square dimensions, respectively, and ~350 μm of height inside a squared hole of 1100 x 1100 μm^2 was machined on a 10 vol.% GNPs/SiC specimen (Fig. 7.1a), and a circular hole of ~350 μm of diameter and ~350 μm of height machined on a 20 vol.% GNPs/SiC specimen (Fig. 7.1b).

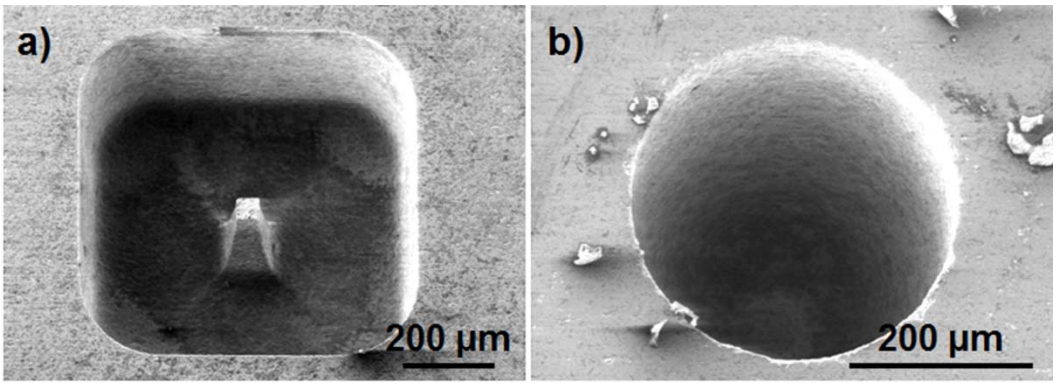

Figure 7.1.- SEM micrographs showing different features (pillar and hole) EDMed on: a) 10 vol.% GNPs/SiC and b) 20 vol.% GNPs/SiC composites. Images courtesy of F. Zeller from the Department of Microsystems Engineering (IMTEK), University of Freiburg (Germany).

More intricate structures are feasible through the implementation of AM techniques. AM techniques offer exceptional future prospects related to the fabrication of ceramic parts and components, as demonstrated in the present manuscript for the case of Robocasting. Consequently, it is important to find new functionalities that profit from these complex morphologies. In the present research activities, two brand-new fields have been opened up towards the implementation of SiC-based scaffolds assembled by Robocasting, in particular, superhydrophobic micro-filters and acoustic metamaterials. Next, preliminary results related to these activities are presented.

7.2. Hydrophobic properties for water/oil micro-filters

7.2.1. Introduction

Nowadays, there are numerous situations where oil-based liquids contaminate water resources worldwide, most of which being linked to oil spills from industrial activities (petrochemical, metal, etc.) or during the transportation of those liquids using tankers.[1] The important impact upon the environment motivates the development of new materials and devices able to efficiently separate oil from water. Inorganic mineral, synthetic organic and organic vegetable products have been widely studied as oil-sorbent materials.[1] Lately, carbon nanotubes (CNTs) appear as an attractive material for the fabrication of oil-water filters considering their superhydrophobic[2] and superoleophilic[3,4] properties. However, the future use of CNTs for oil remediation would require structures with enhanced mechanical resistance in addition to good chemical and thermal stabilities. Therefore, hybrid materials integrating metallic or

ceramic membranes acting as a support for growing CNTs appears to be a novel alternative. The first works based on this concept were carried out by synthesizing vertically aligned CNTs on stainless steel meshes.[5,6] The resulting CNTs/stainless steel filters repelled water and allowed the permeation of oil, but these filters would not be used in the aggressive media where oil spills typically occur (salty, acid, basic, and others). In this sense, chemically inert substrates like SiC ceramics become excellent candidates due to their high resistance to abrasion, wear and corrosion to most chemicals, being twice as resistant to oxidation as the best current superalloys.[7] In addition, SiC exhibits much lower density when compared to metals, a desirable fact for industrial applications. In fact, as discussed in Chapter 1, porous SiC components have already been proved to work under extreme conditions such as those of heat exchangers, burners or catalytic supports.[8]

To date, CNTs grown on SiC membranes have not been reported, and only a few reports are found in the literature on the CNTs growth on SiC particles,[9] whiskers,[10] platelets[11] and, on the surface of SiC fiber cloth.[12] Regarding other ceramic materials for the CNTs growth to form hybrid systems, only three works have been found utilizing CNTs on yttria-stabilized zirconia (YSZ),[13] Al_2O_3[14] or quartz.[15] Therefore, the goal was to grow for the first time aligned multi-walled CNTs (MWCNTs) on a SiC cellular skeleton, exploring the hydrophobicity of such hybrid materials. These research activities were carried out in collaboration with Prof. M. Terrones' group at Shinshu University in Japan.

7.2.2. Aligned carbon nanotube/silicon carbide hybrid materials

3D cylindrical lattices (10.45 mm in diameter and 3.5 mm in height) corresponding to the β7 composition were manufactured by RC. These structures consisted of a regular, porous structure based on ceramic rods of ~ 250 μm in diameter spaced ~700 μm apart. After heating at 600 ºC for 2 h to burn out the organic additives, and SPS at 1800 ºC for 5 min in argon atmosphere to densify these scaffolds, the lattices were treated at 1300 ºC for 1 min in air to slightly oxidize the surface of the SiC rods. This mild oxidation, which is intended to produce a thin SiO_2 layer on the rods surface, is essential to enhance the nanotube growth, as it has previously been described.[10,16] In Fig. 7.2a, b, a cross-sectioned scaffold rod after an oxidation process at 1350 ºC for 1 min is shown, where the secondary phase in the external annulus migrates towards the surface to form the oxide reaction products.

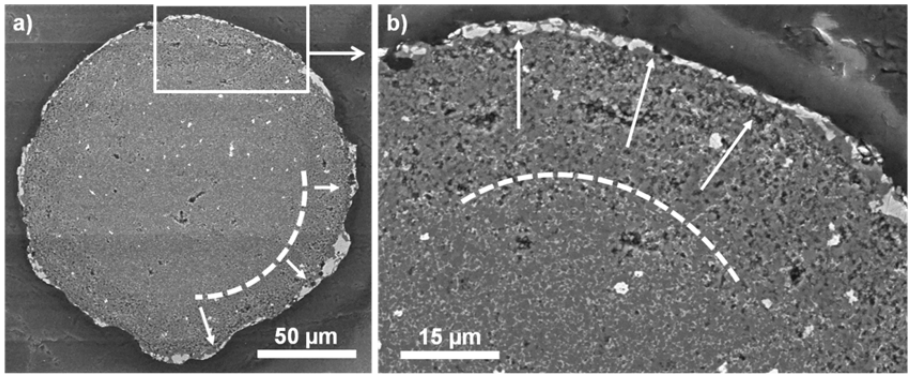

Figure 7.2.- Cross-sectioned scaffold rod after an oxidation process at 1350 ºC for 1 min, where the secondary phase in the external annulus migrates towards the surface to create the external layer consisting of SiO_2 and Y_2SiO_5.

Fig. 7.3a,b illustrate different views of a whole scaffold, and the formation of small amounts of yttrium silicate (Y_2SiO_5) and cristobalite (SiO_2) on the ceramic surface was revealed by XRD (Fig. 7.3c). This layer prevented the reaction between the catalyst and SiC, and enhanced the growth of highly crystalline, aligned MWCNTs. The cylindrical specimens of oxidized SiC were afterwards vertically placed into a quartz tube at 800 ºC in flowing argon to promote the growth of aligned carboxyl functionalized MWCNTs (COx), longer and more crystalline than MWCNTs, by floating catalyst CVD.[17] The maximum temperature was kept constant at times ranging from 15 min to 60 min. The aerosol contained 3 wt.% of ferrocene as iron catalyst source, 96 wt.% of toluene as carbon source, and 1 wt.% of ethanol as oxygen source. It was ultrasonically created and transported through the quartz tube by the Ar flow.[17]

COx vertically grew on the SiC rods within the channels (Fig. 7.3e) with lengths in the range of 200-250 µm, and average diameters around 50 nm (Figs. 7.3f,g). As revealed by Raman spectroscopy (Fig. 7.3h), the three characteristics Raman bands of CNTs (D, G and G', or 2D) were clearly distinguished, having intensity ratios between D and G bands (I_D/I_G) of 0.40. This value is quite low and would confirm the high degree of crystallinity within the carbon nanostructures. In addition, the carbon C1s core level de-convoluted spectrum obtained from the X-ray Photoelectron Spectroscopy (XPS) analyses (Fig. 7.3i) indicated the presence of sp^2- and sp^3-hybridized carbon (284.4 and 285.1 eV, respectively), as well as peaks with binding energies at 286.1 and 286.9 eV, ascribed to C-O and C=O groups, thus confirming the carboxyl functionalization of the synthesized MWCNTs.[18] The peak located at 283.5 eV could be associated to Fe_3C coming from the catalyst (ferrocene) reacting with carbon during the nanotube growth.[19]

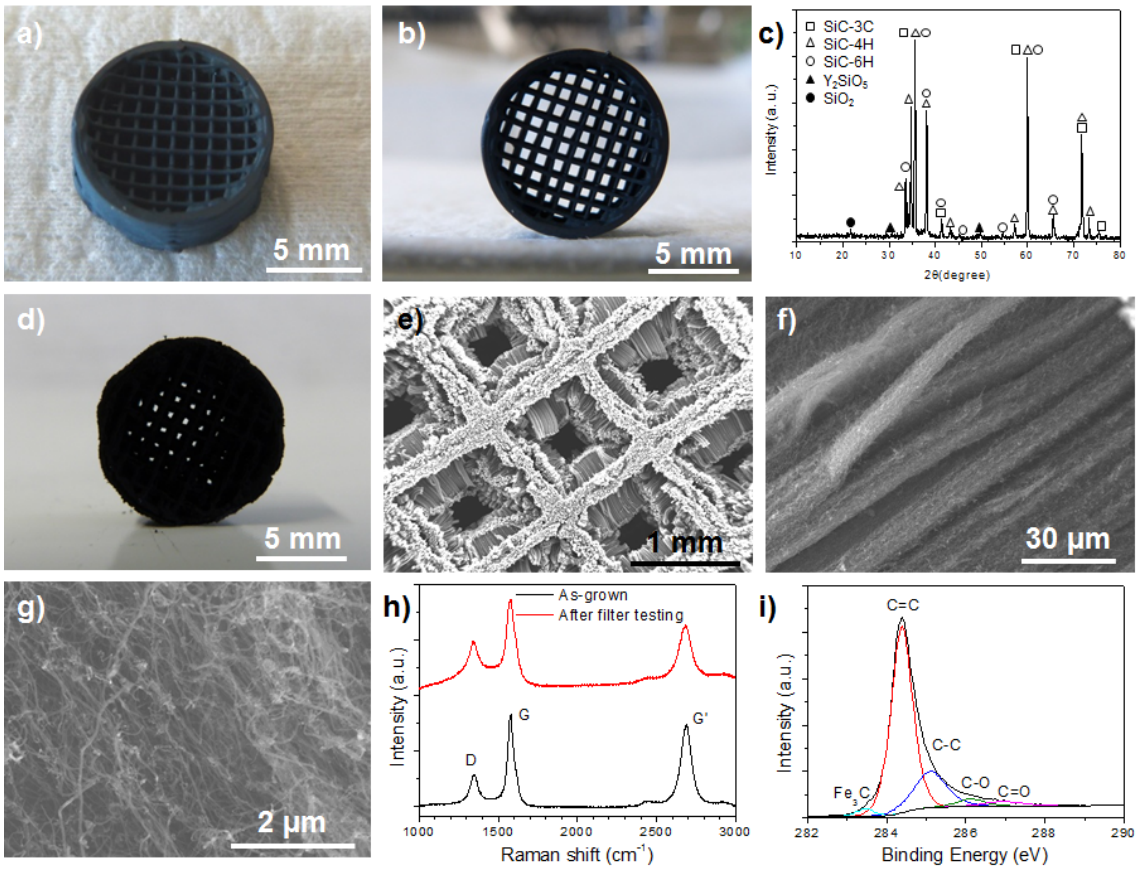

Figure 7.3.- (a,b) Optical views and (c) XRD pattern of the SiC ceramic scaffolds after the oxidizing heat treatment at 1300 ºC, (d) optical and (e) SEM images of the hybrid COx/SiC cellular material, (f,g) SEM images of the nanotubes at higher magnification, (h) Raman spectra of the hybrid COx/SiC cellular material before and after the filtration test, and (i) XPS spectrum of C1s core level for as-grown COx.

7.2.3. Hydrophobic properties and filtration tests

Drops of 1-2 ml of deionized water (DIW, viscosity = 1 mPa·s), 90.2º octane fuel (GAS, Sinergy regular, Exxon Mobil Co.) and mineral oil both pristine (MO, Sigma-Aldrich, Ref. 330760, viscosity = 55-61 mPa·s) and used in a vacuum pump after hundreds of hours (PO), were carefully placed on hybrid COx/SiC cellular specimens under ambient conditions. Bare SiC scaffolds were also tested for comparison. Contact angle (CA) values were assessed using ImageJ analysis program on pictures taken by a digital camera, and performing at least 4 measurements per liquid/specimen pair.

It is noteworthy to mention that the bare robocast SiC scaffolds were highly hydrophilic and oleophilic when using DIW, MO, PO, and GAS. Droplets of the latter

liquids were not stable and they experienced a sudden spread on the bare SiC scaffold with very low CA that were not able to be measured. However, for the synthesized hybrid COx/SiC material, DIW droplets remained stable for long time (Fig. 7.4a), with a CA value of 151 ± 3º, which is consistent with a superhydrophobic behavior[20] of the hybrid material. This property is controlled by the surface roughness and the surface energy. In this sense, the very rough surface provided by the vertically aligned COx would promote hydrophobicity because the water droplets rest on a very large area of air trapped beneath the surface.[21] Actually, Li et al.[22] reported that aligned CNTs films on quartz glass plates exhibited a CA for water of 158.5º, whereas it decreased to 136.5º when the CNTs film was laid flat on the surface. These authors also reported[22] that a low surface energy, which is linked to the chemical surface composition, also favors a higher hydrophobicity. In this way, they were able to modify the CA on as-grown aligned CNTs from 128º, when they were oxidized, to 171º after fluorination. In these hybrid materials, the CA was quite high (151º) despite COx contained certain groups, such as hydroxyl and carbonyl groups, that would reduce the contact angle for water droplets.[23] This fact would indicate that the roughness attained by the vertically aligned COx forests have large influence on the observed superhydrophobicity. Furthermore, the hybrid COx/SiC specimens behaved as superoleophilic when using MO, PO, and GAS; the CA was close to 0º in all cases, considering the lower surface tension of oils (20-30 $mN \cdot m^{-1}$) compared to water (72 $mN \cdot m^{-1}$). In fact, the droplets of all those liquids rapidly spread on the COx/SiC surface and did not show saturation as fully penetrated through the specimen within 1.3, 0.5, and 0.3 s, respectively.

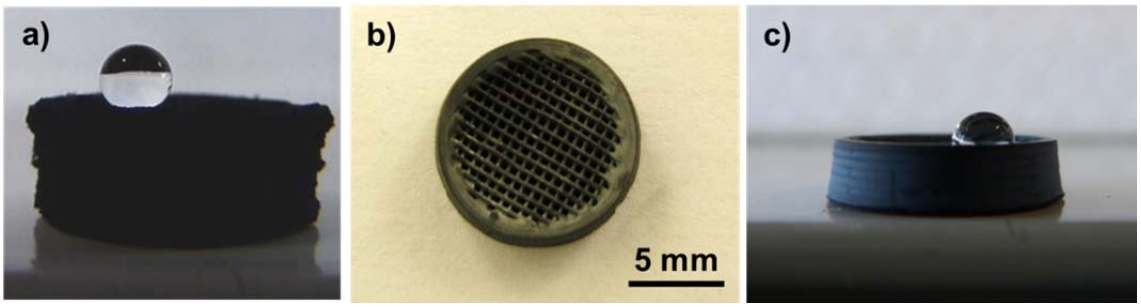

Figure 7.4.- a) DIW droplet on the hybrid COx/SiC surface, b) optical view of the bare SiC ceramic scaffold with ~ 300 x 300 μm^2 channels, and (c) DIW droplet on the latter ceramic surface.

Interestingly, the CA value obtained for a DIW drop placed on a bare SiC surface specifically designed and robocast to have a channel size (~ 300 μm, Fig. 4b) close to the hybrid COx/SiC scaffold (~ 270 μm) was below 115º (Fig. 7.4c), 24% smaller than

for the hybrid material, which evidences the essential role played by the COx on the hydrophobicity.

For the filtration tests, a handmade system was used. It consisted of a glass filter funnel fitted to an Erlenmeyer filter flask through a rubber stopper, two cylindrical rubber stoppers with a hole drilled (0.8 mm in diameter) at the center placed into the glass funnel and between the specimen, and a vacuum pump connected to the Erlenmeyer flask. About 20 ml of each selected liquid were supplied to the filtration module following the sequence: DIW, MO, PO, GAS, and DIW. The effective filtration area of the COx/SiC filter was ~ 3.7 mm^2. As seen in Fig. 7.5a, the liquid did not leak at least during 1 min, and a vacuum pressure of 12.5 kPa (Fig. 7.5b) was necessary for DIW to completely pass through the COx/SiC material, which took place in less than 2 s. This process was repeated twice more and similar results were obtained. Afterwards, pouring of 20 ml of the different oils (MO in Fig. 7.5c, PO in Fig. 7.5d and GAS in Fig. 7.5e) was done demonstrating that these liquids can be pressureless filtrated in about 2 min, without saturation of the hybrid scaffold. To prove that possible residual oil did not affect the filtration of water, 20 ml of DIW were again poured into the funnel and, once more, water did not leak and the same filtration pressure of 12.5 kPa was required (Fig. 7.5f).

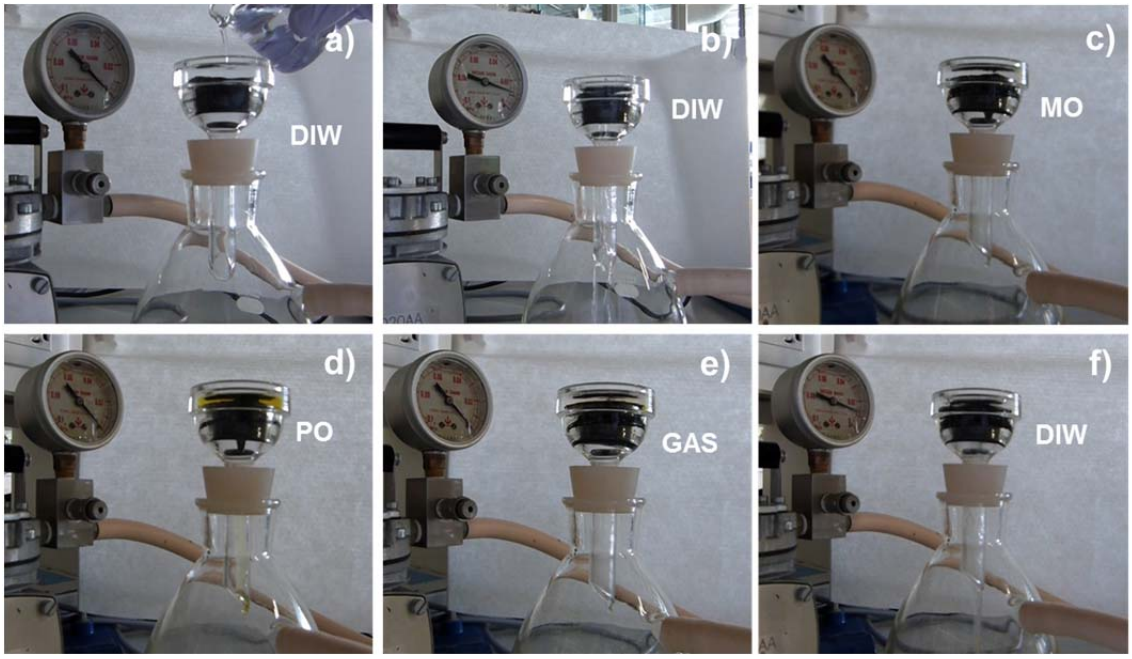

Figure 7.5.- Images taken from the video recorded during the filtration tests sequence: DIW without a) and with b) the assistance of the vacuum pump, c) MO, d) PO, e) GAS, and f) DIW, all of them without using the pump except for DIW tests. The reading of the pressure gauge in b) and f) is clearly visible (0.0125 MPa).

After these tests, the filter was degreased in acetone and, then, COx were analyzed again by Raman spectroscopy and SEM. As seen in Fig. 7.6a, some COx blocks detached from the SiC rods and partially obstructed the channels, but it could have happen during sonication when degreasing the material with acetone to clean the hybrid material after each test. Despite that, the structure of the COx/SiC hybrid material was mostly maintained stable after the filtration experiments. On the other hand, the COx showed small damage. A high magnification view of COx (Fig. 7.6b) revealed some tube densification and alignment loss. In addition, the Raman spectrum of the COx after the filtrations tests (Fig. 7.3h) exhibited a higher intensity of the D-band, with an I_D/I_G value of 0.59 (compared to 0.40 for the pristine COx) which reflects an increase of defects on the COx structure.

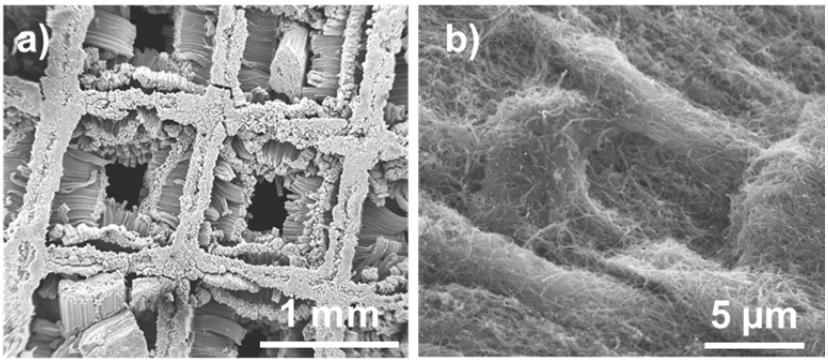

Figure 7.6.- SEM images of the hybrid COx/SiC cellular material (a) and the nanotubes at higher magnification after the whole filtration sequence (b).

7.2.4. Electrical properties of the hybrid structure

DC electrical resistivity (ρ) measurements from room temperature to 2 K were carried out on individual COx/SiC rods room temperature to 2 K using a four probe array and PPMS. Vertically aligned COx showed a semiconducting-like behavior (Fig. 7.7a), with a room temperature ρ value of 0.278 Ω·cm that corresponded to an electrical conductivity value of 360 $S \cdot m^{-1}$. These values indicate that there is also a good ohmic contact at the COx-SiC interface. The electrical data were analyzed with the variable range hopping theory for Coulomb gap, two-dimensions (2D-VRH) and three-dimensions (3D-VRH).[23] At temperatures below 20 K, data were fitted with a straight line against $T^{-1/2}$ (Fig. 7.7b), $T^{-1/3}$ (Fig. 7.7c) and $T^{-1/4}$ (Fig. 7.7d) for Coulomb gap, 2D-VRH and 3D-VRH, respectively. The coefficients of determination (R^2) for each fitting were 0.9905 (for $T^{-1/2}$), 0.9960 (for $T^{-1/3}$), and 0.9978 (for $T^{-1/4}$). These values indicate that the hybrid specimen would behave more according to a 3D-VRH model,

suggesting that the entire sample is a good electrical conductor throughout the three dimensions. This property could be useful for further applications of these hybrid porous materials linked to small electronic devices or sensors.

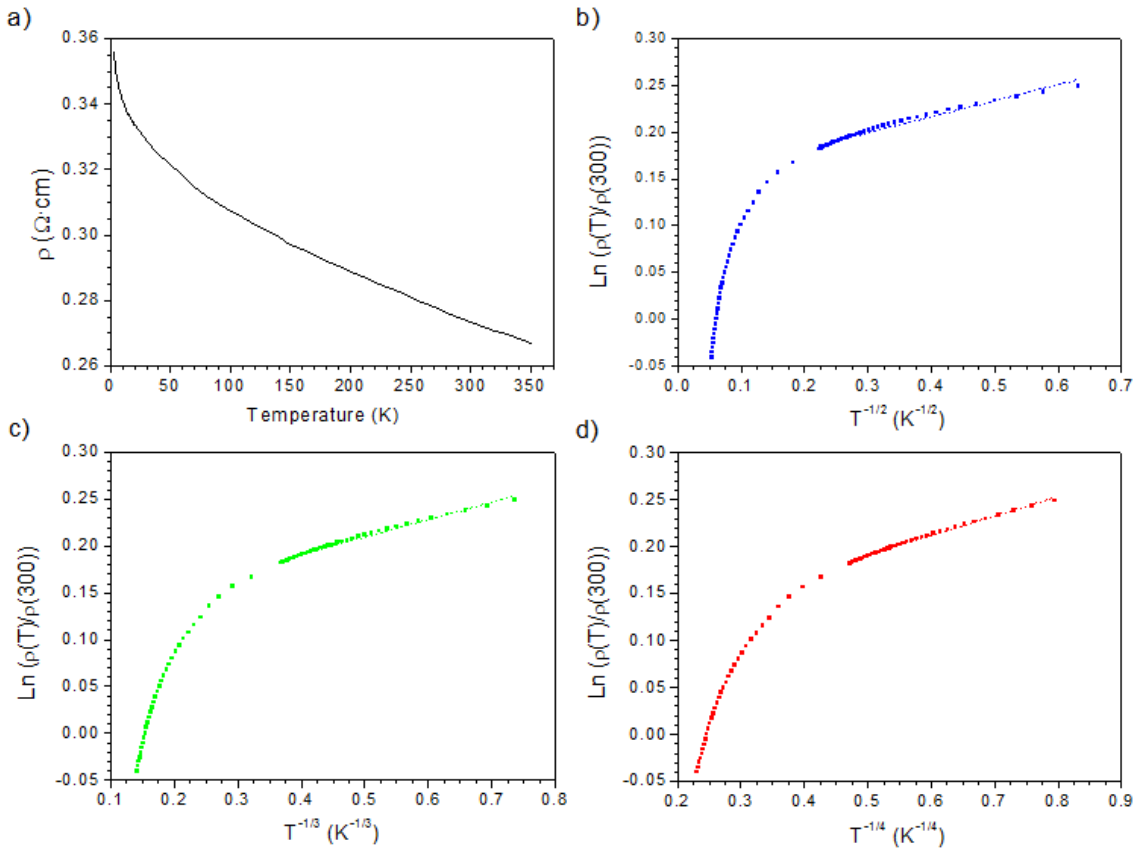

Figure 7.7.- (a) Resistivity (ρ) versus temperature, and variable range hopping fitting for (b) Coulomb gap (d = 1), (c) two-dimensions (2D-VRH), and (d) three dimensions (3D-VRH) for a COx/SiC rod. Points correspond to experimental data and the fittings are represented by dashed lines.

7.3. Acoustic metamaterials

In acoustic metamaterials,[24-27] artificially built architectures enable acoustic wave propagation in extremely anomalous fashions that involve acoustic lensing and cloaking, negative dispersion bands, or negative refractive indices. This class of materials has a potential for various advanced applications that require focusing or redistribution of the acoustic energy.[28-33] A particular type of acoustic metamaterials, typically referred to as phononic crystals,[34-36] consist of arrays of mutually organized periodic structures. Such regular architectures can most accurately be achieved by modern additive manufacturing technologies.

In collaboration with Dr. Hanus Seiner's group, from the Institute of Thermomechanics, Academy of Sciences of the Czech Republic, the elastic and acoustic properties of SPSed SiC scaffolds (Fig. 7.8) were studied to determine whether acoustic anomalies were revealed in these structures.

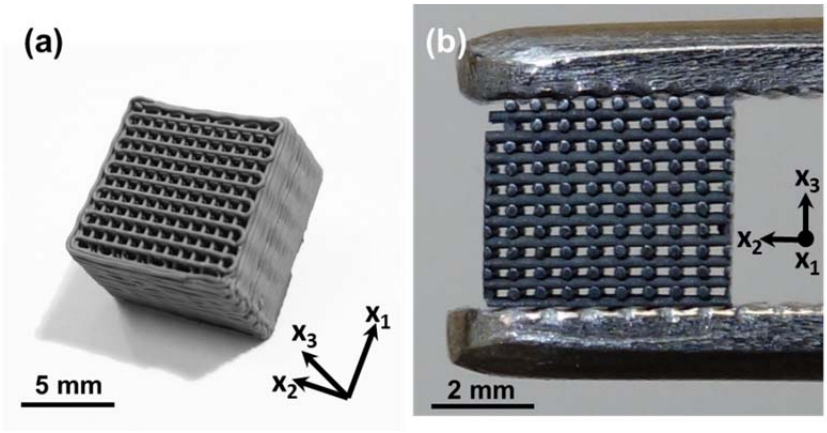

Figure 7.8.- Optical images of the robocast structure: (a) as-designed scaffold and (b) as-measured scaffold (the ceramic frame was eliminated by machining) with the orientation of the used coordinate system.

The robocast structure was characterized by resonant ultrasound spectroscopy (RUS; see Refs. 37–39 or A.2.11): a resonant spectrum of free elastic vibrations of a parallelepiped-shaped sample machined from the central (periodic) part of the scaffold was measured in the frequency range of 100–800 kHz. This spectrum was measured by a contactless, laser-based RUS set-up in which the vibrations were both generated and detected by lasers. In order to obtain also the information on modal shapes of the individual resonant modes in the spectrum, the vibrational response was subsequently recorded at the cross-sections of the individual rods at the largest face of the sample. The result is shown in Fig. 7.9. Surprisingly, despite of the structural complexity of the sample, the resonant spectrum consists of sharp, well-defined resonant peaks (average internal friction parameter[38] Q^{-1} = 2 x 10^{-3}), which directly proves that the scaffold exhibits very low energy dissipation under ultrasonic vibrations, i.e., there are, for example, no weak, friction-like contacts between the rods at the crossing points.

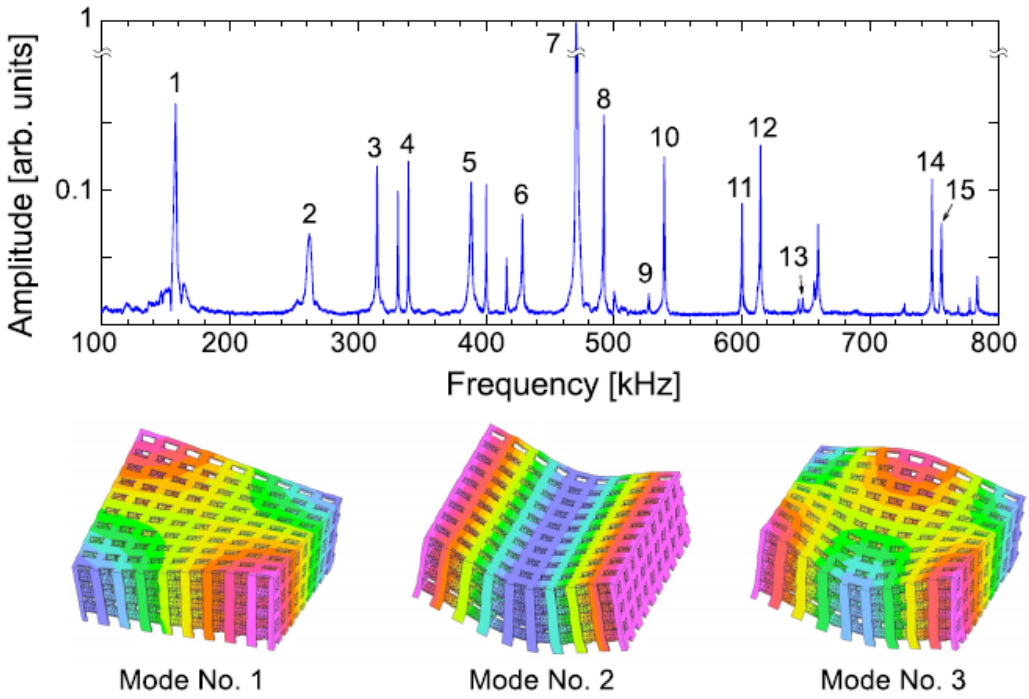

Figure 7.9.- The RUS spectrum used for determination of the elastic constants; the numbered peaks are those for which the modal shapes were clearly identified and, consequently, those which were involved in the inverse calculation of the elastic constants. In the lower row, examples of the corresponding modal shapes for the first three resonant modes are shown; the 3D visualizations were obtained by combining the experimental data from a scanning laser-vibrometer with a finite elements model of the sample.

The obtained set of resonant frequencies was then analyzed in order to determine the effective medium elastic constants of the structure, i.e., the anisotropic elastic constants of an effective homogeneous material with the same macroscopic elastic response as the architectured ceramics. The effective medium for the scaffold was expected to exhibit tetragonal elastic anisotropy, with six independent elastic constants c_{11}, c_{12}, c_{13}, c_{33}, c_{44}, and c_{66} (for the coordinate system outlined in Fig. 7.8). A combination of the conventional RUS approach and FEM was used to calculate these elastic constants with the following result:

c_{11} = 66.0 ± 0.7 GPa
c_{12} = 1.0 ± 0.1 GPa
c_{13} = 3.6 ± 0.1 GPa
c_{33} = 38.5 ± 1.2 GPa
c_{44} = 5.6 ± 0.1 GPa
c_{66} = 2.5 ± 0.1 GPa

For this calculation, the mass density of the scaffold is assumed as that of the effective medium (in this case, $\rho = 1.24\ g \cdot cm^{-3}$).

The resulting elastic constants obviously exhibit very strong anisotropy. The shear constants c_{44} and c_{66} are much lower than the stiffness against shearing along the diagonal symmetry planes $x'_1 = (x_1 + x_2)/\sqrt{2} = 0$ and $x'_2 = (x_1 - x_2)/\sqrt{2} = 0$, which is $c' = (c_{11} – c_{12})/2 = 32.5$ GPa; further on, the constants c_{12} and c_{13} are very low, i.e., the interlinking between the rods is so weak and so localized that the elongation of the rods in one direction does not lead to significant shrinking of the structure in the perpendicular direction. In Fig. 7.10a, this strong anisotropy is visualized by a plot of the directional dependence of the Young's modulus. Sharp maxima of the Young's modulus appear along the directions of the rods, while approximately ten times lower values of the modulus correspond to the diagonal directions. Similar strong anisotropy as for the Young's modulus was also observed for the Poisson's ratio; however, unlike for other anomalously anisotropic tetragonal structures,[40] the Poisson's ratio for the robocast scaffold was found to be positive for all directions (Fig. 7.11). While along the rods ν_{12} is nearly zero, in the diagonal directions it reaches values of as high as 0.85. On the contrary, the out-of-plane contraction (given by the ratio ν_{13}) is nearly zero for these diagonal loads, for which also the Young's modulus is very small. This means that under such loads, the scaffold deforms by soft twisting of the rods about the crossing points and consequent volume-preserving shearing in the tetragonal plane, while the spacing of the rods in the x_3 direction remains nearly untouched.

The FEM model of the scaffold constructed within the analysis of the resonant spectrum was used also to calculate the band structure of the material. In Fig. 7.10b, the lowest branches are shown for wave vectors oriented along the x_1 and x_3 directions, respectively. For each direction, the expected "acoustic" branches are seen, labeled in analogy to phononic branches as LA (longitudinal acoustic) and TA (transverse acoustic); the higher modes are analogous to the "optical" modes for phonons. The acoustic branches are obviously very close to linear in the frequency range where the RUS measurements were performed, which means that the approximation of the structure by the effective elastic medium is sufficiently accurate in this range, and the use of RUS for the determination of the effective medium elastic constants is fully justified. The band structure exhibits several features expected for acoustic metamaterials, for example, the negative derivatives of the frequency with respect to the wave number along the optical branches, which indicates the opposite directions of the wave vector and the group velocity.

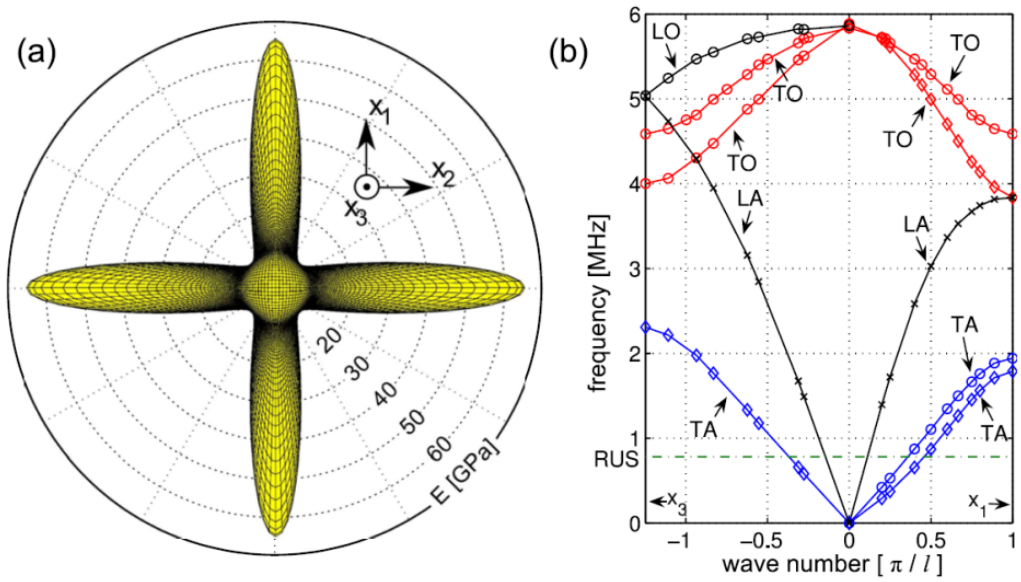

Figure 7.10.- a) Directional dependence of the Young's modulus (E) of the scaffold; b) the lowest frequency bands of the scaffold for wave vectors lying along the x1 direction (to the right from the origin) and along the x_3 direction (to the left); l stands for the spacing between the rods, the labels of the individual branches distinguish between longitudinal (L) and transverse (T) polarizations, and between acoustic (A) and optical (O) modes, in analogy with phonon spectra. The dashed green line denotes the upper limit of the RUS measurement.

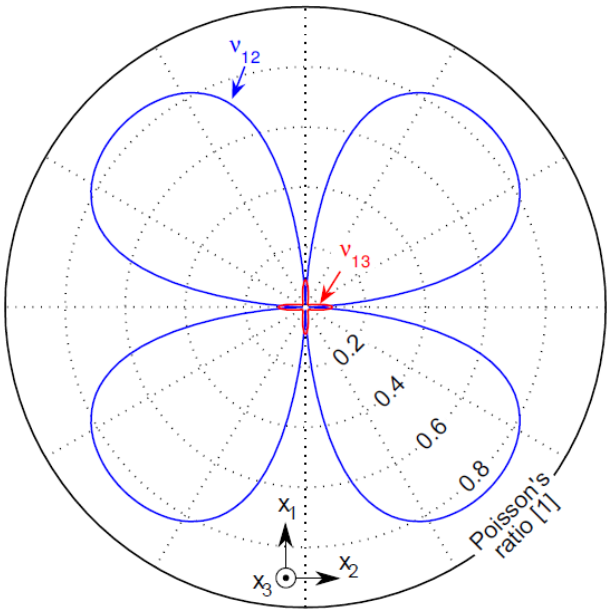

Figure 7.11.- Poisson's ratios for in-plane contraction (ν_{12}) and out-of-plane contraction (ν_{13}) under one-dimensional tensile load lying in the tetragonal (x_3 = 0) plane.

7.4. Conclusions

i) A novel hybrid COx/SiC cellular material, which exhibits superhydrophobic and superoleophilic properties, has been produced consisting on a 3D porous structure of ceramic pillars and micro-channels, where long, crystalline and aligned carboxyl functionalized MWCNTs were grown. The hybrid material also presents a 3D variable range hopping conduction with a room temperature electrical conductivity value of 360 $S \cdot m^{-1}$ that proves the good anchoring of the nanotubes to the SiC.

ii) Robocast SiC scaffolds exhibit several features typical for acoustic metamaterials. In particular, strong elastic anisotropy (that would involve strong energy focusing) and a phononic-like frequency band structure.

iii) The ceramic structure exhibits very low vibration damping, which makes the robocast scaffolds very promising for acoustic focusing applications without significant energy losses.

iv) Compared with other fabrication techniques for acoustic metamaterials, Robocasting provides higher versatility and enables the easy assembly of architectures with prescribed symmetry class of the unit cell, periodicity and size.

7.5. References

1. Adebajo MO, Frost RL, Kloprodge JT, Carmony O, Kokot S. Porous materials for oil spill cleanup: a review of synthesis and absorbing properties. J Porous Mat 2003; 10; 159-70.
2. Lau KKS, Bico J, Teo KBK, Chhowalla M, Amaratunga GAJ, Milne WI, McKinley GH, Gleason KK. Superhydrophobic carbon nanotube forests. Nano Lett 2003; 3; 1701-5.
3. Gui X, Wei J, Wang K, Cao A, Zhu H, Jia Y et al. Carbon nanotube sponges. Adv Mater 2010; 22; 617-21.
4. Hashim DP, Narayanan NT, Romo-Herrera JM, Cullen DA, Hahm MG, Lezzi P et al. Covalently bonded three-dimensional carbon nanotube solids via boron induced nanojunctions. Sci Rep 2012; 2; 1-8.
5. Lee C, Baik S. Vertically-aligned carbon nano-tube membrane filters with superhydrophobicity and superoleophilicity. Carbon 2010; 48; 2192-7.

6. Lee CH, Johnson N, Drelich J, Yap YK. The performance of superhydrophobic and superoleophilic carbon nanotube meshes in water-oil filtration. Carbon 2011; 49; 669-76.
7. Schwetz KA. In: Riedel R, editor. Handbook of Ceramic Hard Materials, Weinheim: Wiley-VCH; 2000, p. 683-748.
8. Roewer G, Herzog U, Trommer K, Müller E, Frühauf S. Silicon carbide-a survey of synthetic approaches, properties and applications. Struct Bond 2002; 101; 59-135.
9. Ci L, Bai J. Novel micro/nano scale hybrid reinforcement: multiwalled carbon nanotubes on SiC particles. Adv Mater 2004; 16; 2021-4.
10. Ci L, Ryu Z, Jin-Phillipp NY, Rühle M. Carbon nanotubes/SiC whiskers composite prepared by CVD method. Diam Relat Mater 2007; 16; 531-6.
11. Li W, Yuan J, Lin Y, Yao S, Ren Z, Wang H et al. The controlled formation of hybrid structures of multi-walled carbon nanotubes on SiC plate-like particles and their synergetic effect as a filler in poly(vinylidene fluoride) based composites. Carbon 2013; 51; 355-64.
12. Veedu VP, Cao A, Li X, Ma K, Soldano C, Kar S et al. Multifunctional composites using reinforced laminae with carbon-nanotube forests. Nat Mater 2006; 5; 457-62.
13. Chen X, Hong L, Xu Y, Ong ZW. Ceramic pore channels with inducted carbon nanotubes for removing oil from water. ACS Appl Mater Inter 2012; 4; 1909-18.
14. Parham H, Bates S, Xia Y, Zhu Y. A highly efficient and versatile carbon nanotube/ceramic composite filter. Carbon 2013; 54; 215-23.
15. Li P, Zong Y, Zhang Y, Yang M, Zhang R, Lic S et al. In situ fabrication of depth-type hierarchical CNT/quartz fiber filters for high efficiency filtration of sub-micron aerosols and high water repellency. Nanoscale 2013; 5; 3367-72.
16. Jung YJ, Wei B, Vajtai R, Ajayan PM, Homma Y, Prabhakaran K et al. Mechanism of selective growth of carbon nanotubes on SiO_2/Si patterns. Nano Lett 2003; 3; 561-4.
17. Botello-Méndez A, Campos-Delgado J, Morelos-Gómez A, Romo-Herrera JM, Rodríguez AG, Navarro H et al. Controlling the dimensions, reactivity and crystallinity of multiwalled carbon nanotubes using low ethanol concentrations. Chem Phys Lett 2008; 453; 55-61.
18. Ago H, Kugler T, Cacialli F, Salaneck WR, Shaffer MSP, Windle AH et al. Work functions and surface functional groups of multiwall carbon nanotubes. J Phys Chem B 1999; 103; 8116-21.

19. Kai-Yu Y, Wei X, Yu Z, Wei-Tao Z, Xin W. Synthesis and characteristics of Fe_3C nanoparticles embedded in amorphous carbon matrix. Chem Res Chinese U 2010; 26; 348-51.
20. Ensikat HJ, Ditsche-Kuru P, Neinhuis C, Barthlott W. Superhydrophobicity in perfection: the outstanding properties of the lotus leaf. J Nanotechnol 2011; 2; 152-61.
21. Lau KKS, Bico J, Teo KBK, Chhowalla M, Amaratunga GAJ, Milne WI et al. Superhydrophobic carbon nanotube forests. Nano Lett 2003; 3; 1701-5.
22. Li H, Wang X, Song Y, Liu Y, Li Q, Jiang L et al. Super-amphiphobic aligned carbon nanotube films. Angew Chem Int Ed 2001; 40; 1743-6.
23. Shklovskii BI, Efros AL. In Electronic properties of doped semiconductors in Spring Series in Solid-State Sciences 45, NY: Springer; 1984.
24. Acoustic Metamaterials: Negative Refraction, Imaging, Lensing and Cloaking, Springer Series in Materials Science Vol. 166, edited by RV Craster and S Guenneau (Springer, London, UK, 2013).
25. Guenneau S, Movchan A, Pétursson G, Ramakrishna SA. Acoustic metamaterials for sound focusing and confinement. New J Phys 2007; 9(11): 399.
26. Torrent D, Sánchez-Dehesa J. Acoustic metamaterials for new two-dimensional sonic devices. New J Phys 2007; 9(9): 323.
27. Lee J-H, Koh CY, Singer JP, Jeon S-J, Maldovan M, Stein O, Thomas EL. Ordered polymer structures for the engineering of photons and phonons. Adv Mater 2014; 26(4): 532-69.
28. Popa B-I, Cummer SA. Homogeneous and compact acoustic ground cloaks. Phys Rev B 2011; 83: 224304.
29. Zigoneanu L, Popa B-I, Cummer SA. Three-dimensional broadband omnidirectional acoustic ground cloak. Nat Mater 2014; 13(4): 352-5.
30. Liang B, Yuan B, Cheng J-C. Acoustic diode: Rectification of acoustic energy flux in one-dimensional systems. Phys Rev Lett 2009; 103(10): 104301.
31. Li J, Fok L, Yin X, Bartal G, Zhang X. Experimental demonstration of an acoustic magnifying hyperlens. Nat Mater 2009; 8(12): 931-4.
32. Ding Y, Liu Z, Qiu C, Shi J. Metamaterial with simultaneously negative bulk modulus and mass density. Phys Rev Lett 2007; 99(9): 093904.
33. Chen H, Chan CT. Acoustic cloaking in three dimensions using acoustic metamaterials. Appl Phys Lett 2007; 91(18): 183518.
34. Gorishnyy T, Maldovan M, Ullal C, Thomas EL. Sound ideas. Phys World 2005; 18: 24.

35. Yang S, Page JH, Liu Z, Cowan ML, Chan CT, Sheng P. Focusing of sound in a 3D phononic crystal. Phys Rev Lett 2004; 93(2): 024301.
36. Zhang X, LiuZ. Negative refraction of acoustic waves in two-dimensional phononic crystals. Appl Phys Lett 2004; 85(2): 341-3.
37. Leisure RG, Willis FA. Resonant ultrasound spectroscopy. J Phys: Condens Matter 1997; 9: 6001.
38. Ogi H, Sato K, Asada T, Hirao M. Complete mode identification for resonance ultrasound spectroscopy. J Acoust Soc Am 2002; 112: 2553.
39. Sedlák P, Seiner H, Zídek J, Janovská M, Landa M. Determination of all 21 independent elastic coefficients of generally anisotropic solids by resonant ultrasound spectroscopy: benchmark examples. Exp Mech 2014; 54(6): 1073-85.
40. Ogi H, Fukunaga M, Hirao M, Ledbetter H. Elastic constants, internal friction, and piezoelectric coefficient of α−TeO_2. Phys Rev B 2004; 69: 024104.

General Conclusions / Conclusiones generales

Conclusions

The overall conclusions of this manuscript can be divided according to the two groups of developed materials, in particular, cellular and bulk graphene/SiC-based ceramics.

- *Cellular materials:*

i) Complex 3D SiC and graphene/SiC lattices with different sizes and pore morphologies have been printed by Robocasting from pseudoplastic colloidal inks containing solids loadings of up to 44 wt.%, using nano- and micro-sized SiC raw particles, and GNPs contents of up to 20 vol.% in the composite structures.

ii) Robust and relatively lightweight 3D SiC and graphene/SiC architectures (0.9-1.6 $g \cdot cm^{-3}$) have been then successfully sintered by a pressureless SPS process, retaining in all cases the shape of the extruded filaments and the overall geometry of the structures.

iii) The individual rods comprising the 3D structures exhibit σ values that increase with the GNPs concentration up to a maximum of ~2300 $S \cdot m^{-1}$ for composites containing 20 vol.% graphene, resulting in an anisotropic electrical behavior of the 3D structures with values of 611 $S \cdot m^{-1}$ and 273 $S \cdot m^{-1}$ in the longitudinal and the transverse directions, respectively. The modelling of the electrical behavior points towards the important role of the rod electrical conductivity, the overlapping between adjacent layers, and the spacing between rods normalized to the rod diameter.

iv) Future applications for the 3D SiC-based structures include the manufacturing of superhydrophobic and superoleophilic advanced hybrid COx/SiC cellular devices for oil remediation, or the development of very promising acoustic SiC metamaterials for acoustic energy focusing applications.

- *Bulk materials:*

v) SPS allows full densification of SiC ceramics and GNPs/SiC composites with up to 20 vol.% GNPs at temperatures of 1800 ºC, when Y_2O_3 and Al_2O_3 are used as liquid phase forming additives. The sintering process has been proved to be controlled by the temperature evolution of the whole system resistance. In this way, electrical current confinement in the graphite foil enclosing the specimen has been induced by the use of an electrically insulating coating, which gives a faster, more effective and energetically profitable densification process of SiC-based ceramics when compared to the standard SPS set-up.

vi) A single-step approach for the in-situ growth of graphene during the ceramic densification by SPS resulting in well dispersed graphene flakes (3-4 vol.%) within the SiC matrix. The in-situ graphene growth mechanism is believed to be due to the simultaneous actions of the high temperature, the electric current passing through the graphite dies and specimen, and the partial vacuum, all of them involved in the SPS process.

vii) The mechanical characteristics of SPSed SiC materials are controlled by the crystalline character of the secondary phase, the SiC grain size, and the in-situ synthesis of graphene-like species. The yield stress and the resistance to quasi-plasticity increase with the microstructural refinement; whereas the presence of multilayered graphene at grain boundaries increases the resistance to cone/ring cracking and the toughness.

viii) The formation of an in-situ graphene-like conducting network within the SiC matrix and the simultaneous SiC doping lead to electrical conductivity values of as high as 935 $S \cdot m^{-1}$, up to eleven orders of magnitude larger than those obtained for similar SiC ceramics fabricated by conventional sintering techniques.

ix) The uniaxial pressure applied during SPS produces a major orientation of GNPs in the plane perpendicular to the pressing axis, leading to the formation of markedly anisotropic GNPs/SiC composites. In this way, GNPs/SiC composites present an electrical conductivity 4 to 6 times higher in the perpendicular than in the parallel direction to the pressing axis, increasing σ of the composites in both directions with the GNPs content up to three orders of magnitude as compared to the monolithic materials, reaching a maximum value at room temperature of 4380 S m^{-1} for composites with 20 vol.% GNPs.

x) The addition of GNPs to a SiC matrix reduces the thermal conductivity in the through-thickness direction but, conversely, increases the in-plane heat flow. K_T values of 152 and 9.9 $W \cdot m^{-1} \cdot K^{-1}$ for GNPs in the basal plane and along the c-axis, respectively, have been estimated using a model based on an equivalent thermal resistances system.

Conclusiones

Las conclusiones generales de este manuscrito se han clasificado según los dos grupos de materiales desarrollados, en concreto, materiales cerámicos celulares y materiales masivos ambos basados en grafeno/SiC.

- *Materiales celulares:*

i) Se han impreso mediante la técnica de robocasting estructuras 3D complejas de SiC y grafeno/SiC que presentan diferentes tamaños y morfologías de poros, todo ello a partir de tintas coloidales pseudoplásticas con un contenido en solidos de hasta el 44% en peso. Además, se han empleado polvos de partida de SiC con tamaños nano- y micrométricos y contenidos de hasta el 20% en volumen de GNPs en los materiales compuestos.

ii) Se han consolidado de forma satisfactoria, mediante un proceso de SPS sin presión, arquitecturas 3D de SiC y grafeno/SiC resistentes y relativamente ligeras (0.9-1.6 $g \cdot cm^{-3}$), reteniendo en todos los casos la forma de los filamentos extrudidos y la geometría global de las estructuras.

iii) Los valores de σ de los rodillos individuales que conforman la estructura 3D aumentan con la concentración de GNPs en el material compuesto hasta un máximo de ~2300 $S \cdot m^{-1}$ para los materiales conteniendo un 20% en volumen de grafeno, dando lugar a un comportamiento eléctrico anisótropo de las estructuras 3D con valores de 611 $S \cdot m^{-1}$ y 273 $S \cdot m^{-1}$ en las direcciones longitudinales y transversales, respectivamente. Se ha simulado el comportamiento eléctrico demostrando el importante papel que juegan la conductividad de los rodillos, el solapamiento entre capas adyacentes, y el espaciado entre rodillos normalizados al diámetro del rodillo.

iv) Las aplicaciones futuras de las estructuras 3D basadas en SiC incluyen la fabricación de dispositivos celulares híbridos de COx/SiC superhidrofóbicos y superoleofílicos para la descontaminación de aceite, o el desarrollo de metamateriales acústicos cerámicos extraordinariamente apropiados para focalización de energía acústica.

- *Materiales masivos:*

v) La técnica de SPS facilita la completa densificación a temperaturas de 1800 ºC tanto de los materiales de SiC monolíticos como de los compuestos grafeno/SiC, con contenidos de GNPs de hasta el 20% en volumen, empleando Y_2O_3 y Al_2O_3 como aditivos formadores de fase líquida. Se ha comprobado que el proceso de sinterización está controlado por la evolución de la resistencia de todo el sistema con la temperatura. Así, el empleo de un recubrimiento eléctricamente aislante, que confina la corriente eléctrica en el papel de grafito que envuelve la muestra, ha dado lugar a un proceso de densificación de los materiales cerámicos basados en SiC más rápido, efectivo y energéticamente rentable comparado con la configuración estándar de SPS.

vi) Es posible crecer grafeno *in situ* dentro del material cerámico durante la etapa de densificación por SPS, dando lugar a materiales nanocompuestos de SiC conteniendo un 3-4% en volumen de grafeno bien disperso en la matriz. Este crecimiento tiene lugar mediante un mecanismo que involucra la acción simultánea en el proceso de SPS de elevada temperatura, baja presión de gas, y la corriente eléctrica.

vii) Las características mecánicas de los materiales de SiC sinterizados mediante SPS están controladas por el carácter cristalino de la fase secundaria, el tamaño de grano del SiC, y la presencia en borde de granode especies carbonáceas basadas en grafeno. El límite elástico y la resistencia a la cuasiplasticidad aumentan con el refinamiento de la microestructura; mientras que la presencia de multicapas de grafeno en los bordes de grano incrementan significativamente tanto la resistencia al agrietamiento del tipo cono/anillo como la tenacidad.

viii) La formación in situ de una red conductora de grafeno dentro de la matriz cerámica, así como el dopaje del SiC durante la sinterización, dan lugar a valores de conductividad eléctrica de hasta 935 $S \cdot m^{-1}$, once órdenes de magnitud mayores que los obtenidos para cerámicas similares de SiC sinterizados mediante técnicas convencionales.

ix) En los materiales compuestos de GNPs/SiC, la presión uniaxial aplicada durante la sinterización por SPS produce la orientación mayoritaria de los GNPs en el plano perpendicular al eje de prensado, dando lugar a materiales con una marcada anisotropía. En concreto, estos materiales presentan conductividades eléctricas mejoradas hasta en tres órdenes de magnitud respecto del SiC monolítico, siendo σ de cuatro a seis veces mayor en la dirección perpendicular al eje de prensado que en la dirección paralela a éste, y alcanzando un valor máximo a temperatura ambiente de 4380 $S \cdot m^{-1}$ para los materiales que contienen un 20% en volumen de GNPs.

x) La incorporación de GNPs a una matriz de SiC reduce la conductividad térmica en la dirección paralela al eje de prensado del SPS pero, por el contrario, aumenta la conductividad en el plano perpendicular dada la orientación de las GNPs. Se han estimado valores efectivos de K_T para los planos basales y a lo largo del eje c de las GNPs de 152 y 9.9 $W \cdot m^{-1} \cdot K^{-1}$, respectivamente, empleando para ello un modelo basado en un sistema equivalente de resistencias térmicas.

Annexes

Annex 1

Abbreviations & Acronyms

A.1.1.- Abbreviations and Acronyms list

3D	Three-Dimensional
3DP	Three-Dimensional Printing
AC	Alternating Current
AFM	Atomic Force Microscopy
AM	Additive Manufacturing
APA	Ammonium Polyacrylate
AR	Aspect Ratio
AR_{50}	Median Aspect Ratio
B	Boron
BN	Boron Nitride
C	Carbon
C_P	Specific Heat
C_V	Heat Capacity per unit Volume
CA	Contact Angle
CAD	Computer Aided Design
C-AFM	Conducting-AFM
CNs	Carbon Nanostructures
CNTs	Carbon Nanotubes
COx	Oxygen-doped Carbon Nanotubes
CVD	Chemical Vapor Deposition
D	Inner diameter of RC nozzles
d(dz)/dt	Time derivative of dz (displacement rate in SPS)
d_{50}	Median grain size
DC	Direct Current
DIW	De-ionized Water
dz	Displacement in the SPS z axis
E	Elastic Modulus
Ec	Energy Consumption
ECAS	Electric Current Assisted/Activated Sintering
EDM	Electro-Discharge Machining
EDS	Energy-Dispersive X-ray Spectroscopy
EELS	Electron Energy-loss Spectroscopy
EG	Epitaxial Graphene

FAST	Field Assisted Sintering Technique
FDC	Fused Deposition of Ceramics
FEM	Finite-Elements Modelling
FESEM	Field Emission Scanning Electron Microscopy
FLG	Few-layered Graphene
FWHM	Full-Width at Half Maximum
G'	Shear elastic modulus
G'_{eq}	Shear elastic modulus at equilibrium
G_A	Area-specific contact conductance
GaN	Gallium Nitride
GAS	Octane Fuel
GFs	Graphene Fillers
GNP	Graphene Nanoplatelets
GO	Graphene Oxide
GPS	Gas-Pressure Sintering
H	Hardness
HA	Hydroxyapatite
HiP	Hot isostatic Pressing
HOPG	Highly Oriented Pyrolytic Graphite
HP	Hot Pressing
H-PEI	High molecular weight PEI
HRTEM	High-Resolution Transmission Electron Microscopy
I	Intensity
I_{2D}/I_G	Intensity Ratio of the Raman 2D- and G-bands of graphene
I_D/I_G	Intensity Ratio of the Raman D- and G-bands of graphene
IEP	Iso-electric Point
I_G	Intensity of the G band of graphene
I_{LO}/I_{TO}	Intensity Ratio of the Raman LO and TO peaks of SiC
K_{IC}	Fracture Toughness
K_T	Thermal Conductivity
$K_T^{\parallel}$	Through-thickness Thermal Conductivity
$K_T^{\perp}$	In-plane thermal conductivity
LA	Longitudinal-Acoustic
LEDs	Light Emitting Diodes
LO	Longitudinal-Optical mode
LOM	Laminated Object Manufacturing
L-PEI	Low Molecular weight PEI
LPS	Liquid Phase Sintering
LPSPS	Liquid-Phase Spark Plasma Sintering
MC	Methylcellulose

MEMs	Microelectromechanical Systems
MG	Micro-mechanically cleft graphene
MO	Mineral Oil
MOSFETs	Metal-Oxide-Semiconductor Field Effect Transistor
Mw	Molecular Weight
MWCNTs	Multi-walled Carbon Nanotubes
N20	Composition of nano-β-SiC powders with 20 wt% additives
P	Power
P_0	Contact indentation pressure
P_C	Critical loads for the onset of cone/ring cracking
P_{scaff}	Macro-Porosity of the Scaffolds
P_Y	Critical load for initiation of quasi-plasticity
PAS	Plasma Activated Sintering
PECS	Pulsed Electric Current Sintering
PEI	Polyethylenimine
pH_{iep}	pH at the IEP
PMMA	Poly Methyl Methacrylate
PMMS	Physical Property Measurement System
PMS	Polymethylsilsesquioxan
PO	Used Pump Oil
PS	Pressureless Sintering
PZT	Lead zirconate titanate
R	Resistance
RC	Robocasting
RC	resistance associated to the contacts
Rdie	resistance associated to the die
Rexp	experimentally measured resistance
rGO	reduced Graphene Oxide
Rmid	resistance associated to the middle part of the SPS assembly
RS	Resistive Sintering
RUS	Resonant Ultrasound Spectroscopy
Seff	Effective Cross-Section between adjacent rods
SEM	Scanning Electron Microscopy
Si	Silicon
SiC	Silicon Carbide
SiSiC	Silicon-infiltrated Silicon Carbide
SLA	Stereolithography
SLS	Selective Laser Sintering
SPS	Spark Plasma Sintering
SYM	Symmetric configuration of SPS
SYM-BN	Symmetric configuration of SPS with a BN layer
TA	Transverse-Acoustic
TaC	Tantalum Carbide

TCP	Tricalcium Phosphate
TGA-DTA	Thermogravimetric analysis-Differential Thermal Analysis
TO	Transverse-Optical mode
Ts	Set-point Temperature
UV	Ultra Violet
V	Voltage
v	x-y printing speed in RC
XPS	X-ray Photoelectron Spectroscopy
XRD	X-Ray Diffraction
Y	Yield stress
YAG	Yttrium Aluminum Garnet
YAM	Yttrium Aluminum Monoclinic
YAP	yttrium aluminium perovskite
YSZ	Yttria-Stabilized Zirconia

A.1.2.- Greek symbols

α	Thermal diffusivity
$\alpha^{\parallel}$	Though-thickness thermal diffusivity
$\alpha\perp$	In-plane thermal diffusivity
$\beta 20$	Composition of β -SiC powders with 20 wt% additives
$\beta 7$	Composition of β -SiC powders with 7 wt% additives
ϕ	Diameter of scaffold rods
$\dot{\gamma}$	Shear rate
$\dot{\gamma}_c$	Transition shear rate
η_{app}	Apparent viscosity
λ	Mean free path of phonons
$\lambda^{\parallel}$	Through-thickness mean free path of phonons
$\lambda\perp$	In-plane mean free path of phonons
μSLA	Microstereolithography
ν	Group velocity of phonons (speed of sound in the material)
ρ	Density, resistivity
ρ_{th}	Theoretical density
σ_f	Flexural strength
σ_L	Longitudinal conductivity of scaffolds
σ_{rod}	Electrical conductivity of single rods
σ_T	Transverse conductivity of scaffolds
τ	Shear stress
τ_y	Yield stress
ζ	Zeta Potential

Annex 2

Materials & Main Experimental Techniques

A.2.1.- Raw ceramic and graphene powders

The fundamental characteristics of the raw ceramic and graphene powders employed for the development of the different SiC-based materials is summarized in Table A.2.1, and Fig. A.2.1 shows FESEM images of the GNPs.

Table A.2.1. Description of the raw ceramic and graphene powders employed in the PhD.

Raw material	**Type, Company**	**Characteristics (d_{50}, polytype, purity)**
α-SiC	S-2022, Cerac	0.8 μm, polytype 6H, 99.9% purity
β-SiC	BF-17A, HC-Starck	0.5 μm, polytype 3C, > 98% purity
Nano-β-SiC	NanoAmor	45-55 nm, polytype 3C, 97.5% purity
Y_2O_3	Grade C, HC-Starck	2.09 μm, 99.99% purity
Al_2O_3	SM8, Baikowski Chimie	0.37 μm, 99.99% purity
GNPs	N006-010-P, Angstron Materials Inc.	10-20 nm thickness, ~14 μm *x-y* plane

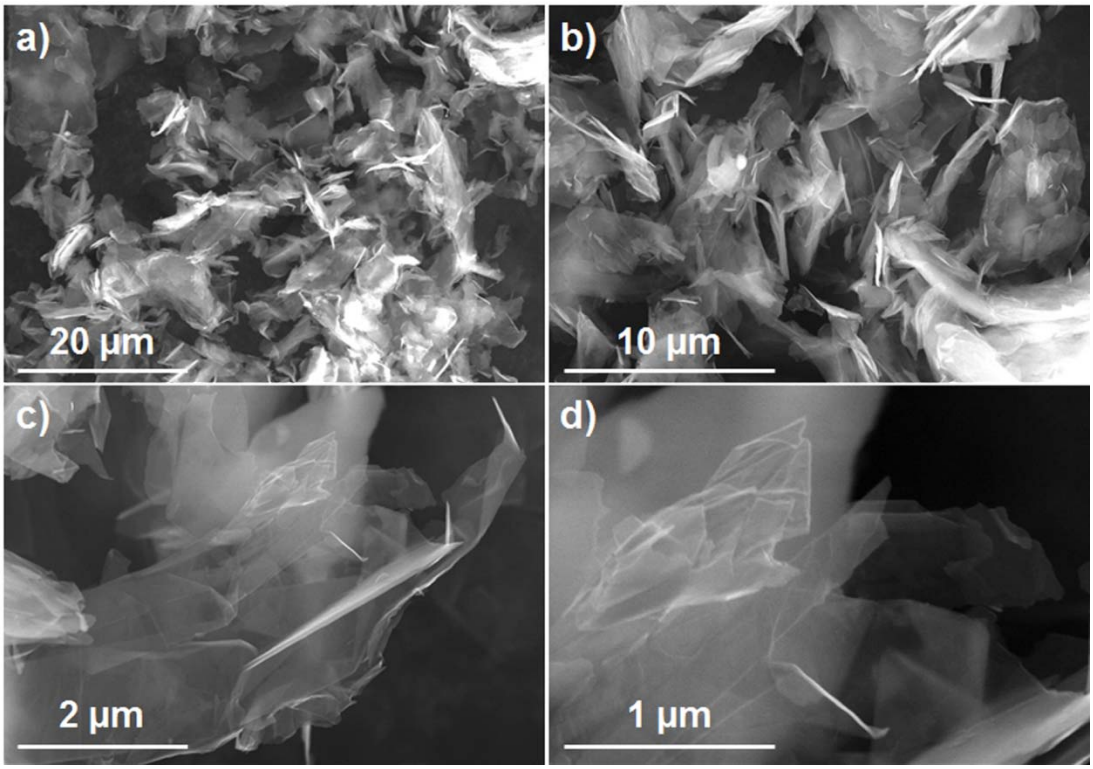

Figure A.2.1.- FESEM micrographs of the as-received GNPs at different magnifications.

Spectra and maps of pristine GNPs were acquired by simply using a drop of alcohol-based GNPs dispersions onto a glass-slide. By way of example, Fig. A.2.2a depicts the optical image of a pristine GNP analyzed by Raman spectroscopy. Fig. A.2.2b,c show the respective Raman maps constructed by integration of the graphene D (at 1358 cm^{-1}) and 2D (~2714 cm^{-1}) peak intensities. In these maps, it is noteworthy to see how the defects are mostly concentrated over the edges of the GNP. Indeed, no signal of defects (D-band) can be seen in the central area of the GNP (see spectrum in Fig. A.2.2d corresponding to position 1), whereas most of the D peak signal is generated over the edges (see spectrum corresponding to position 2). The presence of defects at the edges is also confirmed by the emergence of the D′ peak at ~1628 cm^{-1} overlapped with G as shown in Fig. A.2.2h.

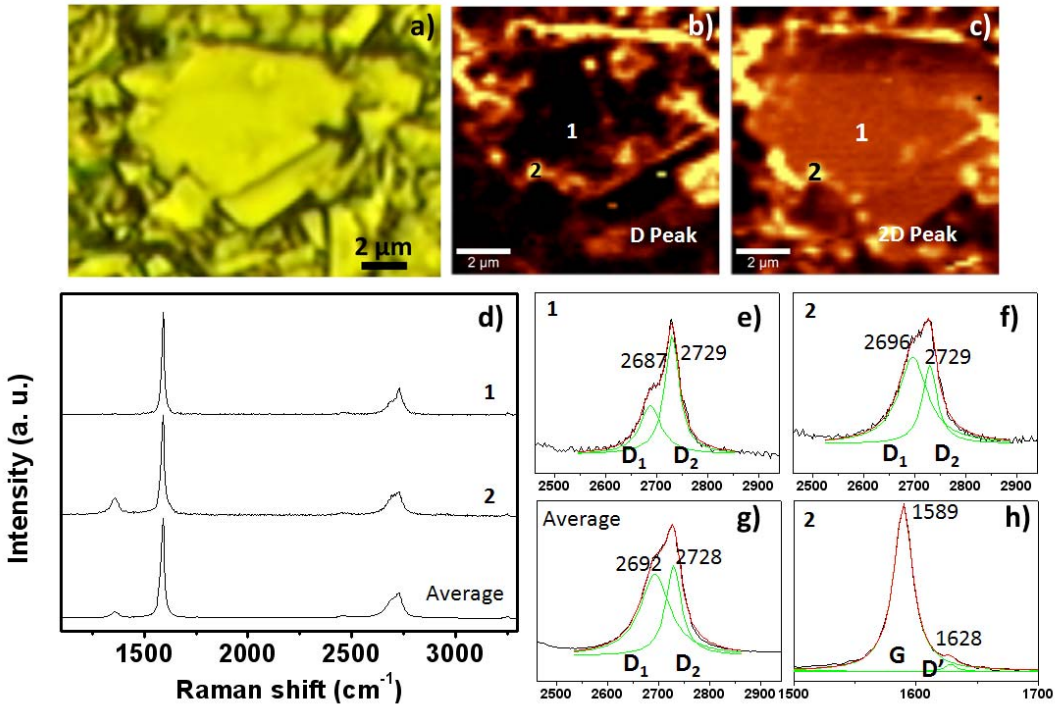

Figure A.2.2.- (a) Optical image of a pristine GNP on a glass slide and Raman maps of the integrated intensity of the D- (b) and 2D- (c) bands. (d) Plot of the Raman spectra collected at positions 1 and 2 in (b) and (c), and the averaged spectrum of the whole map. Deconvoluted 2D peaks corresponding to spectra labelled as 1 (e), 2 (f) and average (g). (h) D′ shoulder overlapped to the G-band on position 2.

As for the SiC powders, in Fig. A.2.3, diffractograms corresponding to the as-received α-SiC, β-SiC and nano-β-SiC powders are shown.

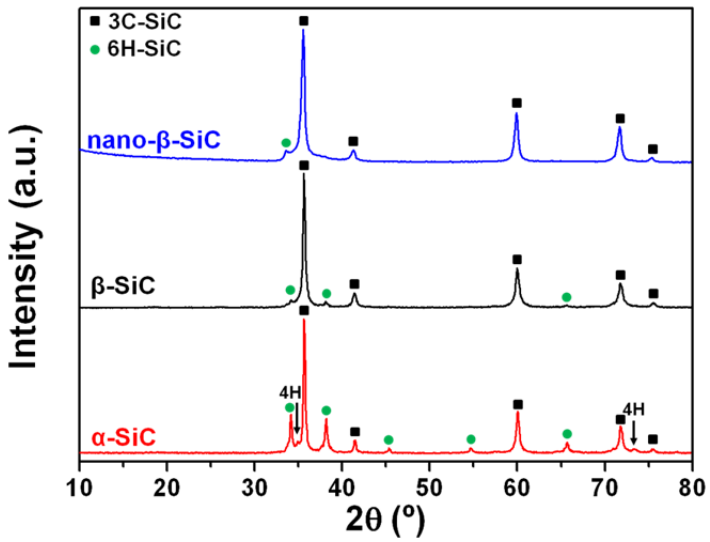

Figure A.2.3.- XRD patterns corresponding to the starting SiC powders used for the compositions prepared in this PhD Thesis.

A.2.2.- Ceramic-based powder compositions

For the preparation of the powder compositions, two procedures were used depending on whether the compositions contained GNPs or not:

i) GNPs-free compositions: SiC and the sintering additives, Y_2O_3 and Al_2O_3, were mixed by attrition milling in isopropyl alcohol for 2 h using Al_2O_3 grinding media. The solvent was evaporated from the suspensions in a rotary-evaporator at 90 °C and the resulting mixture was dried at 120 °C before sieving through a 63 μm mesh. The mass relationships between the three components vary depending on the composition used as explained in the main text.

ii) GNPs-containing compositions: GNPs were first dispersed in isopropyl alcohol by sonication for 1 h in an ultrasonic bath. Simultaneously, powder mixtures of SiC powders together with Y_2O_3, and Al_2O_3 in the proportions of 93:5:2 in wt.%, respectively, were attrition milled for 2 h in isopropyl alcohol using Al_2O_3 grinding media. The resulting ceramic slurry was mixed with the sonicated GNPs suspension and, then, stirred and sonicated for one more hour to obtain a homogeneous mixing of all components. The process continues by evaporating the solvent in a rotary-evaporator at 93 °C, drying at 120 °C and sieving through a 63 μm mesh. For these compositions, β-SiC was employed in all cases maintaining the mass ratio: 93:5:2 for $SiC:Y_2O_3:Al_2O_3$.

A.2.3.- Rheological characterization

A.2.3.1.- Zeta potential measurements

Zeta (ξ) potential measurements were carried out for pure SiC and SiC-PEI (SiC coated with both H-PEI and L-PEI) suspensions (volume fraction φ=0.01) as a function of pH on an electroacoustic spectrometer (DT-1200; Dispersion Technology, Bedford Hills, NY). The pH range probed was accessed by titrating the measurement sample with either 1M HNO_3 or 1M KOH aqueous solution and monitoring with a pH probe. For each suspension, two identical solutions were prepared, the pH value of which was measured as the initial value. One of the samples was titrated with HNO_3 to lower pH values, while the other sample was titrated with KOH to high pH values. Combination of these two branches represents final results. No background electrolyte was added to the suspension, such that the acid or base additions altered the ionic strength slightly. Likewise, measurements were taken for pure Al_2O_3, Al_2O_3-

PEI, Y_2O_3 and Y_2O_3-PEI suspensions (volume fraction φ=0.01). The objective of the measurement was to assess the isoelectric point for each surface chemistry and observe the similarity in colloidal behavior after adsorption of the PEI.

A.2.3.2.- Viscosity and elastic and viscous moduli

Two distinct measurement systems were used for the characterization of the inks: namely the concentric cylinders and the cone-plate systems (see illustration in Fig. A.2.4).

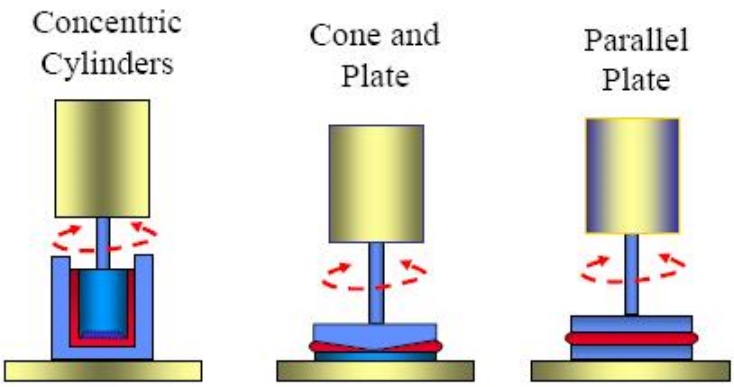

Figure A.2.4.- The three main rheological measuring systems (plastics.tamu.edu).

First, the concentric cylinders were employed to determine shear flow and shear elastic modulus for colloidal gel inks with and without the addition of APA (flocculant), namely weak gel and strong gel, using a stress-controlled rheometer (C-VOR 200; Bohlin Instruments, East Brunswick, NJ). A serrated cup and bob measuring system (C14; Bohlin) was used to mitigate wall-slip effects. The bob had a diameter of 14 mm and the cup had an inside diameter of 16 mm. A solvent trap apparatus consisting of a water reservoir and cover plate was used to minimize evaporation from the sample during the experiment. After loading inks into the measuring system, a pre-shearing of 1 s^{-1} for a period of 60 s and a following equilibration (zero shear rate rest) time of 1800 s were observed prior to each measurement.

The apparent viscosity (η_{app}) of the ink was measured as a function of increasing shear rate ($\dot{\gamma}$, from $\dot{\gamma}$ =0.01–150 s^{-1} at 20 discrete value points with logarithmic spacing). An equilibration time of 30 s was observed at each value of desired shear rate prior to reading the shear stress (τ). Oscillation measurements were performed at a frequency of 1 Hz to detect the elastic (G′) moduli, while an ascending stress sweep (τ = 50-1000 Pa) was applied with logarithmic spacing. Again, a 30 s equilibration was

observed prior to recording the complex modulus data. All measurements were carried out at a constant temperature of 25 °C.

The viscosity of the slurries was also determined with a rheometer (CVO 100 D, Bohlin Instruments, UK) equipped with cone-and-plate geometry (diameter: 40 mm; cone angle: 4º). The rheometer measuring system was covered with a fitting tool to reduce evaporation. η_{app} of the inks was measured as a function of increasing shear rate from $\dot{\gamma}$ = 0.01 -150 s^{-1} at 20 discrete points with logarithmic spacing.

Both systems were proven efficient for the characterization of Robocasting inks.

A.2.4.- Thermogravimetric analysis

These experiments were carried out by using DT-TGA (model SETSYS Evolution1750, Setaram). The TGA instrument weighs the sample as temperature is raised up, typically up to ~1000 ºC in the current experiments, at heating rates of 3 ºC·min^{-1}. When a component of the sample reacts with the chosen atmosphere (air in the present case), weight changes are thus measured. Associated to these processes, heat changes in the sample (either exothermic or endothermic) are identified by DTA.

A.2.5.- X-Ray Diffraction (XRD)

Especially with the objective of determining the phases of the ceramic species present both in the bulk materials and in the 3D scaffolds, either with or without graphene, X-Ray Diffraction (XRD, Siemens D5000, Munich, Germany) patterns were collected in the step-scanning mode using conventional Cu-K_α radiation. Diffractograms were generally acquired in the 10º < 2θ < 80º range, with a scanning rate of 2°·min^{-1} in steps of 0.05° and indexed with the help of the PDF2 database to identify the crystalline phases.

A.2.6.- Elemental analysis

Oxygen determination of the different starting SiC powders was performed using a LECO TC-436 equipment. Samples under analysis are introduced in a graphite crucible undergo voltages of ~ 5 V, generating electrical currents of up to 1200 A, in a

reducing atmosphere. Samples are decomposed and volatilized under these conditions, and the oxygen present in the samples reacts with graphite to form CO. Afterwards, CO is converted to CO_2 and analyzed in the measuring unit by infrared absorption. Thus, the amounts of oxygen present in the samples is inferred.

A.2.7.- Field Emission Scanning Electron Microscopy (FESEM)

The Field Emission Scanning Electron Microscopy technique equipped with an electron-gun source (model S-4700, Hitachi, Japan) was mainly employed in this PhD Thesis to observe the ceramic microstructures of materials as well as the fracture surfaces, and the micro-architectures of the 3D scaffolds. The habitual acceleration voltage employed for the samples was 10 kV, and the resolution was ~ 1-2 nm. Materials were generally sputter-coated for 1 min with an Au thin film prior to observation to prevent the accumulation of electrostatic charge at the surface.

In the case of observing microstructures on polished surfaces, plasma-etching of the surfaces was accomplished first (Emitech K1050X) with a mixture of gases of tetrafluoromethane (CF_4): oxygen (O_2) of 20:1 for ~ 25-30 min, to reveal the SiC grains microstructure. Afterwards, the metal sputter coating was done and, finally, the FESEM observations were carried out. The median size (d_{50}) and aspect ratio (AR_{50}) of the SiC grains were estimated by image analysis using the J-image software from FESEM micrographs, transformed to binary maps, measuring at least 500 grains in each material.

In the case of fracture surfaces, sintered SiC discs were shattered by impact with a WC ball. Fracture surfaces of samples were then sputter-coated with Au, as in the case of polished surfaces.

Finally, 3D-architectures of SiC were directly observed after the sputter-coating process.

A.2.8.- Confocal micro-Raman spectroscopy

The confocal micro-Raman spectroscopy technique was used to observe the different phases present in the SiC-based ceramics and composites used in this PhD Thesis. In particular, Raman spectra and maps give additional information to that of XRD, particularly in the case of carbon nanostructures whose three main bands (D, G and

2D) may indicate purity, crystallinity, defects or thickness in these species. Therefore, this technique has abundantly been employed throughout this thesis for the characterization of graphene. Raman has also proved its versatility for ceramic matrices showing clear differences among the different types of SiC ceramics as a function of the starting powders used, and their level of doping once sintered. The achievement of spectra and maps was carried out with a confocal micro-Raman microscope (model Alpha300, WiTec, Germany), using a laser excitation wavelength of 532 nm, and lenses of 100 x magnification. Normally, 10 x 10 μm^2 areas were scanned for the acquisition of maps, measuring 60 x 60 points (pixels). Acquisition times were typically of 20 ms per pixel. For individual spectra, conditions were adjusted according to the different requirements of the materials. Afterwards, the software supplied by WiTec (WITec Project 2.08) was employed for the elimination of background signals, construction of false-colour maps, etc. Finally, for the analysis of peaks associated to SiC and graphene bands, the Origin 8.0 software was utilized for the fitting of Lorentzian curves.

A.2.9.- The laser-flash method for thermal diffusivity

Thermal diffusivity (α) was measured by the laser flash method, to subsequently obtain the thermal conductivity (K_T) through the relation: $K_T=\rho\ c_p\ \alpha$, where ρ and c_p are the density and the specific heat of the measured materials, respectively. To determine α, the process for this method is as follows. The sample to measure is machined in a plane-parallel fashion with thicknesses below 1 mm and a well-defined geometry: disc-shaped for in-plane α measurements ($\alpha^{\perp}$; sample diameter: 20 mm) and square-shaped for through-thickness α measurements ($\alpha^{\parallel}$; sample size: 8.8 × 8.8 mm^2). After that, the laser-flash method can be applied. A laser pulse hits the sample onto one of the plane-parallel surfaces, producing a sudden heating that propagates throughout the sample; an infrared sensor collects, in the opposite sample side right above the temperature evolution as a function of time, right after the laser flash event, is recorded as an electrical signal, and the resulting V(t) curves are fitted to mathematical models to obtain $\alpha^{\parallel}$. Similarly, temperature measurements can be obtained in that opposite side at a certain distance from the centre with the aid of a mask (Fig. A.2.5), allowing the estimation of the radial propagation of heat. Mask 1 confines the laser pulse into a circle of radius r_0 = 2.5 mm on the center of the sample surface. Accordingly, heat flows through the sample and spreads out on the opposite surface, where a second mask is employed to define an annulus of radius *r* (*r* =

$2.2 \cdot r_0$) facing the IR detector. The temperature rise due to the radial heat flow is fitted by a two-dimensional model that determines an apparent in-plane thermal diffusivity. Thus, $\alpha^{\perp}$ values can be inferred with an implemented 2D model where the sample thickness and the $\alpha^{\parallel}$ values are input parameters. These two measurements enable the accomplishment of a characterization of thermally-anisotropic ceramics.

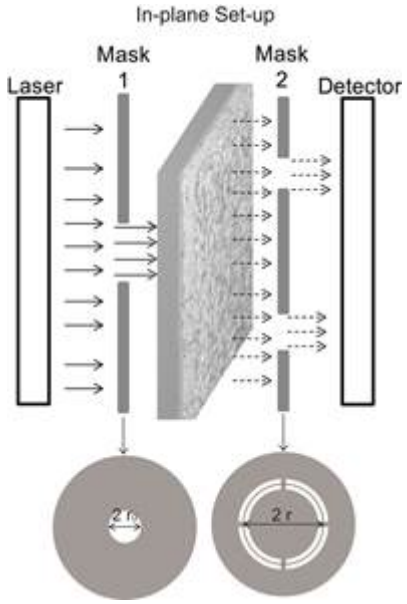

Figure A.2.5.- Schematic illustration of the mask device employed to determine $\alpha^{\perp}$.

The equipment used for the thermal characterization was a model Thermalflash 2200 (Holometrix, currently Netzsch). The $\alpha^{\parallel}$ measurements were carried out as a function of temperature (298-1073 K) in an Ar atmosphere (with experimental reproducibility during cooling, which means that the samples are stable throughout the heating cycle), whereas $\alpha^{\perp}$ measurements were only determined at room temperature, due to limitations of the equipment. All of the α data obtained correspond to the average of at least three measurements for each different temperature.

A.2.10.- Electrical conductivity measurements

A five-week stay at the CICECO (Centre for Research in Ceramics and Composite Materials) of the University of Aveiro under the supervision of Dr Filipe Figueiredo, financed by the Trust of the European Ceramic Society, was employed for the development of most electrical conductivity measurements. Also, the assistance of Dr. Domingo Pérez-Coll at ICV-CSIC is greatly acknowledged for the electrical measurements.

Owing to the anisotropy of the materials, measurements in the directions parallel and perpendicular to the SPS pressing axis were performed. A tubular support of alumina was employed as holder and placed into a furnace in order to perform the measurements under variable temperature (278-523 K) in an air atmosphere. Data were collected both during heating and cooling to verify the stability of the samples and electric contacts during the measurements. Platinum wires ensured the electrical connections between the samples and the measuring instrumentation. In all types of measurements, the conductivity was calculated as $\sigma = L(R \times S)^{-1}$, where R is the electrical resistance, S is the electrode surface area, and L is the distance between the electrodes. The electrical resistance of the platinum wires was recorded separately at the various temperatures and subtracted from the sample resistance.

For the bulk materials, samples were machined into bars of 15.0 × 3.5 × 2.5 mm^3. Therefore, σ for the directions parallel ($\sigma^{\parallel}$) and perpendicular ($\sigma^{\perp}$) to the SPS pressing axis was measured, respectively, with 2-probe *ac* and 4-probe *dc* methods. The impossibility of using 4 electrodes in the case of $\sigma^{\parallel}$, owing to the dimensions of the samples, was the cause for employing these two distinct methods (see Fig. A.2.6) whose results were proved to be reproducible. In *dc* measurements, at least five current values were applied in order to verify the linearity of the *I*–*V* relation, thus confirming the absence of electrode polarization, and allowing the estimation of the resistance by linear regression of the *I*–*V* data. The *dc* resistance was measured by imposing an electrical current (*dc* power supply Agilent E364 × A, USA) through the sample and measuring the potential drop (Fluke precision multimeter, USA) between 2 points separated by a precise distance. The voltage probes were ensured by platinum wires contacting the sample, whereas the current was introduced through the bar edges, painted with silver paste. The resistance between the two outer electrodes was in agreement between *ac* and *dc* values.

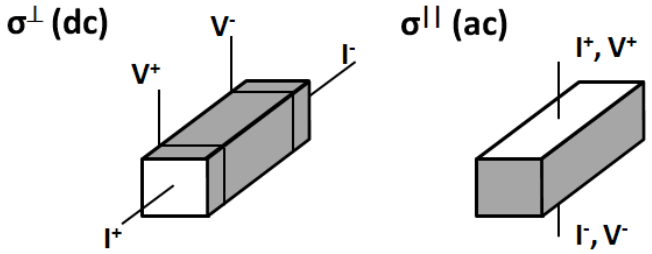

Figure A.2.6.- Diagram of the arrangements used for the *dc* and *ac* electrical conductivity (σ) measurements in the perpendicular ($\sigma^{\perp}$) and parallel ($\sigma^{\parallel}$) directions to the pressing axis of the SPS, respectively. The areas covered with the silver electrodes appear in white.

The *ac* conductivity data were obtained by collecting impedance spectra (potentiostat/galvanostat/frequency response analyser Autolab PGSTAT20, Netherlands) in the frequency range of 1 Hz-1 MHz with test signal amplitude of 100 mV. The impedance was measured between the larger surfaces (15.0 × 3.5 mm^2) of the sample, previously covered with silver electrodes using a commercial paste (Agar 6302, UK).

For the scaffolds, the silver paste was allowed to partially dry in order to increase its viscosity before being applied onto the sample, thus preventing the impregnation of the scaffold inner pores with silver. *Ac* conductance data were obtained by impedance spectroscopy.

A.2.11.- Resonant ultrasound spectroscopy (RUS)

As stated in the main text, RUS measurements were carried out in association with Dr. Hanus Seiner and collaborators, from the Institute of Thermomechanics of the Czech Republic. Resonant ultrasound spectroscopy (RUS) is a technique principally intended for the characterization of elastic properties of materials. Elasticity and geometry of the tested material determine the resonant frequencies of vibration of the materials when mechanically excited; thus, the elastic tensor of each material can be determined based on those resonant frequencies. Actually, the RUS technique allows the achievement of the elastic coefficients matrix.

In the case of the scaffolds, samples for RUS were approximately rectangular parallelepipeds cut from the central part of the robocast structure (see Fig 7.7b), so that it contained only the periodic structure of rods. To minimize the fracture of the individual rods during the cutting, the whole structure was, prior to the sample preparation, filled with a CrystalBond wax that was then dissolved and removed from the final sample. Samples were oriented so that the shortest and the longest edge of the parallelepiped were parallel to the rods, while the third edge was perpendicular to the rods, i.e. lying along the tetragonal axis.

The spectrum of free elastic vibrations of the sample was measured by a contactless, laser based RUS set-up,[1] in which the vibrations were both generated and detected by lasers. In order to obtain also the information on modal shapes of the individual resonant modes in the spectrum, the vibrational response was subsequently recorded at the cross-sections of the individual rods at the largest face of the sample. This was a simplified equivalent to scanning of the largest face of the sample usually adopted

for mode-sensitive RUS measurements. In this case, the density of the scanning mesh was determined by the density of the robocast structure.

[1]Sedlák P, Seiner H, Zídek J, Janovská M, Landa M. Determination of all 21 independent elastic coefficients of generally anisotropic solids by resonant ultrasound spectroscopy: benchmark examples. Exp Mech 2014; 54(6): 1073-85.

A.2.12.- Transmission Electron Microscopy (TEM)

Samples for TEM were prepared using conventional mechanical methods: first cutting, polishing, and finally dimpling. The thinning was completed in the Gatan Precision Ion Polishing System (PIPS) operated at 5 kV and an ion-beam angle of ~8º. After perforation, both the energy and the angle were reduced to ~2 kV and 4º, respectively, and kept thinning for another 5-10 min. The high resolution transmission electron microscopy (HRTEM) analysis was performed in a JEOL EM-2010f equipment with a field-emission source and accelerating voltage operating at 200 kV. This microscope is equipped with Energy-dispersive X-ray Spectroscopy (EDS) and Electron Energy Loss Spectroscopy (EELS, Gatan Model EnfinaTM1000 system).

A.2.13.- Atomic Force Microscopy (AFM)

Atomic force microscopy (AFM) was performed in collaboration with Prof. Carmen Ocal, from the ICMAB-CSIC, Barcelona. AFM measurements were under low humidity conditions (<5% RH, obtained by a continuous N_2 gas flux) using a commercial head and software from Nanotec.[1] Boron-doped diamond coated Si probes mounted on intermediate spring constant (k = 3.0 $N \cdot m^{-1}$) cantilevers were used. In the present conductive AFM (C-AFM) measurements, a horizontal set-up configuration was employed, in which the current is measured between the biased AFM tip (movable electrode) and a metallic counter-electrode clamp attached at the sample surface edge (millimeters apart) and directly contacted to ground. The conducting tip (top electrode) was placed in direct contact with the sample surface, under controlled load i.e. by using a normal force feedback, and the current between tip and sample was measured. Probed areas were mirror finished surfaces. In this nanoscale characterization, a cross sectioned surface parallel to the SPS pressing axis was chosen. The conducting response of the samples was obtained by: (i) simultaneously acquiring topographic images z (x,y) and current maps I (x,y) at a given voltage, and (ii) acquiring I–V curves at selected (x,y) locations. Tip-sample conditions were verified prior to and after each conductivity experiment by a

systematic determination of the adhesion force, from force versus distance curves. Current images were acquired in a non-invasive manner (no sample indentation) by using the contact operation mode at the lowest possible applied load while obtaining stable signals.

[1] Horcas I, Fernández R, Gómez-Rodríguez JM, Colchero J, Gómez-Herrero J, Baro AMWSXM. A software for scanning probe microscopy and a tool for nanotechnology. Rev Sci Instrum 2007; 78: 0137051–8.

A.2.14.- Dilatometry

A differential horizontal dilatometer (model Netzsch Gerätebau 402 EP), with a silica sample holder has been used for the measurements. SiC and GNPs/SiC samples were machined into plane-parallel bars of 12 x 3 x 2 mm^3 size, approximately, and the measurements were carried out in the longer axis of the specimens (coinciding with the direction perpendicular to the pressing axis). All the specimens were subjected to the same measuring conditions: 5 ºC·min^{-1} and up to temperatures of 850 ºC. Length expansions with temperature are transmitted from the push rod in contact with the sample to a transducer that moves into a coil able to translate electromagnetic induction into length variations.

A.2.15.- The Hertzian-indentation tests

Contact-mechanical properties of SiC-based ceramics were evaluated during a three-month stay under the supervision of Angel Luis Ortiz in the University of Extremadura, in Badajoz. Hertzian indentation can be defined as the indentation technique based on hard spherical indenters. The initial parameters for Hertzian indentation are shown in Fig. 1. Letting *F* be the indentation load and *r* the radius of the spherical indenter, a circle of radius *a* is formed on the surface of the plane tested material, whose elastic modulus is *E*, verifying:

$$a^3 = \frac{4kFr}{3E} \quad (1)$$

where *k* is a constant that depends on the Poisson's ratios of the sample and indenter (*v* and *v'*, respectively) and also on their elastic moduli (*E* and *E'*), according to:

$$k = \frac{9}{16}\left[(1 - v^2) + (1 - v'^2)\frac{E}{E'}\right] \quad (2)$$

Primes always indicate properties of the indenter.

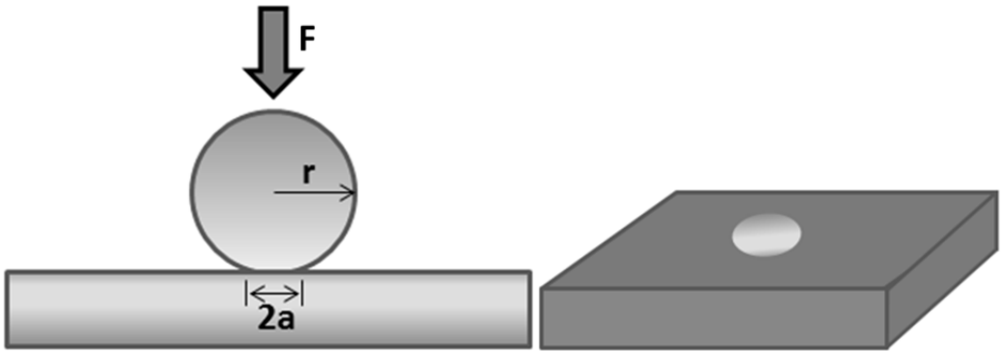

Figure A.2.7.- Schematic illustration of the indentation of flat ceramic surfaces with hard spheres, and their fingerprints on material surfaces.

Analogous to the stress-strain curves in other types of mechanical tests, such as compressive tests, the mean contact pressure, p_0 ($p_0=F/\pi a^2$), exerted on the sample below the indenter is normally represented versus the corresponding strain represented by the normalized radius of the printed circle (a/r). The p_0 parameter can be expressed in terms of *a* and *r*, as:

$$p_0 = \left(\frac{3E}{4\pi k}\right)\frac{a}{r} \qquad (3)$$

showing a linear dependence between p_0 and a/r, analogous to a basic stress-strain mechanical problem. The Hertzian contact tests for SiC were performed in air in the temperature range 25–850 °C using a universal testing machine (AG-IS 100 kN, Shimadzu Corp., Japan) equipped with a split furnace and Al_2O_3 pistons (see Fig. 2). By performing selective 1000 N indentations at two different crosshead speeds (0.05 mm min^{-1} and 0.005 mm min^{-1}), it was confirmed that loading rate does not play any role on the stress–strain curves at these testing temperatures, i.e. indentation diameters are kept constant regardless of the crosshead speed of the indenter even at the highest temperatures. Therefore, there are no creep effects that would distort the apparent size of the residual impressions. Indentations were carried out in sequences, for each sample and each temperature, at the same constant crosshead speed of 0.05 mm min^{-1}. For each sequence of indentations, increasing *F* values were applied within the range of 50–3500 N for all samples, using a Si_3N_4 half-sphere of 3 mm radius (*r*) as the indenter. Before testing, the specimens were first conveniently sputter-coated to facilitate observation of the contact zone even in the elastic regime and then stuck to the lower piston by using Al_2O_3 paste (Ceramabond 569, Aremco Products Inc., USA).

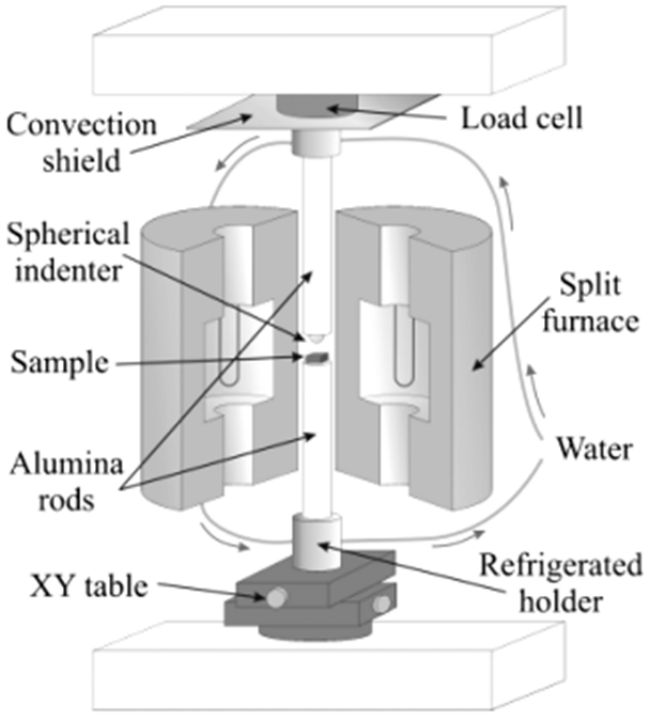

Figure A.2.8.- Schematic of the experimental setup used for the Hertzian tests at elevated temperatures.[1]

Temperature was raised at 6 °C min^{-1} to attain the different set points (25ºC, 400ºC, 700ºC, 850ºC) and maintained at those temperatures for 1 h to ensure thermal equilibrium before performing the tests. The contact radius, *a,* for each peak load was measured at room-temperature using an optical microscope with Nomarski interference contrast.

[1] Sánchez-González E, Meléndez-Martínez JJ, Pajares A, Miranda P, Guiberteau F, Lawn BR. Application of Hertzian tests to measure stress–strain characteristics of ceramics at elevated temperatures. J Am Ceram Soc 2007; 90(1): 149-53.

Annex 3

Dissemination of scientific research

A.3.1. Published papers in the frame of this PhD Thesis

1. “Geometrically complex silicon carbide structures fabricated by Robocasting”. K Cai, B Román-Manso, JE Smay, J Zhou, MI Osendi, M Belmonte, P Miranzo. J Am Ceram Soc 2012, 95(8): 2660-6.

2. “Fabricación de materiales cerámicos de β-SiC mediante Spark Plasma Sintering”. B Román-Manso, C Caravaca, M Belmonte, MI Osendi, P Miranzo. Proc. del XII Congreso Nacional de Materiales - XII Congreso Iberoamericano de Materiales 2012. Pp. 1-4. ISBN: 978-84-695-3316-1.

3. “In situ processing of electrically conducting graphene/SiC nanocomposites”. P Miranzo, C Ramírez, B Román-Manso, L Garzón, HR Gutiérrez, M Terrones, C Ocal, MI Osendi, M Belmonte. J Eur Ceram Soc 2013; 33:1665-74.

4. “Contact-mechanical properties at pre-creep temperatures of fine-grained graphene/SiC composites prepared in situ by Spark Plasma Sintering”. B Román-Manso, E Sánchez-González, AL Ortiz, M Belmonte, MI Osendi, P Miranzo. J Eur Ceram Soc 2014; 34(5): 1433-8.

5. “Microstructural designs of spark-plasma sintered silicon carbide ceramic scaffolds”. B Román-Manso, A de Pablos, M Belmonte, MI Osendi, P Miranzo. Bol Soc Esp Ceram Vidr 2014; 53(2): 93-100.

6. “Acoustic Metamaterial Behavior of 3D periodic architectures assembled by Robocasting”. A Kruisová, H Seiner, P Sedlák, M Landa, B Román-Manso, P Miranzo, M Belmonte. Appl Phys Lett 2014; 105: 211904.

7. “Aligned carbon nanotube/silicon carbide hybrid materials with high electrical conductivity, superhydrophobicity and superoleophilicity”. B Román-Manso, SM Vega-Díaz, A Morelos-Gómez, M Terrones, P Miranzo, M Belmonte. Carbon 2014; 80:120-6.

8. “Effects of current confinement on the Spark-Plasma sintering of SiC ceramics”. B Román-Manso, M Belmonte, MI Osendi, P Miranzo. J Am Ceram Soc 2015; 98(9): 2745-53.

9. “Enhanced electrical conductivity of silicon carbide ceramics by addition of graphene nanoplatelets”. B Román-Manso, E Domingues, FM Figueiredo, M Belmonte, P Miranzo. J Eur Ceram Soc 2015; 35: 2723–31.

10. “Tribological performance under dry sliding conditions of graphene / silicon carbide composites”. J Llorente, B Román-Manso, P Miranzo, M Belmonte. J Eur Ceram Soc 2016; doi: 10.1016/ j.jeurceramsoc.2015.09.040.

11. “Toughened and strengthened silicon carbide ceramics by adding graphene-based fillers”. M Belmonte, A Nistal, P Boutbien, B Román-Manso, MI Osendi, P Miranzo. Scripta Mater 2016; 113: 127-30.

12. “Finite elements modeling of mechanical and acoustic properties of a ceramic metamaterial assembled by robocasting”. A Kruisová, H Seiner, P Sedlak, M Landa, B Román-Manso, P Miranzo, M Belmonte. Accepted in Applied Mechanics and Materials 2016.

13. “3D-architectured graphene/silicon carbide composites with a patterned electrical performance”. B Román-Manso, FM Figueiredo, B Achiaga, R Barea, A Morelos-Gómez, M Terrones, MI Osendi, M Belmonte, P Miranzo. Submitted to Carbon. Ref. CARBON-D-15-02238.

A.3.2. Patents in the frame of this PhD Thesis

1. “IN SITU DEVELOPMENT OF GRAPHENE/SILICON CARBIDE CERAMIC COMPOSITES, METHOD FOR MANUFACTURING AND THEIR APPLICATIONS”.
P Miranzo, MI Osendi, M Belmonte, C Ramírez, B Román, H Gutiérrez, M Terrones, C Ocal.
Application No: WO2013US60614 20130919
Priority No: US201261703495P 20120920
Priority country: United State of America
Application date: 20/09/2012
Holder Entities: The Penn State University (PSU, USA), Consejo Superior de Investigaciones Científicas (CSIC).